University of Southampton
Faculty of Engineering, Science and Mathematics
School of Civil Engineering and the Environment

A NUMERICAL STUDY OF SPADE CELL PENETRATION

by

Siavash Farhangi, B.Sc., M.Sc.

A Thesis Submitted in Fulfilment of the Degree of Doctor of Philosophy
in the School of Civil Engineering and the Environment of the
University of Southampton

November 2005

UNIVERSITY OF SOUTHAMPTON
ABSTRACT
FACULTY OF ENGINEERING, SCIENCE AND MATHEMATICS
SCHOOL OF CIVIL ENGINEERING AND THE ENVIRONMENT

Doctor of Philosophy
A NUMERICAL STUDY OF SPADE CELL PENETRATION
by Siavash Farhangi

Push-in pressure cells (also known as spade cells) have been used in various construction projects in the UK to measure total in-situ stresses. In common with other direct measurement methods, the spade cell readings require interpretation to determine the in-situ stresses, as the process of installing the spade cell alters the initial stress/strain state of the soil. The commonly used empirical interpretation technique recommends a deduction of half of the soil undrained shear strength from the spade cell measurements. The validity of this approach is questionable as it is based on rather limited and inconsistent data, which only considers the soil undrained shear strength. The objective of this research was to quantify the effects of various parameters (e.g. soil strength, interface adhesion and cell geometry) on the stress-strain behaviour of the soil adjacent to a penetrating spade cell.

An extensive literature review has been undertaken to examine the current methods for analysing the soil penetration. It was evident from this review that none of the analysis techniques are individually capable of incorporating all aspects of the penetration process. Parallel numerical fluid flow and soil penetration analyses were therefore conducted to investigate the stress-strain changes that occur around a spade cell during penetration. These analyses were used to assess the influence of various parameters on soil behaviour for a three-dimensional penetration problem.

The results of these analyses showed that: (1) the shape of the spade cell's tip influences the strains generated around the spade cell; (2) the strain path method is capable of predicting soil deformations in deep three-dimensional penetration problems; (3) the deformations generated around the spade cell can only be successfully evaluated by performing three-dimensional analyses; (4) the stress-strain changes generated in the soil adjacent to the spade cell are influenced by to the soil undrained shear strength, soil shear modulus, interface adhesion, and the aspect ratio of the spade cell; (5) the influence of adhesion on deformations in soil penetration analyses is similar to the effect of viscosity in fluid flow analyses; (6) the horizontal stress distributions are relatively uniform along the inner-half of the spade cell width; and (7) horizontal stresses on the spade cell face at the end of penetration are higher in models where the boundary parallel to the spade cell face is displacement-controlled (rather than stress-controlled). It was concluded that the relative influence of various parameters on the spade cell measurements should be considered in comparing the in-situ stresses measured by spade cells in various field and chamber tests.

Keywords: Push-in pressure cell, in-situ stress, penetration, adhesion, three-dimensional numerical modelling

Contents

Lists of figures

Lists of tables

Acknowledgements

I have benefited greatly from the advice and guidance of my supervisors, David Richards and Chris Clayton, throughout this research. Special thanks go to David for initiating the project and his encouragement throughout the period of this work. I am grateful to Chris for his help in keeping me on the right track with his tireless guidance.

I would like to thank Richard Harkness for his enthusiasm and his valuable expertise in interpreting FLAC. I would also like to express my gratitude to other members of the Geomechanics research group for their useful suggestions during this project, especially William Powrie and Antonios Zervos.

I would also like to express my thanks to the School of Civil Engineering and the Environment at the University of Southampton that provided the studentship for pursuing this research.

I am in great debt to numerous friends who have made my stay in the UK enjoyable and prevented my permanent integration with the computer screen by dragging me out of the office every now and then.

Finally, I would like express my sincere gratitude to my mother, father and brother, as their regular phone calls have provided much motivation over the last four years.

List of symbols and abbreviations

Abbreviations

2D	two-dimensional
3D	three-dimensional
CEM	cavity expansion method
CFD	computational fluid dynamics
DMT	dilatometer
FD	finite difference
FE	finite element
FLAC	fast Lagrangian analysis of continua
PFC	particle flow code
NC	normally consolidated
OC	over consolidated
OCR	overconsolidation ratio
OD	oedometer
OP	overburden pressure
OR	over-read
RITSS	remeshing and interpolation technique with small strain
SBL	self-boring load cell
SBP	self-boring pressuremeter
SPM	strain path method
SSPM	shallow strain path method

Symbols

A_C	contact area
C_{int}	interface cohesion
d_i	distance of singularities from origin
B/w	aspect ratio

B/t	width to thickness ratio of sampler
E	modulus of elasticity
G	elastic shear modulus
H	distance from horizontal boundaries
I_r	rigidity index
K	elastic bulk modulus
K_u	undrained bulk modulus
K_0	at-rest earth pressure coefficient
k	interface stiffness
k_n	interface normal stiffness
k_s	interface shear stiffness
L	penetration length
N	number of elements
N_c	cone factor
R	distance from the right boundary
S_u	undrained shear strength
s	length
t	time
U	uniform flow velocity/penetration rate
u, v, w	velocity field
V, V_i	strength of singularities
w	half-width of the penetrating object
x, y, z	coordinates

α	interface adhesion factor
β	normalised horizontal stress change
Δz_{min}	minimum width of an element
ε	strain
$\varepsilon_{xx}, \varepsilon_{yy}, \varepsilon_{zz}$	horizontal (lateral), longitudinal and shear strains
$\varepsilon_{xy}, \varepsilon_{xz}, \varepsilon_{yz}$	shear strains
$\dot{\varepsilon}_{ij}$	strain rate
Φ	flow potential function
ϕ'	effective friction angle

ϕ_{int}	interface friction angle
γ_{oct}	octahedral strain
μ	Poisson's ratio
σ_{xx}, σ_{zz}, σ_{xz}	horizontal, vertical and shear stresses
σ_y	yield stress
τ_m	adhesive strength of the contact
Ψ	flow stream function

Subscripts

inc	increment
max	maximum
min	minimum

Prefixes

m	milli ($\times 10^{-3}$)
k	kilo ($\times 10^{3}$)
M	mega ($\times 10^{6}$)

1 INTRODUCTION

1.1 Background

The work described in this thesis was stimulated by the need for a fundamental examination of the changes that occur in a soil during the penetration of a push-in pressure cell (also known as "spade cell"). Spade cells have been used in various construction projects in the UK to measure total in-situ stresses. The existing interpretation techniques for spade cells are based on the comparison of their measurements with readings from alterative in-situ stress measurement methods. In these interpretation techniques, spade cell measurements are solely corrected by some factor of the undrained shear strength (S_u) of the soil. A more comprehensive assessment should however incorporate the influence of various parameters including soil parameters (e.g. shear strength and modulus), the geometry of the cell, and the adhesion on the cell-soil interface. This thesis presents the first step in quantifying the influence of these parameters on the behaviour of soil into which a spade cell is penetrated.

Numerical modelling has been carried out to investigate the various parameters that may influence the behaviour of a soil adjacent to a penetrating spade cell. Existing field data, which compare spade cell measurements with readings obtained from alterative methods, are relatively few, highly scattered and mainly limited to the London Clay. Chamber tests proved to be unsuccessful in providing results similar to the stress over-reads typically observed in field measurements. Numerical modelling techniques were therefore used to analyse the penetration of the spade cell into a soil and to evaluate the influence of a range of parameters on the stress-strain behaviour of the soil.

FLAC and FLAC^{3D} explicit finite difference programs have been employed in this research to model and analyse the undrained penetration of an idealised two and three dimensional spade cell geometry, termed the "simple wedge" and "chisel" respectively into saturated Tresca soil. FLAC modelling features such as large-strain formulations and interface logic make it particularly suitable for the realistic simulation of the continuous penetration phenomenon. The influences of various parameters on the soil behaviour were accordingly investigated in the 2D and 3D soil penetration models.

In order to verify the numerical analyses, FLAC and FLAC^{3D} outputs were compared with the results from the strain path analytical method (Baligh, 1984). The strain paths determined for an element in the soil penetration analyses were compared with strain paths evaluated for a streamline in the corresponding fluid flow analyses, to demonstrate that the modelling methodology did not introduce artefacts to the predicted soil behaviour.

1.2 Objective

The objective of this research is to identify the effects of various parameters on the behaviour of soil adjacent to a penetrating spade cell. The influence of soil undrained shear strength (S_u), soil shear modulus (G), interface adhesion (α), spade cell aspect ratio (B/w) and the boundary type (stress/displacement controlled) on the stress-strain response of the soil were evaluated in a series of two and three dimensional soil penetration analyses.

A further objective of this study was to assess the three dimensional nature of the changes that occur in the soil around the spade cell during penetration and the role of out-of-plane deformations.

1.3 Methodology

The objectives of this thesis were pursued by an extensive numerical modelling program. The methodology adopted for the numerical modelling can be summarised as follows:

- Determination of strain paths around the "simple wedge" from 2D fluid flow analysis;
- Determination of strain paths around the "simple wedge" from 2D soil penetration analysis;
- Evaluation of the influence of modelling and geometrical parameters (e.g. penetration rate, interface stiffness, mesh density, boundary location and penetration length) on the outputs by comparing the 2D fluid flow and soil penetration analyses;
- Examination of the influence of soil shear modulus, soil undrained shear strength and the interface adhesion on the penetration induced changes in a series of 2D soil penetration analyses for the "simple wedge" geometry;
- Determination of strain paths around the "chisel" from 3D fluid flow analysis; and
- Examination of the influence of soil shear modulus, soil undrained shear strength, interface adhesion, "chisel" aspect ratio and the boundary type on the penetration induced changes in a series of 3D soil penetration analyses for the "chisel" geometry.

1.4 Organisation of the thesis

This thesis is structured into eight chapters:

Chapter 1 provides an introduction to the thesis outlining the background, objectives and methodologies employed in this work.

Chapter 2 reviews the literature relating to the determination of in-situ stresses and interpretation of spade cell measurements. A comprehensive review of soil penetration analysis, with particular emphasis on the strain path method is included in this chapter. The adhesion theory of friction has also been summarized. This chapter concludes with an overview of the calculation methodologies employed by FLAC and FLAC^{3D}.

Chapter 3 presents the 2D fluid flow analyses used to determine strain paths around four geometries: the "simple wall", "simple wedge", "sharp wedge" and "blunt wedge". FLAC outputs were used to determine numerically the flow field around these geometries. The strain paths were also determined analytically for the "simple wall" and the "simple wedge" geometries. The results of 2D fluid flow analyses were used to validate the subsequent 2D soil penetration analyses.

Chapter 4 describes the methodology used to simulate the 2D penetration of the "simple wedge" geometry using the FLAC program. A parametric study was performed to assess the influence of the modelling and geometrical parameters on the computed outputs. The models were then used to evaluate the effects of soil properties and interface adhesion on the behaviour of soil during the penetration.

Chapter 5 presents the 3D fluid flow analyses performed using FLUENT and GAMBIT to determine strain paths for streamlines formed around the "chisel" geometry. The results of 3D fluid flow analyses were used to validate subsequent 3D soil penetration analyses.

Chapter 6 describes the methodology used to simulate the 3D penetration of the "chisel" geometry using the FLAC^{3D} program. The outcomes of the 2D soil penetration analyses (e.g. mesh refinement, boundary locations and penetration rate) were used for the selection of the modelling and geometrical parameters in the 3D analyses. The 3D soil penetration models were used to investigate the influence of soil properties (undrained shear strength and shear modulus), the soil-"chisel" interface adhesions and the "chisel" geometry on the stress-strain behaviour of soil during the penetration.

Chapter 7 discusses and compares the results of the 2D and 3D fluid flow and soil penetration analyses, been presented in Chapters 3 to 6 inclusive. The findings of various analyses are also compared with previous research.
Chapter 8 draws conclusions from the results, provides recommendations for the use of spade cell and makes suggestions for further research.

The arithmetic expressions used for generating the geometry of the "simple wall" and "simple wedge", and the determination of strain paths in 2D fluid flow analyses are presented in the *Appendices*.

2 LITERATURE REVIEW

2.1 Introduction

The magnitude of stresses within the ground has an important influence on the behaviour of buried structures. Furthermore, in-situ stress within the soil is the "most difficult stress to predict analytically or to measure" (Handy *et al.*, 1982). Reliable determination of in-situ stresses requires direct measurement. Push-in pressure cells (also referred to as spade cells) have proved to be robust for measuring in-situ stresses. However, spade cells tend to over-read in firm to very stiff clays and their measurements need to be corrected to determine in-situ stress values.

The uncertainties regarding the current interpretation (i.e. correction) technique, which compares measurements from a spade cell with those from alternative techniques, have illustrated the need for an independent interpretation method. The knowledge of the stress-strain behaviour of soil, as a spade cell penetrates the ground, can be used to determine a more robust interpretation technique for spade cell measurements. Various experimental, analytical and numerical techniques have been utilised to analyse the behaviour of soil around a penetration object (e.g. cone, sampler or pile). In this study, the changes around the spade cell have been determined using the strain path method (fluid flow analyses) and the FLAC and FLAC^{3D} finite difference programs (soil penetration analyses).

The objective of this chapter is to present a literature review on the concept of in-situ stress measurement, as well as a critical review of various techniques for analysing soil penetration with particular emphasis on the adhesion, the strain path method, and FLAC's modelling methodology.

2.2 Determination of in-situ stresses

In-situ stresses play a key role in engineering analysis as well as predictive modelling. A reliable assessment of in-situ stresses in soil is essential for the realistic analysis and optimum design of various geotechnical features, particularly, excavations, earth-retaining structures, and bored piles. The assessment of vertical in-situ stress is relatively straightforward from the profile of bulk unit weight for soil layers (Powrie, 2004). In-situ horizontal stress, however, is highly dependent on stress-strain relation and the geological history of the soil. It is perhaps not surprising that "the first question" tackled by Terzaghi was the determination of the in-situ horizontal stress in soils (Terzaghi, 1925a; Goodman, 1999).

Donath (1891) first suggested the concept of expressing the in-situ horizontal stress as a function of the vertical stress. The at-rest earth pressure coefficient (K_0) was later defined as the ratio of the in-situ horizontal effective stress to the in-situ vertical effective stress (Terzaghi, 1925b). A variety of theoretical and empirical relationships have been postulated for K_0 (Jaky, 1944; Janbu, 1975; Mayne and Kulhawy, 1982; Shohet, 1995). However, these relationships are based on laboratory tests or theories that do not address many of the geological characteristics of soils including structure, weathering, tectonic movements, vegetation and cementation (Hight and Leroueil, 2003). Wherever possible, *laboratory* or *direct* measurements should be made to obtain a realistic picture of the in-situ stress of a soil.

2.2.1 Laboratory and direct measurement methods

In-situ stress measurement methods have been the subject of many investigations over the last 60 years. Various laboratory and direct measurement methods have been proposed for the determination of in-situ stresses. Some of these methods are reviewed in the following paragraphs.

Suction measurements can be used to estimate the in-situ effective stress in clay samples. The pore water suction generated in the specimen when extruded from sampling tube is balanced out with its mean effective stress (Skempton and Sowa, 1963). This initial suction can be estimated by triaxial (Bishop *et al.*, 1965) or by filter-paper (Chandler and Gutierrez, 1986) tests. Hence, the horizontal in-situ stress can be determined from the measured pore water suction and the known value of the vertical effective overburden. This method was recently expanded for anisotropic materials where the horizontal in-situ stress was expressed as a function of cross-anisotropic ratio (Doran *et al.*, 2000). The inevitable disturbance and loss of moisture during tube sampling, sample transportation and extrusion of specimens makes the in-situ stresses estimated by this method unreliable.

The at-rest earth pressure coefficient for overconsolidated soils can be estimated from the overconsolidation ratio (OCR) (Ladd *et al.*, 1977). Oedometer tests (BSI, 1990) are carried out to calculate the preconsolidation pressure and consequently the OCR. The value of the at-rest earth pressure coefficient for an over consolidated soil ($K_{0(OC)}$) can then be determined from an empirical equation (Equation 2-1) where φ' is the effective angle of friction for the examined soil (Mayne and Kulhawy, 1982). The application of high stress values to determine the preconsolidation pressure, however, destroys the structural bonds, making the determined in-situ stresses questionable (Leroueil and Vaughan, 1990).

$$K_{0(OC)} = (1 - \sin\phi')OCR^{\sin\phi'}$$ **Equation 2-1**

Sampling disturbance influences various engineering properties of the soil including its strength, compressibility, porosity and stress (Skempton, 1943). In his state-of-the-art report, Wroth (1975) pointed out that “as our knowledge of the behaviour of real soils expands, so does our appreciation grow of the inadequacy of conventional laboratory testing”. Thus, attempts have been made to measure the horizontal stresses directly. The direct techniques devised to measure the in-situ stress of soil can be divided into four categories:

- **Seismic techniques**: these techniques are based on the dependency of the seismic body wave velocity on the effective stress of the ground (Fioravante *et al.*, 1998);
- **Pre-bored techniques**: devices are installed or tests are performed in a pre-bored hole such as Menard’s pressuremeter (Meigh, 1987) and hydraulic fracturing test (Massarsch *et al.*, 1975b);

- **Self-boring techniques**: disturbance is minimised by extracting the displaced soil as the device advances into soil. Self-boring devices include the self-boring pressuremeter (Baguelin *et al.*, 1972; Clarke, 1995), Camkometer (Wood and Wroth, 1977) and self-boring load-cells (Carder and Bush, 2001); and
- **Insertion techniques**: a cylinder or a blade is pushed into the ground to measure stresses. Devices in this category include push-in pressuremeter (Clayton *et al.*, 1995), Marchetti's flat dilatometer (Marchetti, 1980; Schmertmann, 1980), double membrane flat dilatometer (Tarchetti, 1975), rigid piston flat dilatometer (Akbar and Clarke, 2001), the K_0 stepped blade (Lutenegger and Timian, 1986), the total earth pressure cell (Tavenas *et al.*, 1975) and the miniature push-in pressure cell (Watts and Charles, 1988).

The push-in spade-shaped pressure cell (also known as a spade cell) falls into the last category. Massarsch *et al.* (1975b) reported the first use of spade cells, using a modified Glötzl earth pressure cell. Figure 2.1 shows a typical current spade cell design. The spade cell comprises of a spade-shaped oil-filled chamber formed from two steel sheets welded around the edges. The external dimensions of the oil-filled chamber are 100mm×200mm×7mm. This oil-filled chamber is connected to a vibrating-wire pressure transducer by a short length of steel tube forming a closed hydraulic system. The spade cell body often houses an integral piezometer, in the form of a porous filter disc, connected to a second vibrating-wire transducer. Other notable parts of the spade cell are the support plate and connector boss. Spade cells have also been used with pneumatic transducers. Spade cells are pushed steadily into ground for a distance of 0.5 to 1.0m from the end of a 15cm diameter borehole (Tedd and Charles, 1981).

Over the last thirty years or so, spade cells have been widely used to measure in-situ earth pressures (Massarsch *et al.*, 1975a; Tedd *et al.*, 1989; New and Bowers, 1994; Carder *et al.*, 1999; Powrie *et al.*, 1999; Richards *et al.*, 2005). Robustness, low cost, ease of use, reproducibility of readings, and capacity for long-term monitoring are some of the claimed advantages that have promoted their use.

The direct measurement of in-situ stresses with a spade cell poses the classic mensuration dilemma, as the measuring device, in this case spade cell, alters what is supposed to be measured. The action of pushing the spade cell into the ground alters the pore pressure distribution and the in-situ stress of the soil. In low permeability soils, several weeks may be required for the local pore pressures generated during the installation to dissipate. Even after pore pressures have stabilised, the inevitable disturbance of the soil due to installation causes an over-read in the measured in-situ stress values. For soft clays this over-read is less significant and can often be ignored, for stiff clays however, the spade cell measurements need to be interpreted.

2.2.2 Push-in pressure cell interpretation techniques

Spade cell measurements in stiff clays should be adjusted by a correction factor related to the undrained shear strength (S_u) of the clay (BSI, 1999). In this section, the existing theoretical and experimental interpretation techniques for spade cells are discussed.

The horizontal stress acting on the face of a spade cell can be determined for a prescribed soil displacement using the theory of elasticity (Finn, 1963). However, even if the soil could be modelled realistically as an elastic medium, determination of an equivalent Young's modulus appropriate for the complex stress path that the soil experiences during the installation is impractical (Tedd and Charles, 1983).

The main method for determining the spade cell over-read due to installation is through an experimental approach that involves comparing the stabilised spade cell readings with measurements from alternative techniques at the same site (Tavenas *et al.*, 1975). Table 2.1 lists some of the previous comparisons performed to evaluate the magnitude of the spade cell over-read. Massarsch (1979) used inflatable rubber cushions to apply horizontal pressures on a vertically installed Glötzl pressure cell and calculated the spade cell over-read in the Ska-Edeby site near Stockholm, Sweden. In other investigations in the UK during the last 20 years (Penman and Charles, 1981; Tedd and Charles, 1981; Powell *et al.*, 1983; Tedd and Charles, 1983; Tedd *et al.*, 1984; Tedd *et al.*, 1985; Temporal and Lawrence, 1985; Carder and Symons, 1989; Tedd *et al.*, 1989; Uglow, 1989; Ryley and Carder, 1995; Clark *et al.*, 2004) spade cell measurements have been compared with the overburden pressures

(OP); stresses determined from the oedometer (OD) and suction tests; or measurements made by the dilatometers (DMT), self-boring load cells (SBL) and self-boring pressuremeters (SBP).

Tedd and Charles (1983) used the data from Ska-Edeby (Massarsch, 1979), Cwmwernderi (Penman and Charles, 1981), Bell Common (Tedd and Charles, 1981), Balham, Oxford and Cowden (Powell *et al.*, 1983) to derive a correction factor for spade cells. They concluded that the amount by which a spade cell will over-read when installed in firm to stiff clays depends upon the stiffness of the soil. Due to the difficulties in determining the appropriate soil stiffness, a correlation between the spade cell over-read and the undrained shear strength (S_u) of the soil was proposed by them. This was considered reasonable as the undrained shear strength of a soil is related to its stiffness, and S_u is a commonly determined soil parameter. It was suggested that, if alternative measurements had not been made at a specific site, spade cell readings should be reduced by $0.5S_u$ to account for the installation effects.

Carder and Symons (1989) added measurements made at a site in Berkshire to the previous data (Ska-Edeby, Cwmwernderi, Bell Common, Balham, Oxford and Cowden) to determine the spade cell over-read. They also updated the Oxford test results by assigning a lower S_u to the examined clay (Temporal and Lawrence, 1985). Their work showed that for soils with a higher S_u, the over-read might be significantly greater than $0.5S_u$.

Tedd *et al.* (1989) adopted the data from the following sites: Ska-Edeby, Cwmwernderi, Bell Common (Tedd *et al.*, 1984; Tedd *et al.*, 1985), Balham, Oxford, Cowden, Berkshire, Brent Cross, Grangemouth and Madingley (Uglow, 1989). They concluded that the magnitude of the over-read varies for different soil types. It was suggested, however, that reducing the spade cell readings by $0.5S_u$ generally improves the accuracy of in-situ stress measurements.

Ryley and Carder (1995) compared horizontally aligned spade cell measurements with the calculated overburden pressures for London Clay at the Heathrow Express trial tunnel. They added these measurements to the over-read estimations from previous experiments at Bell Common, Balham, Berkshire and Brent Cross. The significant divergence from a $0.5S_u$ correction for very stiff clays formed the basis of the use of higher correction values for these clays and gave rise to the use of a bilinear correction function. For design purposes, they proposed a correction of $1.5(S_u-100)$ for $S_u>150$kPa and $0.5S_u$ for $S_u<150$kPa.

In a more recent study, Clark *et al.* (2004) compared readings from a horizontally aligned spade cell installed in Atherfield Clay (Xu, 2005) with the overburden pressure at the Channel Tunnel Rail Link, Ashford, Kent. The construction of a large drainage sump provided an opportunity to compare cell readings with the calculated over burden. The spade cell measurements were found to be $0.3S_u$ higher than the estimated overburden pressure. The corrected stress values were consistent with the in-situ total stresses determined from self-boring pressuremeter readings (Clark, 2005).

2.2.3 Validity of interpretation techniques

The validity of the experimental interpretation approaches commonly adopted for spade cell measurements is questionable from various perspectives (Farhangi *et al.*, 2005). Figure 2.2 shows the results of twelve previous experiments performed to evaluate the spade cell over-read values in clays. The correlation between the undrained shear strength and over-read is poor and the data points do not follow a clearly identifiable trend. It is also evident in Table 2.1 that these comparisons have been made for a narrow range of soil types, mainly the London Clay. Determining the spade cell installation effects using alternative measurement techniques is also unsatisfactory since all laboratory (Burland and Maswoswe, 1982) and direct measurement (Jardine, 1992a) techniques inevitably introduce a level of disturbance to the soil.

Perhaps the greatest uncertainty in these correlations stems from the determination of S_u for the soil. In these experiments, S_u was determined from a range of field tests including SPT, self-boring pressuremeter data, plate loading tests (Powell *et al.*, 1983), vane tests (Massarsch, 1979), and undrained triaxial tests on 100mm (Tedd and Charles, 1983; Carder and Symons, 1989) and 38mm (Penman and Charles, 1981; Temporal and Lawrence, 1985) diameter samples. The determined S_u value is dependent on the measurement method used, and is highly sensitive to sample disturbance (Hight *et al.*, 1992; Hight and Leroueil, 2003). Cautions should therefore be exercised when comparing S_u values determined from various methods (Marsland and Randolph, 1977; Wroth, 1984). Consequently, the S_u-correlation does not necessarily give a reliable estimate for the over-read.

Although, spade cells satisfy the requirements for a successful in-situ stress measurement device (Tavenas, 1975; Weiler and Kulhawy, 1982), there is not a robust independent methodology available for the interpretation of their measurements in firm to very stiff clays (S_u>40kPa) (BSI, 1986). An understanding of the changes that occur in the soil as a spade cell penetrates the ground could provide a sound basis for the interpretation of spade cell readings.

2.3 Soil penetration

Many geotechnical topics are associated with penetration, including foundation elements (e.g. push-in piles, caissons), in-situ devices (e.g. cones, dilatometers), and samplers. An understanding of the influence of the penetration process on the stress-strain behaviour of soil is essential for a rational design of foundation elements, interpretation of in-situ tests and assessment of sampler disturbances. The importance of the penetration influence on geotechnical topics is further illustrated by some examples in the following paragraphs.

Pile foundations are used to carry and transfer the load of a structure to the bearing ground located at some depth below the surface. Analytical methods for predicting the bearing capacity or settlement of piles involve assuming a particular failure mechanism and uniform soil properties (Durgunoglu and Mitchell, 1975a; Randolph and Wroth, 1978). However, instrumentation has shown that various soil parameters such as the in-situ stress and shear strength change in the adjacent soil during pile penetration (Roy *et al.*, 1981; Randolph *et al.*, 1994). Consequently, the measured resistance of a pile would be different from the predicted values.

The cone penetration test was developed in Holland in the 1930s (Barensten, 1936) and has been since regularly used to derive soil parameters, estimate pile capacities and evaluate footing settlements (Durgunoglu and Mitchell, 1975b; Vaughan *et al.*, 1988). The simplicity and robustness of the cone tests even made cone penetration tests part of the lunar exploration programme (Sullivan, 1994). Correlations between cone measurements and soil properties are mainly based on cavity expansion solutions (Meigh, 1987). However, owing to the simplifying assumptions made in the cavity expansion method, the suggested correlations can only provide an approximation for the soil parameters (Yu and Mitchell, 1998).

Tube sampling is routinely performed in site investigation programmes (Clayton *et al.*, 1995). High strain levels generated as a result of the penetration of sampler tubes are an inevitable source of soil disturbance that alters soil characteristics including the mean effective stress, its structure and water content. The consequences of these changes are reductions in the strength, stiffness, yield stress and soil compressibility (Hight *et al.*, 1992; Hight, 1993; Hight, 2001; Santagata and Germaine, 2002). Although sampling disturbance has been the subject of extensive research for many years, there is still a lack of widely accepted methods for identifying and quantifying the disturbance effects.

2.4 Analysis techniques for soil penetration

The various techniques adopted to evaluate the influence of the penetration process on piled foundations, in-situ measurements or samplers can be divided into three broad categories: *experimental*, *analytical* and *numerical*. These techniques are reviewed in the following sections.

2.4.1 Experimental techniques

Experimental approaches have always been central to the development of the engineering knowledge. Various experimental approaches utilised to investigate soil penetration problems are:

- Deformation measurement techniques;
- Triaxial tests; and
- Chamber tests

Various techniques have been developed to measure soil deformations adjacent to a penetrating object. These techniques can be divided into three groups, based on the method they employ to measure deformations: *embedded markers*, *exposed-surfaces* and *transparent soils*. The merits of these techniques for measuring deformations encountered in penetration experiments are reviewed in the following paragraphs.

Artificial markers such as lead shots were used in reconstituted soil samples to trace deformations during penetration. Markers could be traced in successive radiographs exposed to the X-ray to measure soil deformations (Gerber, 1929). Bulky equipment, screening conditions required and the influence of the embedded markers on soil behaviour are some of the disadvantages of this method.

A pattern in the exposed surface of soil can be used to determine deformations without the need for the use of embedded markers in the specimen. In the stereo-photogrammetric method, two photographs of an object from different camera stations are used to produce a stereoscopic image. The position of any point during penetration can then be scaled with the aid of a reference point (Butterfield *et al.*, 1970).

Particle Image Velocimetry (PIV) is a more recently developed image processing method, which uses digital photography. In PIV, an image of the exposed soil surface is divided into a grid of patches, patterns within the grid are then compared between subsequent images to evaluate displacements generated due to the penetration (White, 2002). Recent advances in digital photography have made the accuracy and precision of measurements made using the PIV method more reliable and affordable than earlier photogrammetric methods (White *et al.*, 2003). However, the requirement for an exposed surface makes these methods more appropriate for examining plane strain problems (White and Bolton, 2004).

Transparent soils (i.e. a slurry of amorphous silica, mineral oil and solvent) have been used to examine the three-dimensional nature of deformations around penetrating objects (Welker *et al.*, 1999). An optical measuring technique using a monochrome video camera was used to investigate the deformation pattern during the penetration of a flat tip object into the transparent soil (Gill and Lehane, 2001). Optical measurements showed that particles return to their initial vertical position, as the penetration continues (Figure 2.3). Although the three-dimensional deformation patterns were determined from these tests, estimating the complex soil behaviour with a silica slurry is not justifiable. In addition, boundaries have to be set close to the penetrating object, due to the rapid reduction in transparency of the slurry with distance, which consequently influences (i.e. boundary effects) any measurements made using this technique.

Triaxial tests may be performed to assess the changes that occur in a soil during the penetration. Changes in soil characteristics adjacent to a penetrating object can be examined by applying a known stress or strain path to a soil specimen in a triaxial test. For example, to assess the effects of sampling disturbance, a series of triaxial tests with the peak strains set to values typically reached during sampling have been undertaken (Siddique, 1990; Siddique *et al.*, 1999). The main drawback of this method is the requirement for a known stress/strain path to be applied in the test.

Chamber tests have been used to calibrate in-situ devices. In a chamber test, the initial known in-situ stress of the soil is compared with the measurement made by the device penetrating into the chamber. Dilatometers (Baldi *et al.*, 1986) and cone penetrometers (Houlsby and Hitchman, 1988) have been calibrated by chamber tests in dry sands. The main limitation of chamber tests is the influence of boundaries on the test results (Fahey *et al.*, 1989). The results of chamber test have been hence evaluated with analytical solutions (i.e. cavity expansion) in order to assess the effects of the chamber size (Schnaid and Houlsby, 1991; Salgado *et al.*, 1997; Salgado *et al.*, 1998). Attempts have also been made to reduce the influence of boundaries by using a relatively flexible lateral boundary made of a rack of steel rings (Hsu and Huang, 1999).

Chamber tests have also been carried out to investigate the influence of various penetration parameters on the capacity of scaled foundation models. For example, chamber tests were performed with dry sands to investigate the role of wall thickness, pile diameter and in-situ stress on the capacity of open-ended and closed-ended jacked piles (Lehane and Gavin, 2001; Lee *et al.*, 2003). Similar to the calibration tests performed, the influence of boundaries should be minimised and taken into account before generalising the results of these chamber tests.

In the case of spade cells, a series of chamber tests were performed in the University of Pretoria (SA) in collaboration with the University of Southampton in 2001 and 2002 to determine the over-read in controlled laboratory conditions (Grobbelaar, 2002). Figure 2.4 shows a schematic view of the chamber. The vertical load was controlled by air pressure build up in the void between the top lid and rubber membrane (Head, 1998). The spade cell was pushed horizontally into the compacted clay. The tests were however, unable to record any over-read in the stabilised spade cell measurements.

Some suggestions for improving tests from the literature include: use of two-stage consolidation process (rather than the vibrating hammer) to produce stiff cohesive samples (Voyiadjis *et al.*, 1993); use of rigid plates to apply the vertical load (rather than the flexible membrane) to improve the consistency of loading conditions (Kurup *et al.*, 1994); and provision of additional embedded pressure cells to monitor the in-situ stresses within the specimen.

2.4.2 Analytical techniques

Theoretical analysis of soil penetration is difficult due to the large deformations and nonlinearities involved. However, various approximate analytical techniques have been proposed to provide an insight into the complex soil behaviour during the penetration. The main analytical techniques used for studying the penetration of an object into a soil mass include:

- Bearing capacity method;
- Cavity expansion method; and
- Strain path and shallow strain path methods

One of the first analytical techniques to analyse cone penetration was to treat the penetration process as a bearing capacity problem (Skempton, 1951). The cone resistance was assumed to be equal to the collapse load of a deep foundation determined using the limit-equilibrium (Meyerhof, 1961) or the slip-line (Sokolovski, 1965) methods. In the limit-equilibrium method, the global equilibrium equation is solved to determine the failure load for an assumed failure mechanism. In the slip-line method, a yield criterion is combined with equilibrium equations to derive a set of plastic equilibrium equations in the soil mass. The collapse load is consequently determined by solving these equations. However, the stresses are not determined outside the slip-line networks. Other limitations of the bearing capacity method include applicability to simple geometries, the requirement for a failure mechanism assumption and overlooking the effect of the soil stress-strain relationship.

The cavity expansion method (CEM) has been extensively used to determine the stresses in soil around various objects including piles, cones and pressuremeters (Mair and Wood, 1987). The analogy between the penetration and cavity expansion was first noted by Bishop *et al.* (1945). General solutions for the spherical/cylindrical cavity expansion problems within a soil mass have been derived for various constitutive models such as linear elastic/perfectly plastic (Vesic, 1972; Mantaras and Schnaid, 2002), non-linear elastic/perfectly plastic (Bolton and Whittle, 1999) and hypo-plastic (Cudmani and Osinov, 2001) models. In comparison with the bearing capacity method, CEM has the advantage of considering both the elastic and plastic deformations; it does neglect however, the dependency of deformations on the direction of penetration. Furthermore, the CEM is not capable of accommodating the precise geometry of the penetrating object.

Experimental evidence has clearly illustrated that the behaviour of soils in shallow conditions is different from the soil response at depth. The deep condition is defined as the situation at which the depth of the soil of interest is relatively large compared to its lateral extent (Baligh, 1985). The soil behaviour in shallow conditions is mainly dependent on the stress history of the soil, in other words shallow problems are essentially "stress-controlled" (Lambe, 1967). The stress path method was developed to predict the deformation and stability of shallow geotechnical features (Lambe and Marr, 1979). In contrast, the deformations of saturated clays caused by undrained deep penetration are relatively independent of the shearing resistance of soils (i.e. a "strain-controlled" problem) (Baligh, 1975). This hypothesis led to the development of the strain path method (SPM) solution for deep penetration problems by Baligh (1984).

The SPM is an approximate technique that predicts the deformations and strains caused by deep steady-state undrained penetration of a rigid penetrating object into an incompressible saturated isotropic clay (Baligh, 1985). By assuming that the effects of viscoelasticity, gravity and inertia can be neglected, soil deformations during the penetration process may be estimated from particles tracked along streamlines that form around the penetrating object when placed in a uniform fluid flow. A solution therefore comprises three steps: obtaining the deformations and strains from the flow field; calculating the stresses from constitutive models; and determining pore pressures from equilibrium equations. The SPM is more thoroughly discussed in section 2.5.

The shallow strain path method (SSPM) is a relatively recent analytical method for estimating the deformations caused by shallow undrained penetrations (Sagaseta *et al.*, 1997). The influence of the stress-free ground surface was analysed by combining the soil deformations determined from Baligh's (1985) deep penetration method and Sagaseta's (1987) near surface ground loss solution. SSPM analyses have been performed for three geometries, the "simple wall", "simple pile" and "simple tube" to represent the penetration of a sheet pile, closed-ended and open-ended piles respectively (Sagaseta and Whittle, 2001). Comparison of SSPM results with field and laboratory tests has shown that the analyses generally underestimate the surface heave. In addition, SSPM solutions have not yet been combined with constitutive models or equilibrium conditions to estimate the stresses and pore-pressures generated by shallow penetrations.

Analytical techniques such as CEM and SPM have been utilised to derive the pore pressures generated during penetration. Dislocation based method (Elsworth, 1998) is an alternative analytical method to evaluate the generation of pore pressures as well as their dissipation around a cone that penetrates a poro-elastic medium.

2.4.3 Numerical techniques

Numerical analysis of the penetration/indentation process has long been the subject of research in mechanical engineering and special modelling methods have been developed to simulate various penetration/indention problems (Giannakopoulos and Suresh, 1997; Anderheggen and Renau-Munoz, 2000). In soil mechanics, a wide range of numerical techniques have been employed to analyse penetration (Acar *et al.*, 1982; Rust, 1996; Mabsout and Sadek, 2003) over the last two decades.

Simulation of soil penetration is extremely difficult due to the high rates of change adjacent to the tip of the penetrating object. Various simplifications have been adopted to reduce the difficulties related with large deformations. Some of these simplifications include analysing objects with a sharp rather than a flat-ended tip; assuming pre-bored conditions rather than penetrating from the free surface; and providing a narrow opening below the tip and along the direction of the penetration. This section examines some of the numerical techniques used to simulate the soil penetration process from two aspects: the methodology adopted to model the penetration process and their capability of addressing the influence of the interface adhesion.

Early simulations of penetration were performed using small-strain finite element (FE) codes. Griffiths (1982) determined the collapse load of pre-bored plane strain and axisymmetric smooth deep foundations in undrained clays with a Tresca model. The results of these analyses were in the range of values calculated from the classical ultimate bearing capacity predictions (Meyerhof, 1951). De Borst and Vermeer (1984) used the DIANA FE code (Witte and Wolthers, 2002) to evaluate the cone resistance of a pre-bored rough 60° cone penetrated into undrained incompressible clay (Mohr-Coulomb model). Their calculated cone resistance was higher than the experimental findings. The small-strain FE analyses are however unable to simulate the penetration realistically as they cannot address large deformations and the flow of soil around penetrating objects.

Kiousis *et al.* (1988) used a large-strain FE model to study the behaviour of soil during the penetration of a pre-bored smooth 60° cone in clay. The clay was modelled as an elasto-plastic material with a cap constitutive model (DiMaggio and Sandler, 1971). Cone penetration was simulated by allowing the nodes to move freely along the penetrometer boundary using roller boundary conditions, as shown in Figure 2.5(a). The boundary constraints were altered as nodes passed the cone tip or shoulder, marked with 1 and 2 respectively. The nodes beneath the tip were originally fixed to the axis of symmetry. After passing the tip elevation (1), they were allowed to move along the cone surface. As the nodes pass the shoulder (2), the inward movement of them was only restricted by vertical rollers. These simulations predicted the development of a separation zone at a distance of 2~3R (R is the cone radius) above the tip, Figure 2.5(b). The high level of strains determined from these analyses, in relative to laboratory test results, underlined the inadequacy of the adopted modelling strategy as well as the constitutive assumption.

Three approaches were implemented by Teh (1987) to study the cone penetration. In the first approach, the cone resistance was evaluated from a finite difference code used to derive the SPM solution for a von Mises material (Teh and Houlsby, 1991). FE calculation was used in the second approach to determine the resistance of pre-bored cone. Although equilibrium conditions were satisfied, a steady-state solution was not achieved in this approach. In the final approach, in order to determine a solution that satisfied both the steady-state and equilibrium conditions the stresses determined from the SPM (first approach) were used as the starting condition for the FE analyses (second approach). The condition of the cone-soil interface was simulated in these analyses by defining boundary constraints. To model a smooth condition, interface nodes were allowed to slide freely, while in the rough condition they had prescribed displacements. Figure 2.6 shows the interface conditions used to model the smooth and rough penetrations. Due to “unfortunate necessity conditioned by the FE program”, the cone face had prescribed vertical displacements (i.e. was modelled as a rough surface) in both the smooth and rough simulations (Teh, 1987).

These analyses showed that introducing interface roughness increased the penetration-induced displacement and extended the failure zone in the adjacent soil.

Budhu and Wu (1992) used an updated Lagrangian FE formulation (Gadala *et al.*, 1983) to analyse the soil disturbance during sampling for a Modified Cam-Clay material (Wood, 1992). Thin-layer interface elements (Desai *et al.*, 1984) with Mohr-Coulomb shear criterion (C_{int}=25kPa and φ_{int}=30°) were defined along the internal wall of the sampler to simulate the interaction between the soil and sampler tube. The material properties for the thin-layer interface elements were changed from soil to sampler material as penetration took place. The penetration was simulated by splitting group of nodes ahead of the penetration path and creating new nodes, as shown in Figure 2.7. The new nodes (A′, B′, ...) were allowed to displace and follow the external wall of the sampler as penetration continued. The old nodes (A, B, ...) were fixed in the radial direction but were allowed to slide vertically along the internal wall of the sampler. The results of these analyses indicated that the sampling disturbance increased by introducing adhesion on the soil-sampler interface.

Van den Berg (1994) used an arbitrary Lagrangian-Eulerian FE formulation (Haber, 1984) to model the penetration of pre-bored cones and samplers. The frequent remeshing required for analysing large deformations was avoided by uncoupling the node displacements from material displacements. The penetration process was simulated by applying incremental vertical material displacements at the lower boundary of the model. According to a specified convection law, materials moved upwards and compressed around the shaft as penetration continued. Zero-thickness interface elements (Day and Potts, 1994) with a Mohr-Coulomb shear criterion, were incorporated in these analyses to examine the influence of interface adhesion on the soil behaviour. The interface adhesion factor (α), defined as the ratio between the interface adhesion (C_{int}) and soil undrained shear strength (S_u), was varied between α=0, 0.5 and 1. These analyses were performed for von Mises, Drucker-Prager and Mohr-Coulomb constitutive models (Van den Berg *et al.*, 1996). The sampler disturbance and cone resistance predicted by models were compared and validated against analytical solutions as well as experimental measurements. The cone resistance for a rough cone was 1.3 times higher than that determined for a smooth cone. It was also observed that the stress-strain behaviour of soil was strongly altered by introducing interface adhesion to the sampler wall.

The axisymmetric penetration of a pre-bored cone into a clay with a Modified Cam Clay constitutive relationship was modelled using an updated Lagrangian FE formulation implemented into the GAP/CTM program (Abu-Farsakh *et al.*, 1998). The continuous penetration of the cone was simulated by imposing incremental vertical displacement to the cone boundaries. In these analyses, a tension criterion was used to define the soil parting ahead of the cone tip, as shown in Figure 2.8(a). Boundary conditions were accordingly adjusted as the cone advanced. A simple constrained approach based on the principle of virtual work was used to model soil-cone interface (Katona, 1983), where the Mohr-Coulomb criterion ($\varphi_{int}=14°$) was used to define the sliding potential on the external boundary of the cone. The predictions were compared with the calibration chamber results and confirmed that the penetration-induced stresses as well as excess pore pressures were higher for a cone with a frictional interface (Kurup *et al.*, 1994).

Hu and Randolph (1998b) presented an arbitrary Lagrangian-Eulerian FE formulation with an automatic nodal remeshing technique (Ho-Le, 1988; Hu and Randolph, 1998a) using the AFENA FE package, referred to as the "Remeshing and Interpolation Technique with Small Strain" (RITSS). The RITSS method was used to model the continuous penetration of three different penetrating objects: a thin circular plate, a T-bar and a ball (Lu *et al.*, 2001). Analyses showed that by introducing interface adhesion, more soils would be trapped under the penetrating object as it penetrated layers of soil. The RITSS method was also applied to analyse the cone penetration and showed that the cone resistance increased linearly with an increase in the interface adhesion (Lu *et al.*, 2004).

Liyanapathirana *et al.* (2000) used an Eulerian FE approach to simulate displacements of a hammered open-ended pile into soils with a von Mises constitutive model. Thin-layer interface elements were provided between the pile and soil. Normal and radial stresses near the pile shaft were small compared to the shear stress, as a result the interface elements shear strength (i.e. sliding criterion) was set to $\sqrt{3}\sigma_y$ (σ_y is von Misses yield stress). To simulate the pile hammering, the properties of the elements beneath the pile tip were changed in turn from soil to pile material as the pile penetrated successive layers of elements. Large mesh distortions were avoided by allowing the material to flow through the fixed mesh at the end of each hammer blow. Due to the nature of the simulation methodology, the influence of various adhesion levels could not be investigated in these analyses.

A novel FE approach was suggested by Yu *et al.* (2000) to study the steady-state penetration of a 60° cone into undrained clays. Owing to the steady-state nature of cone penetration, the stress of a node such as Q at time T relative to the location of cone tip would be similar to the stress of node P at time (T-dt), as shown in Figure 2.8(b). Based on this characteristic, the current stress of soil at any point can be obtained by integrating the stress of all points below it until the undisturbed initial stress of soil was reached. The behaviour of soil was described using von Mises and Modified Cam Clay constitutive models in these analyses. The influences of cone-soil interface properties were incorporated by specifying a Mohr Coulomb sliding criterion (φ_{int}=0, 7.5, …, 30°). The outputs of analyses showed that the cone resistance increased with an increase in the interface friction angle.

Abu-Farsakh *et al.* (2003a) simulated the penetration of a cone from the free surface in two stages. In the first stage, at a specified depth, the cone was expanded radially from an initial radius of ($0.1r_0$) to the cone radius (r_0), as shown in Figure 2.9(a). This was done to avoid the assumption of an existing pre-bored cone with uniform in-situ stresses. The stresses at the end of this stage were then used as the starting condition for the second stage, which involved incremental vertical displacement of the cone, Figure 2.9(b). This stage was identical to the procedure adopted by Abu-Farsakh *et al.* (1998), which was explained earlier in this section. Model predictions for pore pressures and stresses were in good agreement with cavity expansion results (Abu-Farsakh *et al.*, 2003b). The analysis outputs indicated that cone resistance was highly dependent on the in-situ stress condition and the rigidity index of the soil ($I_r=G/S_u$). The influence of interface adhesion was however, not addressed in these analyses.

The ABAQUS FE program, with an auto-adaptive remeshing technique (Zienkiewicz and Zhu, 1991) was utilised to analyse the penetration of a pre-bored 60° cone into sands with a Drucker-Prager model (Susila and Hryciw, 2003). The penetration was simulated by imposing vertical velocity on the top of the cone shaft. The classical Mohr-Coulomb friction model (ABAQUS, 2003) was used to incorporate the interface resistance with the friction angle of the interface set equal to half of the internal friction angle of the sand. The analysis outputs indicated that the cone resistance would be higher in models with a higher interface friction.

Various approaches have been adopted in FLAC to simulate the penetration of rigid objects. Ahmadi *et al.* (1999) simulated the penetration of a cone in the large-strain mode by continuously deforming the soil boundary that accommodated the geometry of the cone as penetration took place. Although the results of numerical predictions for a Mohr-Coulomb material were in good agreement with chamber results, the cone-soil interface was not modelled in this study. Klar and Einav (2003) proposed a new contact formulation that utilised the equations of motion to describe the interaction between the soil and the rigid object. However, their proposed approach was not capable of analysing the penetration of three-dimensional objects and did not incorporate the effect of interface adhesion.

2.5 The strain path method

The SPM has been extensively used to analyse various penetration problems. In this study, the comparison of strain paths determined from the soil penetration problem and its conjugate fluid flow problem (SPM) has been used as the main validation criterion. In the following sections the SPM *calculation scheme*, the *fluid dynamics* terminology used in the SPM and previous SPM *applications* are reviewed.

2.5.1. The calculation scheme

Experiments have confirmed that due to severe kinematic constraints, soil deformations in deep undrained penetration of saturated clays are largely independent of their shearing resistance (Baligh, 1975). In other words, the soil deformations can be reasonably estimated without considering a constitutive relation for the clay. Baligh and Scott (1976) suggested that soil deformations can be readily determined from the "conjugate problem", in which the soil moved around a fixed penetrating object. The fluid-like behaviour of saturated clays (Terzaghi and Peck, 1962) led Baligh (1984) to approximate soil deformations and strains around a steady-state deep penetrating object from streamline deformations. This approximate analytical method was termed as the strain path method (SPM). The calculation scheme in the SPM consisted of three steps:

1. **Calculation of deformations, strain rates and strains**: deformations were calculated by integrating the velocities along flow streamlines; while the strain rates were derived by obtaining partial derivatives from the velocities; strains were then determined by integrating strain rates along streamlines;
2. **Determination of stresses**: from strain values using the constitutive relationship defined for the soil (Prevost, 1978; Houlsby *et al.*, 1985; Whittle, 1992; Whittle and Kavvadas, 1994); and
3. **Determination of pore pressure values**: from equilibrium considerations

Due to the uncoupling of deformations from stresses, the calculated stresses do not fully satisfy equilibrium equations. Various iterative means have therefore been employed to improve the results and satisfy equilibrium conditions (Baligh, 1985; Teh and Houlsby, 1991).

2.5.2. Review of fluid dynamics

The first step in the SPM calculation involves manipulation of velocities along streamlines in the conjugate flow problem. The streamline passing through a point (x, y, z), is the line tangential to the local fluid velocity vector (u, v, w) at that point (Yih, 1957). Streamlines are represented by the stream function (Ψ) that is determined by solving Equation 2-2 for any flow field that satisfies the continuity equation:

$$\frac{dx}{u}=\frac{dy}{v}=\frac{dz}{w}$$ **Equation 2-2**

There are three analytical approaches to calculate the streamlines and velocity fields around an object placed in a uniform flow, these are:

- Conformal mapping method;
- Superposition of surface singularities (i.e. panel method); and
- Superposition of internal singularities (i.e. superposition method)

In the conformal mapping method, the complex flow field around a penetrating object in the z-plane is transformed to a known flow field (e.g. uniform flow field) in the w-plane where the stream functions are easier to calculate (Milne-Thomson, 1968). A reverse transformation is then implemented to derive the stream function in the z-plane. Conformal mapping (using the Schwartz-Christoffel technique) has been used by various researchers to analyse the flow field around cones and piles (Tumay *et al.*, 1985; Acar and Tumay, 1986; Silvestri and Tabib, 1993). Approximating the infinite soil domain to a finite region, imperfect boundary matching between regions and numerical difficulties are some of the reported shortcomings for this method (Baligh and Chin, 1987).

The other two methods make a direct use of singularities. Three singularities are commonly encountered in fluid dynamics: (a) source/sink, (b) vortex and (c) doublet. These elementary flows are termed as "singularities" because the flow velocity tends to infinity at the centre of them (Chow, 1983). The shape and direction of streamlines for these singularities in two-dimensional flow are shown in Figure 2.10. The shapes of streamlines for a sink are the same as a source while their directions are opposite to that for a source as fluids are drawn into a sink (Streeter, 1961).

In the panel method, singularities are arrayed on the surface of a specified geometry, and boundary conditions are written in terms of these singularities (Hess, 1975). Numerical approaches are then used to solve the integral equations derived from these boundary conditions. Huang (1989) extended the panel method formulations for three-dimensional convex bodies and performed SPM analyses for the dilatometer and cone geometries. Although the panel method makes direct use of the penetrating object geometry, which allows the modelling of sharp corners, additional numerical complexities and approximations are introduced to the overall solution (Baker *et al.*, 1964).

The superposition method has been extensively used in the SPM analyses to determine the flow properties around various objects. In this method, combinations of singularities are superposed on a uniform flow to construct complex flow fields (Nunn, 1989). The unique streamline passing through the stagnation point (i.e. point of zero velocity) in the superposed flow pattern, represents a particular geometry called a simple-body. The simple-bodies generated by the superposition of sources and sinks are also called half-bodies, as they extend to infinity. If the total strength of singularities is equal to zero however, a closed-body is formed. Two of the most well known simple-bodies are Rankine's half-body and oval that are created by superposing a line source or a combination of a line source and a line sink with equal strength to a uniform two-dimensional flow, as shown in Figure 2.11. The important characteristic of the simple-body, which makes the superposition method suitable for the SPM analyses, is that the streamlines and flow properties around the simple-body are identical to those that would form around a solid object with the shape of the simple-body if placed within a uniform flow field. The main challenge in the superposition method is then to determine a combination of singularities that produces a simple-body close to the geometry of the penetrating object.

2.5.3. SPM applications

Various geometries (i.e. simple bodies) have been generated by the superposition method for the SPM analyses (Figure 2.12). A brief review of some of these geometries is presented in the following paragraphs.

Levadoux and Baligh (1980) generated the "simple cone" geometry by superposing a series of vertical finite line sources with various lengths and strengths on a uniform flow, as shown in Figure 2.12(a). The cone resistances determined from the SPM analyses gave a reasonable estimate of cone factors measured experimentally. Further analyses showed that the mechanism of penetration for the sharp 18° cone was different to that of a blunt 60° cone, involving cutting rather than pushing the soil ahead of the cone. The stress and pore pressure fields around these two cone geometries were also determined from the SPM results (Baligh and Levadoux, 1986; Levadoux and Baligh, 1986; Whittle and Aubeny, 1991).

Baligh (1984) superposed a point source on a uniform flow to generate the "simple pile" geometry, Figure 2.12(b). Comparison between strains (on the shaft section of the "simple pile") determined from the strain path method (SPM) and cylindrical cavity expansion method (CEM) revealed that the CEM under predicted shear strains as it neglected all vertical soil deformations (Baligh, 1985). Baligh (1986a) also showed that the pile tip resistance could be readily approximated from the SPM while the application of the spherical CEM led to inadequate predictions of stress-strain within the soil. Baligh (1986b) illustrated that strain paths around the "simple pile" were not monotonic and involved significant reversals and rotations, consequently the strain history should be considered when determining stresses for inelastic materials such as soils.

The "simple sampler" geometry was generated by superposing a ring source on a uniform flow, as shown in Figure 2.12(c). Chin (1986) used complete 1st and 2nd kind elliptical integrals (Kuchemann and Weber, 1953), while Hopper (1992) utilised Bessel's functions (Weinstein, 1946) to derive the stream function and velocity fields for the flow around the "simple sampler". The initial studies showed that the strain paths for the centreline of the sampler were dependent on the width to thickness ratio (B/t) of the sampler (Baligh, 1985). The sensitivity of the results to the shape of the sampler tip, apparent in experiments (La Rochelle *et al.*, 1987), was not investigated in these analyses. Subsequent FE studies, showed that the geometry of a sampler significantly influenced the strain paths determined for the flow around samplers (Siddique, 1990; Clayton *et al.*, 1998). The strain histories determined from the SPM were applied to laboratory specimens (i.e. triaxial tests) in order to investigate the effect of sampling disturbance on the behaviour of clay (Baligh *et al.*, 1987; Siddique *et al.*, 1999). The SPM predictions were consistent with sampler disturbances evaluated from field observations (Hight, 2001).

Chin (1986) superposed a line source onto a uniform flow to produce a plane strain geometry referred to as the "simple wall", which is essentially the Rankine's half-body, Figure 2.12(d). The simple wall simulates a two-dimensional cross section of a wall with infinite length in the out-of-plane direction. Chin (1986) compared strain paths determined for the "simple sampler" with those of the "simple wall" and "simple pile" geometries. These comparisons illustrated that while the far field deformations around the "simple sampler" could be approximated by those determined for the "simple pile", close to the sampler tip deformations were similar to those determined for the "simple wall".

Rafalovich (1989) developed the three-dimensional "simple plate" geometry by superposing a finite line source onto a uniform flow, as shown in Figure 2.12(e). The finite line source was obtained by superposing a semi-infinite line source onto a horizontally offset semi-infinite line sink. Due to associated numerical difficulties, the geometry of the "simple plate" was determined by tracking streamlines close to the simple-body rather than solving the stream functions (Aubeny, 2004). Analyses showed that the strain paths determined for streamlines close to the "simple plate" were strongly influenced by the out-of-plane displacements (Aubeny, 1992).

The "ideal dilatometer" geometry was generated by superposing an array of 10×50 point sources on a uniform flow as shown in Figure 2.12(f) (Finno, 1993). The displacement pattern around the dilatometer was determined using various analytical methods (Figure 2.13). The horizontal deformations determined from the 2D and 3D analyses were similar. In the case of the vertical deformations however, while particles did not return to their initial position in the 2D models, in the 3D models, particles attained their initial vertical position at some distance above the tip. Finno (1993) has also illustrated that for a dilatometer with a lower aspect ratio, lateral (ε_{xx}) and longitudinal (ε_{yy}) strains were higher, while the influence of aspect ratio on the vertical (ε_{zz}) and shear (ε_{xz}) strains were minimal, as shown in Figure 2.14. The outcomes of these simulations were however undermined for to the following reasons: the generated geometry of the "ideal dilatometer" was not identified, closed-form solutions could not be obtained for strain paths, and the results were not compared or validated against an independent solution (Whittle, 1994).

The "ideal self-boring pressuremeter" was simulated by adding a sink point to the flow field around the "simple sampler" as shown in Figure 2.12(g) (Whittle and Aubeny, 1993). Although the self-boring pressuremeter installation was simulated realistically by taking into account the soil extraction, the results of the SPM underestimated peak stresses in comparison with the experiment measurements (Aubeny *et al.*, 2000).

The tapered piezoprobe is a device designed to facilitate the pore pressure measurements in offshore site investigations. Whittle *et al.* (2001) superposed a combination of vertical finite line sources and sinks plus a point source on a uniform flow to generate the "ideal tapered piezoprobe" geometry, as shown in Figure 2.12(h). The predicted pore-pressure dissipation curves from SPM analyses around this geometry agreed well with the experimental measurements.

The SPM utilises the fluid flow properties (e.g. streamline and velocities) determined for a laminar Newtonian inviscid incompressible fluid, to evaluate strains. Nevertheless, experimental evidences have illustrated that at the state of shear failure, clay particles flow similar to a viscous liquid (Terzaghi, 1941). Gill and Lehane (2000) used the ANSYS FE package with FLOTRAN (an internal fluid dynamics solver) to model the viscous flow around a 60° cone geometry. These SPM analyses showed that increasing the viscosity extended the zone of penetration-induced changes within the soil. However, the use of a viscous fluid for SPM analyses introduced two new aspects that have not been addressed before. Firstly, the dependency of flow fields on the Reynolds number introduced a new arbitrary parameter to the analyses. Secondly, the interpretation of the boundary layer in terms of soil behaviour was unclear (Teh, 1987).

Failure to model the development of shear stresses on the soil-penetrating object interface (i.e. adhesion) has been one of the major setbacks in simulating penetration. SPM analyses cannot evaluate the influence of adhesions due to inviscid fluid flow based formulations. The majority of the numerical analyses (refer to section 2.4.3) have also failed in realistically incorporating the adhesion into simulations. The adhesion theory of friction and various methods employed to quantify the adhesion in soil penetration problems are outlined in the next section.

2.6 Adhesion theory of friction

The first known written remarks on frictional characteristics of solid surfaces were made by Leonardo da Vinci (Horn and Deere, 1962). The basic law of frictional behaviour frequently referred to as Amonton's Law states that "the shear force between two bodies is proportional to the normal force between them and is independent of the size of the bodies in contact" (Lambe and Whitman, 1969).

The hypothesis commonly referred to as the *adhesion theory of friction* for explaining the friction process was proved to be valid for a wide variety of materials by Bowden & Tabor (1950) and independently stated for soils in Terzaghi's (1960) pioneering soil mechanics book. The adhesion theory of friction states that the actual contact between two surfaces is a small fraction of the apparent contact area. At these discrete contact points (termed *asperities*) materials are adhered by molecular bonding (Terzaghi, 1925b) or cold welding (Bowden *et al.*, 1943). According to the adhesion theory of friction (Mitchell, 1993), the shear resistance to sliding (T) is dependent on the actual contact area (A_C) and the adhesive strength of the contact (τ_m). Over (i) asperities the total adhesion strength is given as Equation 2-3:

$$T = \sum T_i = \sum A_{Ci} \tau_m$$ **Equation 2-3**

Various experimental techniques have been used to determine the interface shearing resistance between soils and structural materials. In the case of granular materials, shear tests (Uesugi and Kishida, 1986), photographic techniques (Uesugi *et al.*, 1988), instrumented piles (Lehane and Jardine, 1994) and chamber tests (Reddy *et al.*, 2000) have shown that the interface friction is influenced by the soil composition and properties of the structural surface (Subba Rao *et al.*, 2001). Fewer interface tests have been conducted on cohesive soils. Some of them include chamber tests (Tomlinson, 1957), simple shear tests (Tsubakihara *et al.*, 1993; Pedersen *et al.*, 2003) and ring shear tests (Lemos and Vaughan, 2000). These tests have shown that in addition to the soil composition and surface properties, the moisture content of soil influences the interface shearing resistance. Tests on various types of soils have confirmed that the interface shearing resistance is generally less than the shear strength of the soil (Potyondy, 1961).

FLAC and FLAC^{3D} finite difference programs are capable of simulating large-deformations associated with the penetration as well as addressing the influence of interface adhesion on the behaviour of soil during the penetration. The main features of these programs, which are adopted for the penetration simulations, are outlined in the next section.

2.7 The FLAC and FLAC^{3D} programs

As Yu (2004) has pointed out in his Mitchell's lecture, "continuum mechanics is the main theoretical method for rational interpretation of in-situ tests". FLAC and FLAC^{3D} (Fast Lagrangian Analysis of Continua) are two and three dimensional explicit finite difference programs that have been adopted in this thesis for analysing spade cell penetration (i.e. installation). The FLAC and FLAC^{3D} programs were developed for engineering mechanics computation by Itasca in 1986 and 1994 respectively (Itasca, 2004). FLAC programs have been extensively used for the analysis and design of various challenging geotechnical problems over the last two decades including bearing capacity calculations (Burd and Frydman, 1997), retaining wall analyses (Green and Ebeling, 2003), consolidation predictions (Dai and Pells, 1999), slope stability analyses (Norrany *et al.*, 1999) and flow through joints calculations (Konietzky *et al.*, 1999). FLAC was also rated as a "good-excellent" program (Thomas, 2003) according to the six independent quality criteria (functionality, reliability, usability, efficiency, maintainability and portability) defined in ISO 9126 for a modelling software (Bond and MacLeod, 2001).

2.7.1. Calculation methodology

For further understanding of the calculation methodology implemented in FLAC, various characteristics of the FLAC code are listed and defined here:

- **Finite difference method**: every derivative in the equilibrium equations is replaced by an algebraic expression written in terms of field variables at discrete points in the space (Hoek *et al.*, 1991);
- **Explicit technique**: in the explicit technique (or dynamic relaxation), stresses are derived from strains in each element independently and without iteration. In the implicit technique (or matrix solutions), a series of simultaneous equations should be solved iteratively to calculate the stress values (Cundall, 1976);
- **Time Marching scheme**: in a time-marching scheme, each loop of the calculation cycle occupies one time step;
- **Lagrangian code**: as opposed to an Eulerian code, grid points move and deform with the material they represent in a Lagrangian code (Haber, 1984);
- **Lumped-mass method**: as opposed to the consistent-mass, the mass of elements are lumped on nodal points; and
- **Large-strain calculation**: although, the constitutive formulation adopted in FLAC at each step is small-strain; large-strain calculations are performed by updating the geometry of the mesh and consequently the stress tensor as displacements occur.

The explicit calculation cycle utilised in FLAC (Figure 2.15) consisted of four steps:

- **Step 1**: velocities set either by boundary conditions or derived from equilibrium equations are used to update nodal displacements and to calculate strain rates for elements;
- **Step 2**: the constitutive law is utilised to determine stresses in elements;
- **Step 3**: the stresses derived from the previous step and those set by boundary conditions are used to calculate nodal forces; and
- **Step 4**: equilibrium equations are used to update velocity values for grid points.

This calculation cycle is performed for all grid points at each cycle (i.e. step) until the user defined convergence limit is achieved. Convergence of the solution is assessed in FLAC by monitoring the value of the maximum "unbalanced force ratio" among all grid points, where the unbalanced (i.e. out of balance) force ratio is the unbalanced force divided by the applied force magnitude at any grid point. It should be noted that in the FLAC terminology, element/zone, mesh/grid and grid-point/node are used interchangeably.

2.7.2. Features

The development of FLAC finite difference code was an "attractive alternative to conventional FE analyses" adopted in geotechnical engineering (Carter *et al.*, 2000). Various features of FLAC make it an appropriate program to analyse soil penetration. The Lagrangian code with implemented large-strain formulations enables FLAC to simulate large deformations associated with penetration. Moreover, the time marching scheme can be used to simulate the steady-state penetration process as incremental displacements. As there is no need to determine and solve large simultaneous equilibrium equations in the explicit method, large-strain or non-linear problems can be solved without excessive memory or calculation time in FLAC (Frydman and Burd, 1997). Some of other FLAC features are:

- **The FISH language**: This programming language embedded in FLAC (short for FLACish) enables defining new variables and functions that are not incorporated in the standard FLAC code (Coetzee *et al.*, 1993);
- **Library of constitutive models**: with 10 basic constitutive models and the capacity of modifying the existing models as well as defining new models;
- **Fluid-flow calculation**: FLAC can analyse flow problems independently or coupled with mechanical calculations;
- **Interface logic**: FLAC has an interface logic implemented in it, which can be used to simulate sliding and separation of two objects (i.e. sub-grids). This feature will be further discussed in section 2.7.3.

The penetration of a push-in pressure cell in a saturated clay is an undrained process due to the low permeability of clays that does not allow any drainage to occur during the penetration and for a long time after it. Two modelling approaches are available in FLAC to model an undrained problem: "wet simulation" and "dry simulation" (Itasca, 2002b). In the wet simulation, problems are analysed as a coupled mechanical-flow model (**CONFIG gw**) in which the fluid flow is restricted (**SET**

fluid off). Dry density and drained properties are defined for materials, as well as the density and bulk modulus of the water in wet simulations. In the dry simulation, the undrained problem is solved without taking fluid explicitly into account. This is done by defining the wet density and undrained properties for the materials. The uncoupled approach (i.e. dry simulation) was adopted in the extensive two-dimensional soil penetration analyses, as the coupled approach was extremely time consuming. For three-dimensional analyses, however, full-coupled analysis was performed.

2.7.3. Interface Logic

Various methods developed to incorporate the behaviour of a rock discontinuity or a soil-structure interface in numerical analyses can be categorised into four groups (Potts *et al.*, 2002):

- **Thin elements**: thin two-dimensional elements with standard constitutive models are used as interface elements (Pande and Sharma, 1979);
- **Special interface elements**: special interface elements with either finite (Desai *et al.*, 1984) or zero (Goodman *et al.*, 1968; Day and Potts, 1994; Day and Potts, 1998) thicknesses that follow special constitutive laws (Fakharian and Evgin, 2000; Ghionna and Mortara, 2002; Hu and Pu, 2004) are adopted;
- **Linkage elements**: the connection between nodes on apposite sides of the interface is defined (Hermann, 1978; Frank *et al.*, 1982); and
- **Hybrid methods**: separately modelled soil and structure are linked through constraint equations (Katona, 1983).

FLAC uses a *contact logic* (i.e. linkage elements) to model the interface between two objects. This approach is similar to that employed by Cundall and Hart (1992) in the Distinct Element Method (one of four classes defined in the Discrete Element Method) by forming normal and shear (k_n, k_s) springs between opposite sides of the interface plane. The calculation scheme adopted for interface elements in FLAC and FLAC^{3D} are different and is discussed in the following paragraphs.

Interface elements are two-sided in FLAC as shown in Figure 2.16(a). Nodes on either sides of the interface (e.g. interface node P) are in turn checked for contact on the "target face", which is defined as half the distance of the interface node (P) from the nearest left-side (M) and right-side (N) nodes on the opposite side. At any time step, the incremental relative displacement in the shear and normal directions are used to determine the shear and normal forces acting on the contact length (L). Potyondy (1961) proposed to express the interface resistance with the Coulomb failure envelope. FLAC uses the same criterion to limit the shear force on the interface element, by specifying the effective cohesion and friction angle.

FLAC^{3D} uses one-sided interface elements. An interface node (P) is checked for interpenetration with any other face (i.e. target face), which might come into contact during iteration of a model, Figure 2.16(b). Similar to FLAC, the shear force acting on the contact area (A) is determined from the incremental relative displacement in the shear direction. The normal force is however, calculated from the absolute normal penetration distance of an interface node into the target face. In common with FLAC, the Coulomb shear criterion is used to limit the shear force developed on the interface element.

In contrast to discontinuities in rocks (Kulhawy, 1975), the elastic stiffnesses defined for interfaces are simply a means to simulate the slip and separation of one sub-grid relative to another sub-grid in penetration models. The FLAC and FLAC^{3D} manuals recommend using the lowest stiffness consistent with a small interface deformation (Itasca, 2002a; Itasca, 2002b). The normal and shear stiffness of interface elements were hence set to ten times the equivalent stiffness of the neighbouring zone, Equation 2-4:

$$k = 10 \times \max\left\{\frac{(K + 4/3G)}{\Delta Z_{\min}}\right\} \qquad \textbf{Equation 2-4}$$

Where K and G are the shear and bulk moduli and ΔZ_{min} is the minimum width (in the direction perpendicular to the interface element) of the neighbouring zones along the interface plane.

All the two and three dimensional soil penetration analyses were performed using FLAC 4.00-327 (in double precision mode) and FLAC^{3D} 2.10-249 respectively.

2.8 Summary

This wide-ranging chapter has reviewed two broad topics: determination of in-situ stresses and penetration analysis techniques.

Determination of in-situ stresses

- Determination of realistic values for the in-situ stresses in the ground is a challenging step in the design and analysis of various geotechnical problems;
- Calculation of in-situ horizontal stresses is difficult due to its dependence on the geological history of the soil and as a result various techniques have been employed to measure it;
- In order to eliminate the influence of sampling disturbances, various measurement devices such as spade cells have been utilised to measure in-situ stresses directly;
- Push-in pressure cells (i.e. spade cells) are routinely used in the UK to measure in-situ stresses; and
- Although spade cells are robust and easy to operate, an independent comprehensive analytical interpretation method has not yet been devised for their measurements.

Penetration analysis techniques

- Various analysis techniques have been adopted to analyse soil penetration;
- Experimental techniques used to evaluate the stress-strain behaviour of soil during penetration included visual inspection, triaxial and chamber tests;
- Due to the three-dimensional nature of changes around the spade cell and the unknown strain history during spade cell penetration, visual inspection and triaxial tests were not applicable for examining the spade cell penetration.

Furthermore, previous chamber tests have not been able to replicate the over-reads observed in field measurements;

- Analytical techniques used to assess the behaviour of soil during penetration included the bearing capacity, cavity expansion and strain path methods;
- The strain path method provided the most realistic solution by incorporating the kinematics of the penetration process. However, it failed to address the adhesion as it was based on fluid flow formulations;
- Various numerical methods have been employed to simulate the perpetration. However, the majority of these analyses were limited to two-dimensional geometries. Furthermore, most of these methods were not capable of simulating the flow of soil around the penetration object. In addition, due to modelling constrains, the interface between the soil and penetrating object has been modelled either as rough or smooth and the influence of various degrees of adhesion has not been assessed on the behaviour of the soil; and
- The FLAC explicit finite difference codes are capable of incorporating the influence of interface adhesion in penetration analyses.

In this study a combination of the SPM analytical and FLAC numerical approaches was used to simulate the penetration of a spade cell and to investigate the influence of various soil and interface parameters on the stress-strain behaviour of the adjacent soil. The methodology and results of 2D and 3D fluid flow (SPM) and soil penetration (FLAC) analyses are presented in the following four chapters (Chapters 3, 4, 5 and 6).

Table 2-1 Alternative techniques used for determining the spade cell over-read

Site	Soil type	Alternative technique
Ska-Edeby (Stockholm)	Soft NC	Applied horizontal pressure
Cwmwernderi (Wales)	Puddle clay	SBP, SBL
Balham (London)	London Clay	OP
Bell Common (Essex)	London Clay	SBP
Brent Cross (London)	London Clay	SBP, OD
Madingley (Cambridge)	Gault Clay	SBP, suction
Grangemouth (Edinburgh)	Soft alluvium	SBP, OD
Cowden (Hull)	Glacial till	OD, suction, OP
Berkshire (Reading)	London Clay	SBP, DMT
Oxford (UK)	Oxford Clay	OP
Heathrow (UK)	London Clay	OP
Ashford (Kent)	Atherfield Clay	OP

Notes: Dilatometer (DMT), Normally consolidated (NC), Overburden pressure (OP), Oedometer (OD), Self-boring load cell (SBL) and Self-boring pressuremeter (SBP).

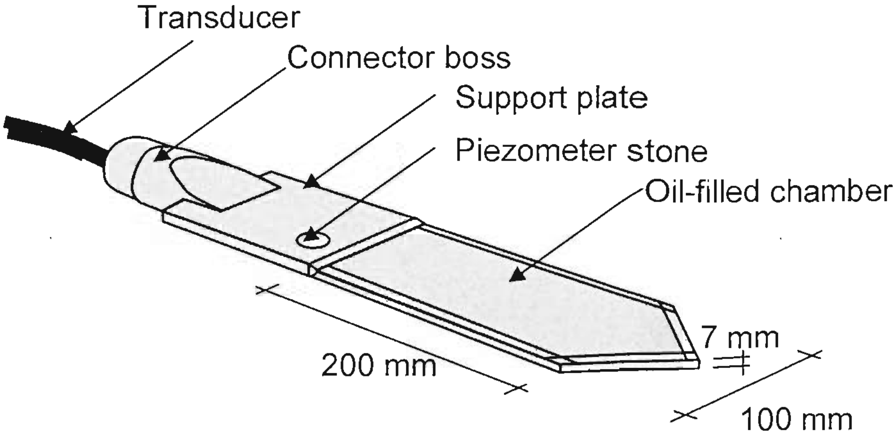

Figure 2-1 Isometric view of a spade cell (Manufacturer: Soil Instruments)

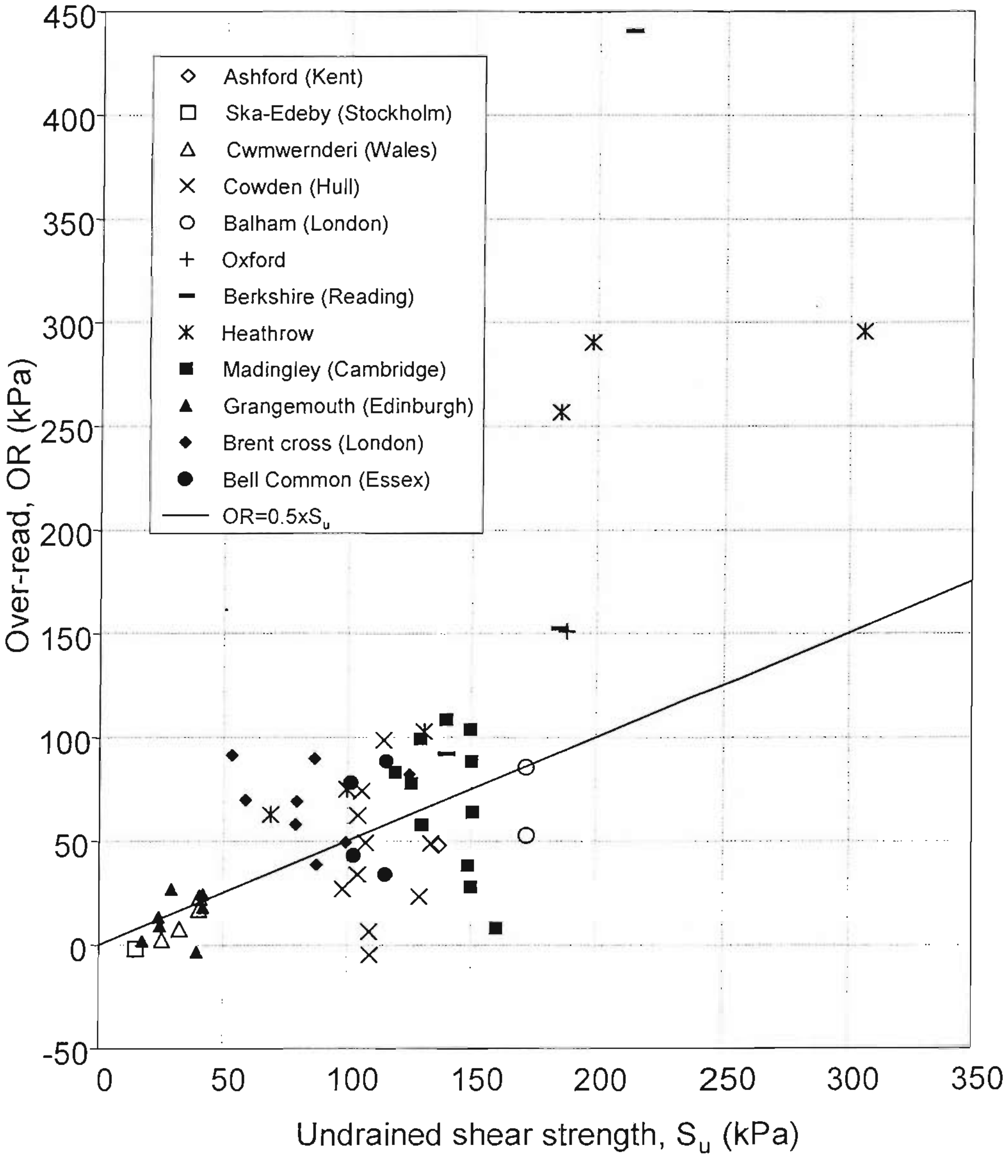

Figure 2-2 Correlation between spade cell over-read (OR) and soil undrained shear strength (S_u)

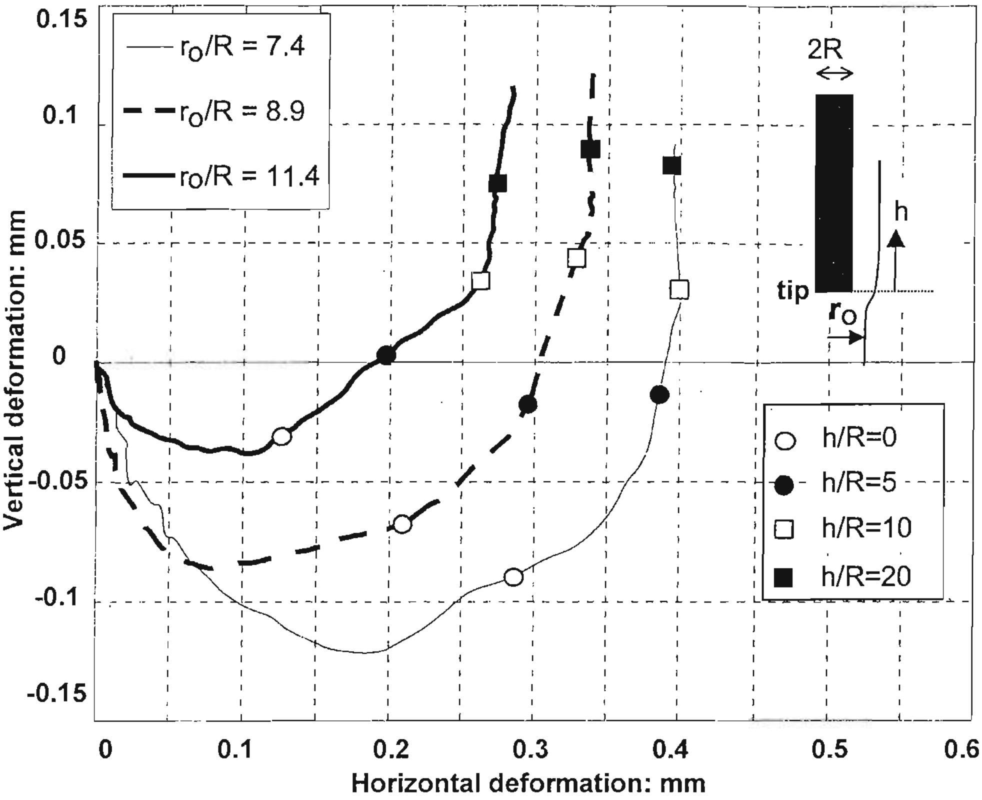

Figure 2-3 Computed displacements around a flat-tip penetrometer from optical measurements in transparent soil (Gill and Lehane, 2001)

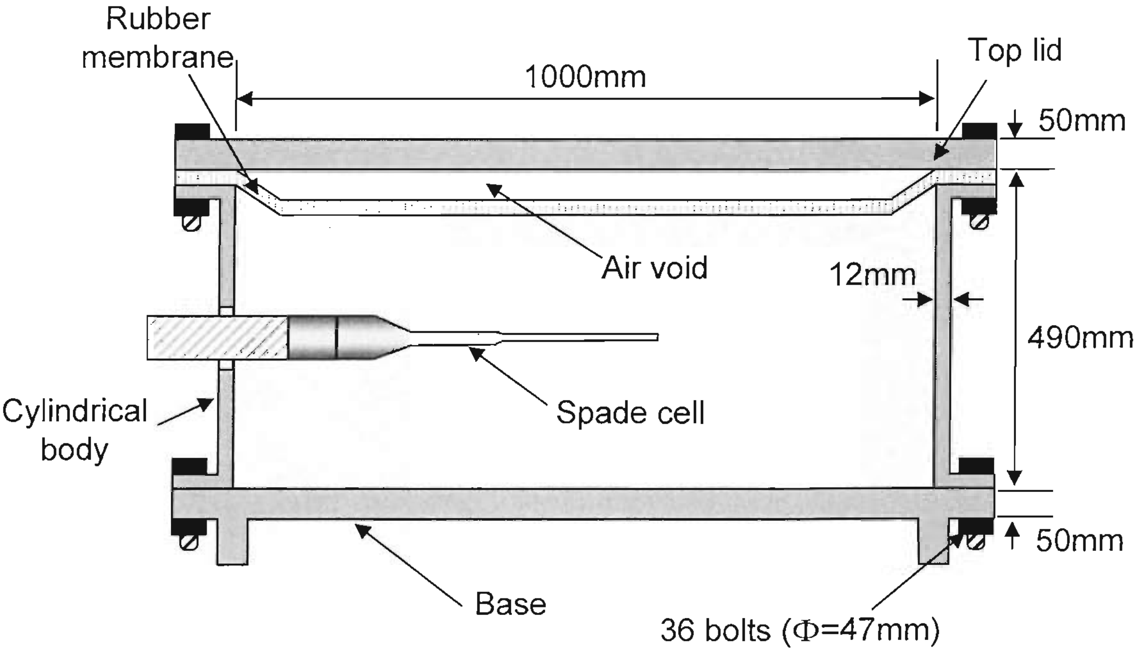

Figure 2-4 Cross-section of Rowe chamber used for spade cell calibration

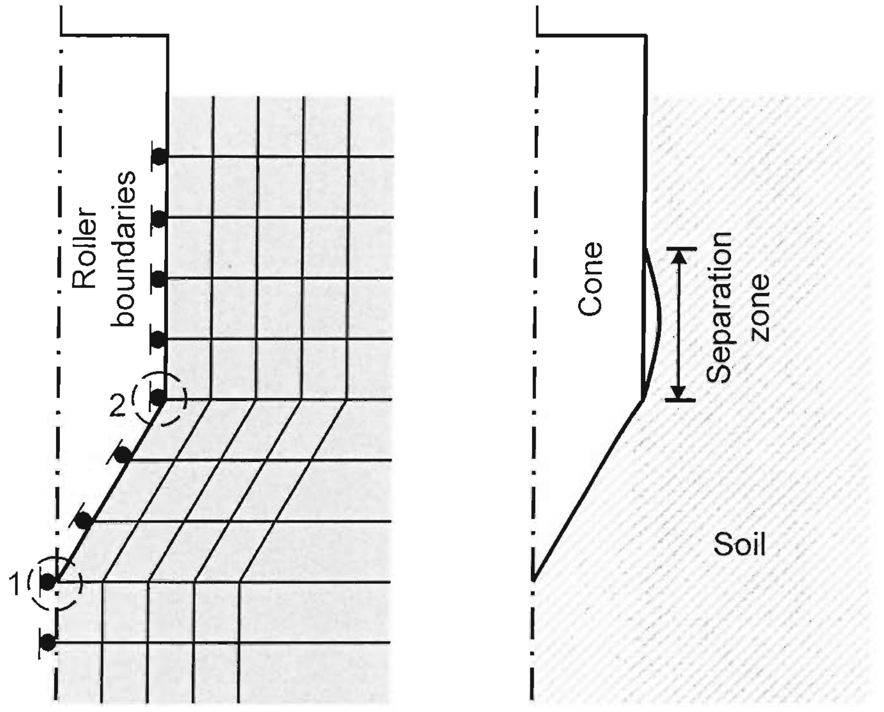

(a) Boundary conditions (b) Soil-cone separation

Figure 2-5 (a) Penetration simulation by alternating boundary conditions and (b) Schematic view of the separation zone

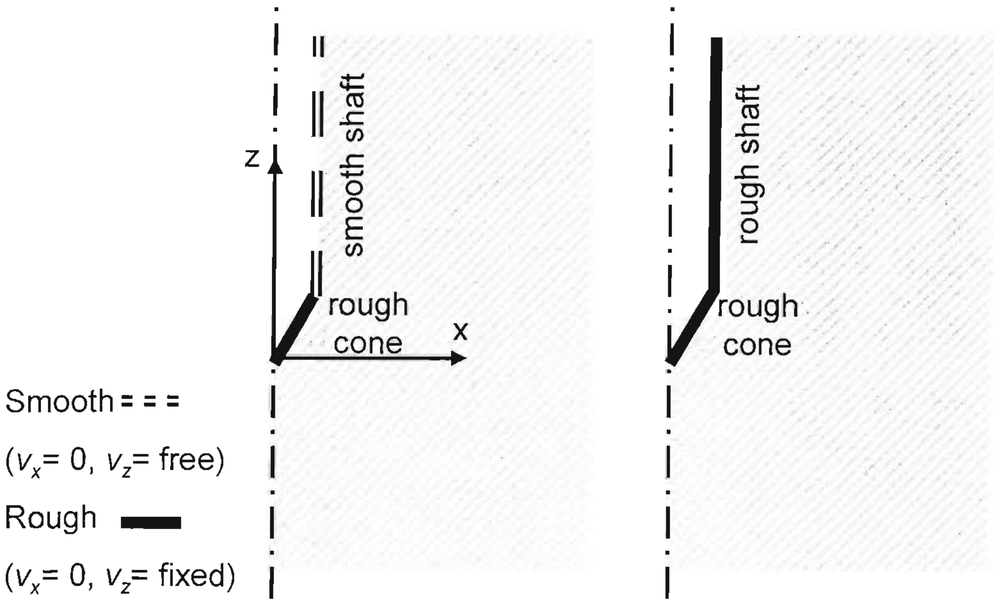

(a) Smooth interface (b) Rough interface

Figure 2-6 Penetration simulation by prescribing displacements: (a) Smooth interface and (b) Rough interface

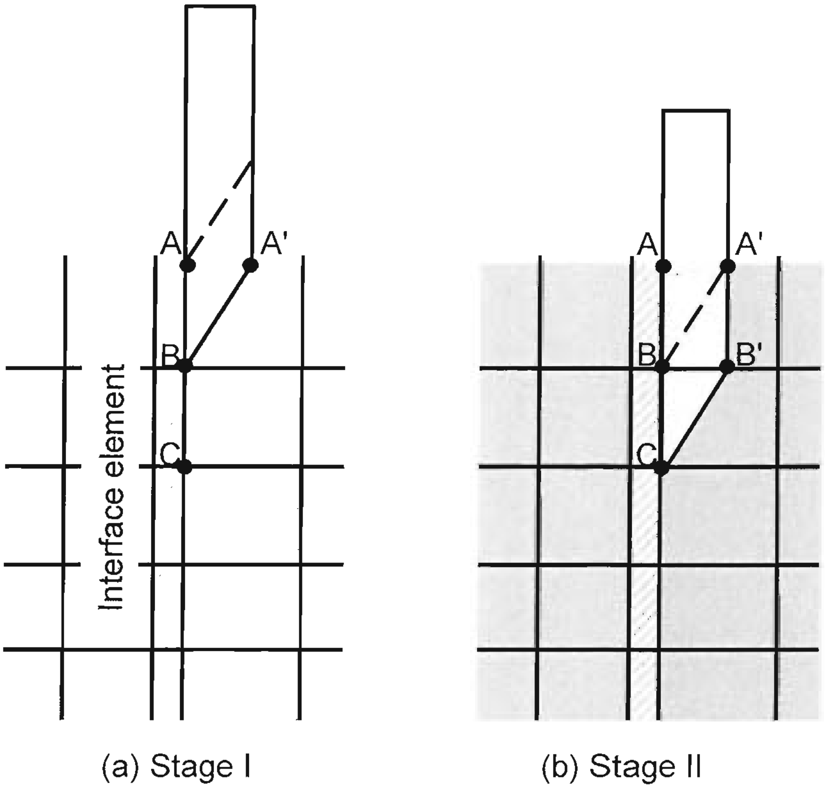

Figure 2-7 Penetration simulation by splitting nodes: (a) Stage I and (b) Stage II

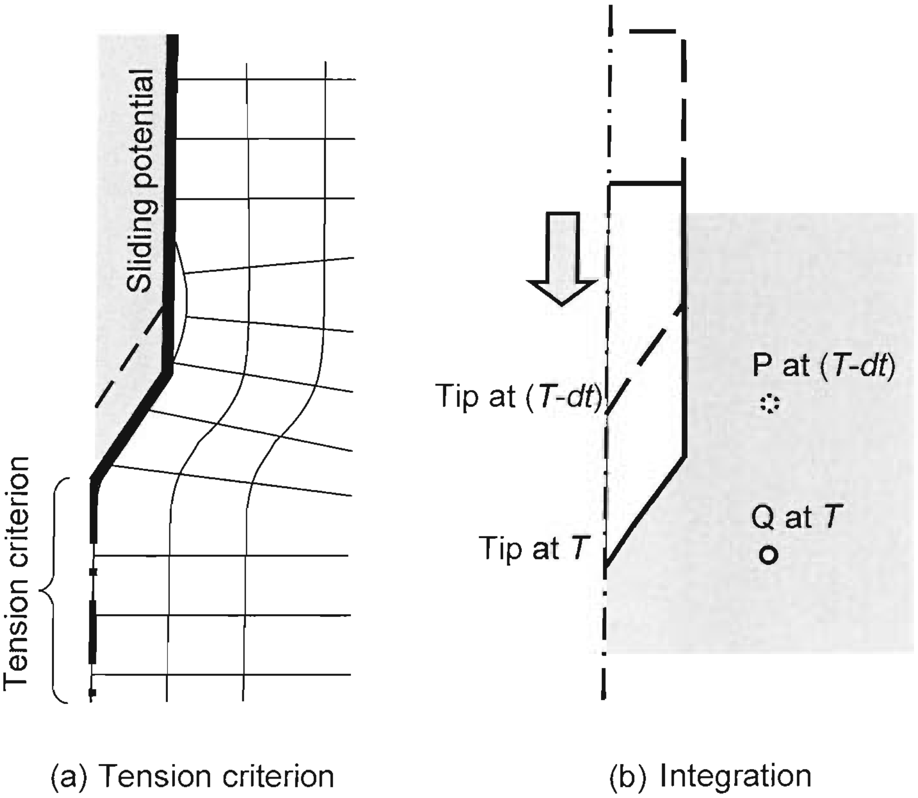

Figure 2-8 Penetration simulation by: (a) Specifying a tension criterion and (b) Integration

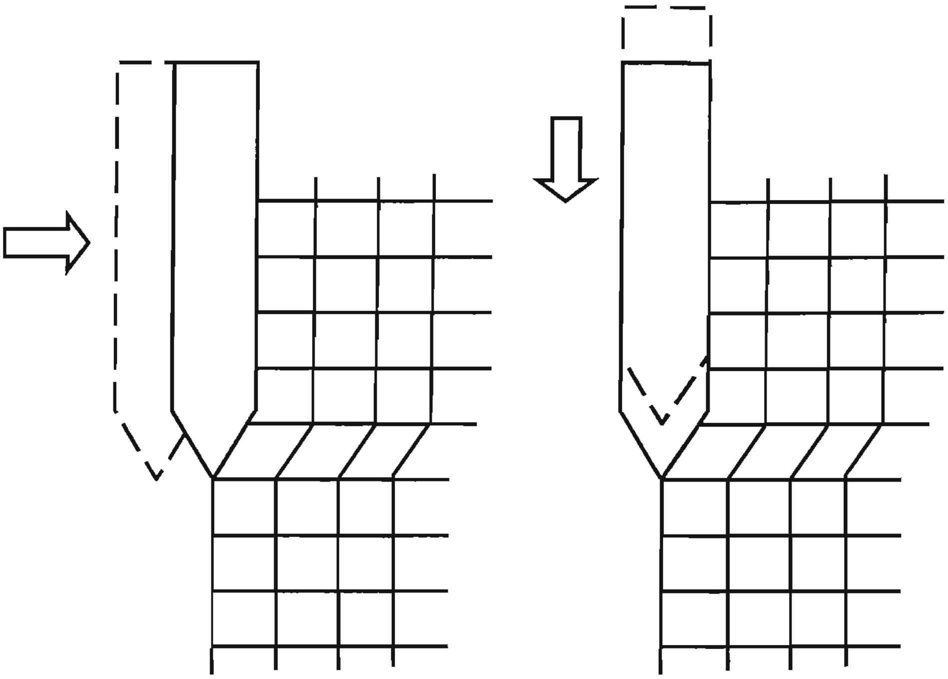

(I) Radial expansion (II) Vertical displacement

Figure 2-9 Two–stage penetration simulation: (I) Radial expansion and (II) Vertical displacement

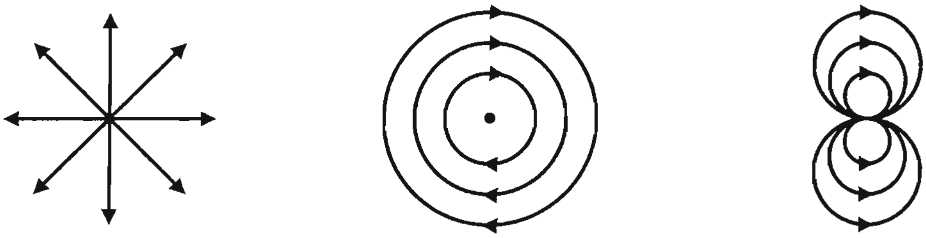

(a) source (b) vortex (c) doublet

Figure 2-10 Streamlines for two-dimensional singularities: (a) Source, (b) Vortex and (c) Doublet

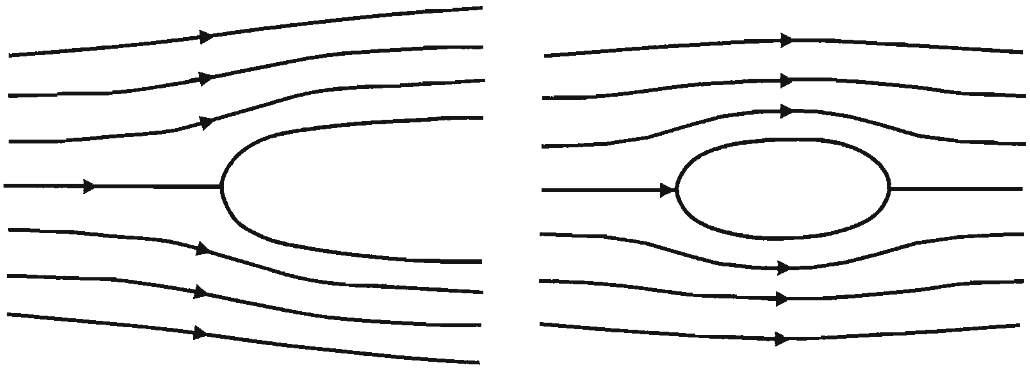

(a) Rankine's half-body (b) Rankine's oval

Figure 2-11 Streamlines around simple bodies: (a) Rankine's half-body and (b) Rankine's oval

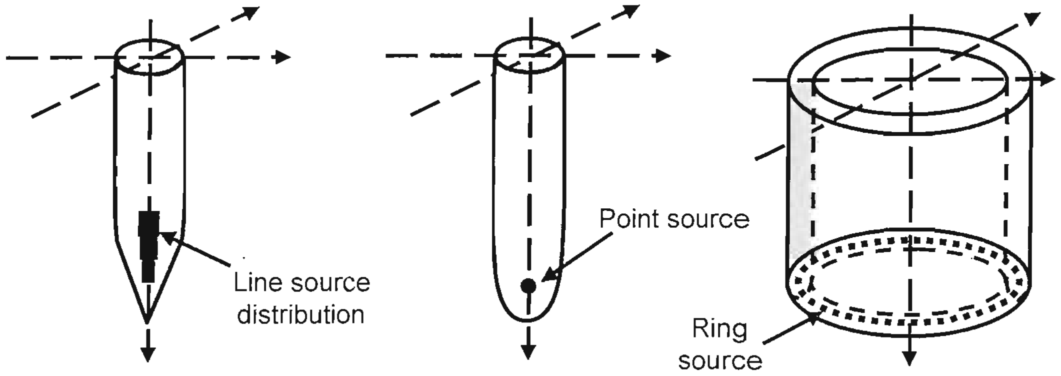

(a) "simple cone" (b) "simple pile" (c) "simple sampler"

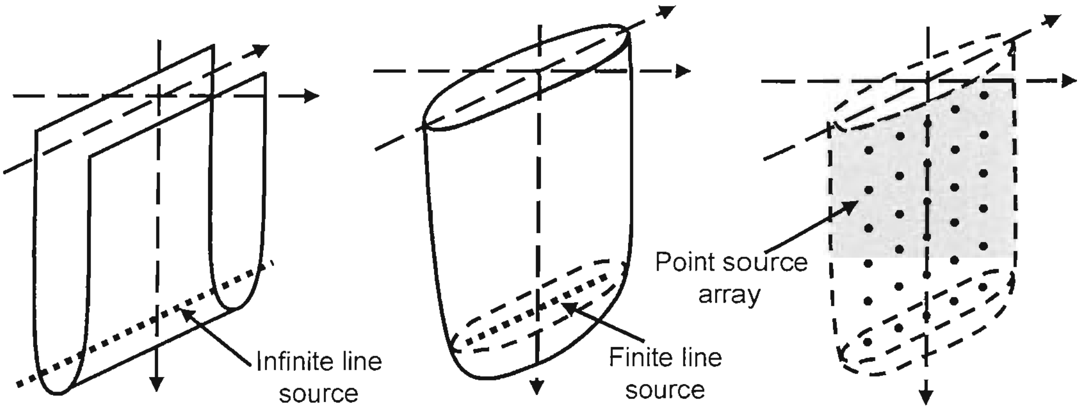

(d) "simple wall" (e) "simple plate" (f) "ideal dilatometer"

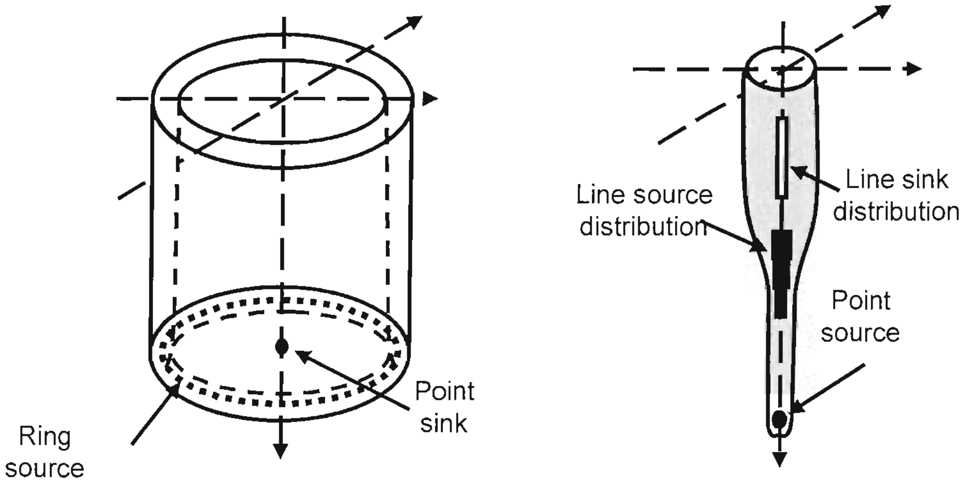

(g) "ideal self-boring pressuremeter" (h) "ideal tapered piezoprobe"

Figure 2-12 Various "simple bodies" generated for the SPM analysis using the superposition method

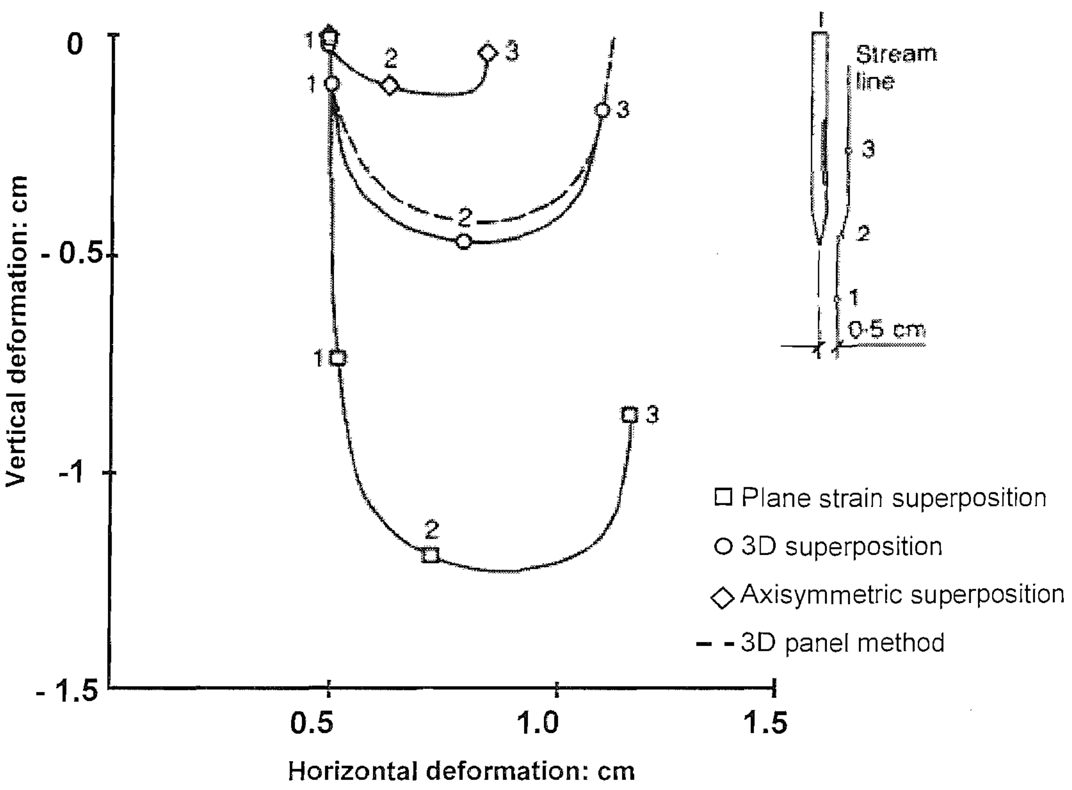

Figure 2-13 Computed displacements around a dilatometer from fluid flow analyses (Finno, 1993)

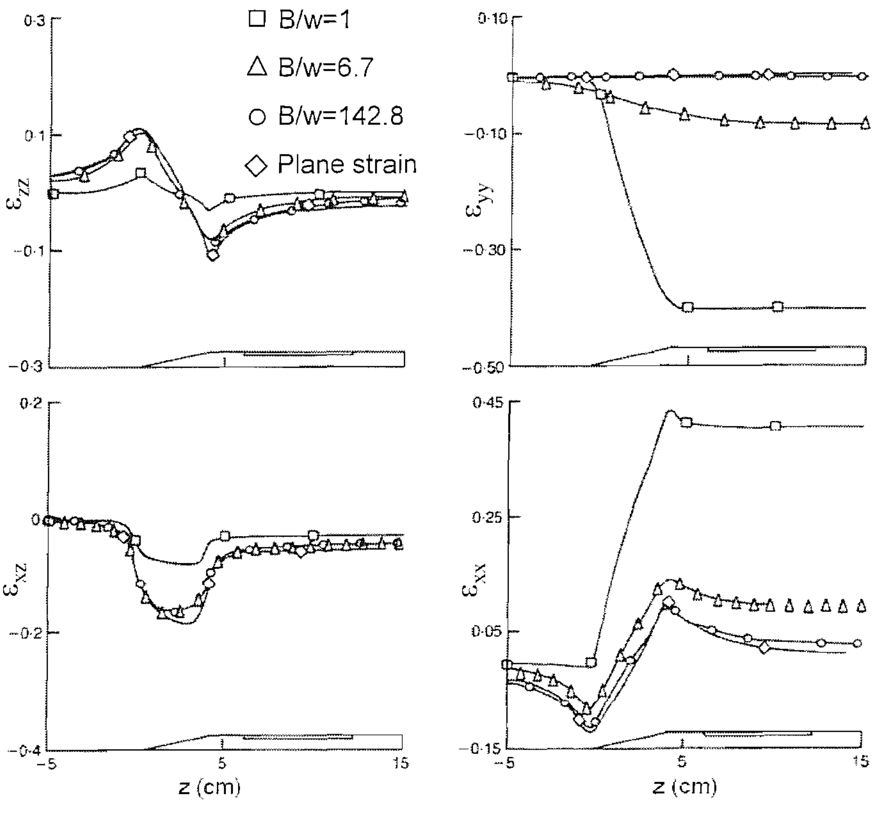

Figure 2-14 Influence of aspect ratio (B/w) on strain paths determined from 3D fluid flow analyses around dilatometer (Finno, 1993)

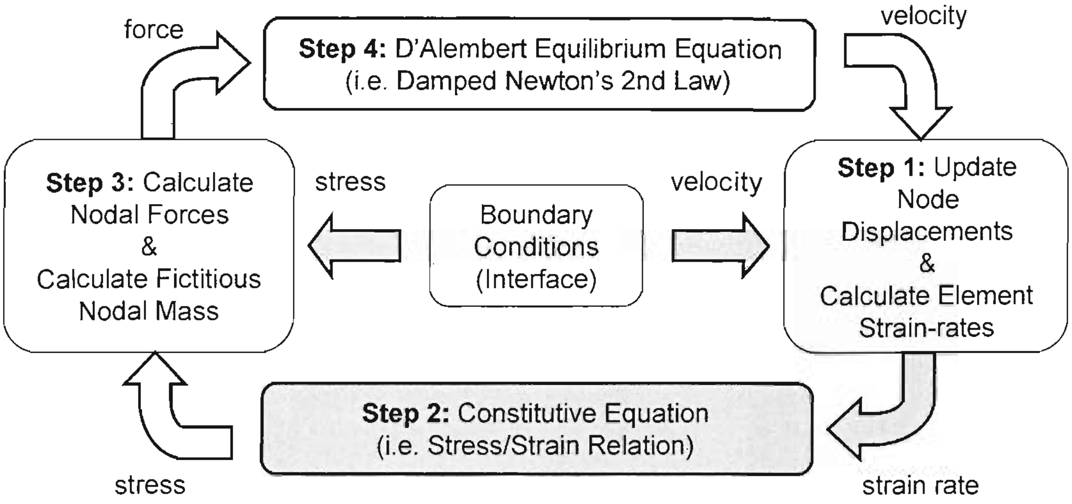

Figure 2-15 Explicit calculation cycle implemented in FLAC and FLAC^{3D}

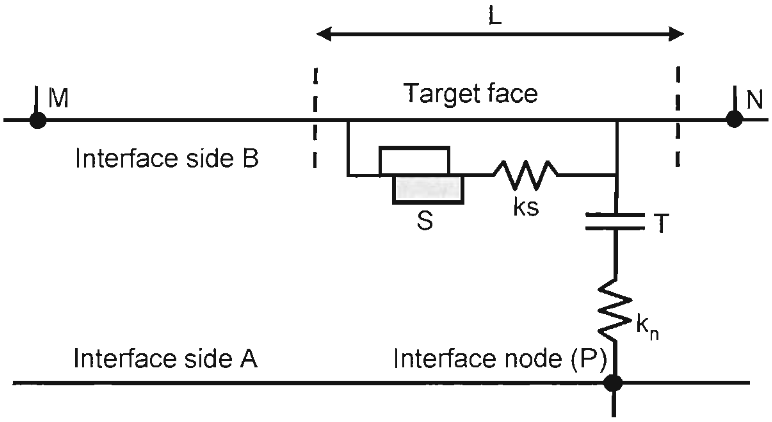

(a) FLAC

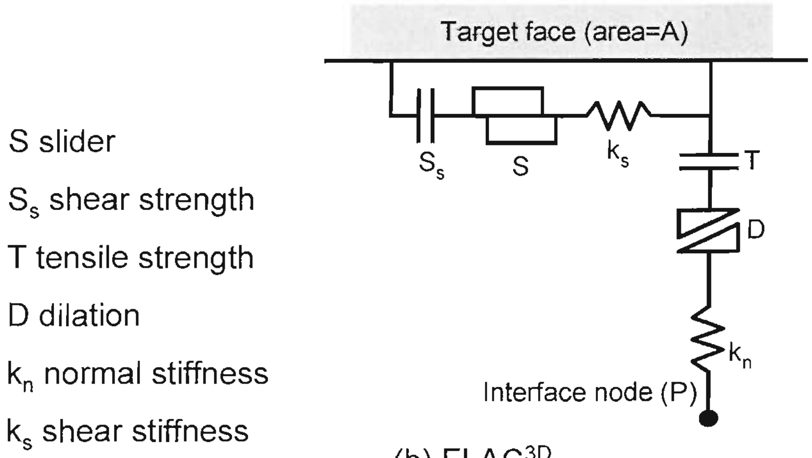

(b) FLAC^{3D}

Figure 2-16 Interface parameters in (a) FLAC and (b) FLAC^{3D}

3 TWO DIMENSIONAL FLUID FLOW ANALYSIS

3.1 Introduction

In this chapter, strain paths are determined for flow fields around the "simple wall" (Figure 3.2) and the "simple wedge" (Figure 3.14) half-bodies. To assess the approximations present in the solutions, strain paths were calculated using two independent methods: numerical (FLAC) and analytical (superposition). The "simple wall", which has a flat-rounded tip, was one the first geometries utilised in the strain path method (Chin, 1986). Due to the existence of a mobilised triangular zone of soil underneath flat-ended penetrating objects, the penetration of flat objects is better estimated by modelling the penetration of a wedge. The "simple wedge" geometry, which represents the idealised spade cell geometry in plane strain analyses, was consequently built by superposing a series of line source/sink(s) with various strengths on a uniform flow. In addition, strain paths were also evaluated numerically for the "sharp wedge" and "blunt wedge" geometries. Various features of the strain paths around these objects are presented in this chapter.

3.2 Determination of strain paths for "simple wall"

The "simple wall" is the half-body of the flow field built by superposing a line source on a uniform flow, as shown in Figure 3.1. For a uniform flow with a velocity of $U[LT^{-1}]$ and a line source with strength of $V[LT^{-3}]$ located at the origin $O(0,0)$, the half-width of the "simple wall" is $w=V/(2U)$ and its tip is located at $S(0, -V/(2\pi U))$ (refer to Appendix 10.1).

Strain paths around the “simple wall” were determined using both an analytical and a numerical method. In the analytical method, closed-form solutions for strain paths were derived from fluid flow equations. In the numerical method, strain paths were determined from a boundary value problem that modelled a region of flow around the “simple wall”. Strain paths determined from these methods were compared to determine optimum modelling parameters (e.g. mesh density and boundary locations) required for reproducing the closed-form solution of the “simple wall”.

3.2.1 The analytical method

In the analytical method, strain paths were derived from fluid equations for the superimposed flow using the following procedure. In the first step, velocity (v_X, v_Z) equations were determined for the flow around the “simple wall” (Equation 3-1):

$$v_x = \frac{V}{2\pi r}\cdot\frac{x}{r},\ v_z = \frac{V}{2\pi r}\cdot\frac{z}{r} + U,\ r = \sqrt{x^2 + z^2}$$

Equation 3-1

Strain rates ($\varepsilon^{\cdot}_{ij}$) were then derived from partial derivatives ($\partial v/\partial$) of the velocity equations (Equation 3-2):

$$\dot{\varepsilon}_{ij} = \frac{1}{2}\cdot\left(\frac{\partial v_i}{\partial j} + \frac{\partial v_j}{\partial i}\right)$$

Equation 3-2

Strain rates were integrated on the time domain (dt) along each streamline to evaluate the strain paths (ε). On a small segment (ds) of the streamline, the velocity (v) can be assumed constant, and the strain path integral can be rewritten on the displacement domain (ds) as Equation 3-3:

$$\varepsilon = \int \dot{\varepsilon}dt = \int \frac{\dot{\varepsilon}}{v} ds$$

Equation 3-3

These steps are expanded in detail and the equations for various components of strain rate and strain tensors are given in Appendix 10.1.

The analytical solution for strain paths around the "simple wall" was solved within a MATLAB (MathWorks, 2004) script. The script uses Equations 3-1 and 3-2 directly to calculate velocity and strain rates at any point in the superimposed flow. The strain path integral (Equation 3-3), however, was calculated numerically using an adaptive Gauss/Lobatto quadrature rule (Gander and Gautschi, 2000; Biran and Breiner, 2002). For numerical calculation reasons, the lower boundary of the strain integral, the undisturbed flow (at $z= -\infty$), was estimated by a finite value (z_0). The lower boundary (i.e. undisturbed flow) was assumed to be at a level below the tip, where the vertical velocity (v_z) of the superimposed flow was close to (=99%) the velocity of the uniform flow (U). According to this condition, the lower boundary of the integral was assumed to be at a distance greater than 31.5w below the origin ($z_0< -31.5w$), where (w) is the half-width of the "simple wall" (refer to Appendix 10.1).

Figure 3.2 shows the "simple wall" geometry with a half-width of w=4.2mm. Two features of this geometry should be considered when interpreting the results. Firstly, the "simple wall" has a flat-rounded tip. Secondly, half-width of the "simple wall" increases gradually until infinity. The axes have different scales in this figure.

Strain paths are plotted for streamlines around the "simple wall" in Figures 3.3, 3.4 and 3.5. By convention, compression is shown as positive in all outputs. The lower boundary of strain integrals was set to 64w beneath the tip level (i.e. twice the value determined from the 99%U criterion). In these figures, strain paths were plotted for three streamlines that have initial distances of $x_0=4w$, 10w and 20w from the plane of symmetry. Strain values along streamlines are plotted against the normalised vertical distance (z/w), where z/w=0 indicates the tip level.

Figure 3.3 shows the strain path for horizontal (ε_{xx}) strains in the flow field around the "simple wall". The horizontal strain path consisted of three distinguishable sections: the extension ($\delta\varepsilon_{xx}<0$), compression ($\delta\varepsilon_{xx}>0$) and re-extension ($\delta\varepsilon_{xx}<0$). The length of the compression zone (i.e. distance between maximum and minimum strains) was larger for streamlines located further away from the "simple wall". It is also observed that streamlines closer (e.g. $x_0/w=4$) to the "simple wall" had higher peak strains. The peak compression and extension strains were located at approximately equal distances from the tip (e.g. at z/w= -4 and z/w=5 for the $x_0/w=4$ streamline).

The vertical (ε_{zz}) strain is equal and opposite to the horizontal strain due to conservation of volume. As a result, the shape of strain path for vertical strain shown in Figure 3.4 is the mirror of the horizontal strain path (Figure 3.3). This is also evident from the strain expressions derived in Appendix 10.1.

Figure 3.5 shows the strain path for shear (ε_{xz}) strains. The maximum shear was reached at the "simple wall" tip level for all streamlines. It was noticed that the peak shear strains were higher for streamlines closer to the "simple wall". It is also evident that the shear strain values observed at z/w=30 level above the tip were higher than the shear values at the opposite level below the tip (i.e. z/w= -30).

Figure 3.6 shows the relationship between the horizontal (ε_{xx}) and shear (ε_{xz}) strains along the streamlines initially located at x_0=4w, 10w and 20w away from the plane of symmetry. The strain paths had the form of an incomplete circle. As penetration proceeded, a particle initially below the tip ($\varepsilon_{xz}=\varepsilon_{xx}=0$), experienced the following conditions subsequently: the minimum horizontal strain ($\varepsilon_{xx\ min}$), maximum shear strain ($\varepsilon_{xz\ max}$) and maximum horizontal strain ($\varepsilon_{xx\ max}$). However as the particle got far above the tip, it returned to its initial strain level ($\varepsilon_{xz}=\varepsilon_{xx}=0$). It was also evident that the peak compressive horizontal strain was higher than the peak extensive strain.

3.2.2 The numerical method

Strain paths were also derived for the "simple wall" geometry using a numerical method. A region of flow around the "simple wall" was modelled using FLAC by solving Darcy's law (Itasca, 2002b). FLAC outputs (i.e. flow velocity) were then used to determine strains rates along streamlines. Finally, the strain rates were added along particular streamlines to calculate strains and plot strain paths. These steps are explained in detail below.

The boundary conditions and meshing strategy used to simulate flow around half-bodies in FLAC are shown in Figure 3.7. The upper and lower boundaries were horizontal and located at distance H from the tip. The left boundary followed the "simple wall" geometry, which was determined analytically. The shape of the right boundary, which had a distance of R from the plane of symmetry at the lower boundary, was determined from the stream function of the flow, $\Psi(x,z)$. Streamlines were also used to determine the horizontal location of the internal grid points within the model, whereas in the vertical direction, the grid points were spaced uniformly. In addition, a finer mesh was defined for a region above and below the "simple wall" tip (H1), as streamlines became highly distorted in this region.

FLAC calculates the flow velocity from the pressure conditions specified on boundaries of the model. The left and right boundaries were defined as impermeable, as they were streamlines. To define the flow problem around the "simple wall" numerically, the pressure on the upper and lower boundaries were fixed to values derived from the potential function, $\Phi(x,z)$. The determination of the potential function for the flow around the "simple wall" is expanded in Appendix 10.1. FLAC outputs were then transferred to MATLAB to calculate the strain paths.

The calculation of strain rates and strain paths from FLAC outputs was performed using a script developed within MATLAB. FLAC outputs were read into the script in binary format in order to reduce the truncation errors. FLAC outputs included the grid point coordinates along streamlines and the velocity components of the flow at centroids of FLAC zones. The calculation of strain rates was a two-step procedure. In the first step, strain rates were calculated numerically from the velocity field, using the 3-point centered differentiation rule (Equation 3-4):

$$\frac{df(x)}{dx} = \frac{f(x+\Delta x) - f(x-\Delta x)}{2\Delta x}$$

Equation 3-4

In the second step, strain rates were calculated at internal grid points, which were along streamlines, using a planar interpolation scheme. The script finally calculated strain paths by adding up the strain increments along streamlines, assuming a zero strain level at the lower boundary. The discrete form of strain path expression is shown in Equation 3-5:

$$\varepsilon = \int \dot{\varepsilon} dt = \sum \dot{\varepsilon} \frac{ds}{v}$$ **Equation 3-5**

In this equation, (ds) is the length of a small segment on the streamline and (v) is the velocity of flow, which was assumed constant over (ds).

3.2.3 Results

The influence of mesh density and boundary locations on the strain paths determined numerically were assessed by comparing the peak strain values determined numerically with those derived analytically. Table 3.1 lists various boundary conditions and number of elements used in a range of fluid flow models. To quantify the influences of these modelling parameters, peak strain values calculated from the two methods (numerical and analytical) were compared. The relative difference, which shows the difference between peak strains determined numerically and analytically, normalised by the analytical peak strain, were calculated in various models and are listed in Table 3.2 for the streamline initially located at $x_0/w=4$. The average of relative differences, in various models, is plotted for this streamline in Figure 3.8.

It is observed from these results that the location of the upper and lower boundaries had a significant effect on the results. These boundaries need to be positioned far from the tip to provide a satisfactory estimation of the undisturbed flow at infinity. It can be seen from the bar chart (Figure 3.8) that the TALL model gave the best solution with only 1.88% average difference. Models were, however, insensitive to changes in the mesh density, as the density of the mesh used in the MAIN model was adequate to capture severe distortions of streamlines adjacent to the tip. FLAC models were not particularly sensitive to the location of the far right boundary, since this was along a streamline and therefore presented a real fluid boundary.

The numerically determined strain paths for the TALL model are plotted along with the analytical results for the flow around the "simple wall" (Figures 3.9-3.12 inclusive). In the TALL model, the right boundary was located at R=134.4mm(32w), the horizontal boundaries at H=268.8mm(64w) and the extent of fine region adjacent to the tip was H1=33.6mm(8w). The agreement between the numerically and analytically determined strain paths for three streamlines initially located at $x_0/w=4$, 10 and 20 is evident in these figures.

3.3 Determination of strain paths for “simple wedge”

Many of push-in devices (e.g. dilatometers, samplers and pressuremeters) utilised in geotechnical applications have a sharp cutting edge. This sharp tip minimises the soil disturbance created during the installation of push-in devices. Experimental studies have confirmed that during penetration of a flat-ended device a triangular dead zone of soil is formed beneath the tip, which moves with the penetrating object (Johnson, 1970; Baligh and Scott, 1975). Due to the existence of this zone, the deformation patterns around a flat-ended penetrating object are better estimated by modelling the penetration of a wedge-shaped object (Gupta, 1991). In addition, fewer numerical modelling problems are encountered when simulating the penetration of a wedge-shaped object, in comparison to modelling the penetration of a flat-ended object. The spade cell geometry was approximated by a newly developed half-body termed the “simple wedge”. In this section, strain paths determined for the flow field around the “simple wedge” are discussed.

The “simple wedge” geometry is the simple-body of the flow field created by superposing a series of line sources and sinks with various strengths on a uniform flow, as illustrated in Figure 3.13. For a uniform flow with velocity of $U[LT^{-1}]$ and (n) source/sink lines with strengths of $V_i[LT^{-3}]$ $(i=1,\ldots,n)$ located at distances of d_i in the vertical direction from the origin O(0,0), the half-width of the “simple wedge” is $w=\sum V_i/(2U)$. The location of the tip of the “simple wedge” can be derived numerically from the definition of the stagnation point.

The strengths and locations of singularities (i.e. sources and sinks) were selected primarily to incorporate two features into the new half-body geometry: a sharp tip and a vertical shaft. The locations of source/sinks lines used to generate the simple “wedge geometry” are indicated by black/white circles in Figure 3.14. The relative strength of singularities is also illustrated by the length of horizontal arrows in this figure. The strength of the source lines located in the triangular section of the "simple wedge" was varied to ensure the creation of a sharp tip. Alternating sources and sinks were used to ensure that the shaft section of the "simple wedge" was vertical. Table 3.3 lists the locations (d_i) and relative strengths (V_i/U) of the singularities used to create a "simple wedge" with a half-thickness of w=4.2mm. A procedure similar to that adopted for the "simple wall" was followed to determine strain paths in the flow around the "simple wedge" geometry.

3.3.1 The analytical method

In the analytical method, strain paths were determined entirely from the fluid flow equations. The steps taken to calculate strain paths around the "simple wedge" were:

1. Determination of velocity equations for the superimposed flow around the "simple wedge", given in Equation 3-6:

$$v_x = \sum_i \frac{V_i}{2\pi} \cdot \frac{x}{x^2 + (z-d_i)^2}, \quad v_z = \sum_i \frac{V_i}{2\pi} \cdot \frac{(z-d_i)}{x^2 + (z-d_i)^2} + U$$

Equation 3-6

2. Calculation of strain rates ($\dot{\varepsilon}_{ij}$) by obtaining partial derivatives ($\partial v/\partial$) from the velocity equations (Equation 3-2); and
3. Evaluation of strain paths by adding up the strain rates along each streamline.

Due to the existence of sigma ($\sum$) in the velocity and strain rate expressions, the strain path integral was estimated numerically by adding up the strain increments along streamlines, shown in Equation 3-7:

$$\varepsilon = \int \frac{\dot{\varepsilon}}{v} ds \simeq \sum \dot{\varepsilon} \frac{ds}{v}$$

Equation 3-7

Where (ds) was a small segment of the streamline. The velocity (v) and strain rate ($\dot{\varepsilon}$) were assumed constant over (ds).

A MATLAB script was written to perform the computational steps described above and to calculate strain paths for the flow around the "simple wedge". The starting position for the strain path sum (Equation 3-7), which is the undisturbed flow elevation, was estimated by the 99%U criterion (refer to section 3.2.1). For singularities used to create the "simple wedge" geometry with a half-width of w=4.2mm, the 99%U criterion was achieved at 28.4w below the origin.

Strain paths around the "simple wedge" are plotted in Figures 3.15, 3.16 and 3.17 for three streamlines initially located at distances of x_0=4w, 10w and 20w from the plane of symmetry. The lower boundary of strain sums was set to 64w beneath the tip level (i.e. more than twice the value determined from the 99%U criterion).

Figure 3.15 shows the strain path for the horizontal (ε_{xx}) strains derived using the analytical technique. In common with the "simple wall" results, three distinguishable sections of extension, compression and re-extension were evident in the horizontal strain path. The compression section was larger for streamlines located further away from the "simple wedge". The streamlines closer to the "simple wedge" had higher peak strains. Although, the value of peak strains (i.e. maximum and minimum) for the "simple wedge" were similar to those for the "simple wall", there was a clear shift in the location of peak strains in the "simple wedge". For example, for the x_0/w=4 streamline the extension peak was reached at z/w= -2 below the tip, while the compression peak was at z/w=8.5 above it.

The strain paths for vertical (ε_{zz}) strains are presented in Figure 3.16, which due to conservation of volume, are the mirror images of the horizontal (ε_{xx}) strain paths (Figure 3.15). This is also evident from the strain expressions given in Appendix 10.2.

The strain paths for shear (ε_{xz}) strains are shown in Figure 3.17. Similar to the changes observed in the horizontal and vertical strain paths, the location of maximum shear strain was shifted upwards to z/w=3.5 above the tip in the "simple wedge" results. Peak shear strains were generally higher for the streamlines closer to the "simple wedge". The shear strain values observed at z/w=30 were higher than the strain values at the corresponding level below the tip (i.e. z/w= -30). Peak shear strains for the "simple wedge" were generally lower than the values observed for the "simple wall".

The horizontal (ε_{xx}) strains are plotted against shear (ε_{xz}) strains in Figure 3.18. Strain paths had the form of an incomplete circle and particles returned to their initial strain level as they got far away from the tip (ε_{xz}=ε_{xx}=0). For streamlines close to the "simple wedge" (e.g. x_0/w=4), both the horizontal and shear strains did not return to zero at the end of the path. For streamlines further away however, the shear strains tend to zero at the end of the strain path. It is also evident that the peak compressive horizontal strain was higher than the peak extensive strain.

3.3.2 The numerical method

A numerical procedure similar to that adopted for the "simple wall" was used to determine strain paths for the flow around the "simple wedge", consisting of three steps:

1. Simulation of a region of flow around the "simple wedge" in FLAC;
2. Determination of strain rates along streamlines from FLAC outputs; and
3. Summation of the strain increments along streamlines to derive strain values.

The boundary conditions and the meshing strategy used for modelling the fluid flow around the "simple wedge" were similar to those adopted for the "simple wall", which were illustrated in Figure 3.7. For further description of the numerical method adopted, refer to section 3.2.2. The potential function Φ(x,z) used to calculate the pressure on the external boundaries is presented in Appendix 10.2.

3.3.3 Results

The boundary positions and mesh densities used in the MAIN, TALL, SHORT, WIDE, NARROW, FINE and COARSE models were similar to those used in the "simple wall" analyses (Table 3.1). The relative differences in peak strain values (the difference between numerical and analytical results normalised by the analytical output) for the $x_0/w=4$ streamline in various models were compared to assess the influence of modelling parameters and are listed in Table 3.4. The agreement between the numerically and analytically determined strain paths improved by locating the horizontal boundaries far from the tip. Models were however, less sensitive to the location of the right boundary and the mesh density as the values adopted for these two parameters in the MAIN model were adequate for the analyses. It can be seen in Figure 3.19 that the TALL model gave the best convergence with only 1.51% average difference.

Strain paths obtained for the TALL model from both the numerical and analytical methods are presented in Figures 3.20–3.23 inclusive, for the streamlines initially located at $x_0/w=4$, 10 and 20. In the TALL model, the right boundary was located at R=134.4mm(32w), the horizontal boundaries were at H=268.8mm(64w) and the extent of the fine region adjacent to tip was H1=33.6mm(8w). The agreement between the numerically and analytically determined strain paths is evident in these figures.

3.4 Determination of strain paths for "sharp" and "blunt" wedges

Although the superposition method used to generate simple bodies has the advantage of expressing flow characteristic as closed-form solutions, it fails to reproduce geometries with angular corners (as opposed to rounded-corners). In this section, strain paths are determined numerically for fluid flow around a "sharp" and a "bunt" wedge with apex angles of 18° and 60° respectively (Figures 3.25 and 3.26).

3.4.1 The numerical method

The numerical method for determining strain paths for the "sharp" and "blunt" wedges involved an additional step to the procedure adopted earlier for the half-bodies. Since the mesh columns should be aligned along streamlines for numerical calculations, the first step was to determine the streamlines for the flow around the wedges. Therefore, the procedure adopted to determine strain paths around a wedge involved:

1. Determination of the streamed mesh;
2. Simulation of a region of flow around the wedge in FLAC;
3. Determination of strain rates along streamlines from FLAC outputs; and
4. Summation of strain increments along streamlines.

Figure 3.24(a) shows the boundary conditions and meshing strategy adopted in the initial mesh. The lateral boundaries were impermeable, while a pressure difference was defined between the lower and upper boundaries to create the flow around the wedge. The mesh rows were horizontal, with a finer mesh spacing provided adjacent to the tip. Grid points on each row were spaced equally between the wedge-shaped left boundary and the vertical right boundary. This initial flow model was solved within FLAC and streamlines were determined from the velocity field by a MATLAB script. The internal mesh columns were then aligned along streamlines. This new mesh is termed the streamed mesh (Figure 3.24(b)). The next three steps for numerically determining strain paths have already been described in section 3.2.2.

3.4.2 Results

Strain paths were determined numerically for the flow around the "sharp" and "bunt" wedges with a half-width of w=4.2mm. The locations of boundaries were set to the dimensions specified for the TALL model (Table 3.1). Strain paths were determined for streamlines located at $x_0/w=4$ and 10 from the plane of symmetry and are discussed here.

The strain paths for horizontal (ε_{xx}) and vertical (ε_{zz}) strains around wedges, which are presented in Figures 3.27 and 3.28 respectively, showed two new characteristics. Firstly, in contrast to the "simple wedge", where the peak extension and compression strains were approximately equal, the peak strain below the tip was less than ½ of the peak strain above the tip. This difference may be due to the presence of the angular corner in sharp/blunt wedges in contrast to the rounded corner for the "simple wedge". Secondly, unlike the "simple wedge" where the values of strain were different for various streamlines, strain values converged to a constant value of 0.03 for the examined streamlines. This could be due to the vertical section of the wedges that makes all the streamlines vertically aligned along the shaft. The final value of the horizontal strain agrees with the value derived from the definition of horizontal strain (i.e. the relative horizontal displacement of streamlines). ε_{xx}=w/R=1/32=0.03, where (R) and (w) are the location of right boundary and half-width of the wedge respectively.

Comparison of the strain paths determined for the "blunt" and "sharp" wedges, illustrated in Figures 3.27–3.30 inclusive, also highlights the following points. Peak strain values for all strain components (i.e. horizontal, vertical and shear) were higher for the "blunt wedge" than the "sharp wedge". Peak strains in the "blunt wedge" were reached earlier along streamlines compared to the "sharp wedge". The differences between the strain paths determined for the "sharp" and "blunt" wedges became less significant for streamlines further away from the plane of symmetry.

3.5 Summary

In this chapter, strain paths were determined for flow fields around two-dimensional objects. The "simple wall" was the initial geometry examined and strain paths were determined numerically and analytically for the flow around it. To represent the spade cell geometry more realistically, a new simple-body with a sharp tip was created using the superposition method, termed the "simple wedge". The strain paths were determined for the flow around this geometry, numerically as well analytically. A range of modelling parameters were assessed and it was demonstrated that the fluid flow models in FLAC were particularly sensitive to the location of upper and lower boundaries (Farhangi *et al.*, 2006). A difference of less than 2 percent between the numerical and the analytical results was achieved by positioning these boundaries at 64w away from the tip, where (w) is the half-width of the penetrating object. In addition to these simple-bodies, strain paths were determined numerically for two angular-corner (rather than rounded-corner) wedges, with apex angles of 18° and

60°, the “sharp” and “blunt” wedges. The influences of an angular corner and a vertical shaft were evident in comparison with the “simple wedge” results. The effect of the apex angle was also investigated by comparing the strain paths determined for the flow around the “sharp” and “blunt” wedges.

The “simple wedge” geometry will be used as the idealised spade cell geometry for the two-dimensional soil penetration analyses in the next chapter (Chapter 4).

Table 3-1 Location of boundaries and number of elements used in FLAC fluid flow models

				Distance from origin (mm)		
No	Model	Description	Number of Elements	(H) Upper/Lower boundaries	(H1) Fine mesh region	(R) Far right boundary
1	MAIN	Standard mesh	2048	134.4 (32w)	16.8 (4w)	134.4 (32w)
2	TALL	Influence of upper & lower boundaries	4096	268.8 (64w)	33.6 (8w)	134.4 (32w)
3	SHORT	Influence of upper & lower boundaries	1024	67.2 (16w)	8.4 (2w)	134.4 (32w)
4	WIDE	Influence of right boundary	4096	134.4 (32w)	16.8 (4w)	268.8 (64w)
5	NARROW	Influence of right boundary	1024	134.4 (32w)	16.8 (4w)	67.2 (16w)
6	FINE	Influence of mesh refinement	8192	134.4 (32w)	16.8 (4w)	134.4 (32w)
7	COARSE	Influence of mesh refinement	512	134.4 (32w)	16.8 (4w)	134.4 (32w)

Table 3-2 Relative differences (%) of numerically determined peak strains from analytical results for $x_0/w=4$ streamline in "simple wall" models

No	Model	Minimum vertical strain	Maximum vertical strain	Minimum horizontal strain	Maximum horizontal strain	Minimum shear strain	Average (%)
1	MAIN	-19.47	-21.11	22.37	22.94	-3.44	17.86
2	TALL	2.76	1.23	1.23	1.73	-2.43	1.88
3	SHORT	-67.48	-59.66	61.07	72.27	-2.91	52.68
4	WIDE	-24.59	-24.91	26.38	28.32	-3.13	21.47
5	NARROW	-12.40	-14.96	17.54	17.66	-3.56	13.22
6	FINE	-20.58	-21.87	23.07	23.37	-1.41	18.06
7	COARSE	-16.54	-17.10	18.71	19.20	-8.86	16.08

Table 3-3 Relative strength (V_i/U) and location (d_i) of singularities used to create the "simple wedge" geometry

No (i)	Relative strength (V_i/U) mm^2	Distance (d_i) mm	No (i)	Relative strength (V_i/U) mm^2	Distance (d_i) mm
1	300	1.25	11	-200	36.25
2	600	3.75	12	200	38.75
3	500	6.25	13	-200	41.25
4	800	8.75	14	200	43.75
5	700	11.25	15	-200	46.25
6	1000	13.75	16	200	48.75
7	900	16.25	17	-200	51.25
8	1200	18.75	18	200	53.75
9	1800	21.25	19	-400	56.25
10	800	23.75	20	200	58.78

Note: U: velocity of uniform flow (mm/sec) and V_i: the strength of singularity (mm^3/sec)

Table 3-4 Relative differences (%) of numerically determined peak strains from analytical results for $x_0/w=4$ streamline in "simple wedge" models

No	Model	Minimum vertical strain	Maximum vertical strain	Minimum horizontal strain	Maximum horizontal strain	Minimum shear strain	Average (%)
1	MAIN	-7.32	-11.81	11.37	8.33	0.50	7.86
2	TALL	2.30	1.47	-2.50	-0.22	-1.07	1.51
3	SHORT	-25.95	-34.04	34.01	26.33	4.12	24.89
4	WIDE	-7.21	-11.68	11.46	8.44	0.51	7.86
5	NARROW	-7.18	-11.62	11.40	8.41	0.51	7.82
6	FINE	-10.44	-12.59	12.34	10.82	0.73	9.38
7	COARSE	0.36	-8.87	8.87	1.53	0.66	4.06

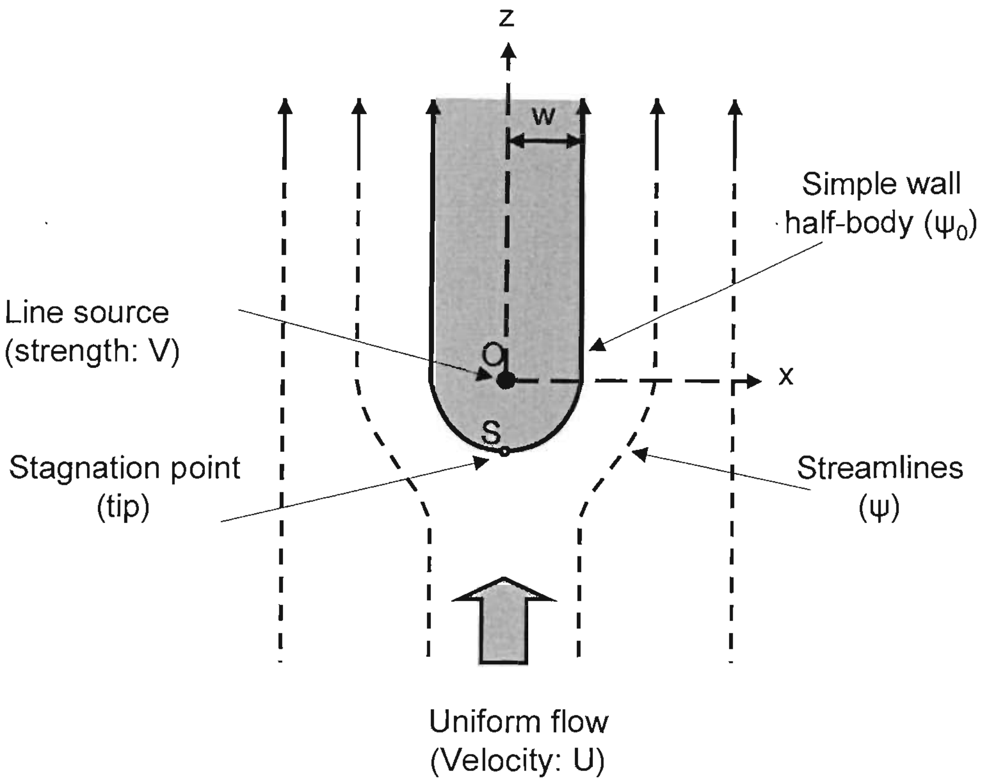

Figure 3-1 Schematic view of flow field around the "simple wall"

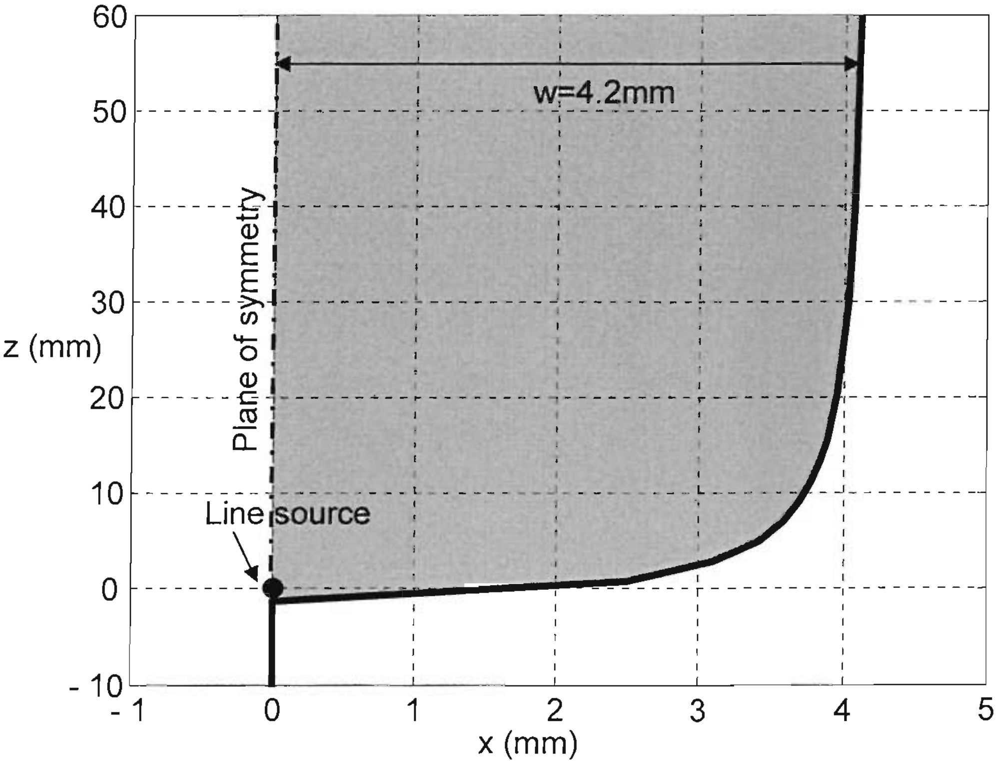

Figure 3-2 The "simple wall" geometry

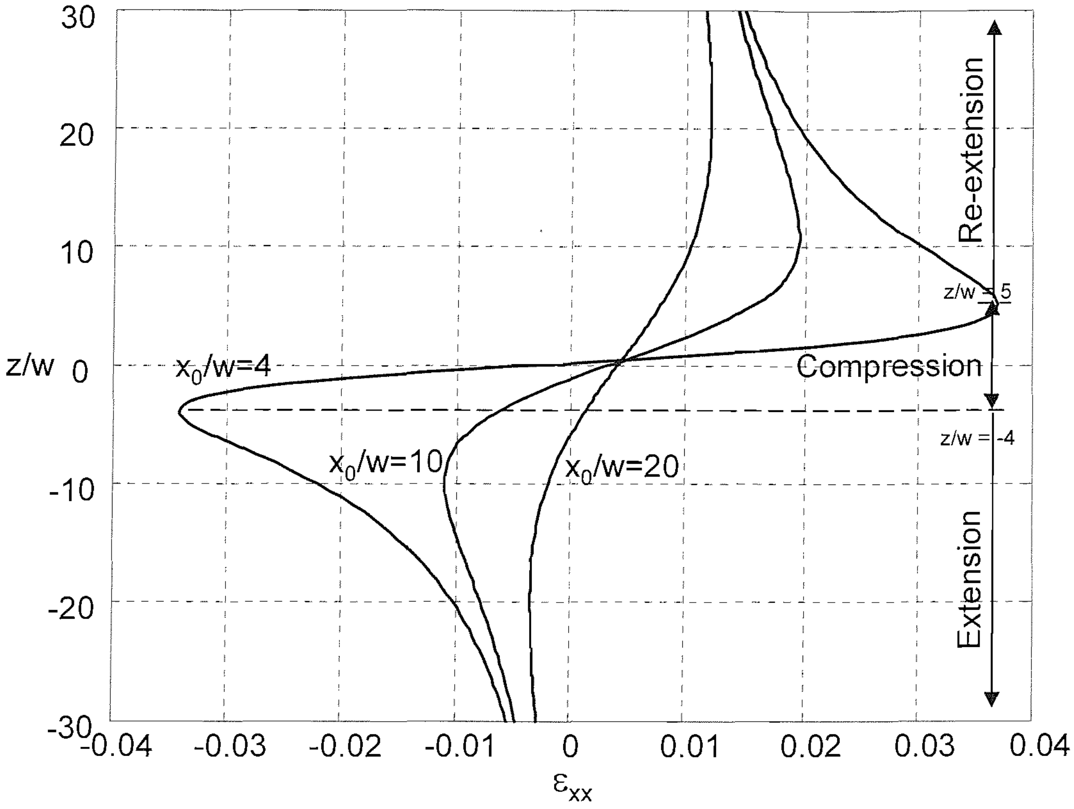

Figure 3-3 Analytical strain paths for (ε_{xx}) strain around "simple wall" in 2D fluid flow

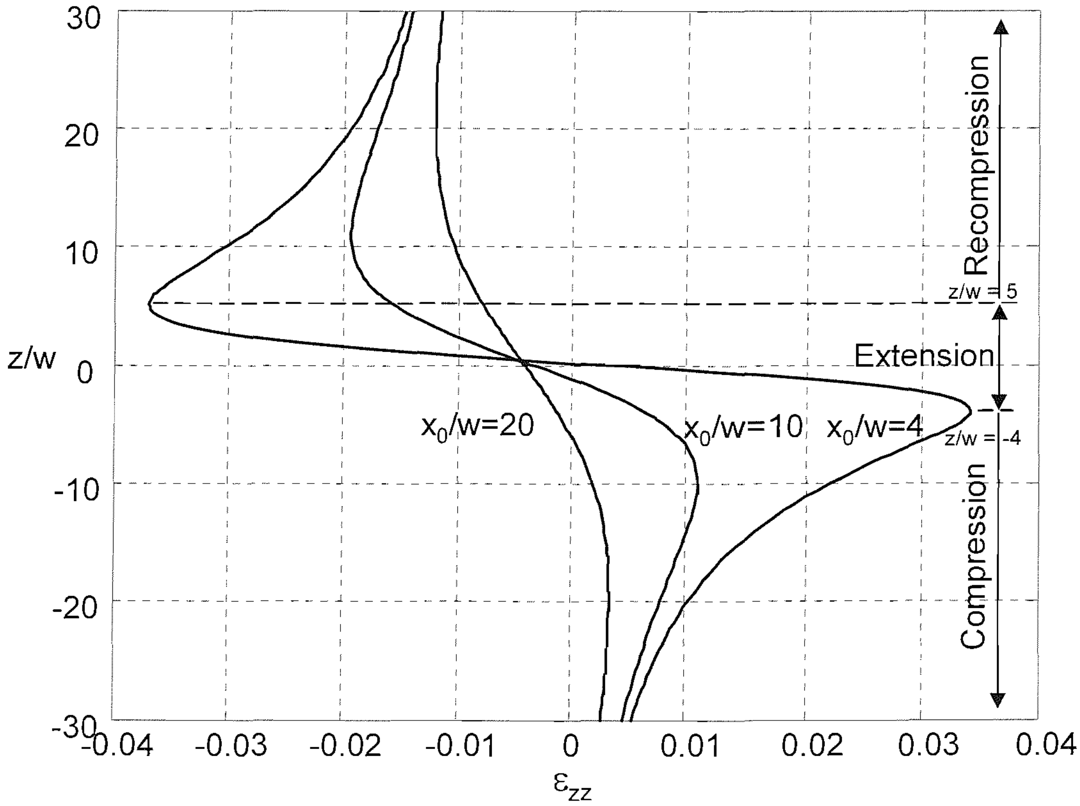

Figure 3-4 Analytical strain paths for (ε_{zz}) strain around "simple wall" in 2D fluid flow

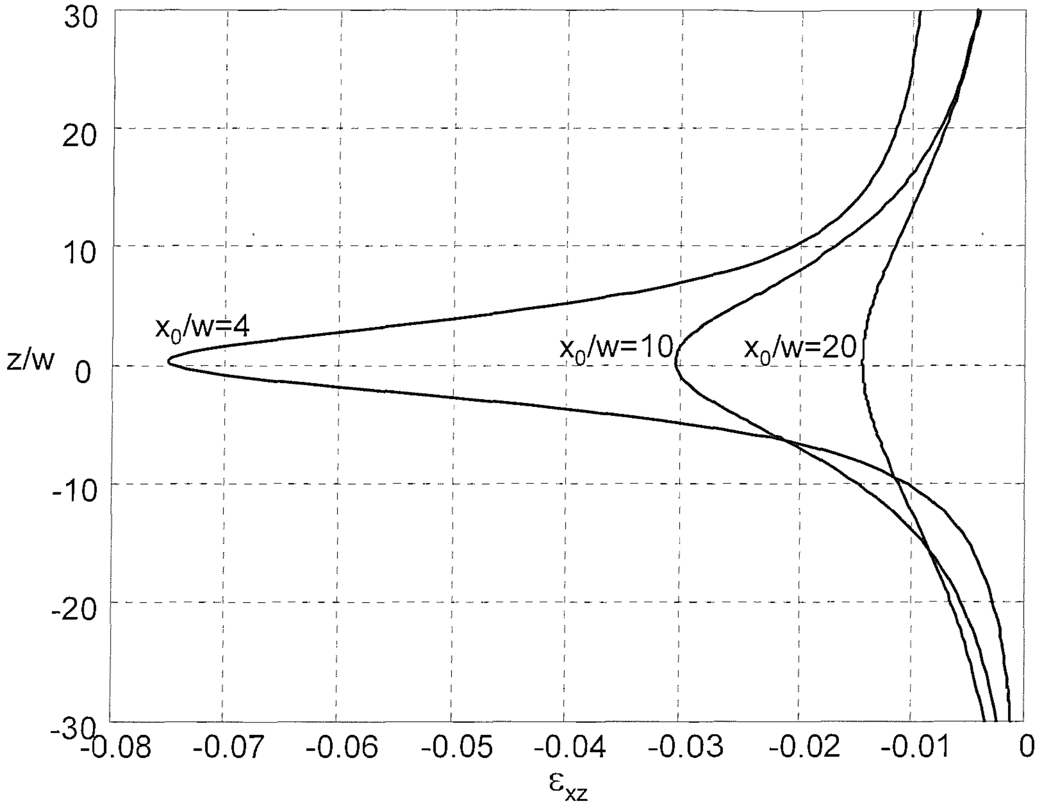

Figure 3-5 Analytical strain paths for (ε_{xz}) strain around "simple wall" in 2D fluid flow

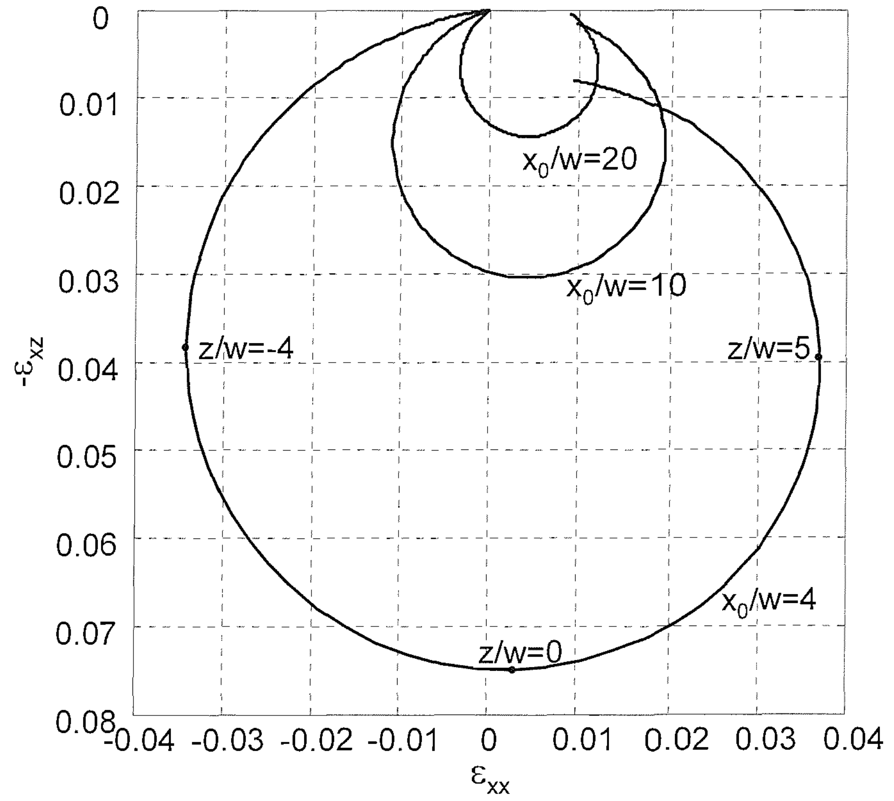

Figure 3-6 Analytical (ε_{xz}) strain vs. (ε_{xx}) strain for streamlines around "simple wall" in 2D fluid flow

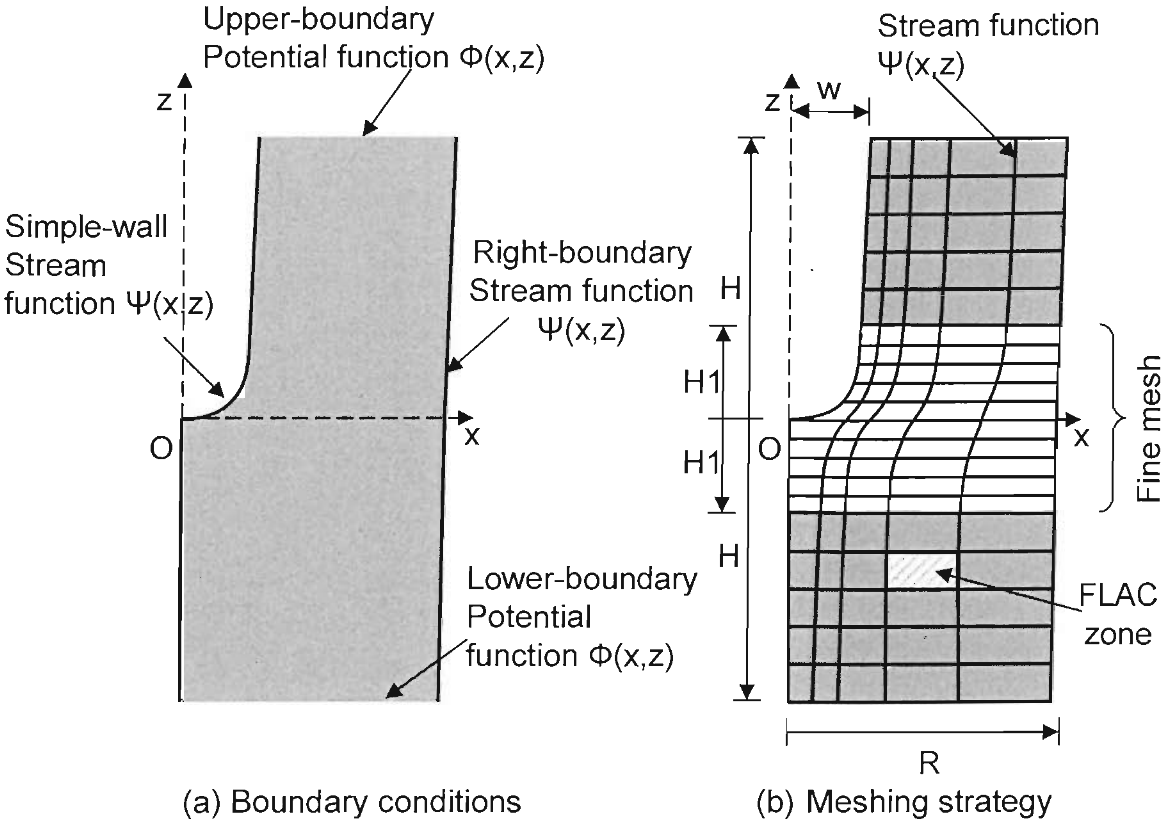

Figure 3-7 Numerical flow models: (a) Boundary conditions and (b) Meshing strategy

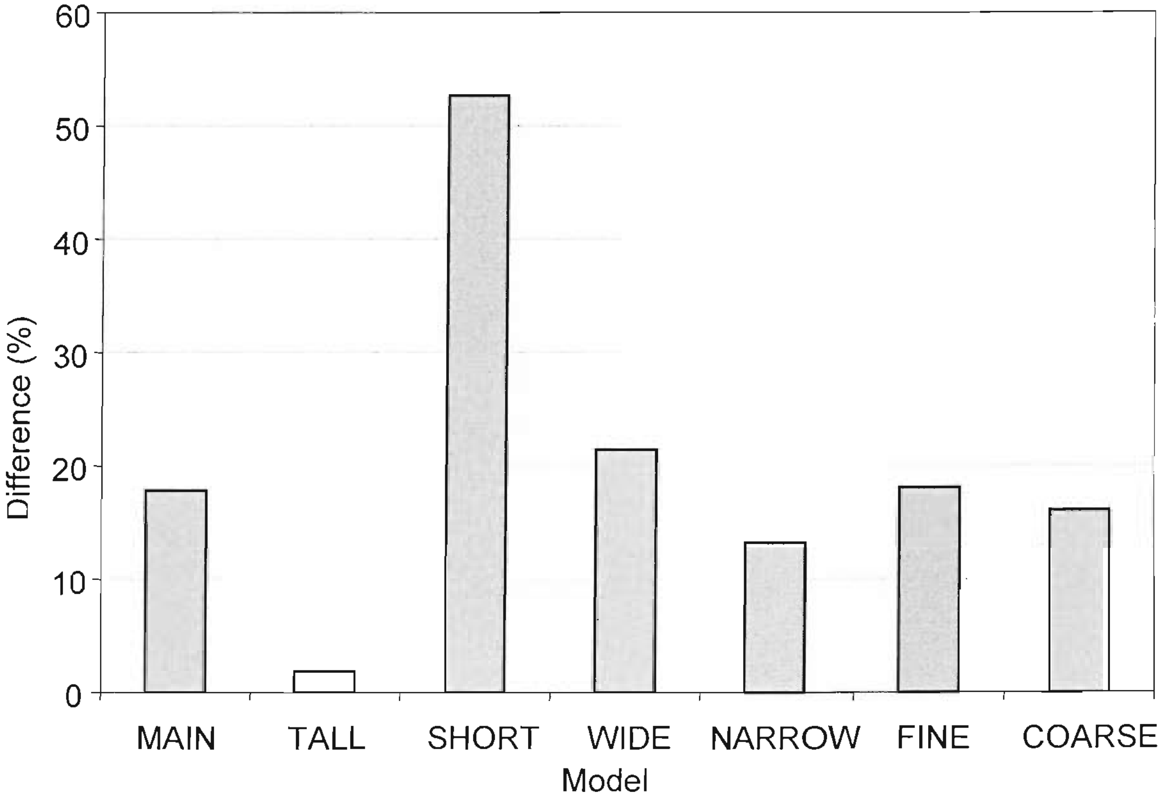

Figure 3-8 Average relative differences (%) in peak strains for the $x_0/w=4$ streamline in "simple wall" flow models

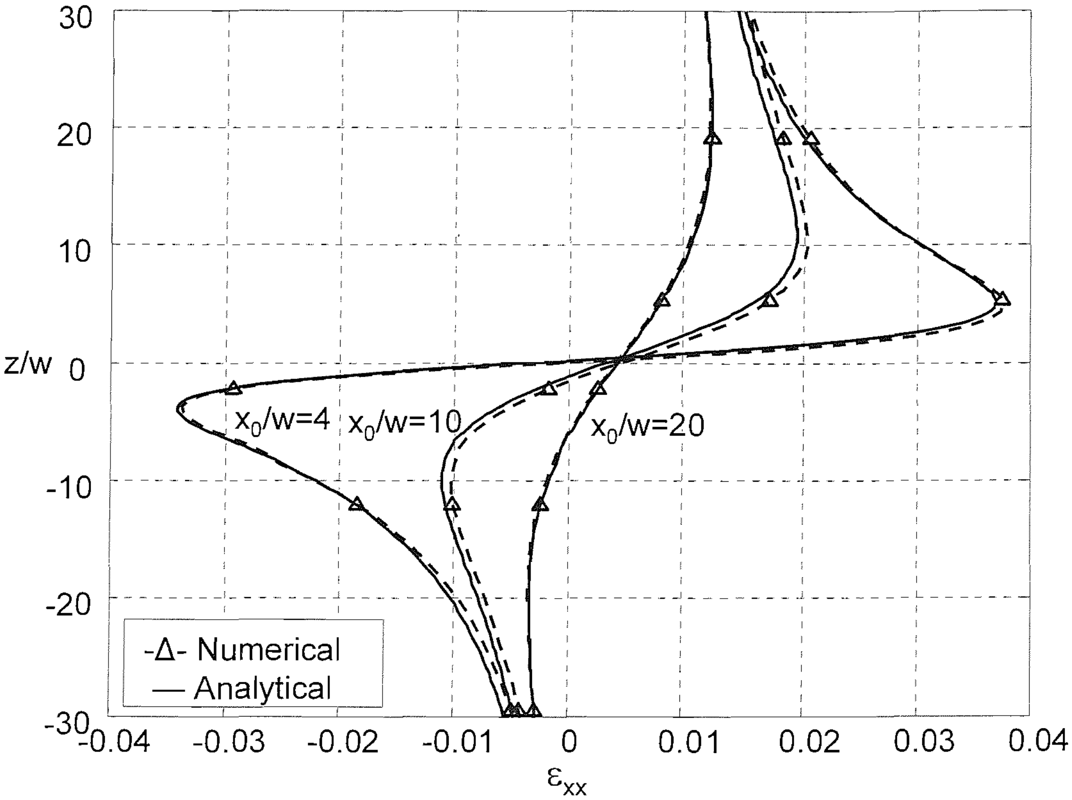

Figure 3-9 Comparison of numerical (TALL model) and analytical strain paths for (ε_{xx}) strain around "simple wall"

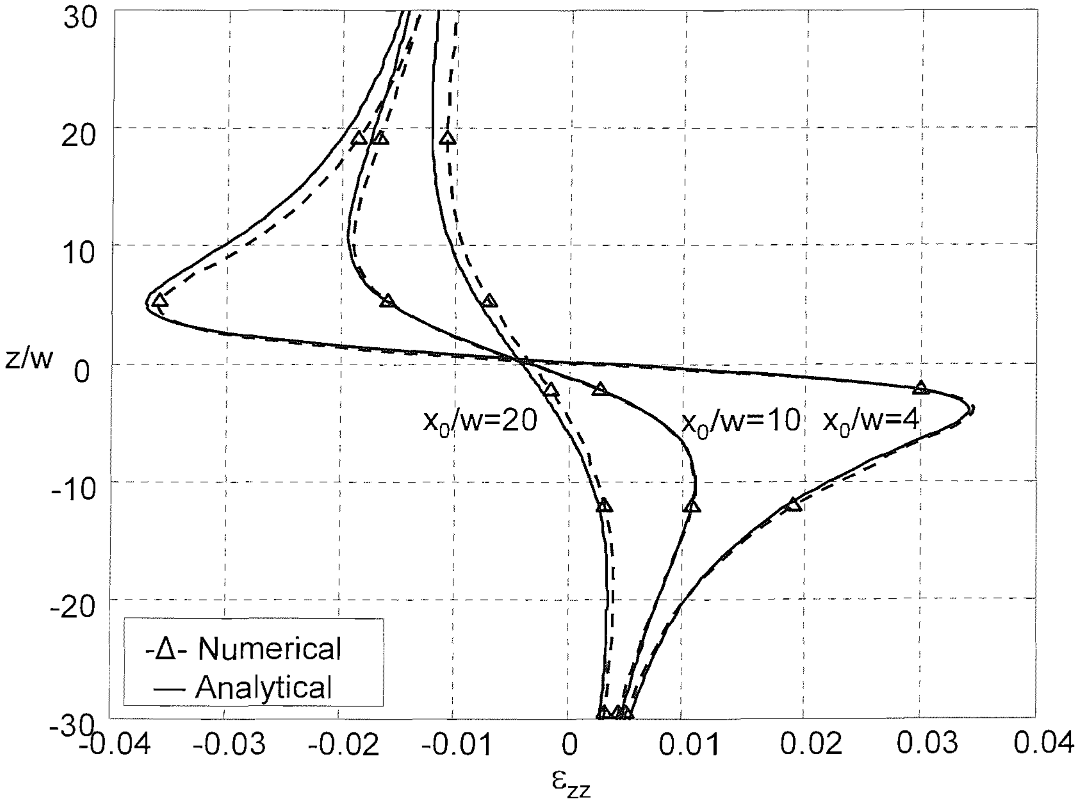

Figure 3-10 Comparison of numerical (TALL model) and analytical strain paths for (ε_{zz}) strain around "simple wall"

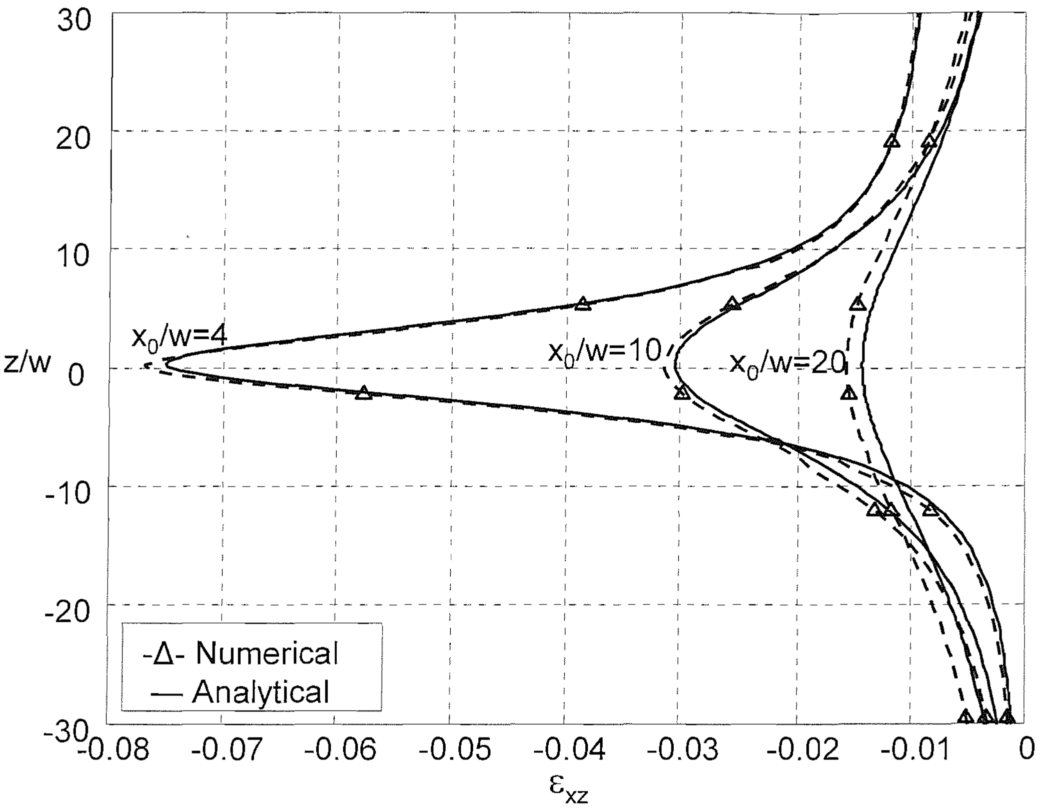

Figure 3-11 Comparison of numerical (TALL model) and analytical strain paths for (ε_{xz}) strain around "simple wall"

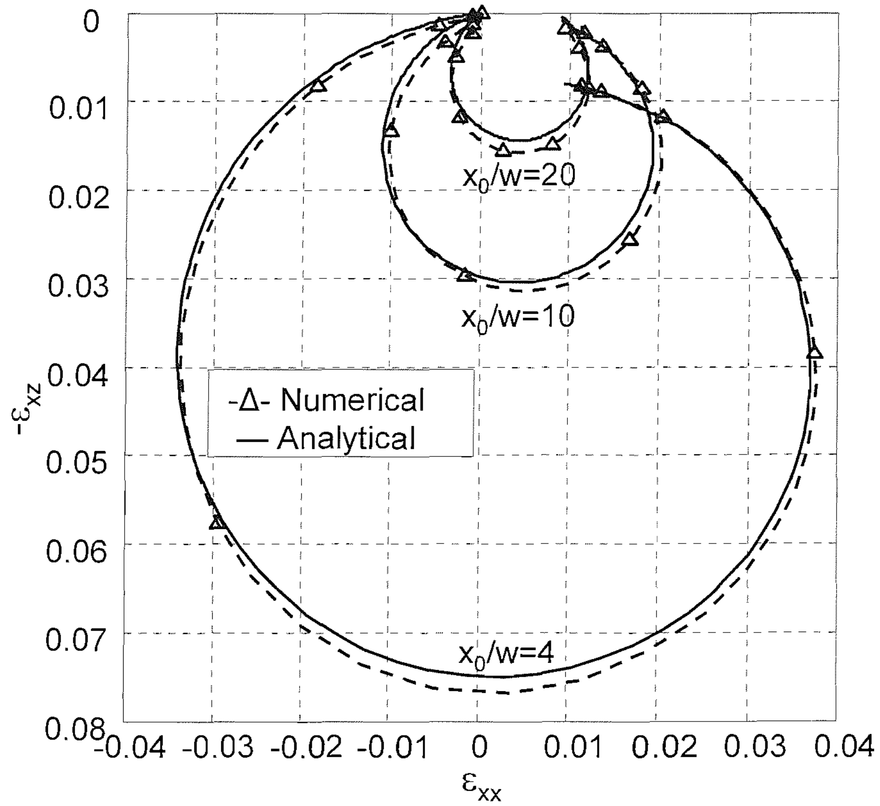

Figure 3-12 Comparison of numerical (TALL model) and analytical (ε_{xz}) strain vs. (ε_{xx}) strain for streamlines around "simple wall"

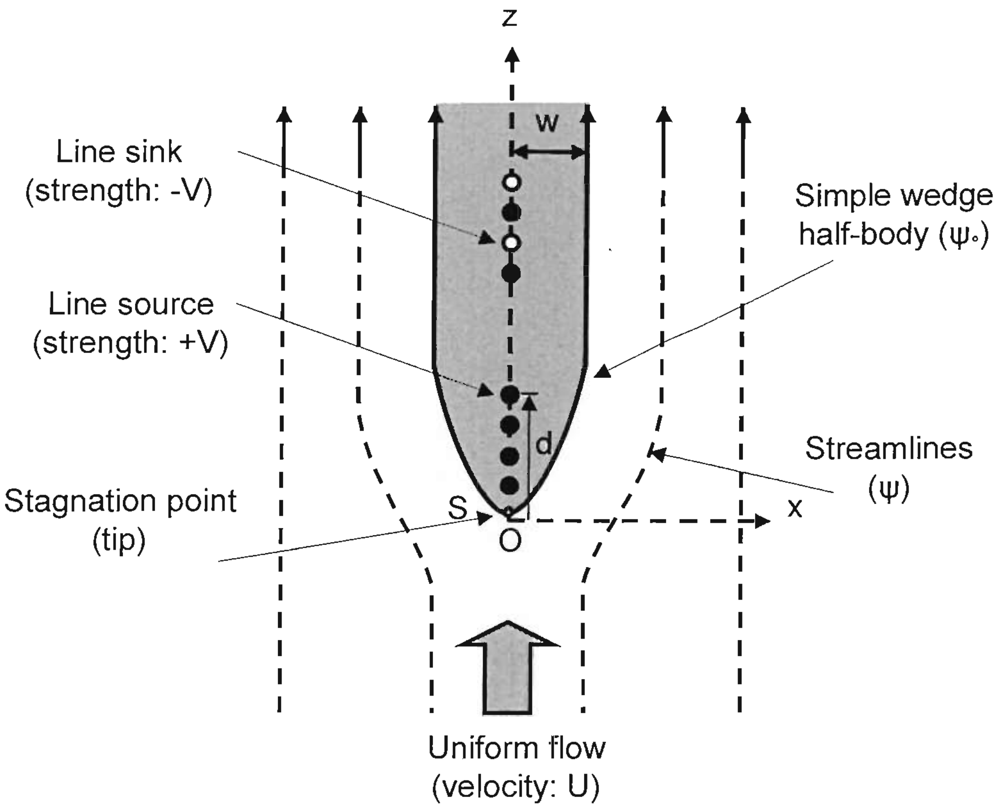

Figure 3-13 Schematic view of flow field around the "simple wedge"

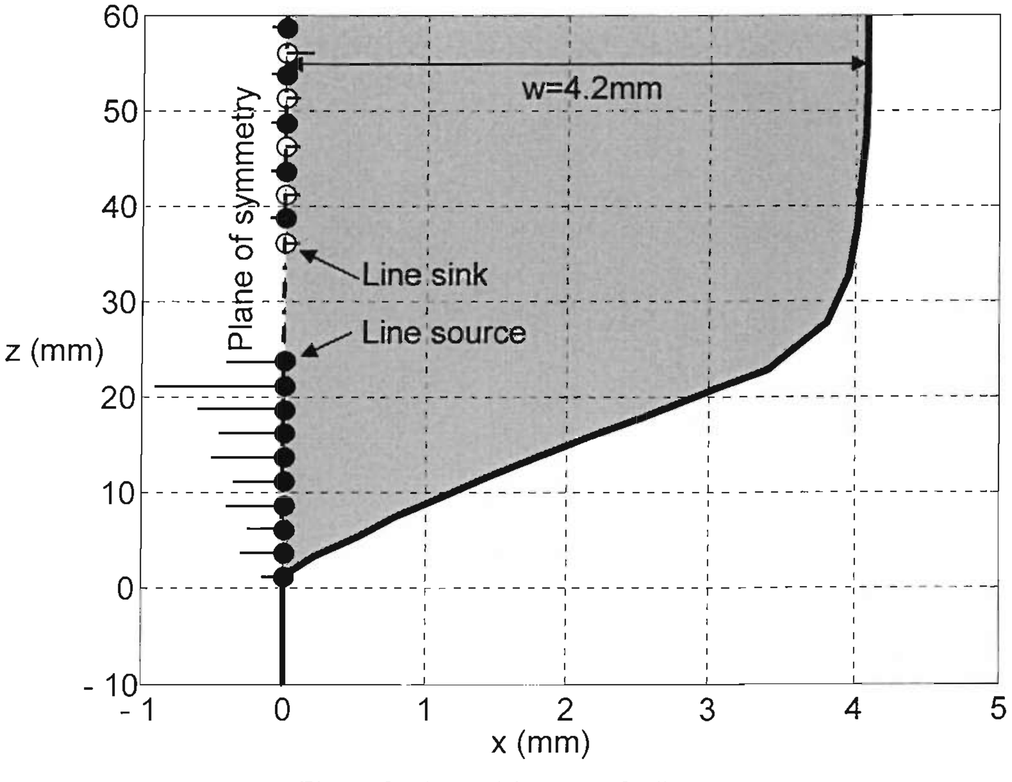

Figure 3-14 The "simple wedge" geometry

Note: Horizontal markers show the relative strength of line source/sink(s)

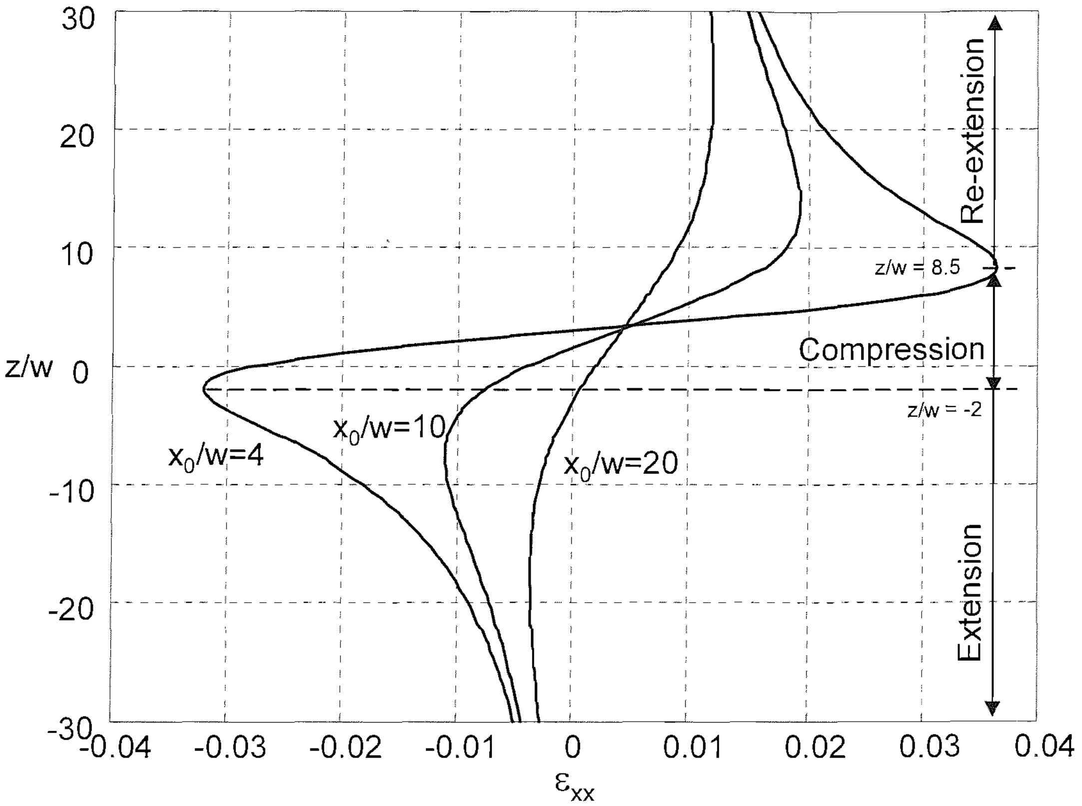

Figure 3-15 Analytical strain path for (ε_{xx}) strain around "simple wedge" in 2D fluid flow

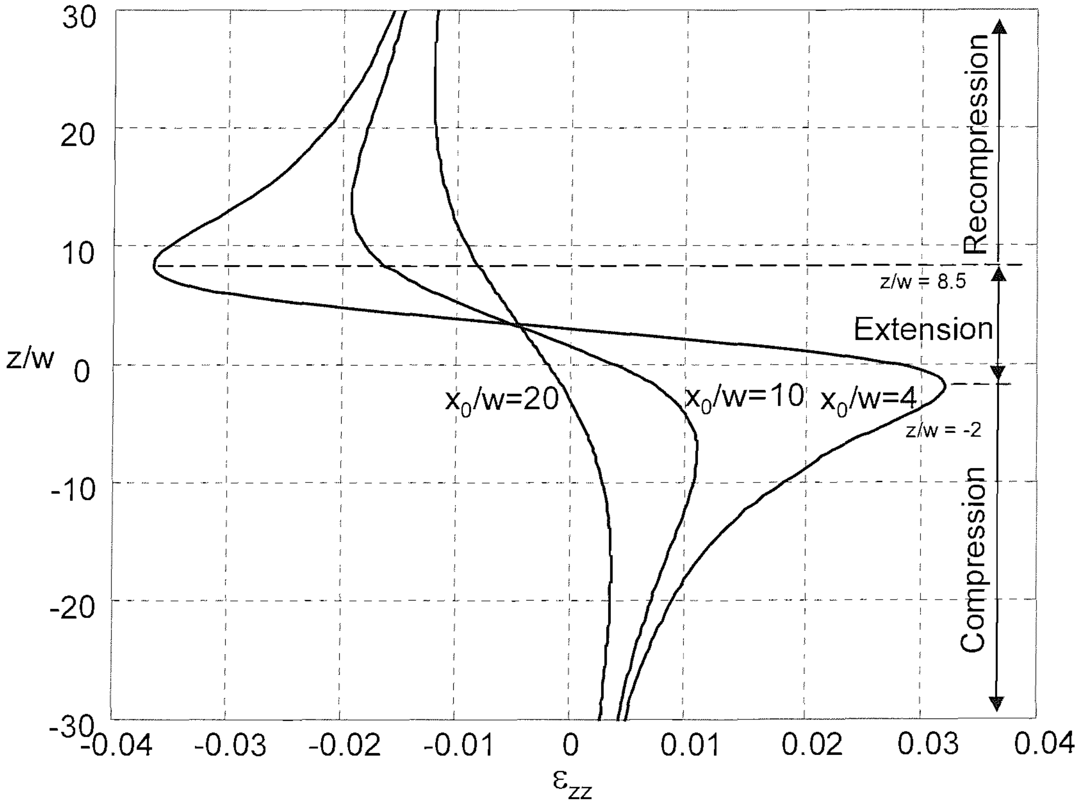

Figure 3-16 Analytical strain path for (ε_{zz}) strain around "simple wedge" in 2D fluid flow

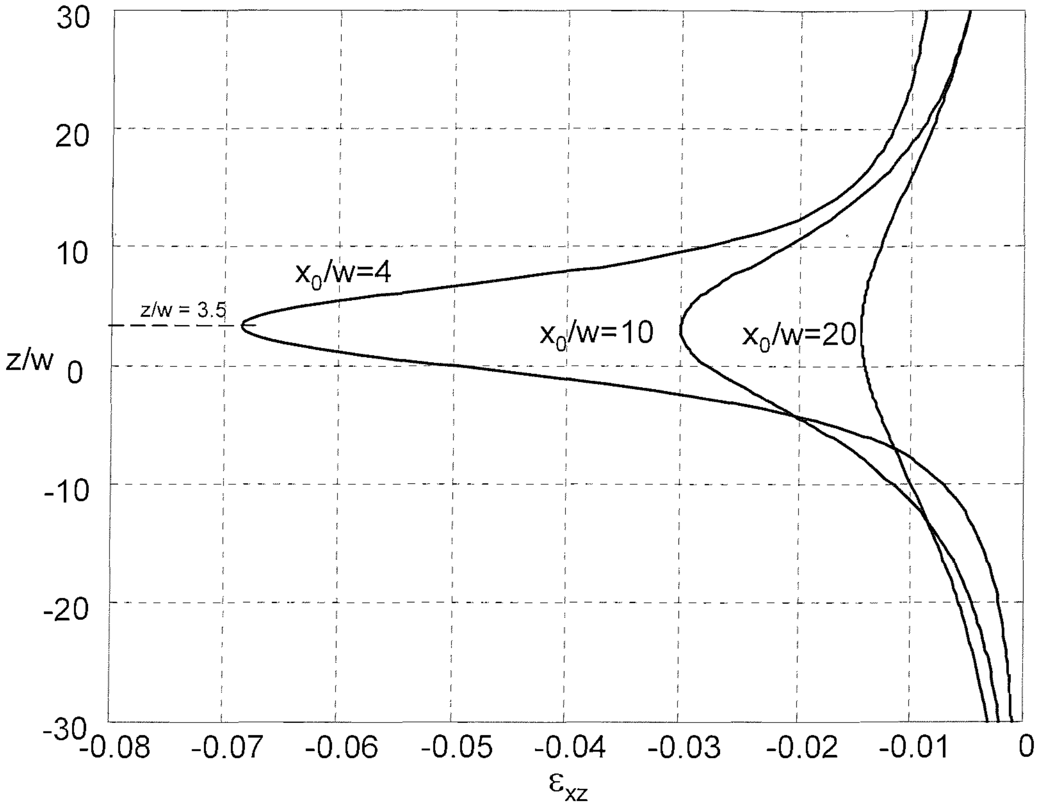

Figure 3-17 Analytical strain path for (ε_{xz}) strain around "simple wedge" in 2D fluid flow

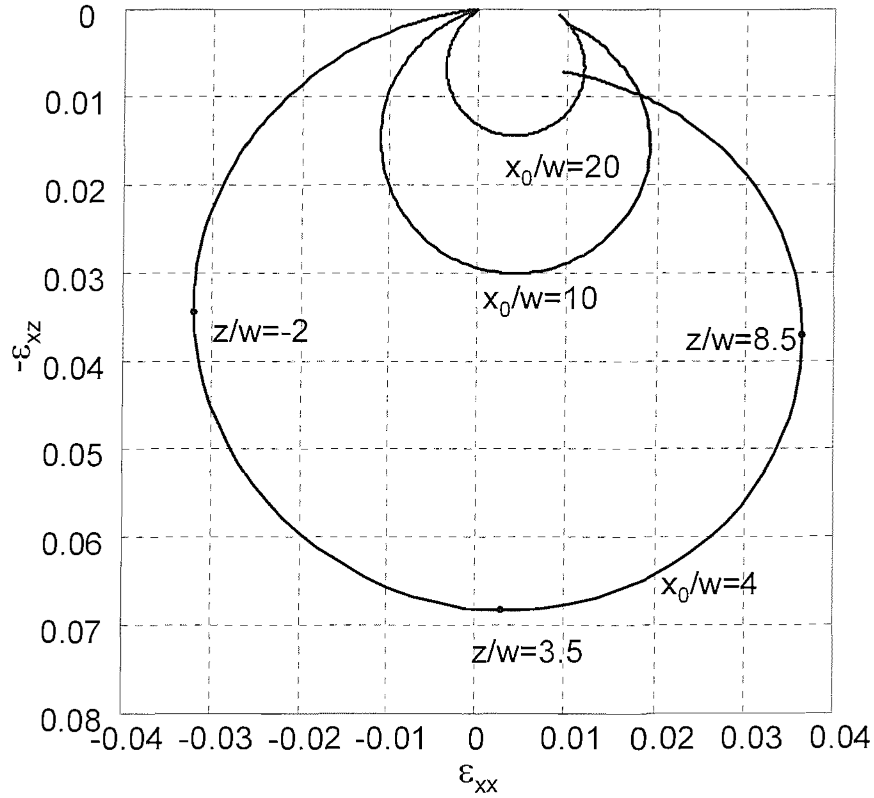

Figure 3-18 Analytical (ε_{xz}) strain vs. (ε_{xx}) strain for streamlines around "simple wedge" in 2D fluid flow

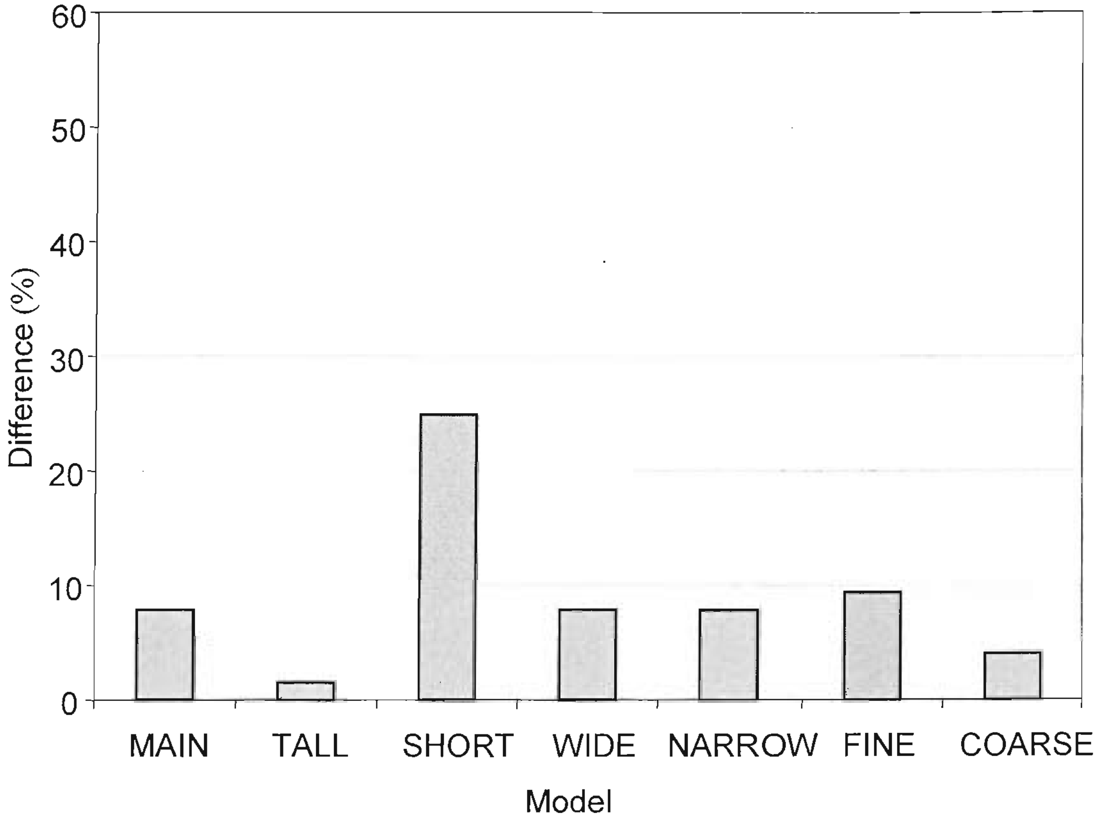

Figure 3-19 Average relative differences (%) in peak strains for the $x_0/w=4$ streamline in "simple wedge" flow models

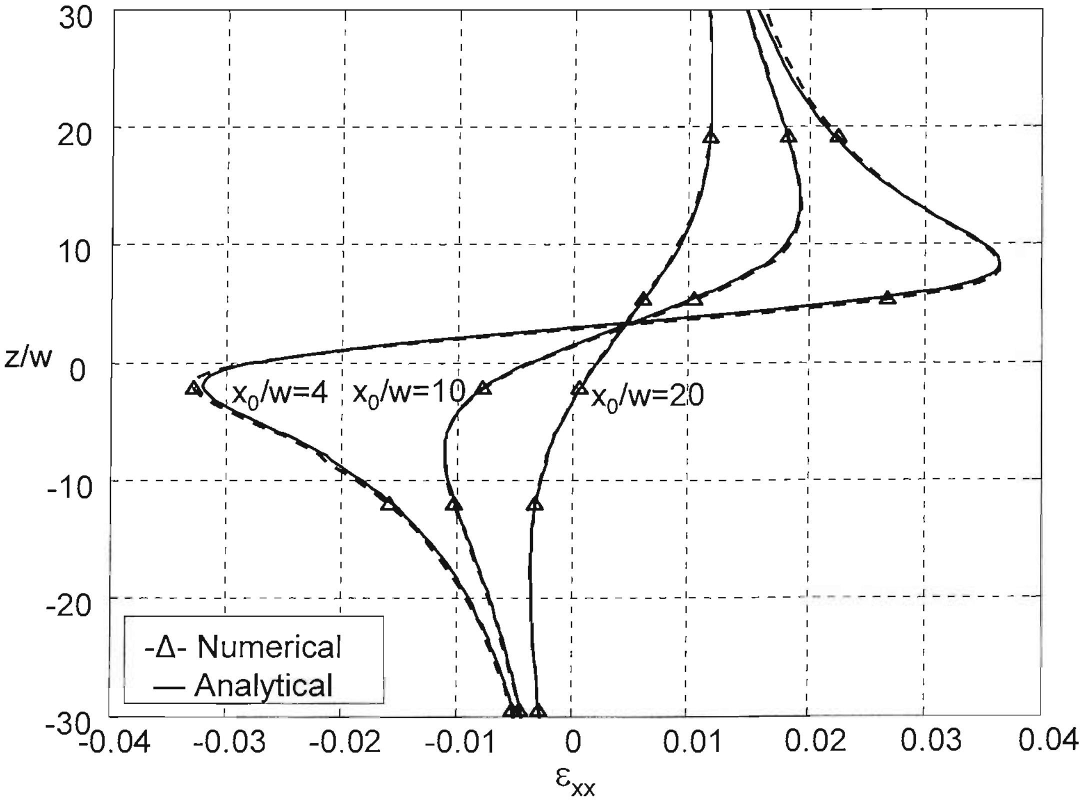

Figure 3-20 Comparison of numerical (TALL model) and analytical strain path for (ε_{xx}) strain around the "simple wedge"

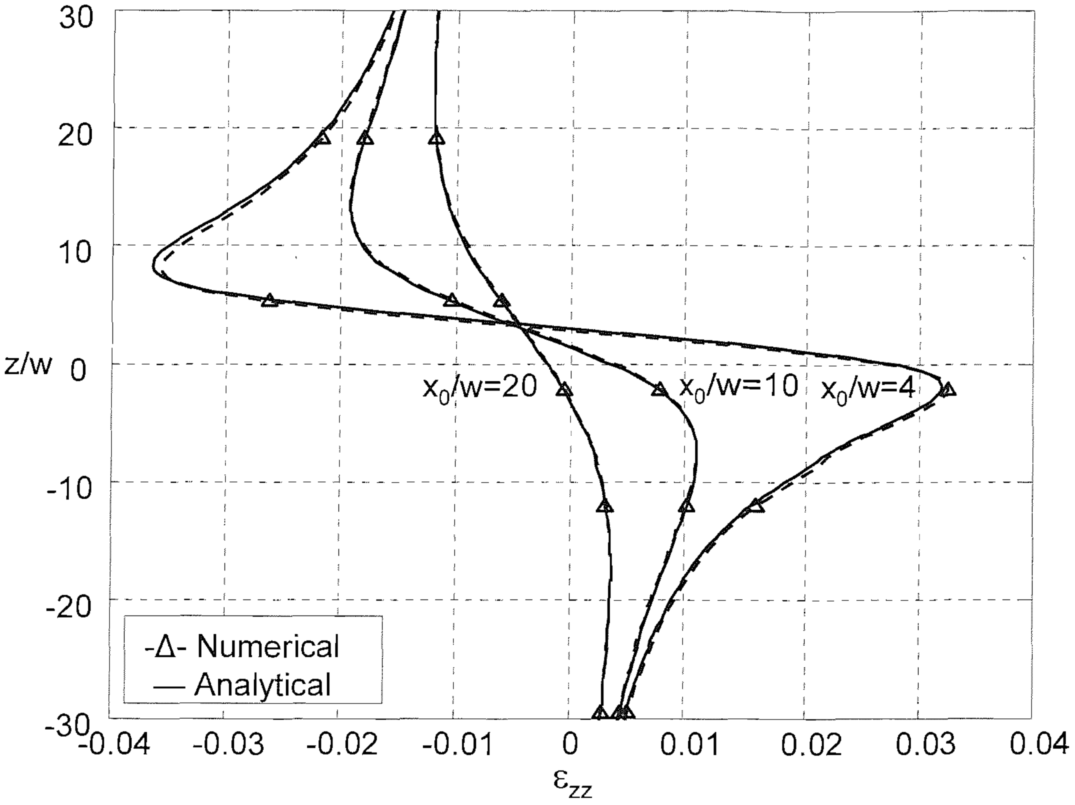

Figure 3-21 Comparison of numerical (TALL model) and analytical strain paths for (ε_{zz}) strain around "simple wedge"

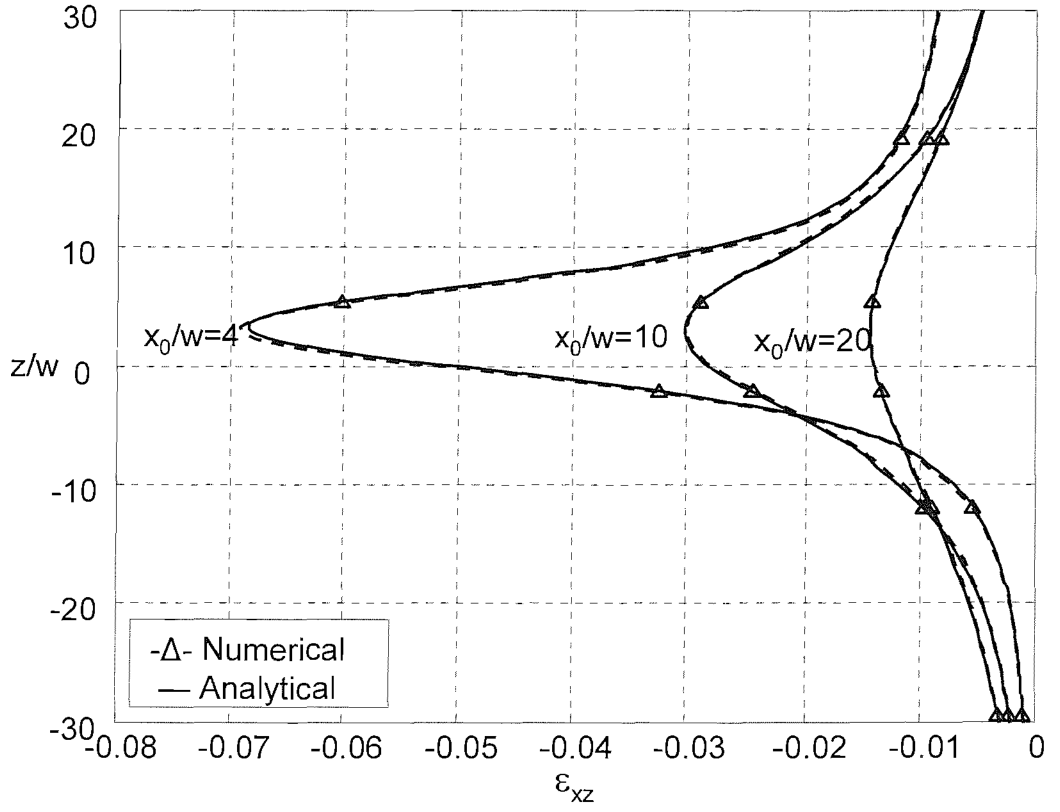

Figure 3-22 Comparison of numerical (TALL model) and analytical strain paths for (ε_{xz}) strain around "simple wedge"

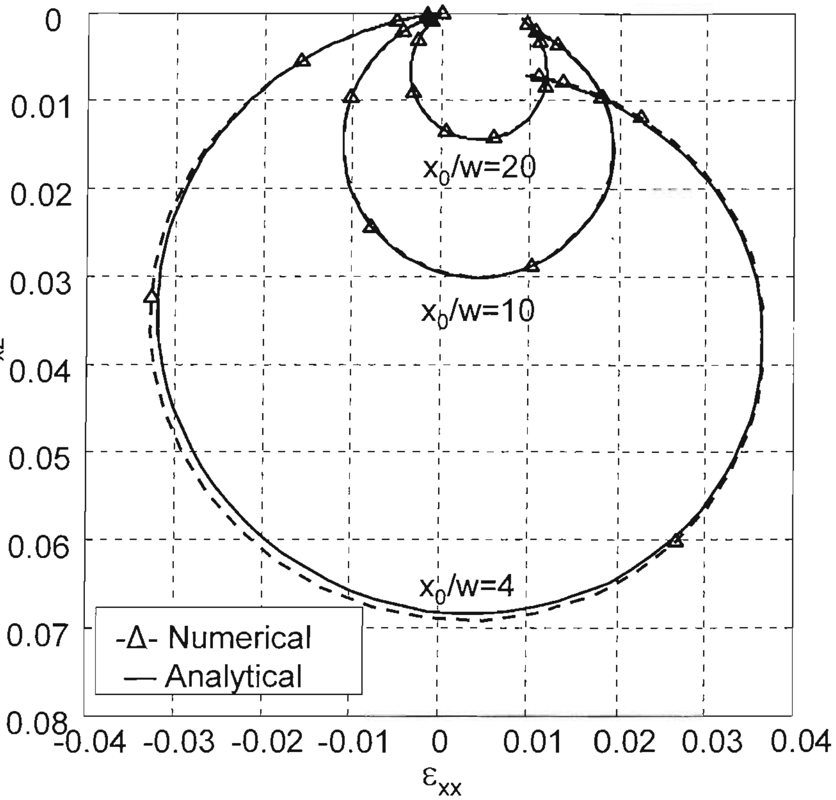

Figure 3-23 Comparison of numerical (TALL model) and analytical (ε_{xz}) strain vs. (ε_{xx}) strain for streamlines around "simple wedge"

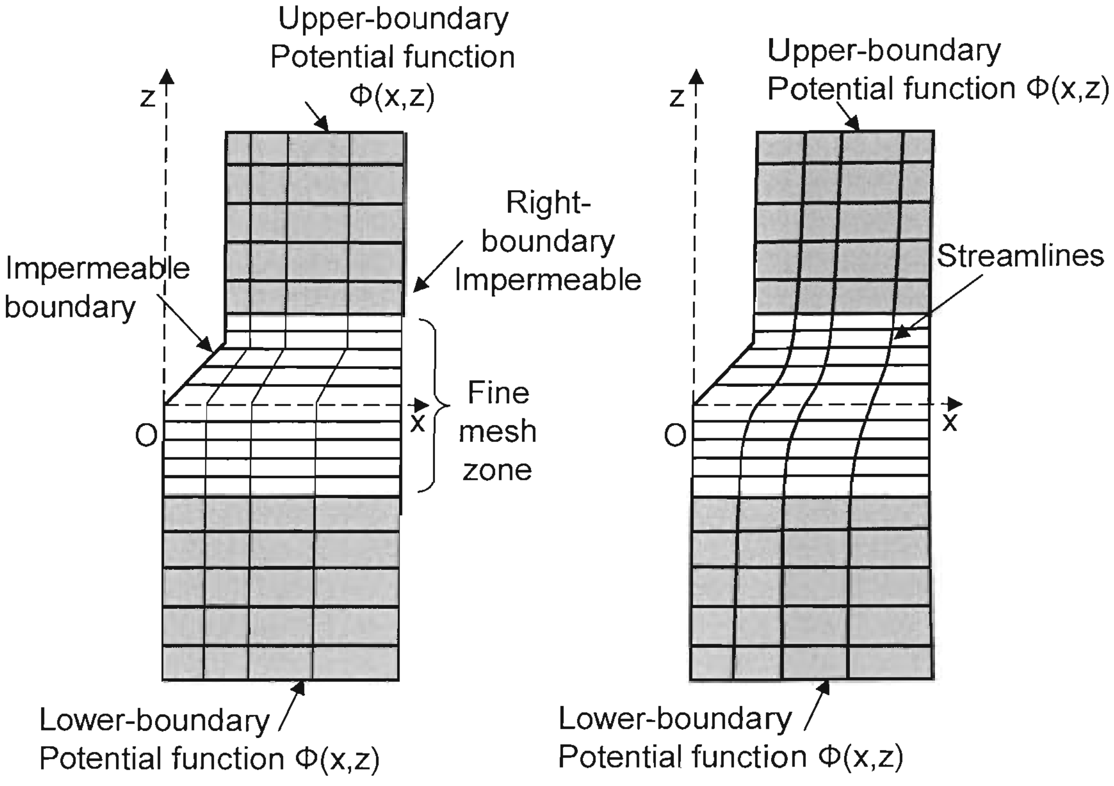

(a) Initial mesh (b) Streamed mesh

Figure 3-24 Numerical flow models: (a) Initial mesh and (b) Streamed mesh

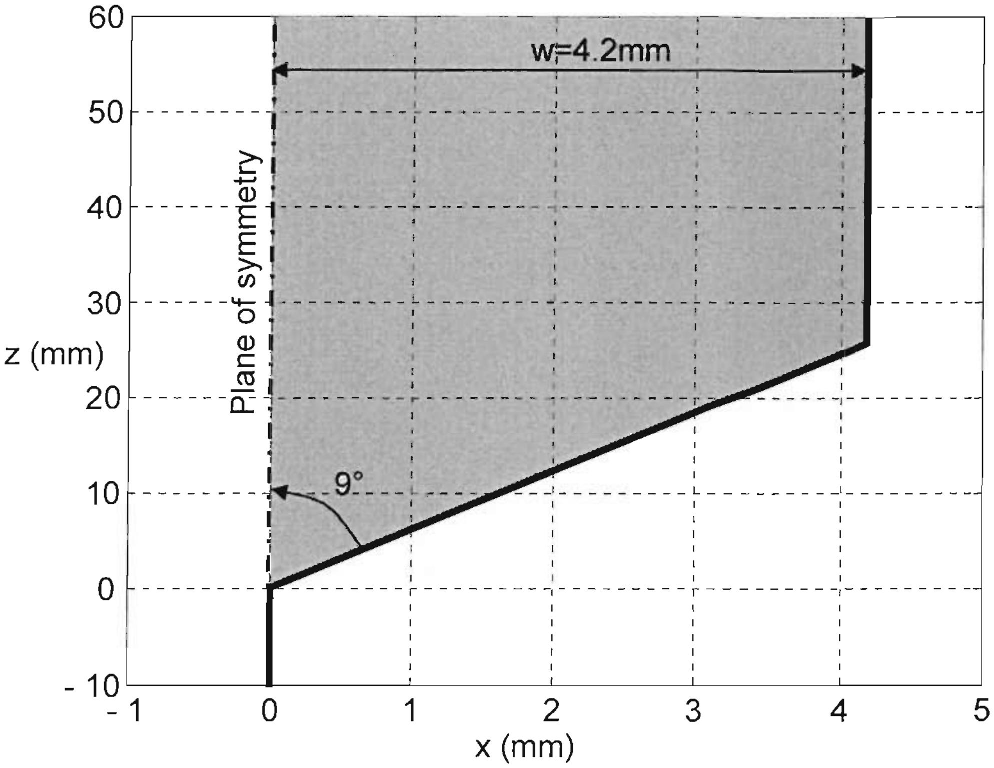

Figure 3-25 The "sharp wedge" geometry

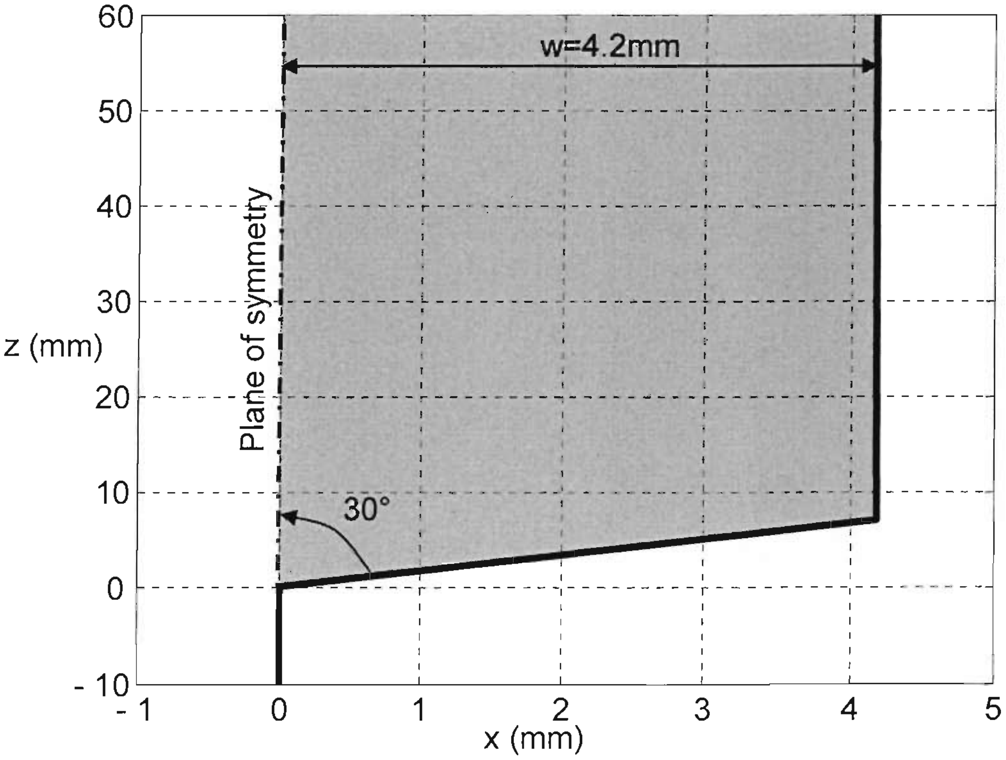

Figure 3-26 The "blunt wedge" geometry

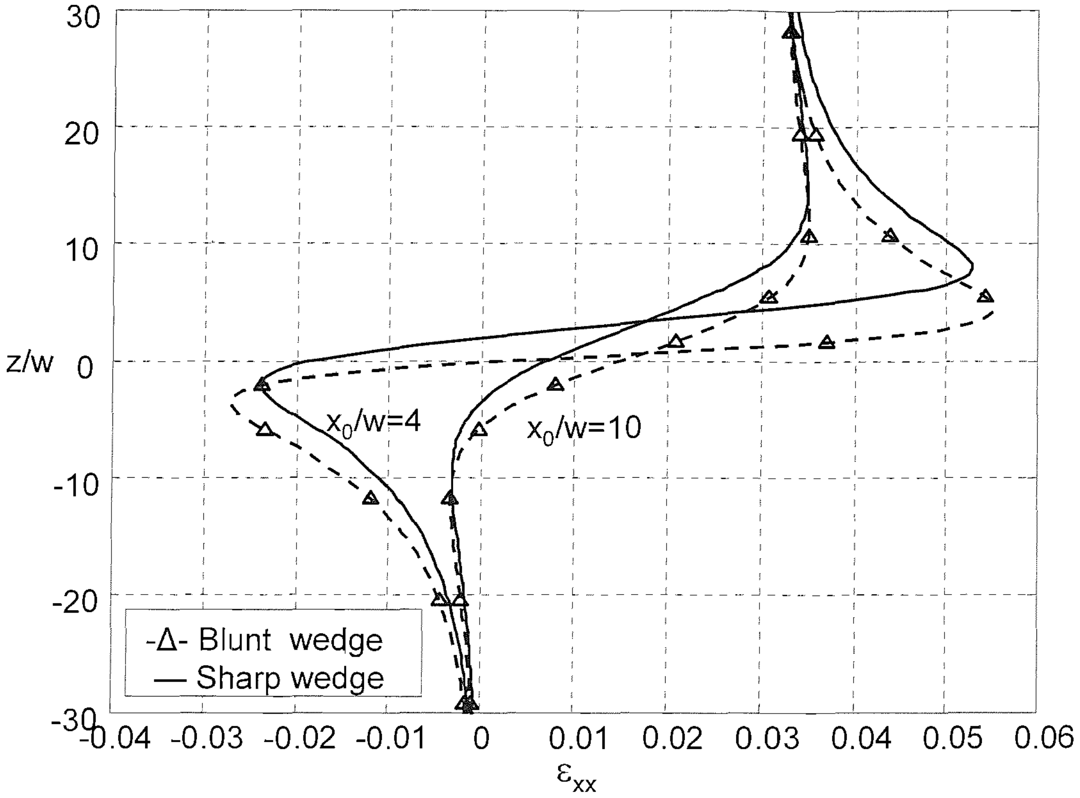

Figure 3-27 Comparison of strain paths for (ε_{xx}) strain around "blunt wedge" and "sharp wedge"

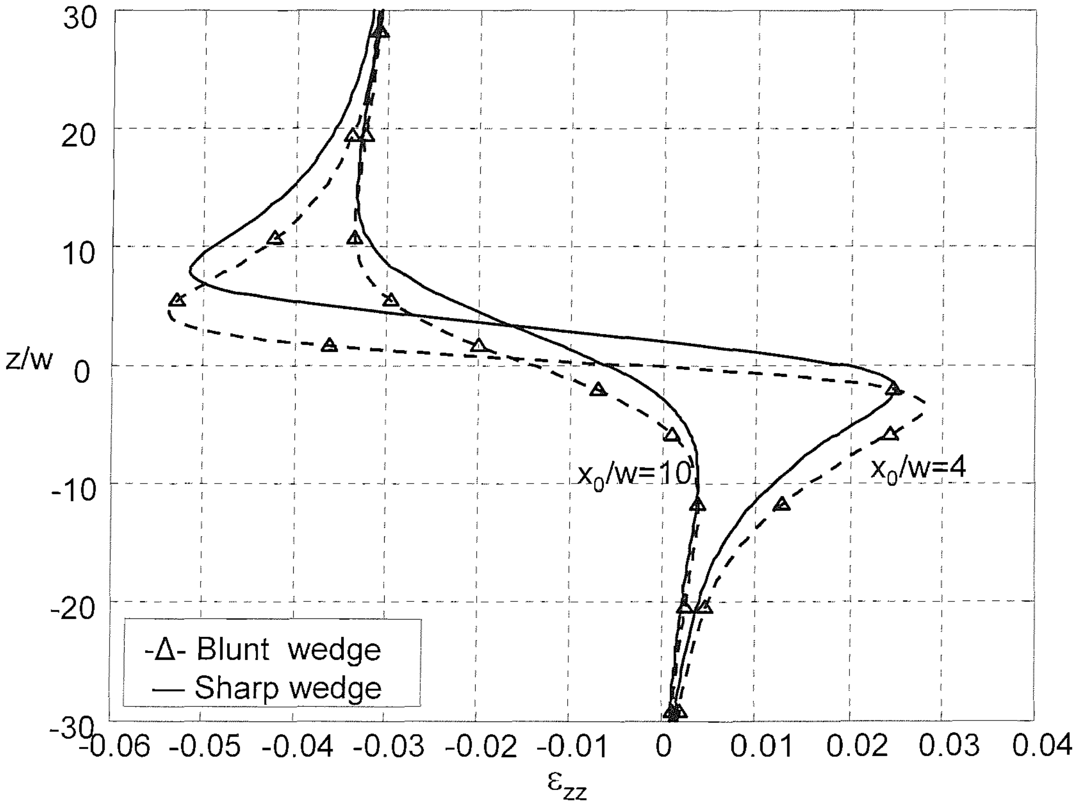

Figure 3-28 Comparison of strain paths for (ε_{zz}) strain around "blunt wedge" and "sharp wedge"

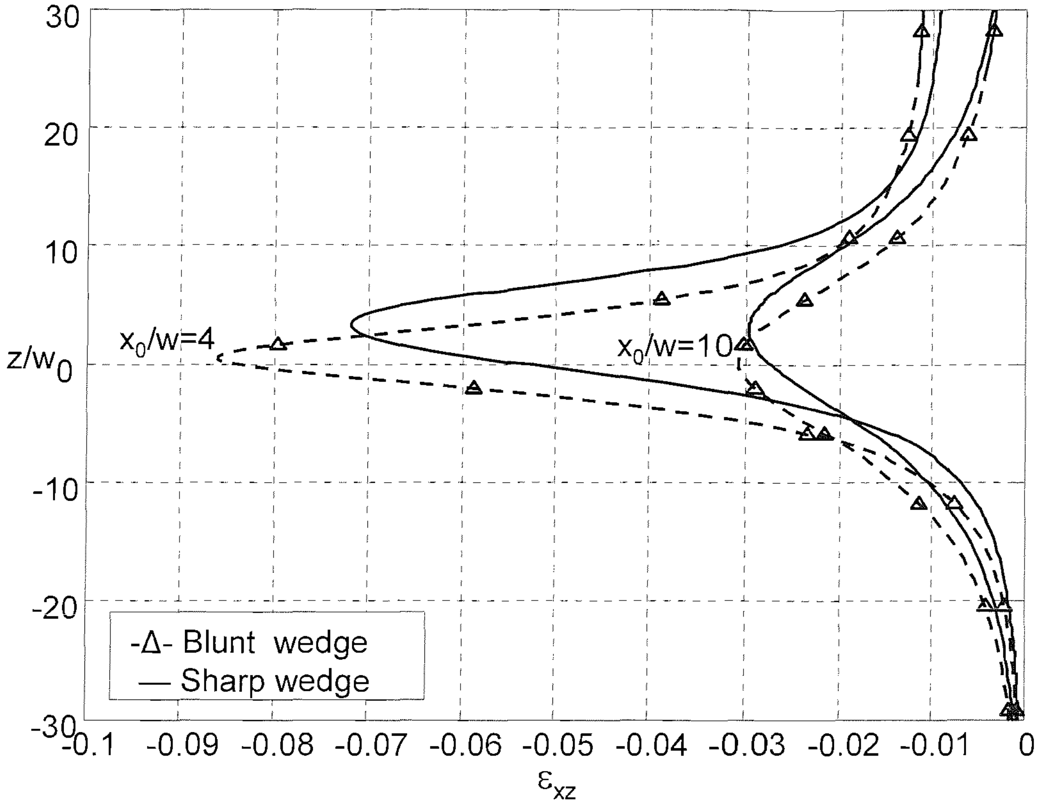

Figure 3-29 Comparison of strain path for (ε_{xz}) strain around "blunt wedge" and "sharp wedge"

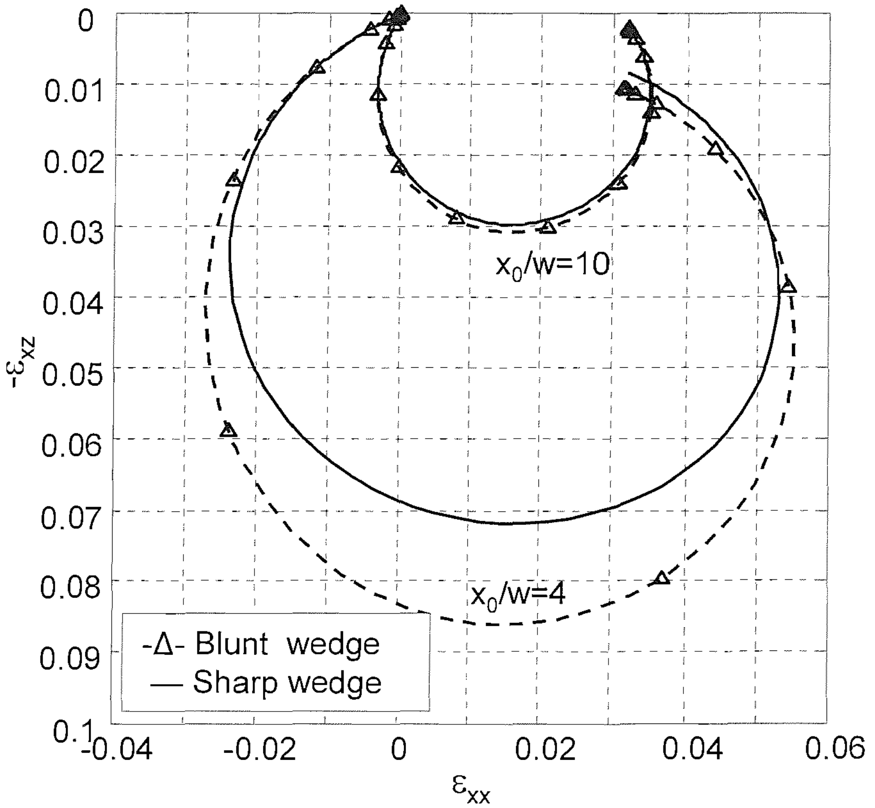

Figure 3-30 Comparison of (ε_{xz}) strain vs. (ε_{xx}) strain around "blunt wedge" and "sharp wedge"

4 TWO DIMENSIONAL SOIL PENETRATION ANALYSIS

4.1 Introduction

The "simple wedge" was used as the idealised spade cell geometry in two-dimensional soil penetration analyses performed within FLAC. Consequently, strain paths determined from the soil penetration analyses could be readily compared with the strain paths derived from the fluid flow analyses presented in the previous chapter. The influence of various modelling (e.g. penetration rate and interface stiffness) and geometrical parameters (e.g. mesh density and boundary locations) on the results was identified. The effects of soil and interface properties on the stress-strain behaviour of the soil during the penetration of the "simple wedge" were then determined in a range two-dimensional analyses. This chapter presents the methodology used and results obtained from the 2D soil penetration analyses.

4.2 Model description

Two-dimensional models were developed using FLAC to assess the soil behaviour during the penetration of the "simple wedge". Total stress formulations (refer to section 2.7.2) were employed to analyse the undrained penetration of a "simple wedge" geometry in a series of plane-strain models. Various aspects of 2D soil penetration models are discussed in the following sections.

4.2.1 Grid geometry and interfaces

The procedure adopted to generate a suitable grid for 2D soil penetration analyses consisted of four steps:

- **Step one**: a rectangular grid was created for the intended number of zones, as shown in Figure 4.1(a);
- **Step two**: elements were removed from the initial rectangular grid to create three sub-grids named the WEDGE, MIRROR, and SOIL as shown in Figure 4.1(b);
- **Step three**: these sub-grids were then formed to generate the intended geometries, as illustrated in Figure 4.1(c); and
- **Step four**: interface locations were specified on the external boundaries of various sub-grids prior to assembling them to generate the final model geometry (Figure 4.1(d)).

The three rectangular sub-grids were deformed to create the intended geometries. The MIRROR was a rectangular sub-grid located on the plane of symmetry. This auxiliary sub-grid facilitated the boundary conditions during the penetration, which will be described in section 4.2.2. The right boundary of the WEDGE sub-grid was profiled along the shape of the "simple wedge". The left boundary of the SOIL sub-grid was hence profiled to accommodate the "simple wedge" at the start of the penetration. The mesh defined for the SOIL sub-grid had two features. First, the mesh columns were aligned with streamlines in order to use complete quadrilateral elements through out the entire model (rather than cutting elements). This alignment also reduced the occurrence of modelling problems (i.e. Illegal Geometry Error) during large deformations. Secondly, the density of elements in the SOIL sub-grid was increased in all directions (i.e. +x and ±z) towards the initial position of the "simple wedge" tip. This was due to the requirement for a finer mesh adjacent to the tip, where significant distortions due to penetration were envisaged.

Interface elements were utilised to simulate the penetration of the "simple wedge". As discussed in section 2.7.3, the two sides of the potential contact surface must be specified for each interface, making the modelling of contact surfaces an elaborate process in FLAC. The potential contacts between the sub-grids were modelled by identifying three interfaces, as shown in Figure 4.2(a) between the MIRROR and SOIL (Interface #1), the MIRROR and WEDGE (Interface #2), and the WEDGE and SOIL (Interface #3). For the non-adhesive (smooth) analyses, the interface elements had only a normal stiffness (k_n). In order to analyse the effect of adhesion in the rough analyses, shear stiffness (k_s) and adhesion (C_{int}) values were also defined for the WEDGE-SOIL contact (Interface #3).

4.2.2 Boundary conditions and initial loading

Boundary conditions adopted for the penetration models are shown in Figure 4.2(b). Prescribed-displacements were used to define the boundary conditions on external boundaries for various sub-grids. As displacements are not explicitly incorporated into the FLAC calculation cycle, velocities must be prescribed for the boundaries. The MIRROR and WEDGE sub-grids were constrained in both horizontal and vertical directions (**fix X Z**). The lower and right boundaries of the SOIL sub-grid were fixed in the vertical (**fix Z**) and horizontal (**fix X**) directions, respectively. The boundary conditions for grid points on the left boundary of the SOIL sub-grid at various stages of penetration were defined by their contacts with the MIRROR and WEDGE sub-grids.

The MIRROR is an auxiliary sub-grid incorporated into the model to simulate alternating boundary conditions for grid points on the left boundary of the SOIL sub-grid. During the penetration process, the grid points on the left boundary of the SOIL sub-grid were constrained in the horizontal direction while they were below the tip of the advancing WEDGE. As the WEDGE tip passed these grid points, they were allowed to move along the WEDGE boundary in both horizontal and vertical directions.

The initial loading condition used in the penetration models was specified through the application of a 150kPa vertical load across the upper boundary of the SOIL sub-grid, as shown in Figure 4.2(b). An isotropic in-situ stress condition was assumed within the SOIL sub-grid in all models. The initial equilibrium time required for the analyses following the assembly of various sub-grids and prior to the penetration was reduced by setting the initial in-situ stress in the SOIL sub-grid equal to the value of the applied stress across the SOIL upper boundary.

4.2.3 Constitutive model and material properties

FLAC in-built elastic and Tresca models were used as constitutive models for the WEDGE and the SOIL sub-grids respectively. Penetration analyses were made under no-gravity condition and as a result, it was not necessary to define the mass density. The material properties specified for various sub-grids are reviewed below.

The WEDGE sub-grid, which represented the penetrating "simple wedge", was modelled as steel. The shear (G) and bulk (K) moduli were calculated for this elastic sub-grid by assuming a modulus of elasticity of E_w=200GPa and a Poisson's ratio of μ_w=0.33. As the MIRROR sub-grid only provided a boundary condition for the models, its properties did not influence the response of penetration analyses. For simplicity, steel properties were also used for the MIRROR sub-grid.

The Tresca constitutive model was used for the SOIL sub-grid, as saturated soils show a purely cohesive behaviour in undrained conditions (Bishop and Eldin, 1950). The SOIL sub-grid was assumed to be incompressible (μ_s=0.499) (Bishop and Hight, 1977). To simulate the undrained penetration, the SOIL was given a high bulk modulus of K_u=4GPa (Woods and Clayton, 1993). As the penetration models were validated by comparing strain paths determined from them with the strain path method results (fluid flow analyses), low shear modulus was assigned for the SOIL sub-grid in the initial analyses. The SOIL sub-grid had a shear modulus of G=1MPa and an undrained shear strength of S_u=100kPa (rigidity index was I_r=G/S_u=10) in all models, unless specified otherwise.

4.2.4 Penetration simulation and analysis methodology

The penetration of the "simple wedge" was simulated by assigning a constant vertical velocity (defined as displacement per calculation step in FLAC) to the WEDGE sub-grid. To simulate the penetration, models with prescribed velocities were stepped through the analyses until the intended length of penetration was reached (length=velocity×time). As the WEDGE sub-grid slid along the MIRROR, the elements within the SOIL sub-grid were deformed and displaced around the penetrating WEDGE. The outputs of the FLAC model were saved at consecutive stages during the penetration process for later examination. At the end of the penetration process, the models were allowed to equilibrate. The equilibrium was assumed to be the state at which the "maximum unbalanced force ratio" in the model became less than 1×10^{-4} (refer to section 2.7.1).

The methodology adopted for two-dimensional penetration analyses consisted of two steps. In the first series of analyses, the effects of modelling/geometrical parameters (e.g. penetration rate and boundary locations) on the computed outputs of penetration models were identified and minimised. The optimum modelling/geometrical parameters were then utilised in the second series of analyses to evaluate the influence of soil/interface properties on the computed stress-strain behaviour of soil during the penetration.

The strain paths determined from the penetration analyses of the "simple wedge" were compared with the strain paths evaluated from the fluid analyses for the flow field around the "simple wedge". This strain path comparison formed the basis of the validation process for penetration analyses. In soil penetration analyses, the locations of an element relative to the position of the "simple wedge" tip were stored at various stages of the penetration. These coordinates were then used to calculate strain increments between successive stages of the penetration. The strain increments were summed to calculate strain paths as the penetration took place. This strain path can be compared with the strain path determined from the streamline passing through the centreline of the examined element in the corresponding fluid flow problem (refer to section 3.3.1).

The resemblance between the strain paths determined from soil penetration and fluid flow analyses is illustrated in Figure 4.3. An element located at A_0 at time t_0 (Figure 4.3(a)) in the soil penetration model moved to the new location of A_1' at time $t_0+\Delta t$ (Figure 4.3(b)) after the "simple wedge" has penetrated a length of $\Delta t/U$, where U was the penetration velocity. In the corresponding fluid flow model, a particle that was located at A_0 at time t_0 moved along the streamline and reached A_1'' at time $t_0+\Delta t$, as shown in Figure 4.3(c). The deformation pattern the soil element experienced relative to the location of the "simple wedge" tip was analogous with the change in the location of the fluid particle along the streamline.

4.3 Results

FLAC outputs were stored in BINARY format and transferred to MATLAB for post-processing. The MATLAB outputs were presented in forms of strain paths, normalised horizontal stress changes, principal stress indicators and displacement vectors. The convention for positive stress-strains in 2D soil penetration analyses is illustrated in Figure 4.4. This figure also shows the starting and final positions of the "simple wedge" tip (i.e. z=+L/2 and z= -L/2). In all comparisons, the strain paths were evaluated for a soil element located vertically at the middle of the model ($z_0/w=0$) and horizontally at $x_0/w=10$, indicated by A. The stresses acting on the face of the "simple wedge" were obtained from the stress values determined for a soil element adjacent to the "simple wedge" and 100mm(20w) above the final tip position, indicated by B.

The influences of the following parameters on the behaviour of soil were investigated in 2D soil penetration analyses:

- Modelling parameters: penetration rate (U) and interface stiffness (k_n);
- Geometrical parameters: mesh density of soil (N), location of right boundary (R), location of horizontal boundaries (H) and penetration length (L);
- Soil parameters: shear modulus (G) and undrained shear strength (S_u); and
- Interface adhesion (α).

4.4.1 Influence of modelling parameters

The influence of the penetration rate and the interface stiffness were assessed in a series of models. The values of these two parameters in various models are listed in Table 4.2. The geometrical and soil/interface parameters in these models were set to values defined for the MAIN model listed in Tables 4-1 and 4-3 respectively.

Penetration rate

Differences in model outputs resulting from changes in the penetration rate are due to modelling issues and not a result of any physical process, since viscous behaviour is not simulated. Physical time is not incorporated directly into FLAC and the penetration rate, defined as penetration length per step, is solely a modelling parameter. The selection of an acceptable penetration rate for the penetration analyses was based on a compromise between the available computational resource and the intended equilibrium level. The computational time (i.e. number of steps to reach the penetration length) will be reduced by using higher penetration rates. However, as each step is equal to one iteration in the calculation cycle (i.e. time marching), the model will have a higher unbalanced force ratio by adopting higher penetration rates.

The effect of the penetration rate (U) on the analyses was assessed by using a range of vertical penetration increments per step of computation, in various models. The assigned penetration rates were U=0.0003, 0.0006, 0.0012, 0.0024 and 0.0048 mm/step. Strain paths for horizontal (ε_{xx}) and shear (ε_{xz}) strains are plotted for models with penetration rates of U=0.0003, 0.0012 and 0.0048 mm/step in Figures 4.5 and 4.6 respectively. It can be seen that the minimum horizontal strain value was only 0.09% higher in the 0.0012mm/step model in comparison with the 0.0003mm/step model. Due to the small differences observed and the large computational time required for the smaller penetration rates, the median penetration rate (U=0.0012mm/step) was selected for all subsequent analyses.

Interface stiffness

The only parameter defined for a smooth interface is the normal stiffness (k_n). The normal stiffnesses for the interfaces were set to values suggested by FLAC guidelines (refer to section 2.7.3). Analyses were however, performed to assess the sensitivity of the penetration model outputs to the value of interface stiffness.

The normal stiffnesses assigned to the interfaces in various models were set to k_n=30(FLAC guideline), 3 and 0.3GPa/mm. Figures 4.7 and 4.8 show the strain paths for horizontal (ε_{xx}) and shear (ε_{xz}) strains in these models respectively. It can be seen that the models were relatively insensitive to the interface normal stiffness value. For example, the absolute difference between minimum horizontal strains determined from models with k_n=30 and 0.3GPa/mm was only 0.005%. Hence, the

FLAC guideline was used in the remainder of penetration models to calculate the value of stiffness for various interfaces.

4.4.2 Influence of geometrical parameters

The influence of various geometrical aspects of penetration models was examined. Values of geometrical parameters (i.e. the mesh density, boundary locations and penetration length) in various models are listed in Table 4.1. The modelling and soil/interface parameters were similar to those defined for the MAIN model, listed in Tables 4-2 and 4-3 respectively.

Mesh density

The number of elements used for the SOIL sub-grid in various analyses were N=2385, 8500 and 14040. Comparison of the strain paths for identical elements was not possible due to different successive ratios adapted for defining the mesh density in various models (refer to section 4.2.1). Strain paths for horizontal (ε_{xx}) and shear (ε_{xz}) strains for the closest element to point A(10w, 0) (refer to Figure 4.4) are shown in Figures 4.9 and 4.10 respectively. It can be seen that the changes in the strain paths due to mesh refinement were insignificant. For example, the absolute difference in minimum horizontal strains determined from the models with fine and coarse meshes was only 0.13%. It was therefore concluded that the initial mesh density adopted in the MAIN model was adequate and further mesh refinement was not necessary for soil penetration analyses.

Boundary locations

External boundaries should be located at distances sufficiently remote from the penetrating wedge such that their locations do not influence the model outputs. The locations of the horizontal (i.e. upper and lower) and right boundaries were varied in a range of models. The sensitivity of soil penetration analyses to the location of boundaries were assessed by comparing the strain paths and stresses determined from these models.

The distance between the upper and lower boundaries was 2H. The magnitude of (H) in various models was set to 126mm(30w), 210mm(50w) and 420mm(100w) while other parameters were kept constant. Figures 4.11 and 4.12 show the influence of the location of horizontal boundaries (H) on the strain paths for horizontal (ε_{xx}) and shear (ε_{xz}) strains respectively. The changes in strain paths due to a shift in the location of the horizontal boundaries were insignificant. For example, changing H from 126mm to 420mm reduced the maximum horizontal strains by only 0.36%.

The effect of the far right boundary location was also evaluated. The distance of the right boundary (R) from the plane of symmetry was set to 105mm(25w), 210mm(50w), 420mm(100w), 630mm(150w) and 840mm(200w) in various penetration models while other parameters were unchanged. The strain paths for horizontal (ε_{xx}) and shear (ε_{xz}) strains are plotted in Figures 4.13 and 4.14 respectively in models with R=105mm, 420mm and 840mm. In contrast to the horizontal boundaries, the location of the far right boundary had a significant influence on the strain paths. The difference between the maximum horizontal strains determined from the fluid flow and soil penetration analyses was reduced by 2.30% when the far right boundary was moved from R=105mm to R=840mm.

In order to further assess the influence of the right boundary location, the horizontal stresses adjacent to the face of "simple wedge" and 100mm above the tip (point B in Figure 4.4) were examined. Figure 4.15 shows the normalised horizontal stress change (β) adjacent to the face of the "simple wedge" for penetration models with various right boundaries (R). The normalised horizontal stress change (β) was defined as the difference between the initial in-situ stress (σ_{xx0}) and the measured horizontal (σ_{xx}) stress at the end of penetration, divided by the soil initial in-situ stress ($\beta=\Delta\sigma_{xx}/\sigma_{xx0}$). Shifting the far lateral boundary location (R) from 105mm to 840mm had a noticeable influence on the normalised horizontal stress change (β). The changes in β were insignificant for models where R>420mm. Consequently, it was considered appropriate to position the right boundary at a distance of R=420mm away from the plane of symmetry in subsequent analyses.

Penetration length

The strain path method was developed based on the "theory of deep penetration" (Baligh, 1975). The strain path method assumes that soil deformations during undrained, steady-state, deep penetration can be estimated, "without considering the constitutive relationship" of the soil (Baligh, 1984). This independency of soil deformations from the shearing resistance of soil is due to the kinematic constraints inherent in the "deep steady-state" penetration problems (Baligh, 1985).

Increasing the penetration length should improve the agreement between strain paths determined from the fluid flow (strain path method) and soil penetration analyses, for two reasons. Firstly, by increasing the penetration length, the model height will also increase and as a result, the examined element, which is at the mid-height of the model, will be at a greater depth. Secondly, by increasing the penetration length, steady-state deformations will exist for longer, due to the increased distance between the beginning and end of penetration.

To assess the effect of the penetration length (L) on strain paths, a series of analyses were undertaken where (L) was varied between 201.6mm(48w), 403.2mm(96w) and 806.4mm(192w). Figures 4.17 and 4.18 show the strain paths for horizontal (ε_{xx}) and shear (ε_{xz}) strains in these models. The strain path for horizontal (ε_{xx}) strains derived in the LONG model (L=806.4mm) took a symmetrical shape and converged to the strain path determined from the fluid flow analyses. For example, the minimum horizontal strain was only 0.25% less than the value predicted by fluid flow analyses. The agreement between the shear (ε_{xz}) strain paths determined from soil penetration and fluid flow analyses also improved by increasing the penetration length (L). For example, the difference between peak shear strains determined from soil penetration and fluid flow analyses was reduced to 0.14%, in the LONG model. Consequently, the LONG model geometry was chosen for all subsequent soil penetration analyses. Figure 4.16 shows the dimensions and the mesh density used for the LONG model.

4.4.3 Influence of soil properties

As already noted, Baligh (1975) argued that in deep penetration problems, the constitutive relationship (i.e. shearing resistance) of soil has a relatively small effect on the deformations and strains developed around the penetrating object. It was observed in the previous section that for soils with a low shear modulus (G) and subsequently a low rigidity Index ($I_r=G/S_u$), the strain paths determined from fluid flow analyses (strain path method) agreed with those determined from the soil penetration analyses. The influences of various soil shear moduli (G) and shear strengths (S_u) were investigated on the stress-strain behaviour of soil during penetration in a range of models. The values of S_u and G in various models are listed in Table 4.3. The geometrical and modelling parameters used in these models were similar to the values listed for the LONG model in Tables 4-1 and 4-2 respectively.

The influence of an increase in the rigidity index (I_r) of soil was initially examined by reducing the undrained shear strength (S_u) while shear modulus was kept constant (G=1MPa). Soil penetration analyses were carried out for models with undrained shear strengths of S_u=12.5, 25, 50, 75 and 100kPa. Figure 4.19 shows the strain path for horizontal (ε_{xx}) strains in three models with S_u=25, 50 and 100kPa. Although the change in the undrained shear strength (S_u) influenced horizontal strains adjacent to the "simple wedge" tip, strain values at the end of the penetration path were in the same range. Due to the conservation of volume, the shape of the strain path for the vertical (ε_{zz}) strain was the mirror of the horizontal strain path (Figure 4.20). The strain path for shear (ε_{xz}) strain is shown in Figure 4.21. It can be seen that the shear strains increased by increasing the rigidity index of the soil. For example, by reducing the undrained shear strength from S_u=100 to 25kPa (i.e. increasing rigidity index from 10 to 40), the difference between the peak shear strains determined from the fluid flow and soil penetration analyses increased by 1.33%. Above the tip level, shear strain values were higher for models where the soil had a higher rigidity index.

The influence of increasing the rigidity index was also investigated by increasing the shear modulus (G) of the soil. The rigidity index was varied between 10, 20 and 40 by increasing the shear modulus (G=1, 2 and 4MPa), while keeping the undrained shear strength constant (S_u=100kPa). Similar to the influence of the undrained shear strength on normal strain paths, it was observed that a change in the soil shear modulus (G) only affected the ε_{xx} and ε_{zz} strain paths at the tip level, as shown in Figures 4.22 and 4.23 respectively. Figure 4.24 shows the strain path for shear (ε_{xz}) strains in these models. It can be seen that the shear strains increased by increasing the rigidity index of the soil. For example, by increasing the shear modulus from G=1 to 4MPa (i.e. increasing rigidity index from 10 to 40), the difference between the peak shear strains determined from the fluid flow and soil penetration analyses increased by 1.57%. The divergence of the shear strain path (determined from soil penetration analyses) from the fluid flow analyses was greater in models with a higher rigidity index.

Further investigations into the effects of undrained shear strength (S_u) and shear modulus (G) on the behaviour of soil during the penetration were conducted by evaluating the horizontal stresses on the face of the "simple wedge". Figure 4.25 illustrates normalised horizontal stress changes (β) for penetration models with a constant shear modulus (G=1MPa) and various undrained shear strengths (S_u=12.5, 25, 50, 75 and 100kPa). Figure 4.26 shows the values of β in a range of penetration models with a constant undrained shear strength (S_u=100kPa) and various shear moduli (G=1, 2, 4, 6 and 8GPa). These figures show that an increase in both the undrained shear strength and shear modulus of soil increased the measured horizontal stress on the "simple wedge" face and consequently the β. Of these two however, the shear modulus (G) appeared to have a more significant effect.

4.4.4 Influence of interface adhesion

Baligh's strain path method (1985) approximates soil deformations around a penetrating object with streamline deformations in the flow field formed around that object. Because the strain path method is based on inviscid fluid flow formulations, it is incapable of addressing the influence of interface adhesion on soil deformations. The influence of interface adhesion on the stress-strain behaviour of soil has been evaluated by comparing the outputs of various models. The geometrical, numerical and soil parameters for models used in this section were similar to the parameters assigned to the LONG model, listed in Tables 4-1, 4-2 and 4-3 respectively. The interface adhesion factor, $\alpha=C_{int}/S_u$ (where C_{int} is the interface shear strength) for the WEDGE-SOIL interface was varied between $\alpha=0$, 0.25, 0.5, 0.75 and 0.95 in a range of penetration models. The $\alpha=1$ model gave Illegal Geometry Error, due to severe mesh distortion and became unstable half-way through the penetration. The outcomes of these analyses are summarised here.

The interface adhesion influenced the normal as well as shear strain paths. Figures 4.27 and 4.28 show the strain paths for horizontal (ε_{xx}) and vertical (ε_{zz}) strains in models with various adhesion factors (α). Increasing adhesion caused the horizontal strain of the examined soil element to decrease as it passed the tip level. For example, the final horizontal strain value for the adhesive model ($\alpha=0.95$) was 1.18% lower than that determined for the non-adhesive model ($\alpha=0$). The vertical strains above the tip were also higher in models with higher interface adhesions. Figure 4.29 shows the changes in the shear (ε_{xz}) strain paths due to various interface adhesions. Above the tip level, shear strains were higher in models where the interface had a higher adhesion. For example, the final shear strain value was 3.06% higher in the adhesive ($\alpha=0.95$) model compared with the non-adhesive model ($\alpha=0$).

Due to significant changes observed in the strain paths by introducing adhesion to the interface, it was felt necessary to re-assess the influence of geometrical parameters used in soil penetration models. As was illustrated in section 4.4.2, soil penetration models were only sensitive to the location of the right boundary (R). Consequently, the influence of the right boundary location (R) on stresses measured on the “simple wedge” face was further investigated for an adhesive WEDGE-SOIL interface ($\alpha=0.95$). The soil and modelling parameters used in these analyses are similar to those listed for the LONG model in Tables 4-2 and 4-3, while the geometrical properties for these models are listed in Table 4.4. Figure 4.30 shows the normalised horizontal stress change (β) plotted against the right boundary location (R) in these models. It can be seen that in common with the non-adhesive model (Figure 4.15) moving the far right boundary from 105mm to 840mm had a noticeable effect on β. The changes in β were however, insignificant when the distance from the right boundary (R) was greater than 420mm. Consequently, it was concluded that the existing location of the far right boundary R=420mm(100w) was adequate and did not influence the outputs of adhesive penetration models either.

The normalised horizontal stress changes (β) on the "simple wedge" face determined from the 2D soil penetration models with various adhesion levels assigned to the WEDGE-SOIL interface were evaluated. As shown in Figure 4.31, β increased linearly when the interface adhesion was varied between α=0 and 0.95.

The influence of the interface adhesion during the penetration of the "simple wedge" can be graphically presented by the displacement vectors and principal stress indicators. Figures 4.32 and 4.33 show the displacement vectors and principal stress indicators at the end of penetration for 2D soil penetration analyses with α=0 (adhesive) and α=0.95 (non-adhesive). The "simple wedge" tip was positioned at x=0 and z=0 at the start of penetration, and the penetration was simulated for a length of L=806.4mm(192w). It is evident that the directions of displacement vectors for soil elements changed by the introduction of adhesion on the interface, Figure 4.32. For example, by introducing adhesion, the displacement vectors at the adjacency of the "simple wedge" rotated and pointed diagonally down and away from the "simple wedge". Although, it is evident that the location of the right-hand boundary has influenced the displacement vectors adjacent to the boundary, the displacement pattern in the area of interest (i.e. near the penetrating object) were unaffected by the boundary location. Figure 4.33 shows that the principal stress indicators were significantly rotated in the area adjacent to the penetration length as adhesion was introduced to the interface.

4.4 Summary

FLAC finite difference program has been used to analyse the undrained penetration of the "simple wedge" into a Tresca soil. The soil penetration models were validated by comparing the strain paths determined from the penetration analyses with the results of the fluid flow analyses (Chapter 3). Models were then used to investigate the affects of various soil/interface parameters on the stress-strain behaviour of soil adjacent to the penetrating “simple wedge”. The outcomes of these analyses are summarised below:

- The values of normal strains (ε_{xx} and ε_{zz}) at the end of the penetration were relatively insensitive to the shear modulus (G) and undrained shear strength (S_u) of soil;
- As the soil element passed the tip level, the shear (ε_{xz}) strain determined from soil penetration analyses were higher for soils with a higher rigidity index (I_r);
- The horizontal stresses measured on the “simple wedge” face increased by an increase in either the shear modulus (G) or undrained shear strength (S_u) of soil. However, the influence of the shear modulus was larger than the undrained shear strength;
- At the end of the penetration, horizontal (ε_{xx}) stains were lower while vertical (ε_{zz}) and shear (ε_{xz}) strains were higher in models with a higher interface adhesion (α); and
- The horizontal stresses recorded on the “simple wedge” face increased almost linearly by increasing the interface adhesion (α).

The changes in the stress-strain behaviour of soil during the penetration of a spade cell can only be estimated by two-dimensional models, as the spade cell installation is a three-dimensional problem. However, it is economical to perform sensitivity analyses within 2D models. The 2D models have shown that the soil shear modulus, soil undrained shear strength and interface adhesion influence the soil behaviour as penetration takes place.

Table 4-1 Geometrical parameters used in FLAC soil penetration analyses

Model	Description	SOIL elements (N)	Right boundary R (mm)	Horizontal boundaries H (mm)	Penetration length L (mm)
MAIN	Main model	8,500	420 (100w)	210 (50w)	201.6 (48w)
MESH_1	Mesh density	14,040	"	"	"
MESH_2	Mesh density	2,385	"	"	"
HORI_1	Horizontal boundaries	14,365	"	420 (100w)	"
HORI_2	Horizontal boundaries	5,695	"	126 (30w)	"
RIGH_1	Right boundary	15,400	840 (200w)	210 (50w)	"
RIGH_2	Right boundary	11,900	630 (150w)	"	"
RIGH_3	Right boundary	5,000	210 (50w)	"	"
RIGH_4	Right boundary	3,300	105 (25w)	"	"
LENG_1	Penetration length	11,305	420 (100w)	310.8 (74w)	403.2 (96w)
LENG_2 (LONG)	Penetration length	16,915	"	512.4 (122w)	806.4 (192w)

Table 4-2 Modelling parameters used in FLAC soil penetration analyses

Model	Description	Penetration rate U (mm/step)	Interface stiffness k_n (GPa/mm)
MAIN/LONG	Main model	0.0012	30
RATE_1	Penetration rate effect	0.0048	"
RATE_2	Penetration rate effect	0.0024	"
RATE_3	Penetration rate effect	0.0006	"
RATE_4	Penetration rate effect	0.0003	"
STIFF_1	Interface stiffness effect	0.0012	0.3
STIFF_2	Interface stiffness effect	"	3

Table 4-3 Soil/interface parameters used in FLAC soil penetration analyses

Model	Description	Shear modulus G (MPa)	Shear strength S_u (kPa)	Interface adhesion α (C_{int}/S_u)
MAIN	Main model	1	100	0
STRE_1	Undrained shear strength	"	75	"
STRE_2	Undrained shear strength	"	50	"
STRE_3	Undrained shear strength	"	25	"
STRE_4	Undrained shear strength	"	12.5	"
MODU_1	Shear modulus	2	100	"
MODU_2	Shear modulus	4	"	"
MODU_3	Shear modulus	6	"	"
MODU_4	Shear modulus	8	"	"
ADHE_1	Interface adhesion	1	"	0.25
ADHE_1	Interface adhesion	"	"	0.50
ADHE_1	Interface adhesion	"	"	0.75
ADHE_1	Interface adhesion	"	"	0.95

Table 4-4 Geometrical parameters used in FLAC analyses to assess the influence of right boundary location in adhesive models (α=0.95)

Model	Description	Soil elements (N)	Right boundary R (mm)	Horizontal boundaries H (mm)
ADRI_1	Right boundary (adhesive)	15,400	840 (200w)	210 (50w)
ADRI_2	Right boundary (adhesive)	11,900	630 (150w)	"
ADRI_3	Right boundary (adhesive)	8,500	420 (100w)	"
ADRI_4	Right boundary (adhesive)	5,000	210 (50w)	"
ADRI_5	Right boundary (adhesive)	3,300	105 (25w)	"

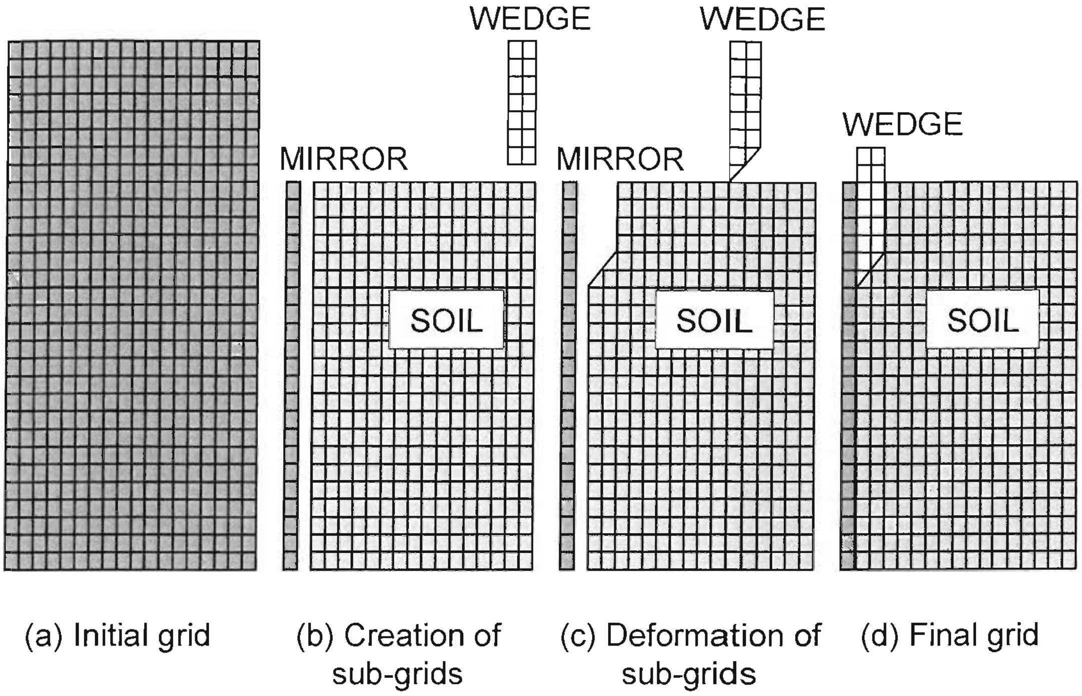

Figure 4-1 Schematic view of the procedure used to generate the geometry for FLAC penetration models

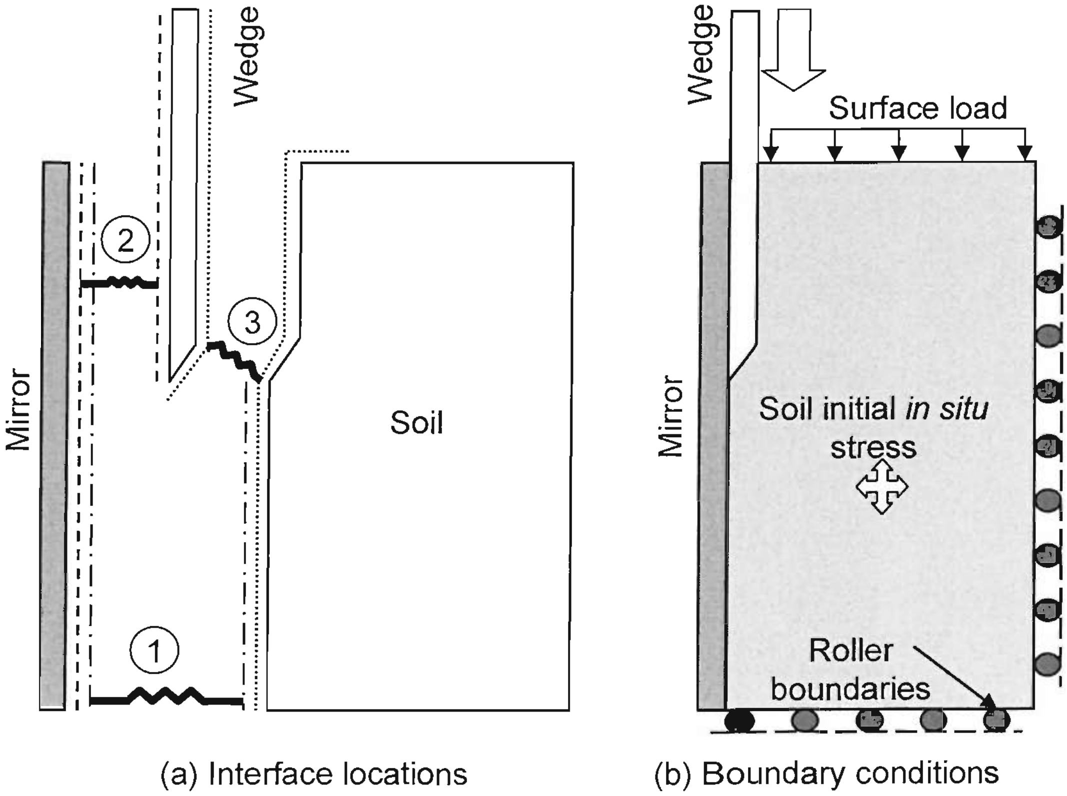

Figure 4-2 FLAC penetration models: (a) Interface locations and (b) Boundary conditions

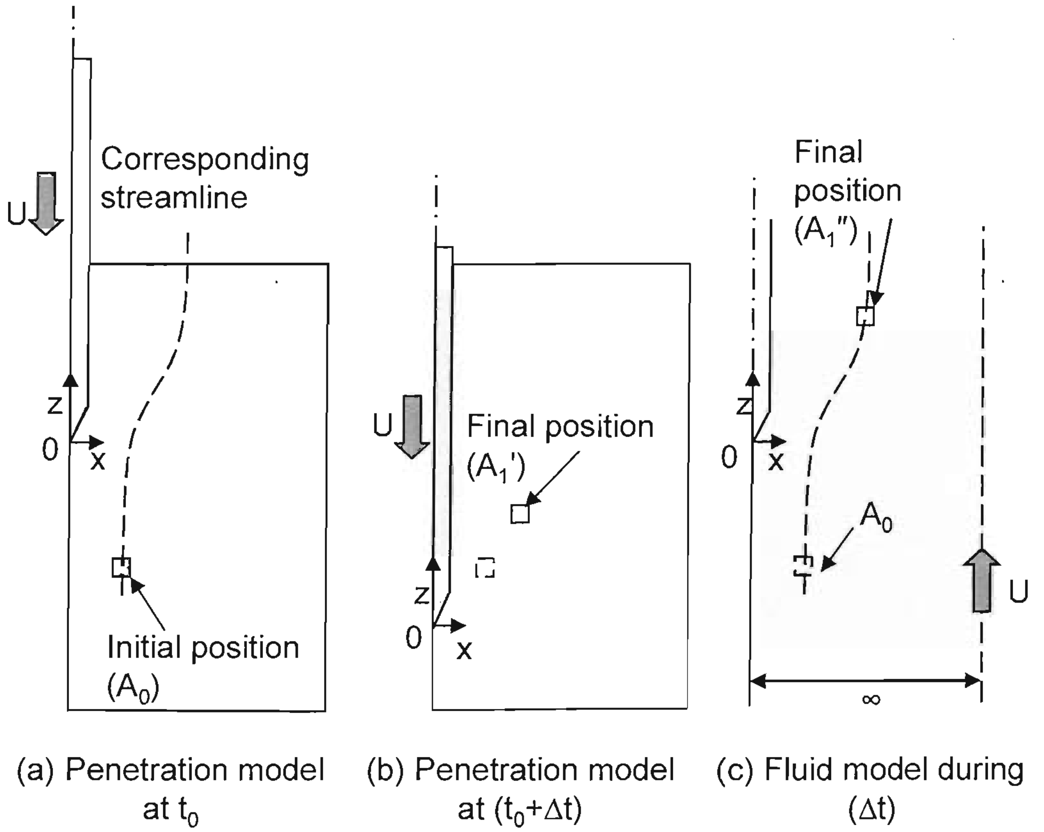

Figure 4-3 Strain path calculations in fluid flow and soil penetration models

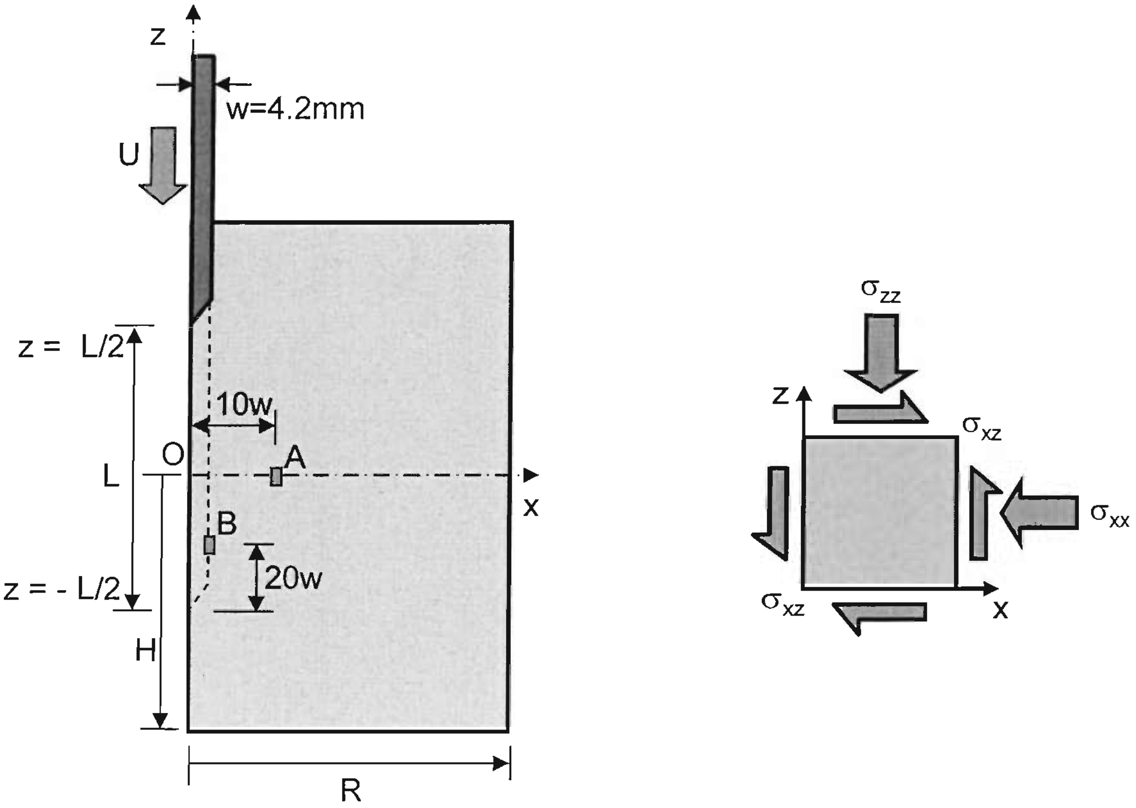

Figure 4-4 Schematic view of penetration models and the 2D convention for positive stress-strain

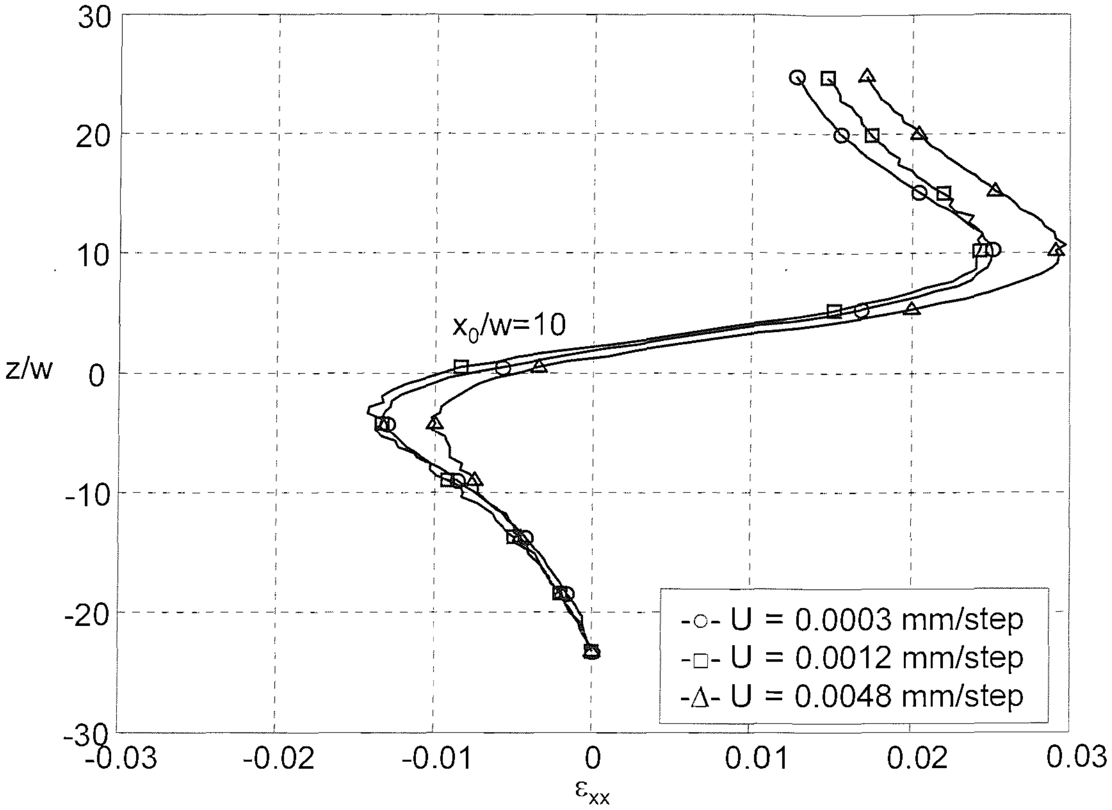

Figure 4-5 Influence of penetration rate (U) on strain paths for (ε_{xx}) strain in 2D penetration models

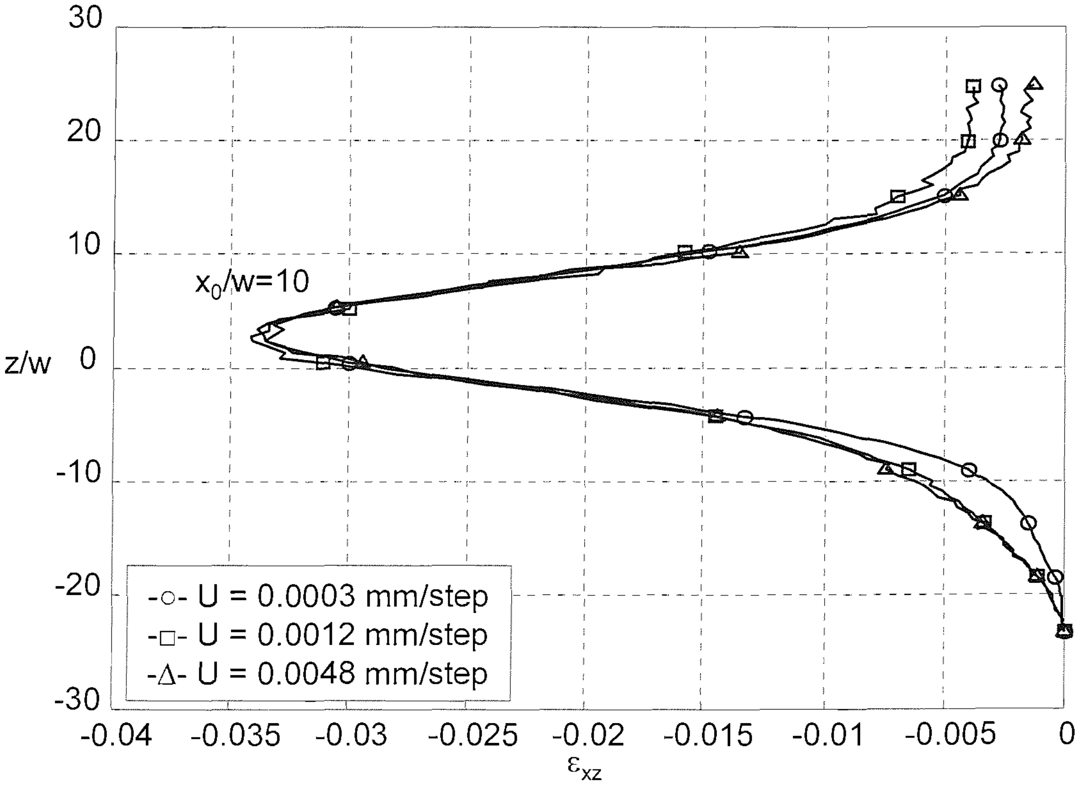

Figure 4-6 Influence of penetration rate (U) on strain paths for (ε_{xz}) strain in 2D penetration models

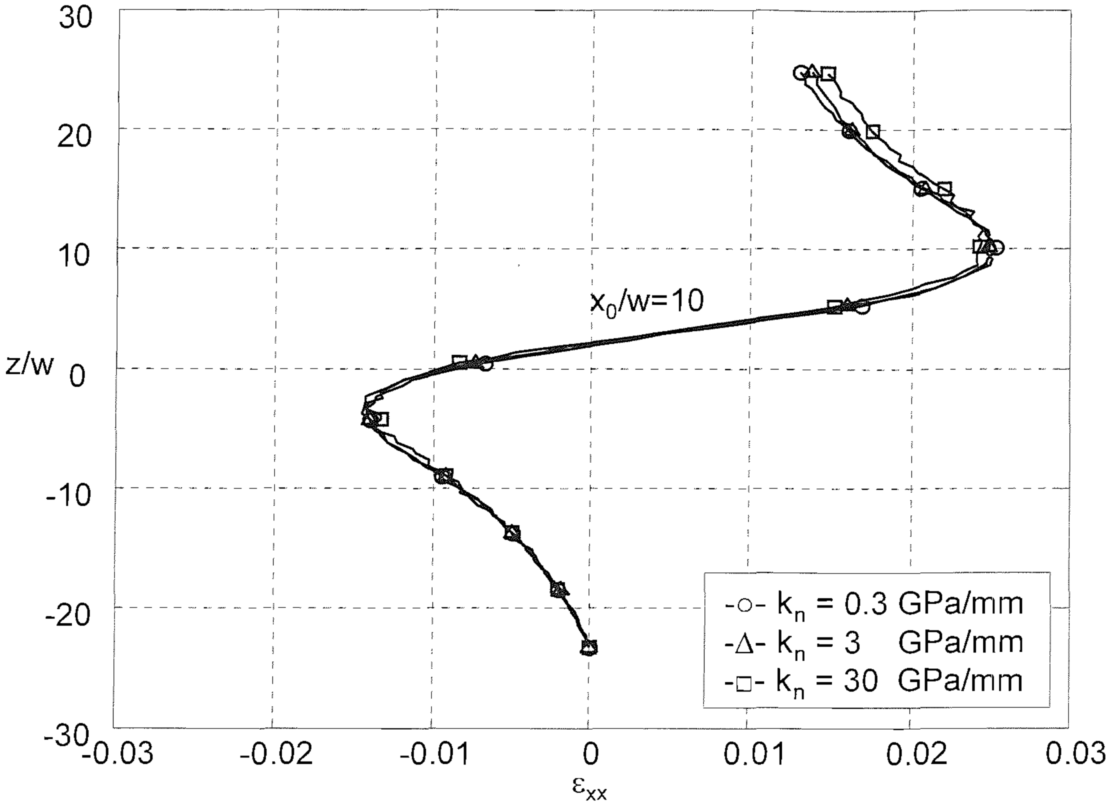

Figure 4-7 Influence of interface stiffness (k_n) on strain paths for (ε_{xx}) strain in 2D penetration models

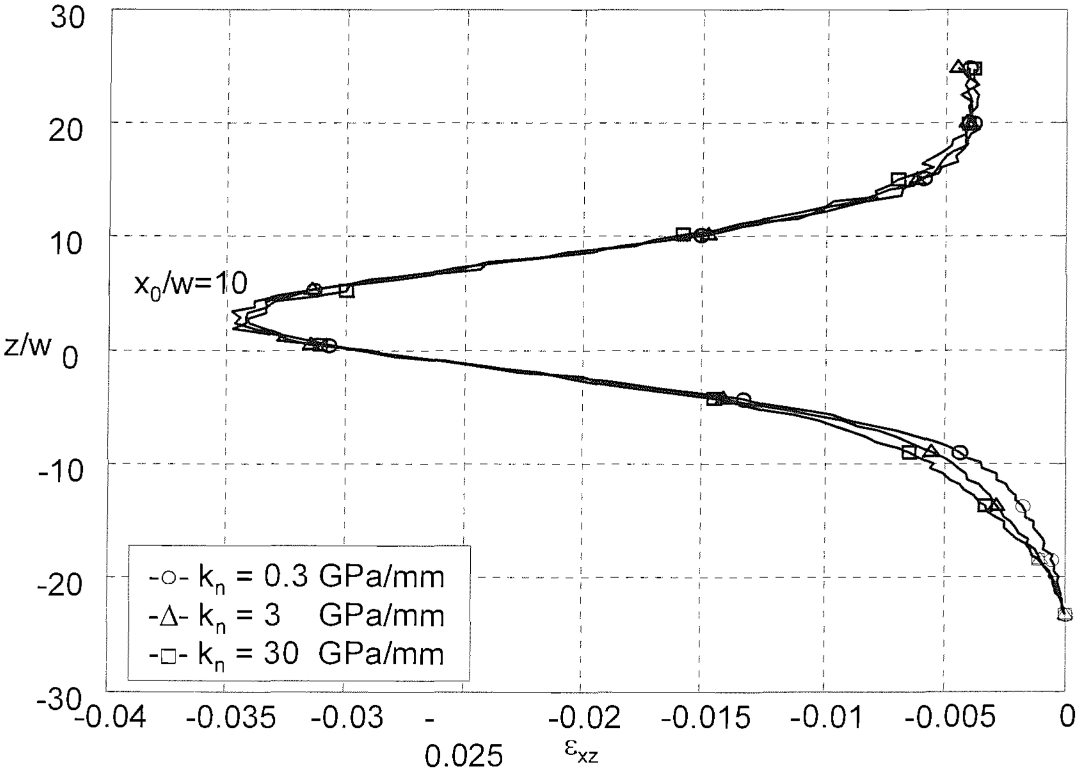

Figure 4-8 Influence of interface stiffness (k_n) on strain paths for (ε_{xz}) strain in 2D penetration models

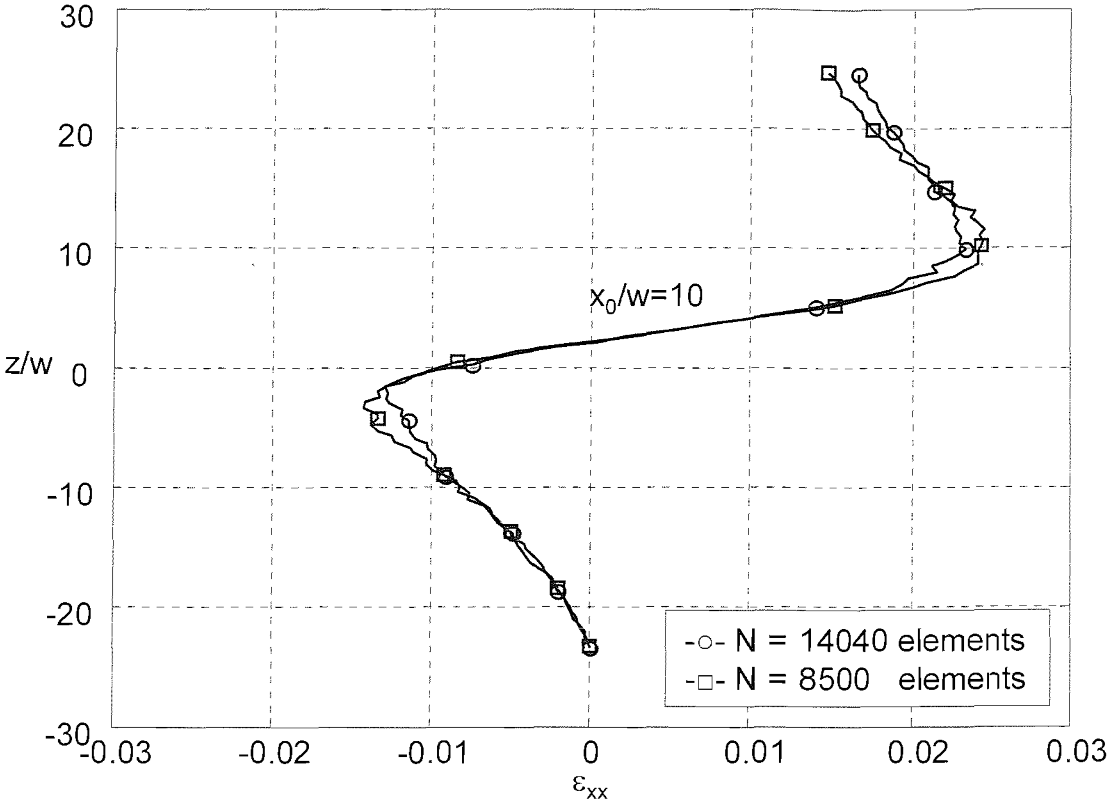

Figure 4-9 Influence of mesh density (N) on strain paths for (ε_{xx}) strain in 2D penetration models

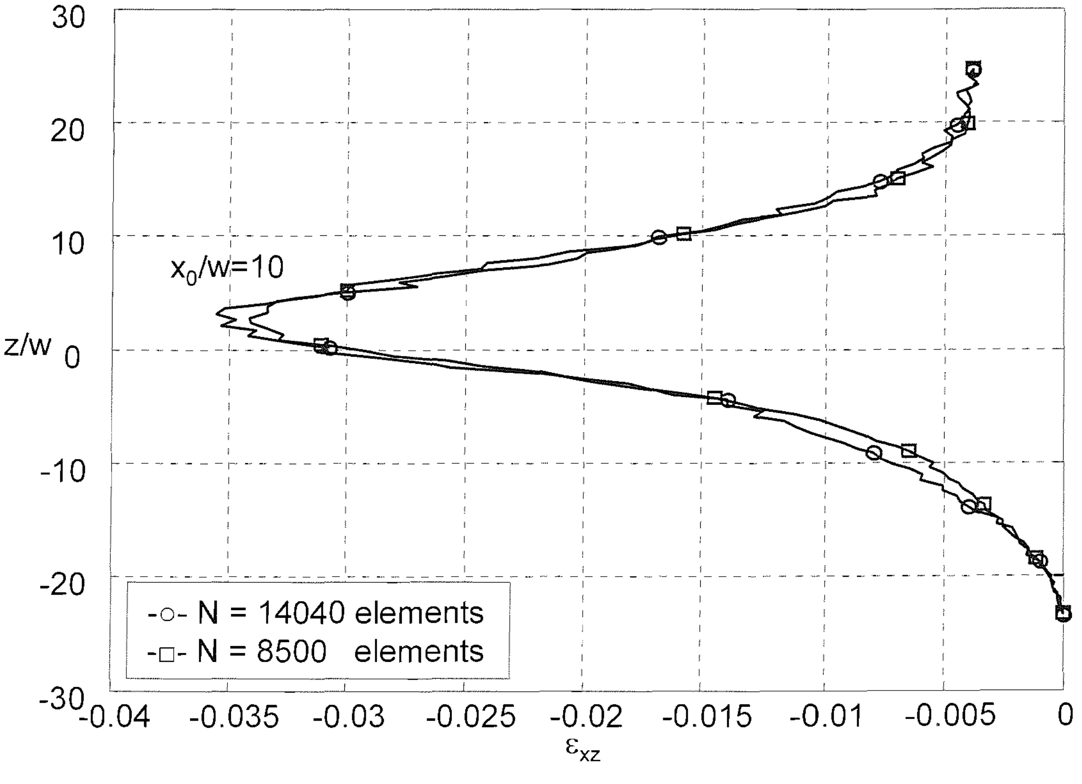

Figure 4-10 Influence of mesh density (N) on strain paths for (ε_{xz}) strain in 2D penetration models

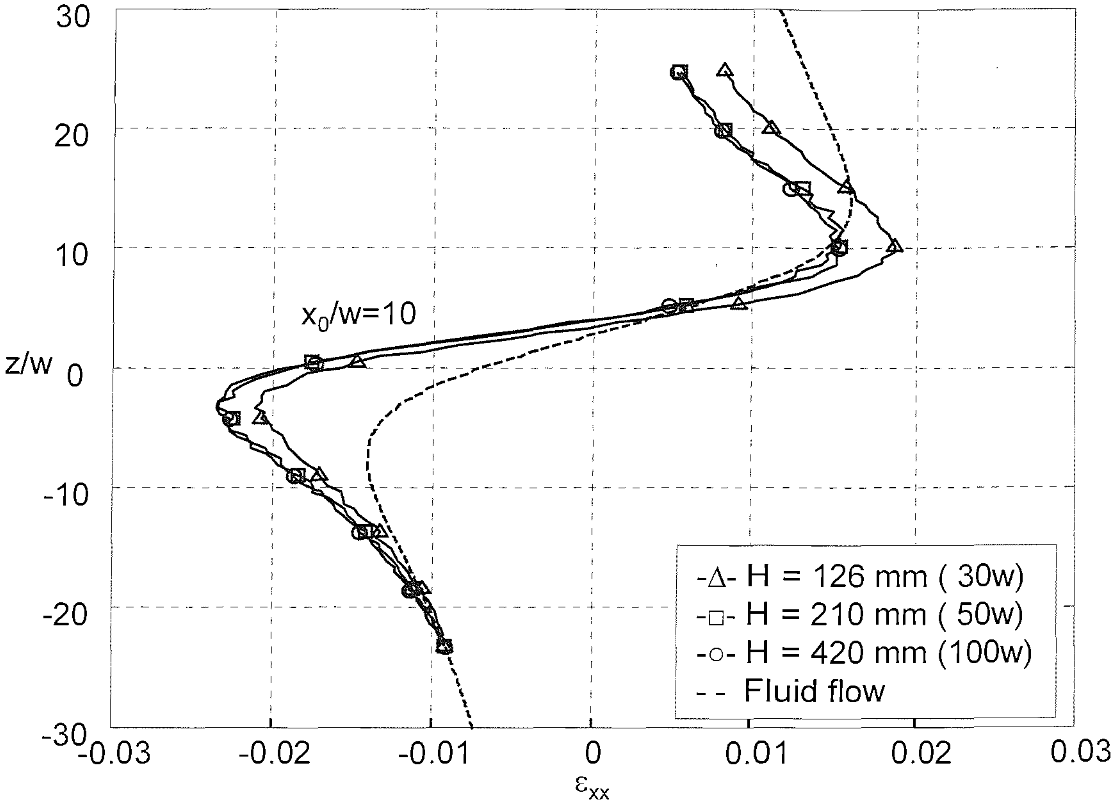

Figure 4-11 Influence of location of horizontal boundaries (H) on strain paths for (ε_{xx}) strain in 2D penetration models

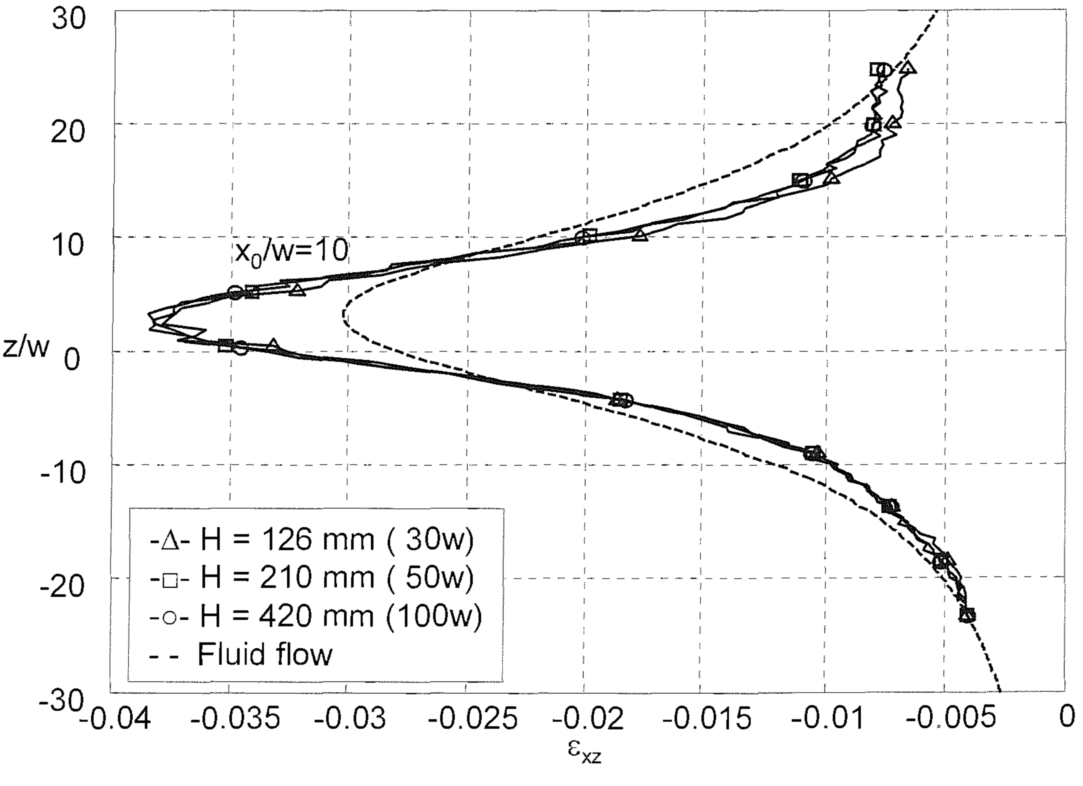

Figure 4-12 Influence of location of horizontal boundaries (H) on strain paths for (ε_{xz}) strain in 2D penetration models

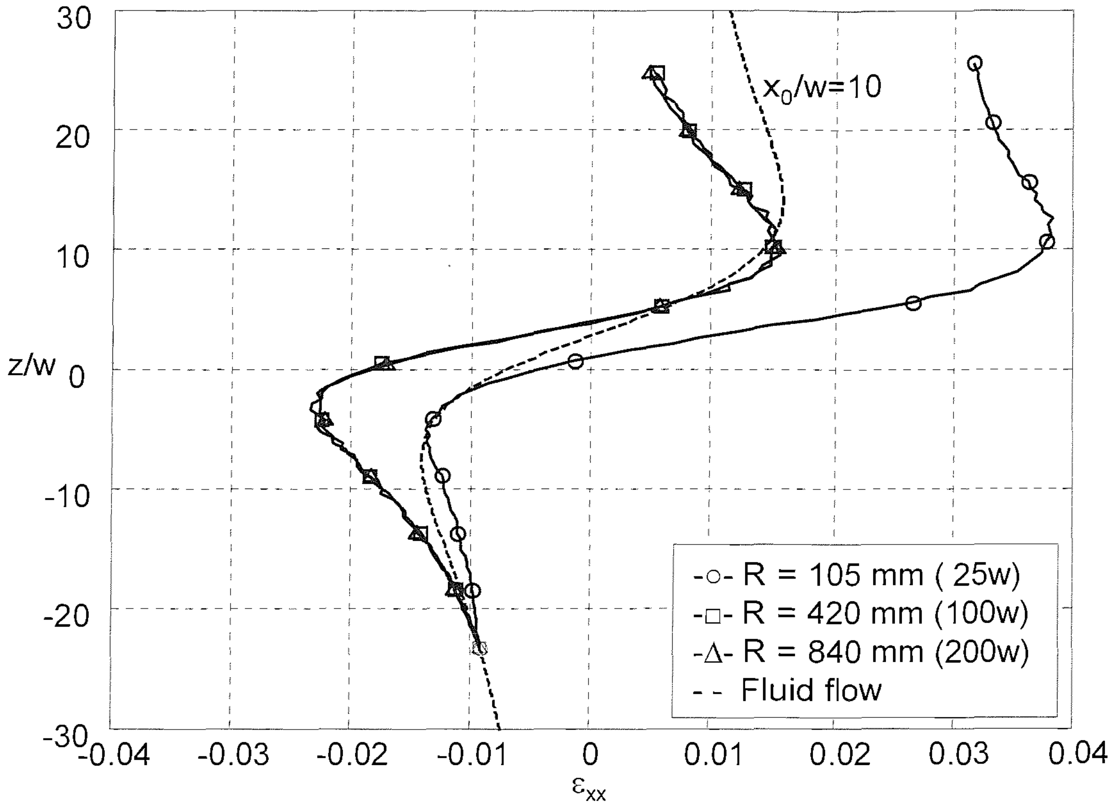

Figure 4-13 Influence of location of right boundary (R) on strain paths for (ε_{xx}) strain in 2D penetration models

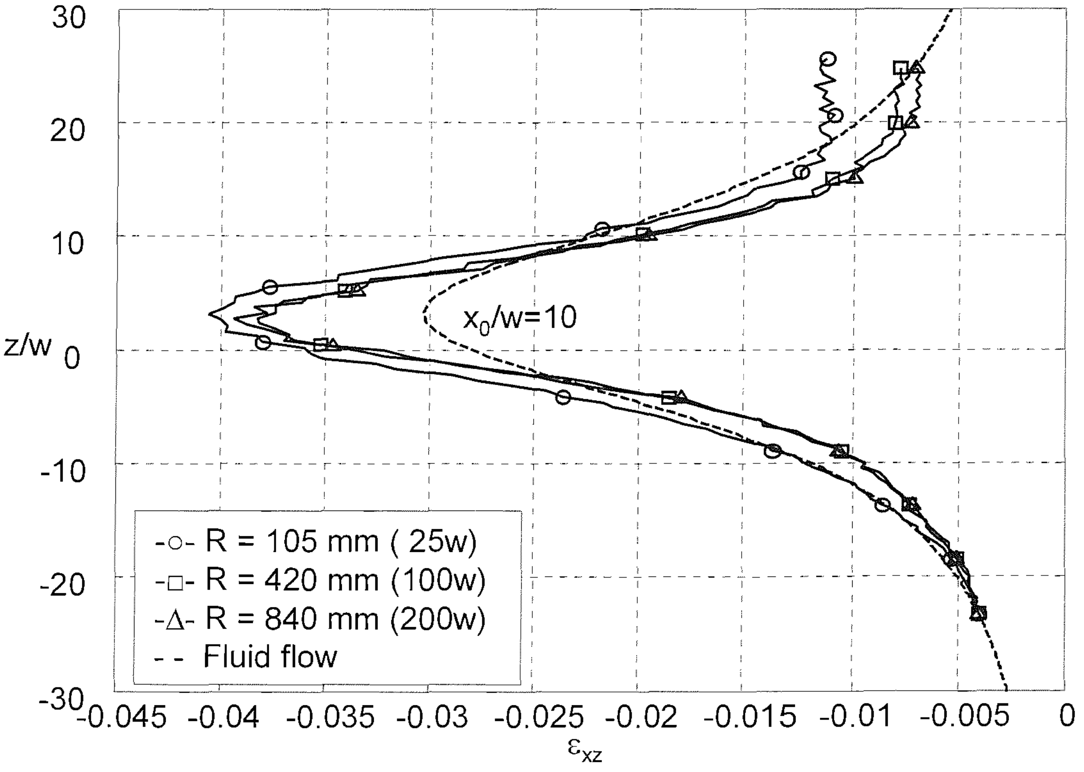

Figure 4-14 Influence of location of right boundary (R) on strain paths for (ε_{xz}) strain in 2D penetration models

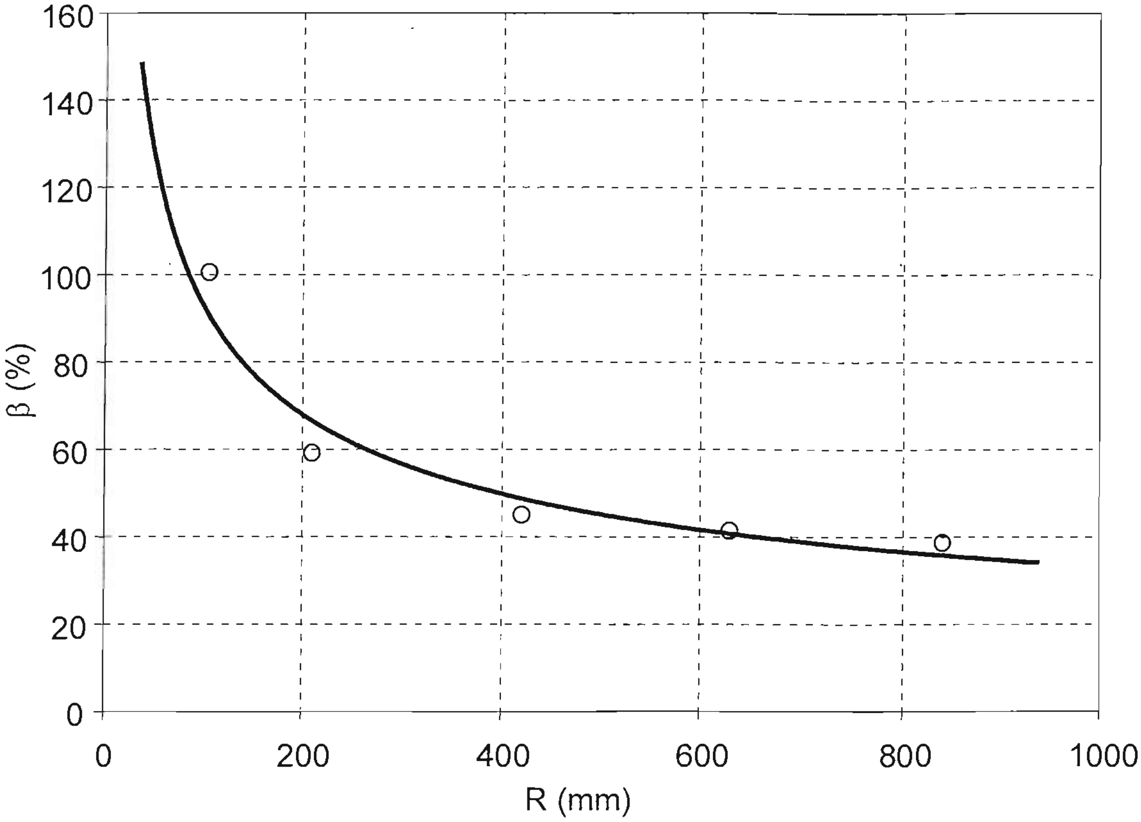

Figure 4-15 Influence of right boundary location (R) on normalised horizontal stress change (β) in models with smooth interface (α=0)

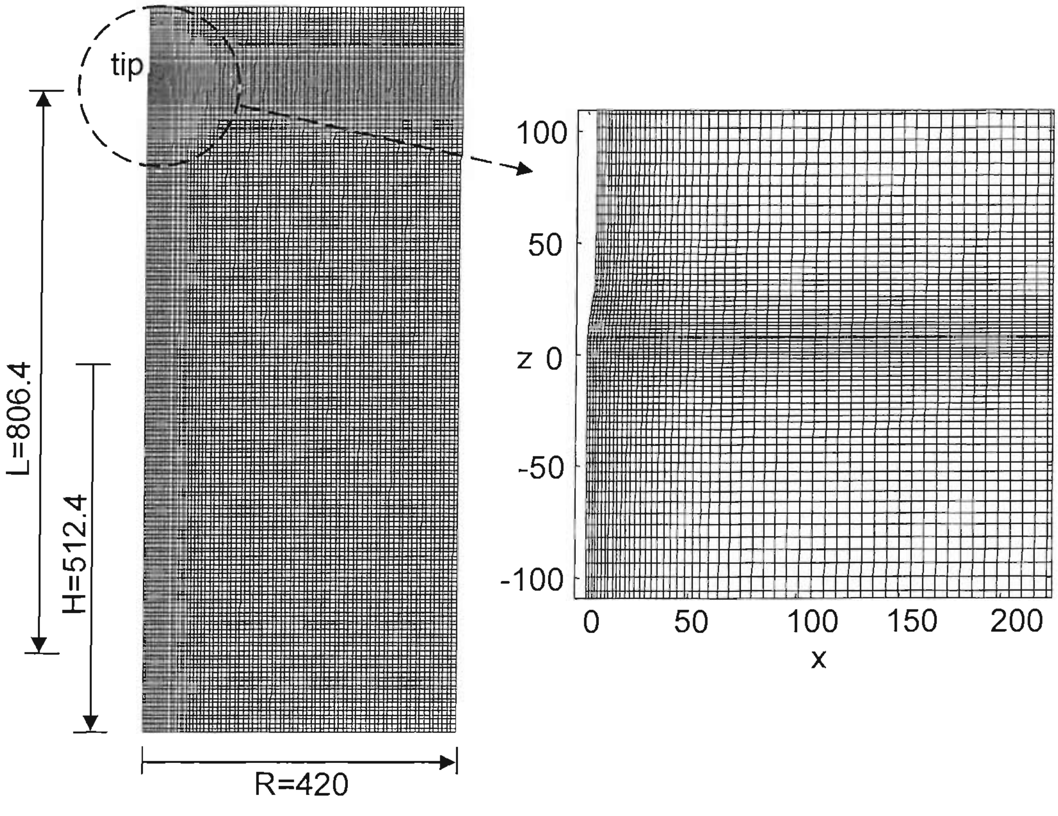

Figure 4-16 Boundary locations and mesh density in the LONG penetration model (mm)

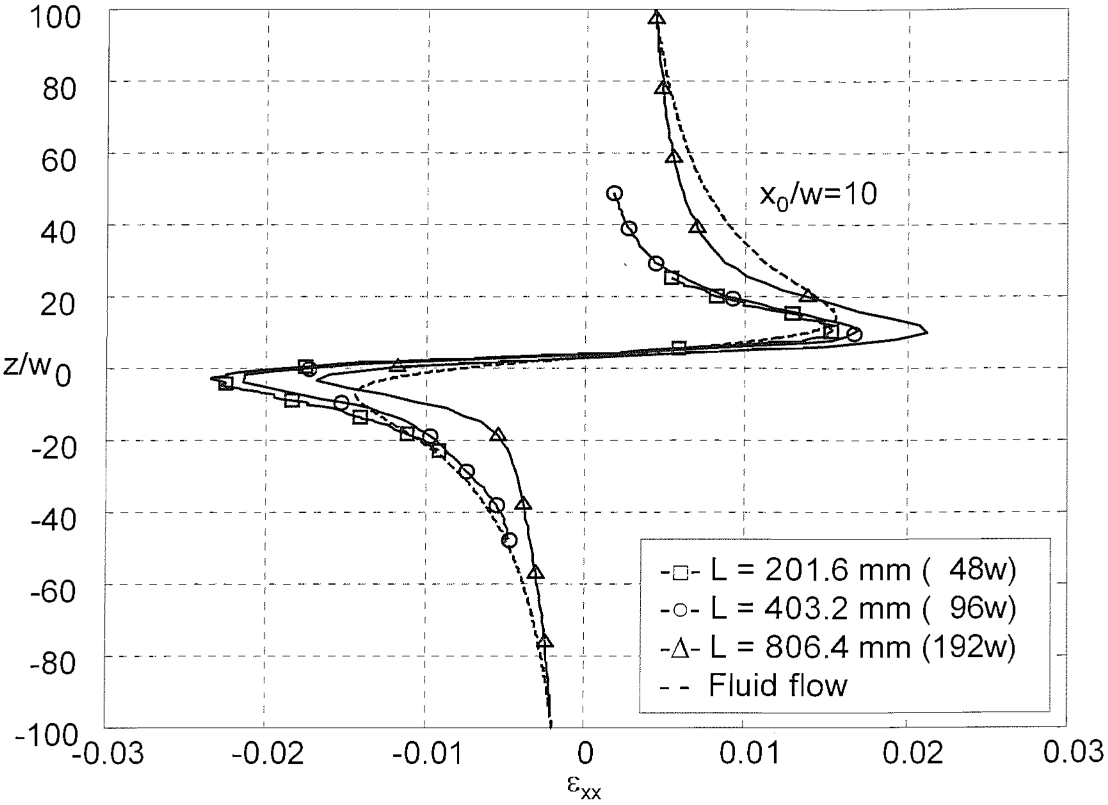

Figure 4-17 Influence of penetration length (L) on strain paths for (ε_{xx}) strain in 2D penetration models

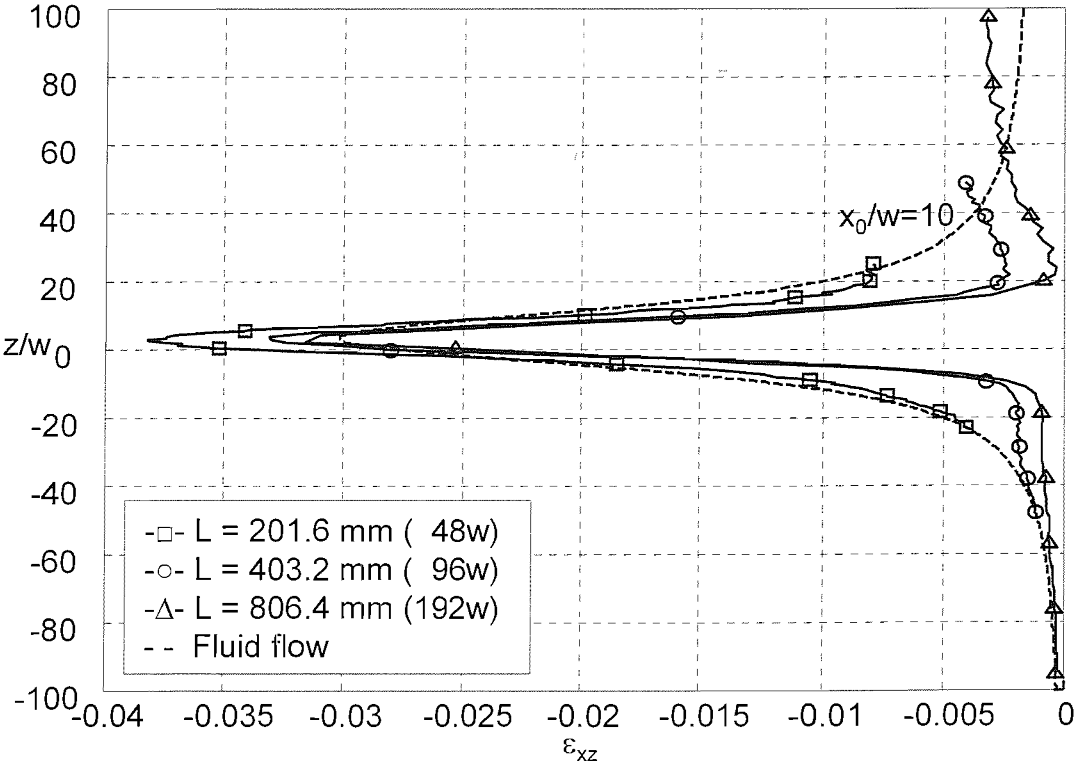

Figure 4-18 Influence of penetration length (L) on strain paths for (ε_{xz}) strain in 2D penetration models

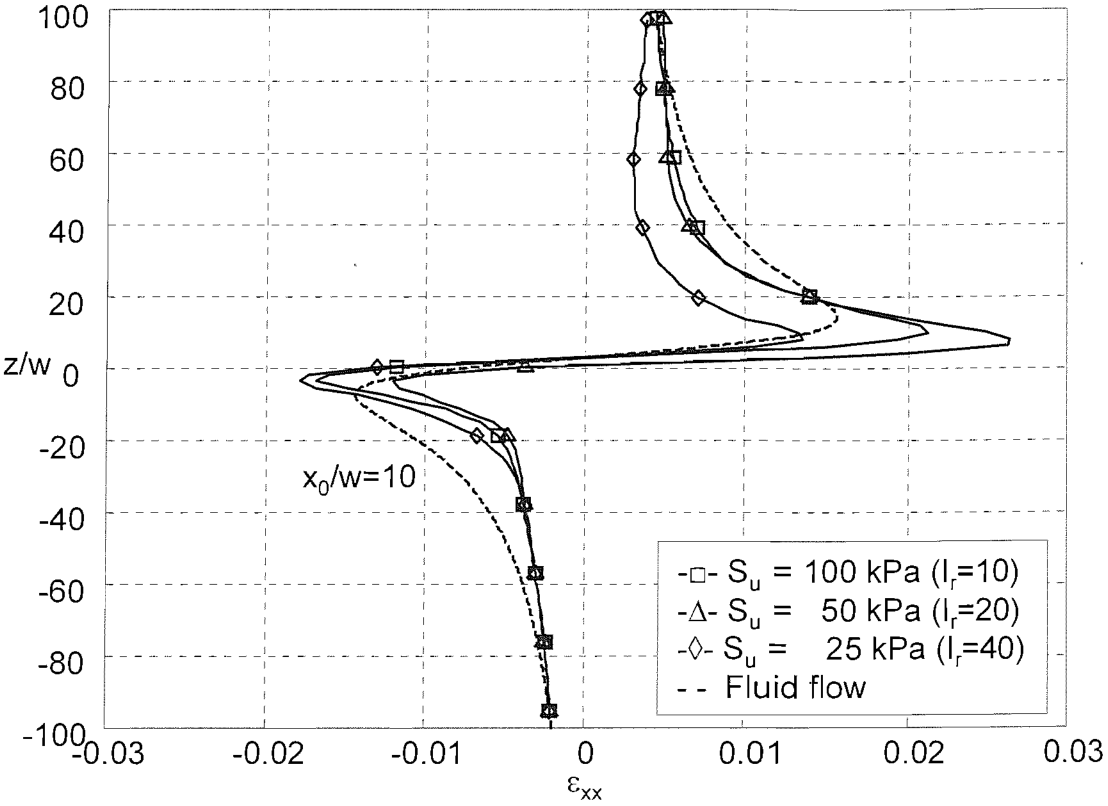

Figure 4-19 Influence of undrained shear strength (S_u) on strain paths for (ε_{xx}) strain in 2D penetration models

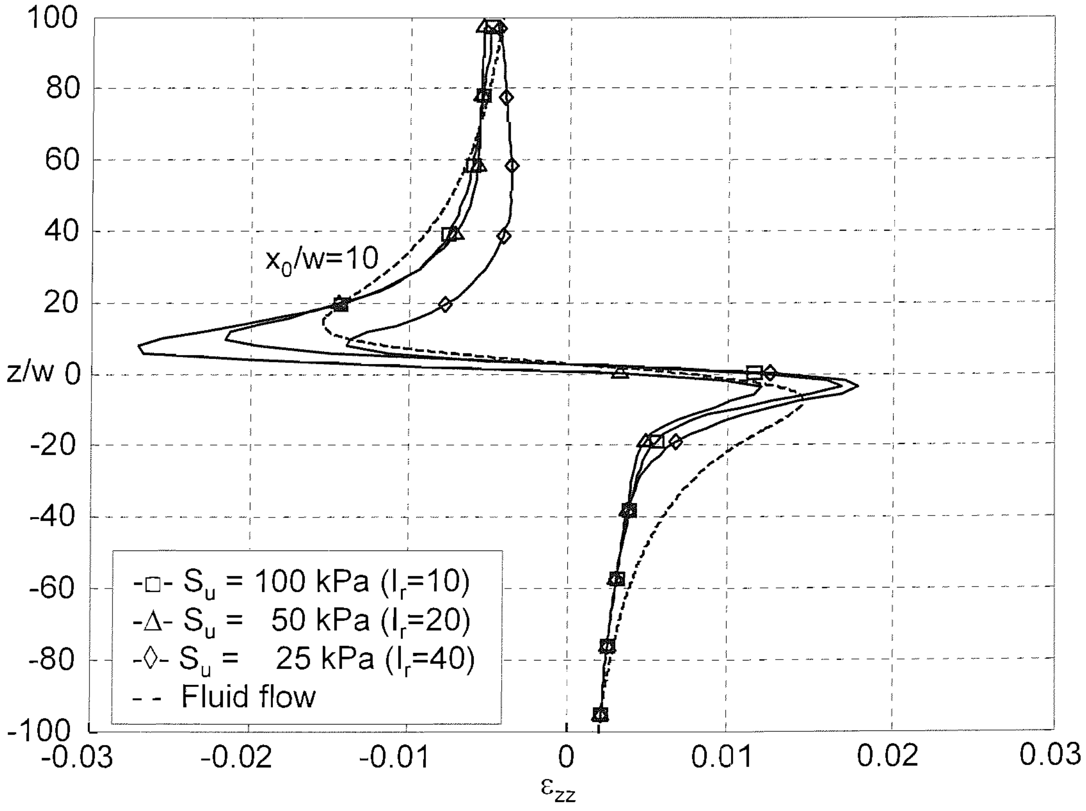

Figure 4-20 Influence of undrained shear strength (S_u) on strain paths for (ε_{zz}) strain in 2D penetration models

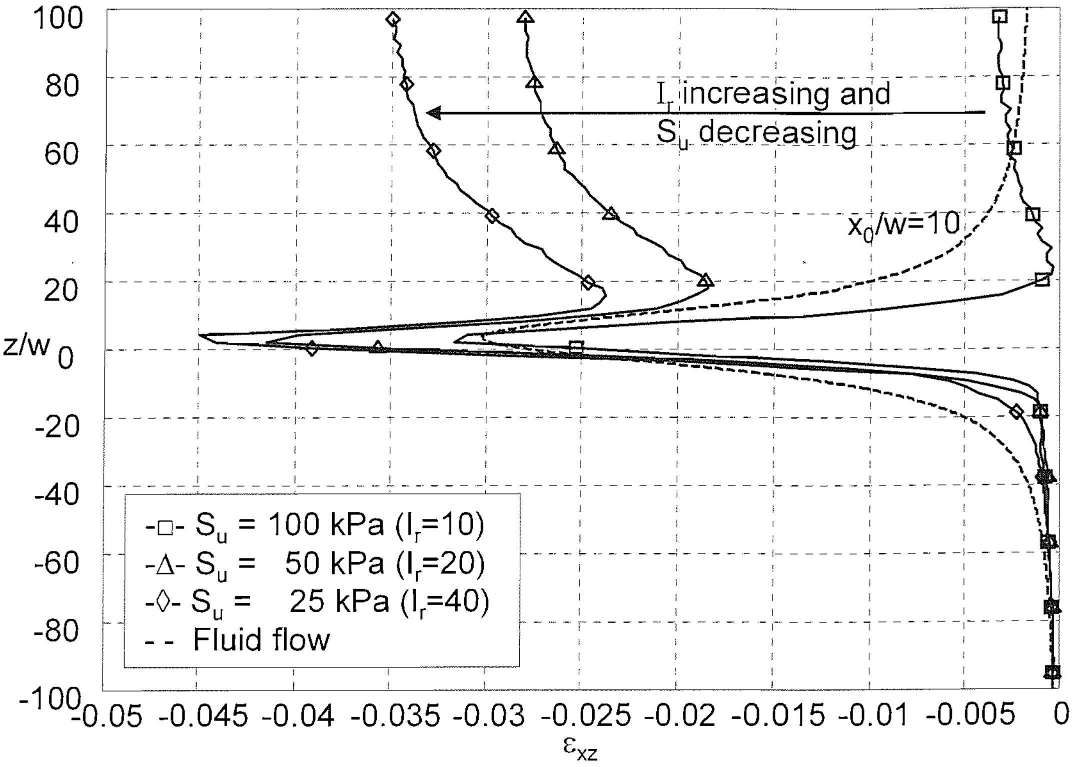

Figure 4-21 Influence of undrained shear strength (S_u) on strain paths for (ε_{xz}) strain in 2D penetration models

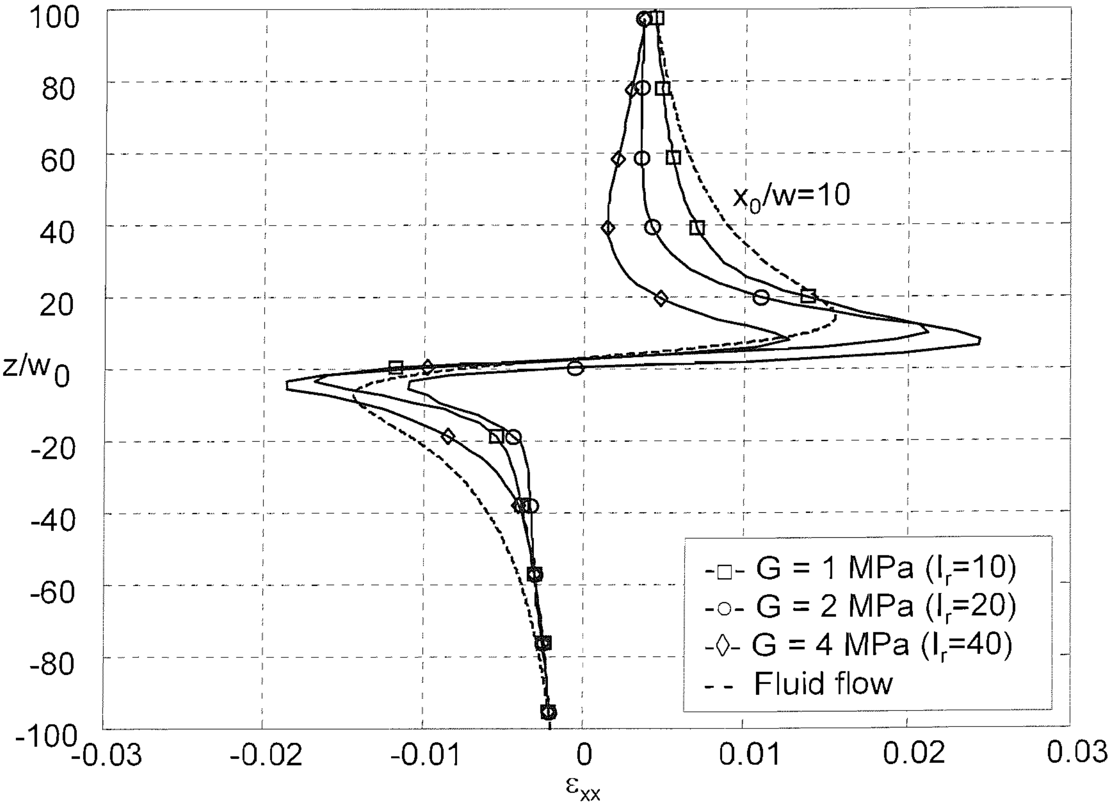

Figure 4-22 Influence of shear modulus (G) on strain paths for (ε_{xx}) strain in 2D penetration models

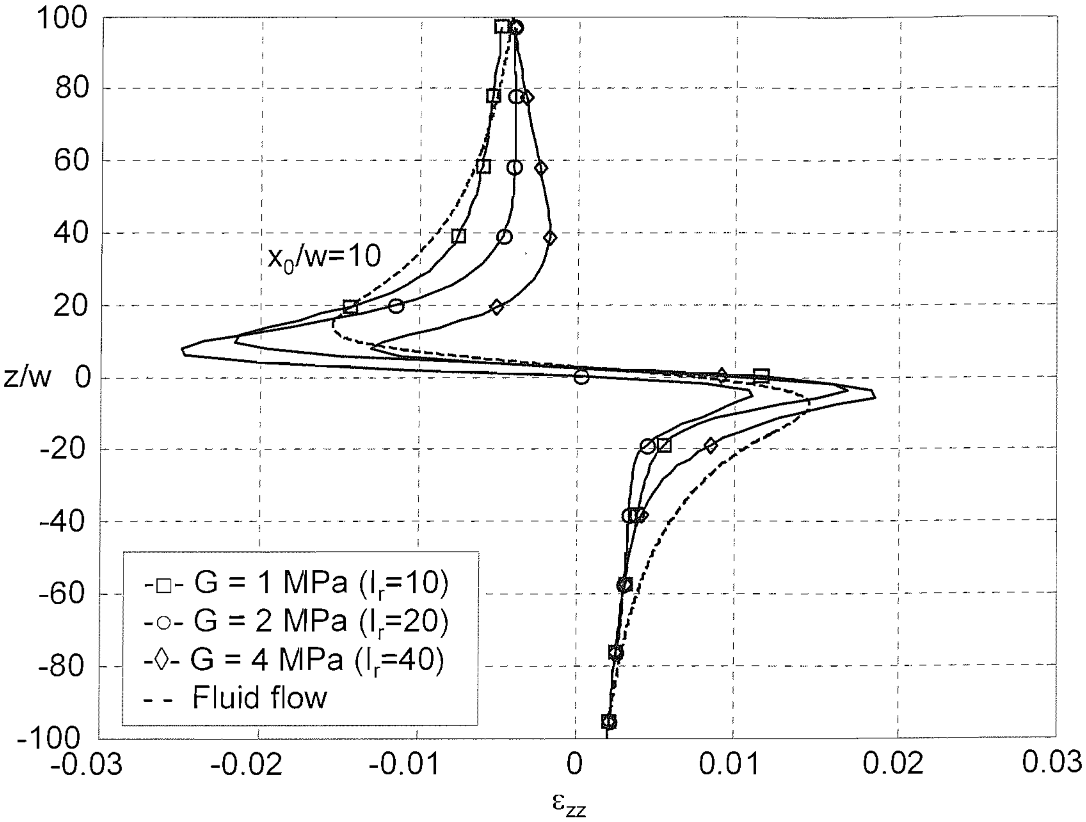

Figure 4-23 Influence of shear modulus (G) on strain paths for (ε_{zz}) strain in 2D penetration models

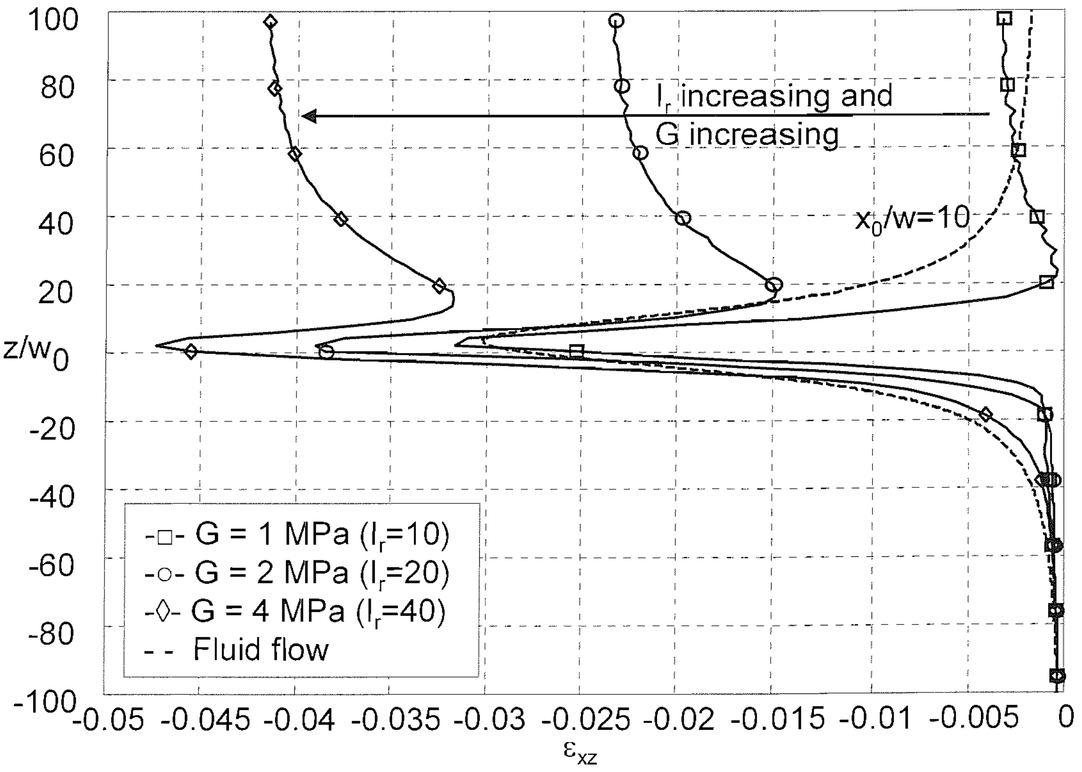

Figure 4-24 Influence of shear modulus (G) on strain paths for (ε_{xz}) strain in 2D penetration models

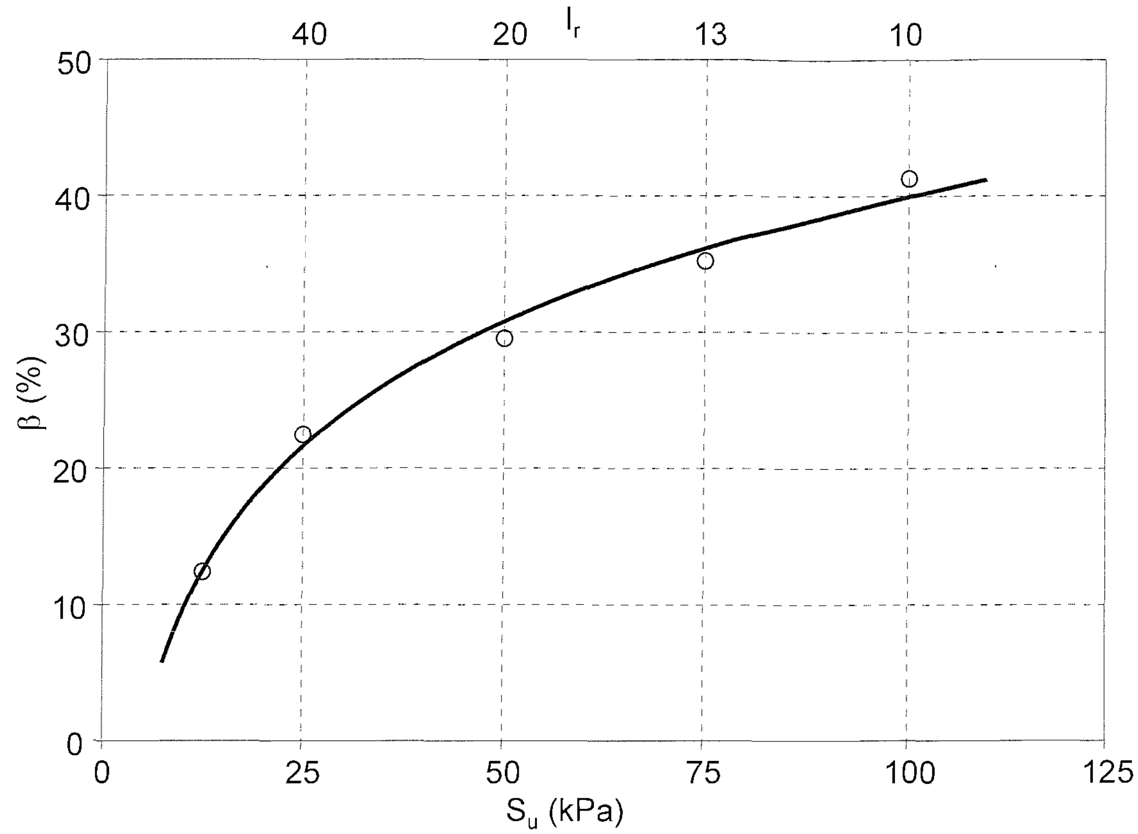

Figure 4-25 Influence of undrained shear strength (S_u) on normalised horizontal stress change (β) in 2D penetration models (G=1MPa)

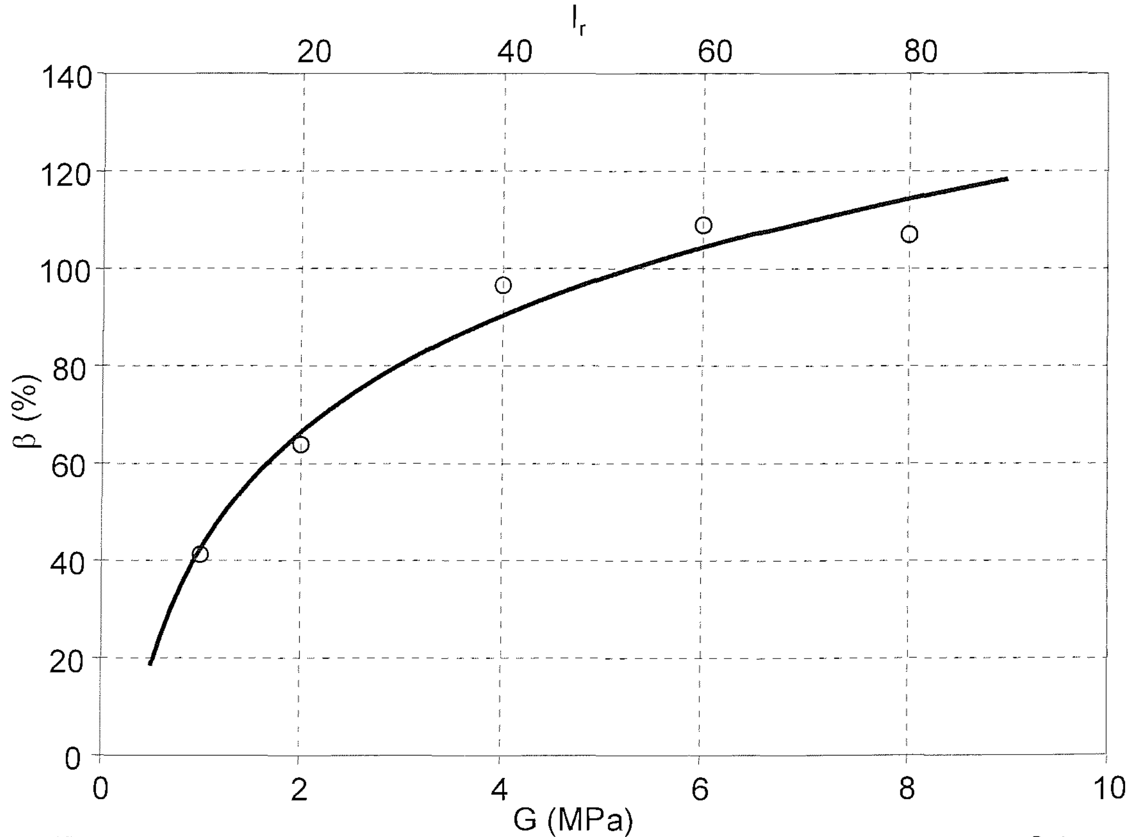

Figure 4-26 Influence of shear modulus (G) on normalised horizontal stress change (β) in 2D penetration models (S_u=100kPa)

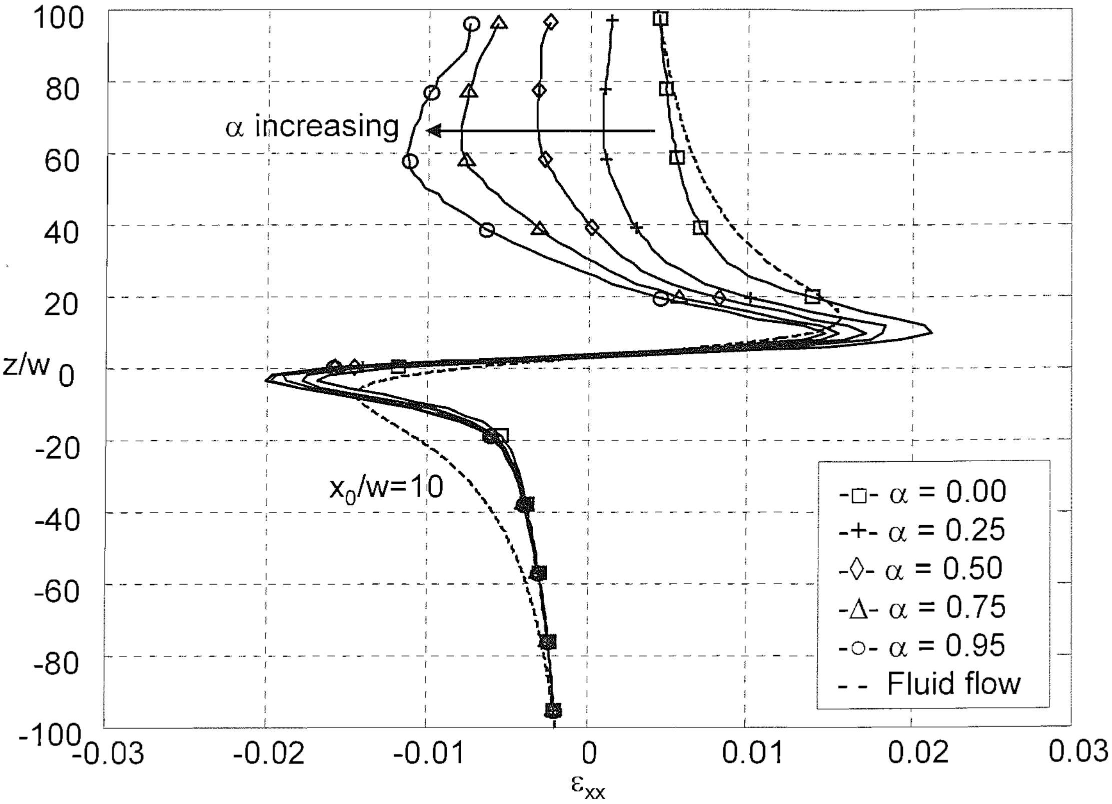

Figure 4-27 Influence of interface adhesion (α) on strain paths for (ε_{xx}) strain in 2D penetration models

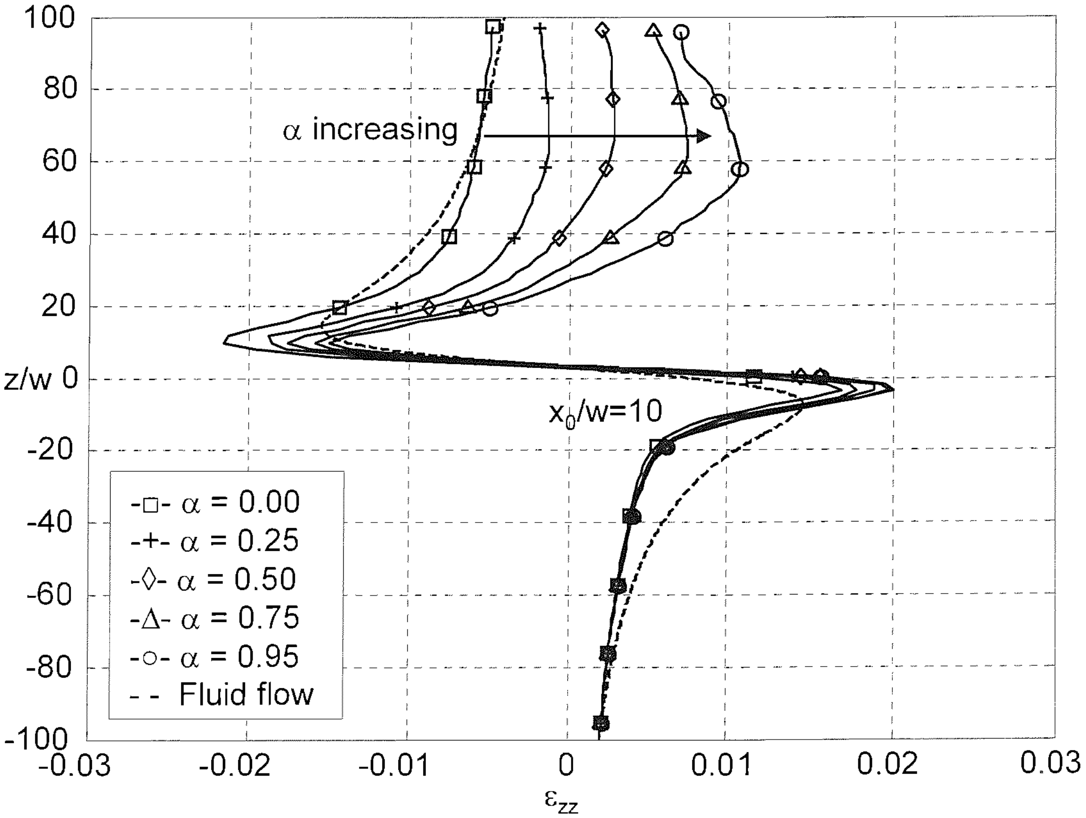

Figure 4-28 Influence of interface adhesion (α) on strain paths for (ε_{zz}) strain in 2D penetration models

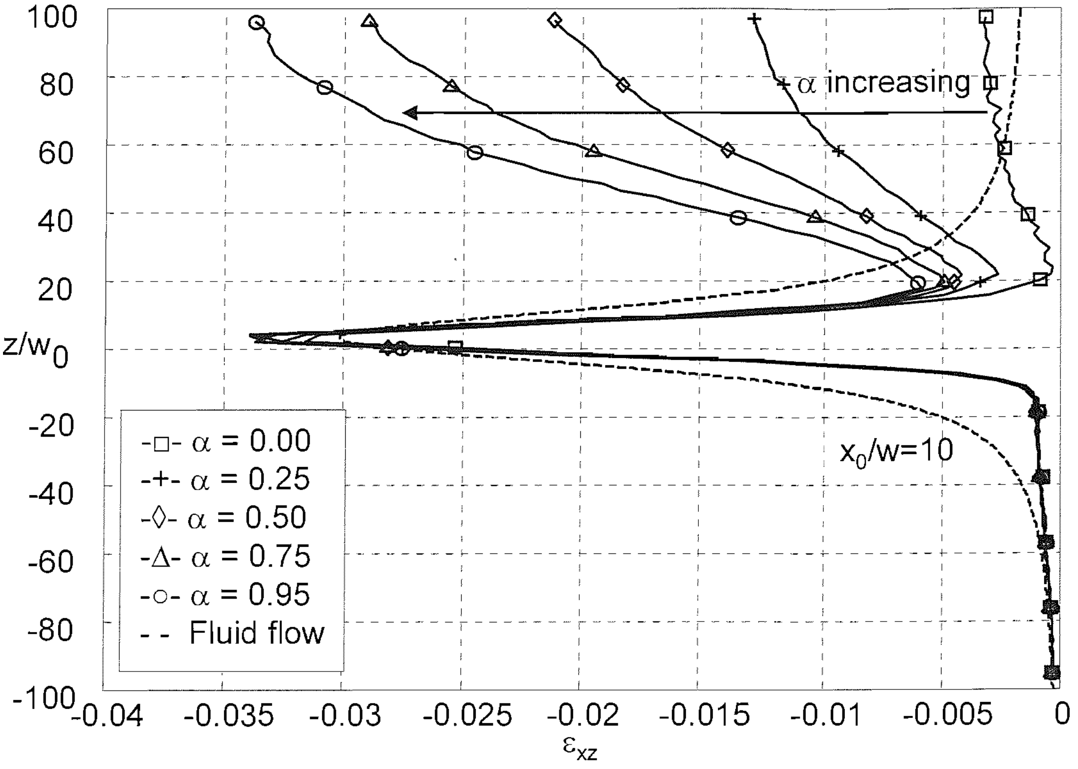

Figure 4-29 Influence of interface adhesion (α) on strain paths for (ε_{xz}) strain in 2D penetration models

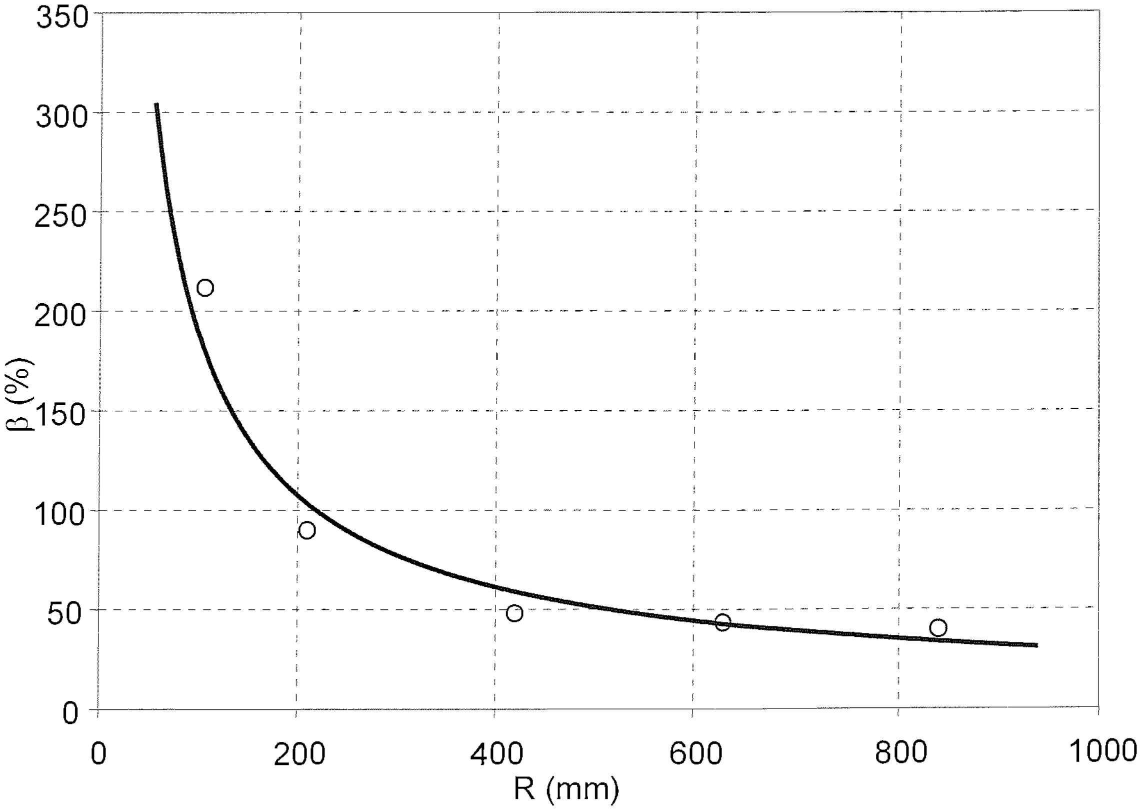

Figure 4-30 Influences of right boundary location (R) on normalised horizontal stress change (β) in models with rough interface (α=0.95)

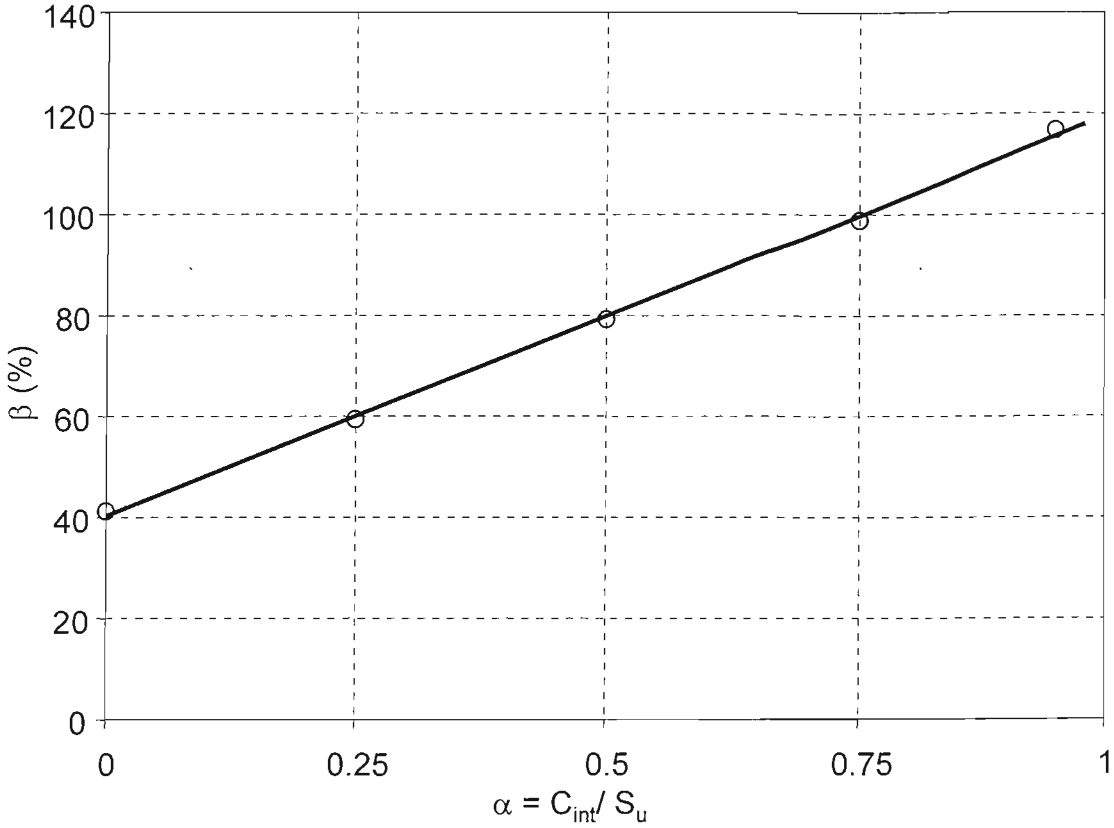

Figure 4-31 Influences of interface adhesion (α) on normalised horizontal stress change (β) in 2D penetration models (G=1MPa, S_u=100kPa)

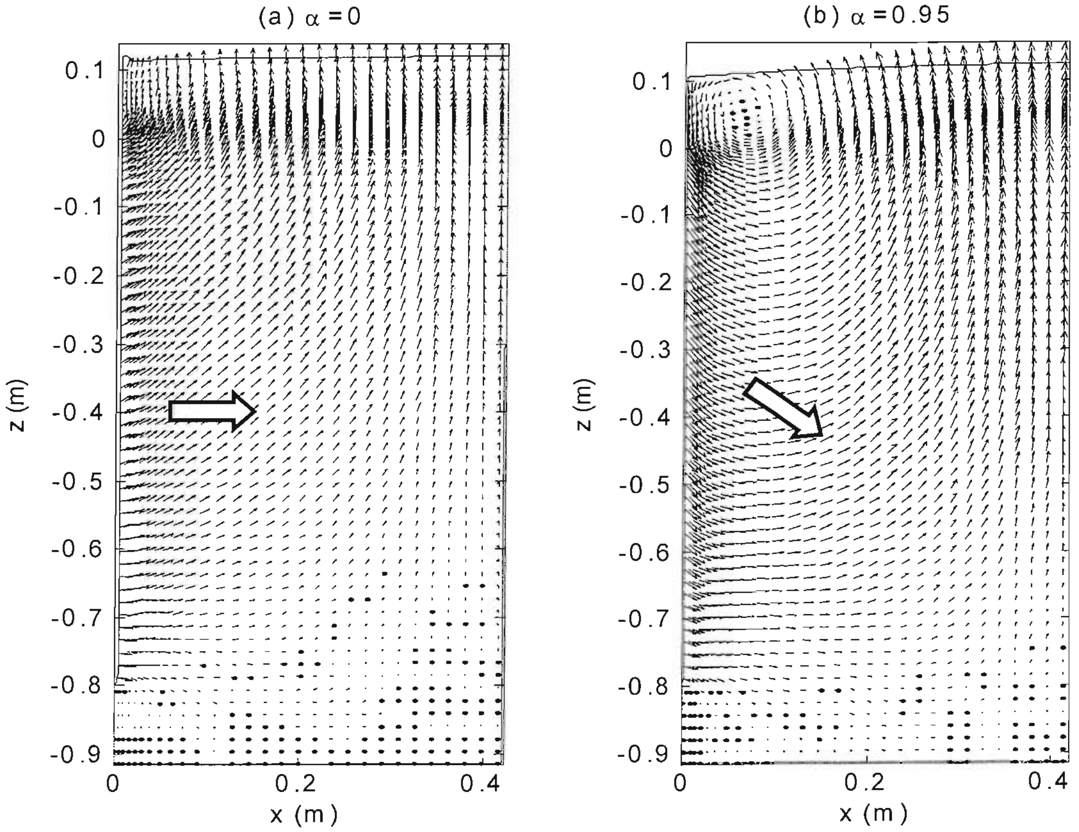
(a) α =0

(b) α =0.95

Figure 4-32 Influence of interface adhesion (α) on displacement vectors at the end of penetration (2D models)

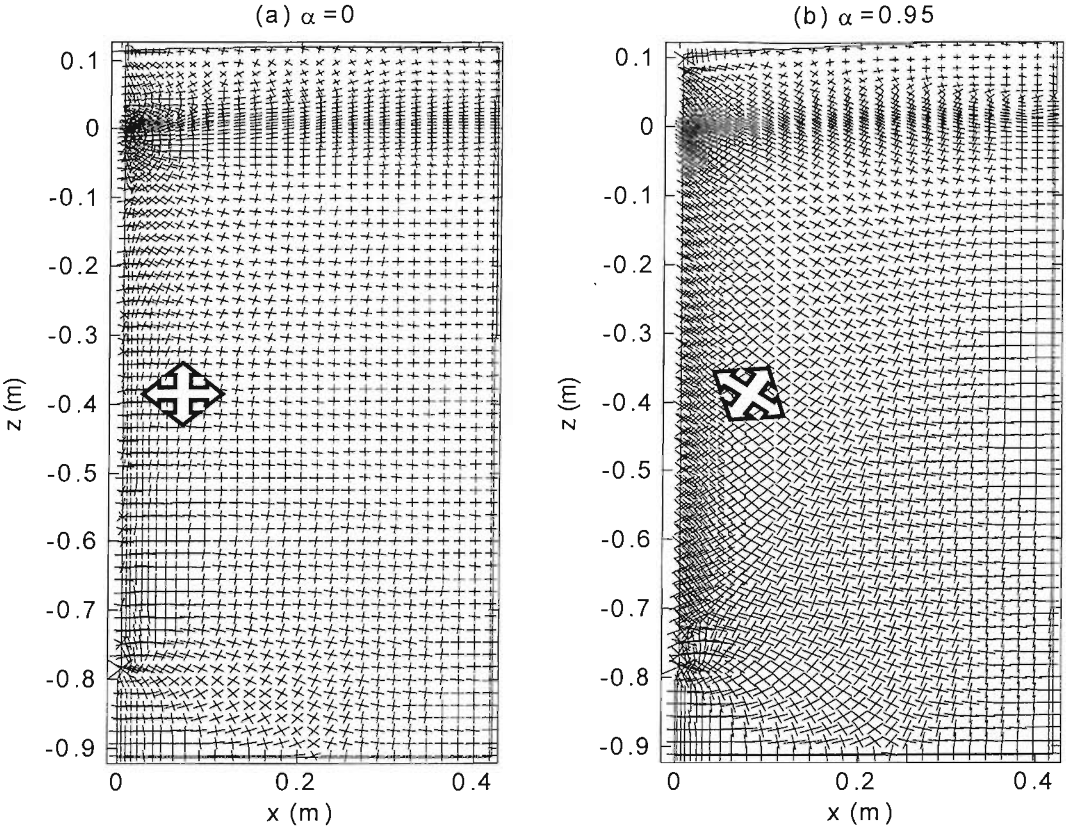

Figure 4-33 Influence of interface adhesion (α) on principal stress indicators at the end of penetration (2D models)

5 THREE DIMENSIONAL FLUID FLOW ANALYSIS

5.1 Introduction

Two-dimensional analyses provide an approximation for the mechanisms involved in spade cell penetration. Therefore, three-dimensional analyses must be conducted to provide a realistic picture of changes around a penetrating spade cell. Strain paths have been determined from the fluid flow analyses for the idealised three-dimensional spade cell geometry, termed the “chisel”. The FLUENT Computational Fluid Dynamics (CFD) package was used to simulate the flow field around the “chisel”. Outputs from the FLUENT program were manipulated in MATLAB to determine strain paths. This chapter contains a brief review of the modelling methodology adopted together with the results obtained from the 3D fluid flow analyses.

5.2 The FLUENT program

FLUENT is a commercially available CFD program that uses finite difference numerical formulations to solve governing fluid-flow equations for a specified problem (Fluent, 2005). The domain of the fluid problem is discretised into a series of finite cells also known as “control volumes”. A large set of simultaneous equations are formed by deriving the discrete form of the governing flow equations for all cells. These equations are in turn solved by iterative means until a converged solution is achieved.

Although two-dimensional fluid-flow calculations were readily accomplished by processing FLAC outputs (i.e. flow velocity vectors) in MATLAB, this was not computationally justifiable for three-dimensional analyses. Some of the justifications for using the FLUENT package for the three-dimensional fluid flow analyses are given here. The FLAC TRACK structure, which tracks particles along streamlines, is not available in FLAC^{3D}. The determination of streamlines from velocity vectors is a tedious task for three-dimensional fluid flow problems (Kenwright and Mallinson, 1992). In addition to tracking, FLUENT is also capable of calculating any field function (e.g. velocity and strain rate) along a streamlines. Flexible meshing strategies and efficient computational processes also make FLUENT a more suitable package for three-dimensional fluid flow analyses. FLUENT 6.0.20 (in double precision mode) and the GAMBIT 2.0.4 meshing pre-processor were used in this thesis to analyse the 3D flow around the "chisel" geometry.

5.3 Modelling methodology

The methodology adopted to evaluate strain paths consisted of three stages:

- *Generation* of the model (pre-processing using GAMBIT);
- *Iteration* of the model to derive a solution (processing using FLUENT);
- *Interpretation* of results (post-processing using MATLAB)

GAMBIT is the pre-processing package used to create the model geometry for fluid flow calculations. The geometry of the model was created by defining vertices; connecting pairs of vertices to define edges, connecting co-planar edges to generate faces (i.e. planes); and connecting closed faces to generate volumes. The volumes were then meshed according to the meshing pattern (i.e. number of nodes and successive ratios) defined on their edges. In addition to the geometry and mesh, boundary types were also specified in the GAMBIT pre-processor, prior to exporting the model into the correct format for FLUENT.

Figure 5.1 shows a schematic view of the "chisel" geometry, the shape used as the idealised geometry for the spade cell in all three-dimensional fluid flow and soil penetration analyses. The "chisel" had a half thickness of w=4.2mm and half width of B=50.4mm(12w) in all analyses, unless specified otherwise. The corners of the "chisel" were chamfered in two planes as shown in this figure.

The "chisel" was placed in the middle of a flow channel with a length of 2H and a square cross section of size 2A×2C. Due to the symmetry of the problem, it was sufficient to analyse a quarter of this geometry (2H×A×C), as shown in Figure 5.2. Figure 5.2 also shows the various boundary conditions defined within the model. The lower and upper boundaries were set as VELOCITY-INLET and PRESSURE-OUTLET boundaries respectively. Planes of SYMMETRY were specified on the x-z(y=0) and y-z(x=0) planes. All other external boundaries were by default set to WALL. The properties of the WALL and VELOCITY-INLET boundaries were set later in the FLUENT environment.

Various parameters were assigned in the FLUENT environment before the fluid flow equations were solved by iterative means. These parameters included:

- **Solution Methodology**: the sequence of solving the governing flow equations;
- **Boundary conditions**: boundary parameters for various boundary types;
- **Custom field functions**: based on basic field variables;
- **Initial solution**: an initial "guess" for the flow field solution; and
- **Convergence criteria**: the convergence criteria for ceasing the iteration

The three-dimensional laminar non-viscid steady-state flow equations were set to be solved consequently (i.e. segregated). A vertical velocity of U=1.2E-3mm/sec was defined at the VELOCITY-INLET boundary. To simulate the full-slip boundary, the vertical velocity of the fluid on the WALL boundaries was also set to the inlet velocity (Gill and Lehane, 2000). Various components of the strain rate tensor (i.e. partial derivatives of the velocity field) were defined as custom functions. The model was initiated by setting the vertical velocity of the flow field equal to the value defined on the inlet boundary. The iteration will cease when the scaled residual value in the continuity equation drops below 1E-5 (convergence criterion).

Fluid flow field characteristics (e.g. coordinates, velocity magnitudes and strain rates) were recorded at fixed intervals along each streamline. These FLUENT outputs were then manipulated within MATLAB to calculate strain paths (i.e. the cumulative strain increments along streamlines) according to Equation 3-5.

5.4 Results

The mesh density was increased gradually towards the location of the "chisel" tip in all directions (i.e. +x, +y and ±z). Various starting element length (a_1) and successive ratio (r) values were adopted in three models (MAIN, COARSE and FINE) to assess the adequacy of the mesh density. The number (N) of hexahedral cells (i.e. mesh density) accordingly used in these models, were:

- COARSE: a_1=4.00mm, r=1.10, N= 24,187
- MAIN: a_1=2.00mm, r=1.05, N=187,264
- FINE: a_1=1.33mm, r=1.03, N=709,239

Peak strain values for the streamline passing through $x_0/w=10$, $y_0/w=2$ and $z_0/w= -20$ were compared to assess the influence of the mesh density on the solution convergence. The differences in peak strains were insignificant (less than 5%) between models with various mesh densities. Due to the small improvement observed in the FINE model (in comparison to the MAIN model) and in order to achieve reasonable computational times, the mesh density utilised in the MAIN model was adopted for all subsequent fluid flow analyses.

In the 2D fluid flow analyses, the influence of boundary locations was investigated by comparing strain paths determined numerically with the closed-form solution. However, since an analytical solution does not exist for the fluid flow characteristics around the "chisel", the influence of the boundaries could not be assessed directly. External boundaries were therefore located further away than the necessary distances derived from the 2D fluid flow analyses. Boundary locations (as defined in Figure 5.2) and the corresponding mesh density utilised for the 3D fluid flow analyses are summarised below:

- **Upper/lower boundaries**: at H=630mm(150w) away from the tip level;
- **Far lateral boundaries**: at A=C=420mm(100w) away from symmetry planes;
- **Mesh pattern**: a_l=2mm and r=1.05 on all edges (N=461,750 hexahedral cells)

The result of 3D fluid flow analyses are presented in the form of strain paths determined for the streamline passing through point $P_0(x_0=10w, y_0=2w, z_0= -96w)$. Strain paths show the cumulative strain increments along the streamline plotted against the vertical coordinate (z) of the particle, normalized by the half thickness (w) of the “chisel” (z/w=0 indicates the tip level). The general patterns of various strain paths in the flow field around the “chisel” are summarised in the following paragraphs.

Figure 5.3 shows the strain path for the lateral (ε_{xx}) strains. The lateral strain path consisted of three sections: an initial extension, followed by compression and finally a re-extension. The lateral strain reached a minimum extensive strain value of ε_{xx}= -0.25% at z/w= -10 beneath the tip. From this point onwards the strain change became compressive and the maximum strain value of ε_{xx}=3.5% was reached at z/w=15 above the tip. The strain path demonstrated an extensive behaviour for a short length and the lateral strain dropped to ε_{xx}=3.3% at z/w=50. The strain levels were relativity stable from this point onwards until the end of the strain path. Figure 5.4 shows the strain path for the longitudinal (ε_{yy}) strains. The longitudinal strains showed an entirely extensive behaviour, reaching a final value of ε_{yy}= -3.25% at the end of the path. The lateral and longitudinal strains at the end of the strain path cancel each other out, $\varepsilon_{yy\_end} \approx -\varepsilon_{xx\_end}$.

The vertical strain path (ε_{zz}) is shown in Figure 5.5. The vertical strain path also consisted of three sections. The initial section was compressive with the maximum strain of ε_{zz}=0.92% reached at z/w= -3. This section was followed by an extensive section with a peak strain of ε_{zz}= -1.05% at z/w=10. The strain change became compressive again and strains dropped to values close to zero (ε_{zz}=0.1%) at the end of the path.

Various shear strain paths (ε_{xz}, ε_{yz} and ε_{yz}) were also examined for the 3D fluid flow around the "chisel". The (ε_{xz}) shear strain path is shown in Figure 5.6. The maximum ε_{xz} strain was experienced as the particles tracked along streamlines passed the tip level. The shear strains increased to ε_{xz}= -2.3% just above the tip level. From this point onwards the shear strains reduced until they reached ε_{xz}= -0.3% at z/w=40. The shear strains increased gradually for the remainder of the path. Figure 5.7 shows the strain paths for ε_{xy} and ε_{yz} strains. These shear components were relatively smaller than the ε_{xz} strain. The changes in (ε_{xy}) shear strains were insignificant for the z/w<-30 section of the path. The ε_{xy} shear increased between z/w= -30 and z/w=30, however, it became relatively stable afterwards reaching a value of ε_{xy}=0.68% at the end of the path. The pattern of (ε_{yz}) shear strain path was similar to that observed for the (ε_{xz}), with its peak (ε_{yz}=0.22%) attained at the tip level.

The octahedral strain (γ_{oct}) defined as Equation 5-1 can be used to evaluate the overall strain introduced in three-dimensional analyses as it incorporates all the strain components (Huang, 1989):

$$\gamma_{oct} = \frac{2}{3}\sqrt{\left(\varepsilon_{xx}-\varepsilon_{yy}\right)^2+\left(\varepsilon_{xx}-\varepsilon_{zz}\right)^2+\left(\varepsilon_{yy}-\varepsilon_{zz}\right)^2+6\left(\varepsilon_{xy}{}^2+\varepsilon_{xz}{}^2+\varepsilon_{yz}{}^2\right)} \quad \textbf{Equation 5-1}$$

Figure 5.8 illustrates the octahedral strain (γ_{oct}) for a particle tracked along the streamline in the flow field around the "chisel". The octahedral strain initially increased up to γ_{oct}=5.45% at z/w=10 above the tip. The octahedral strain dropped from this local peak to γ_{oct}=5.35% at z/w=30. From this point onwards, the strain increased slightly until the end of the path.

5.5 Summary

The methodology used to determine strain paths from the fluid flow analyses around the idealised three-dimensional spade geometry, the "chisel", has been outlined. The FLUENT CFD package was used to determine strain paths around the "chisel". The adequacy of the adopted mesh density was evaluated by determining the sensitivity of outputs to the mesh refinement. The boundary location criteria derived in the 2D fluid flow analyses were directly adopted for the 3D models. The strain paths were determined in these 3D fluid flow analyses for a streamline close to the "chisel" plane of symmetry ($y_0/w=2$). It was observed that at the end of the strain path, the dominant normal strain components were the lateral (ε_{xx}) and longitudinal (ε_{yy}) strains, while the vertical (ε_{zz}) strain values returned to zero. The ε_{xz} strain was the dominant shear strain component, with its peak value attained at the tip level. The octahedral strain path also showed that the greatest strain change occurred between $z/w= -30$ and $z/w=10$. The strain paths determined from these fluid flow analyses will be used to validate the soil penetration analyses in the next chapter (Chapter 6).

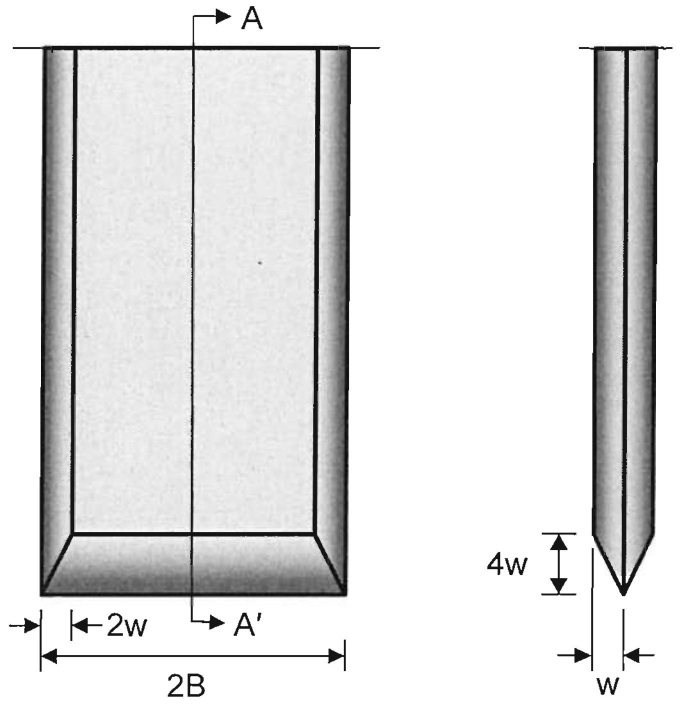

(a) Elevation (b) Cross-section (A-A′)

Figure 5-1 Schematic view of the "chisel" geometry (w=4.2mm)

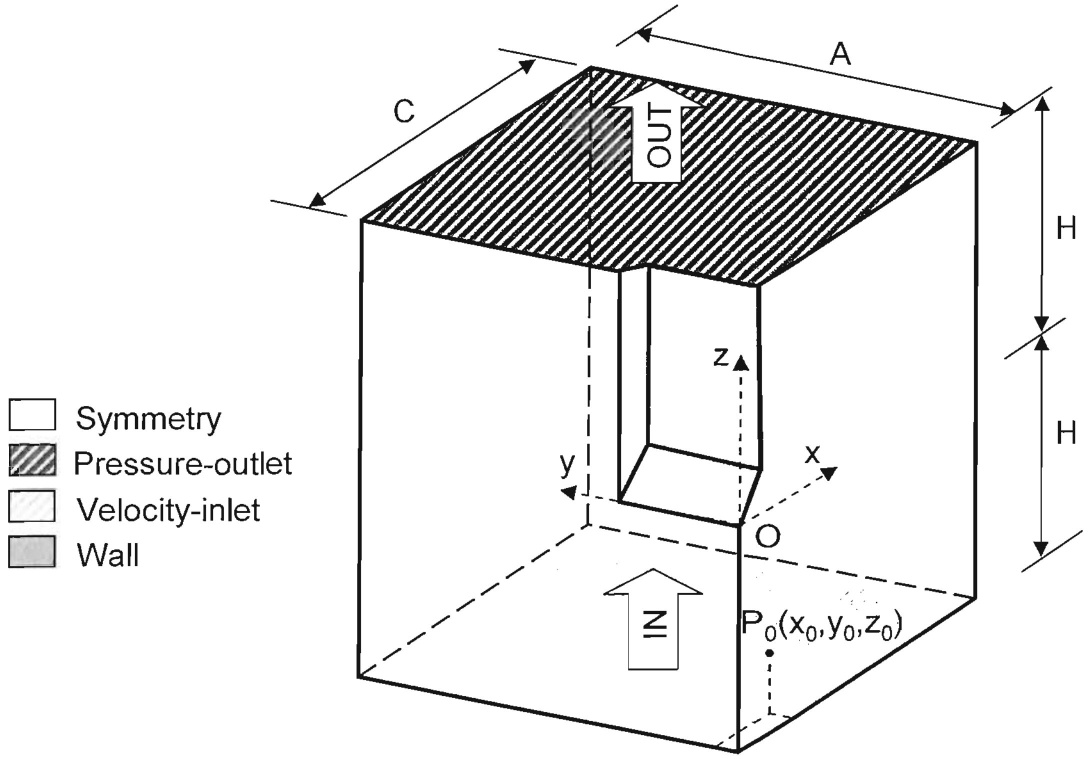

Figure 5-2 Boundary locations and types defined in GAMBIT

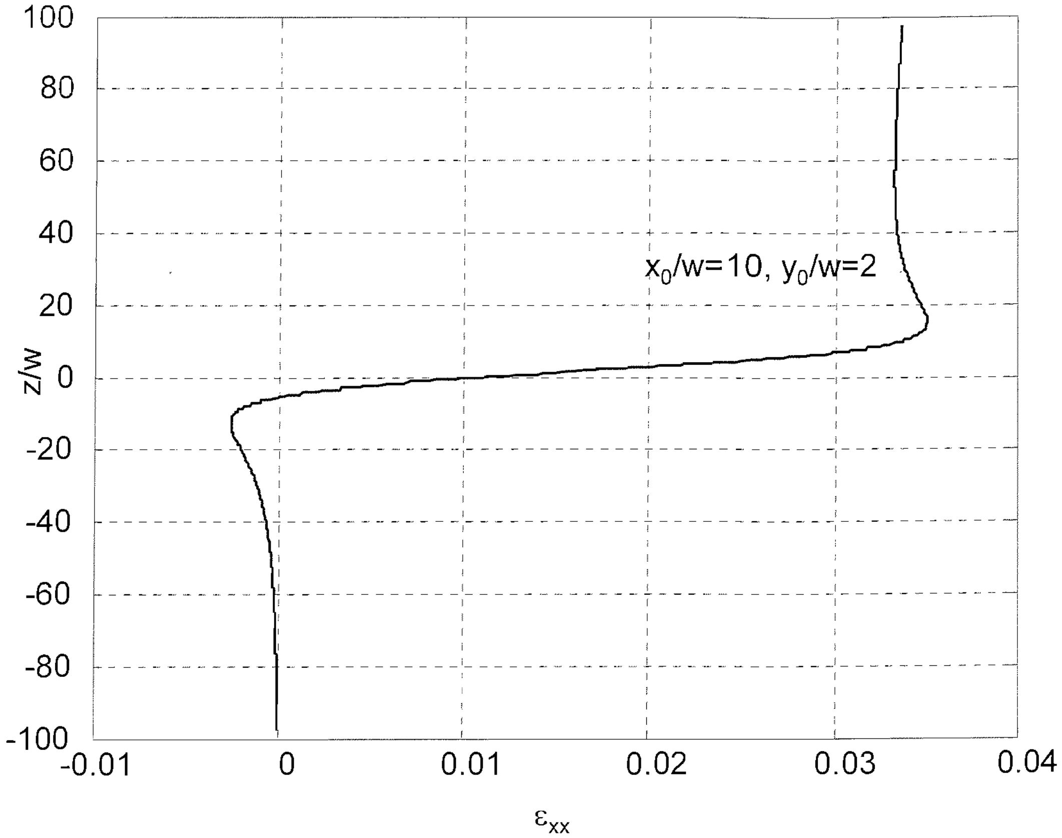

Figure 5-3 Strain path for lateral (ε_{xx}) strain in 3D fluid flow around the "chisel"

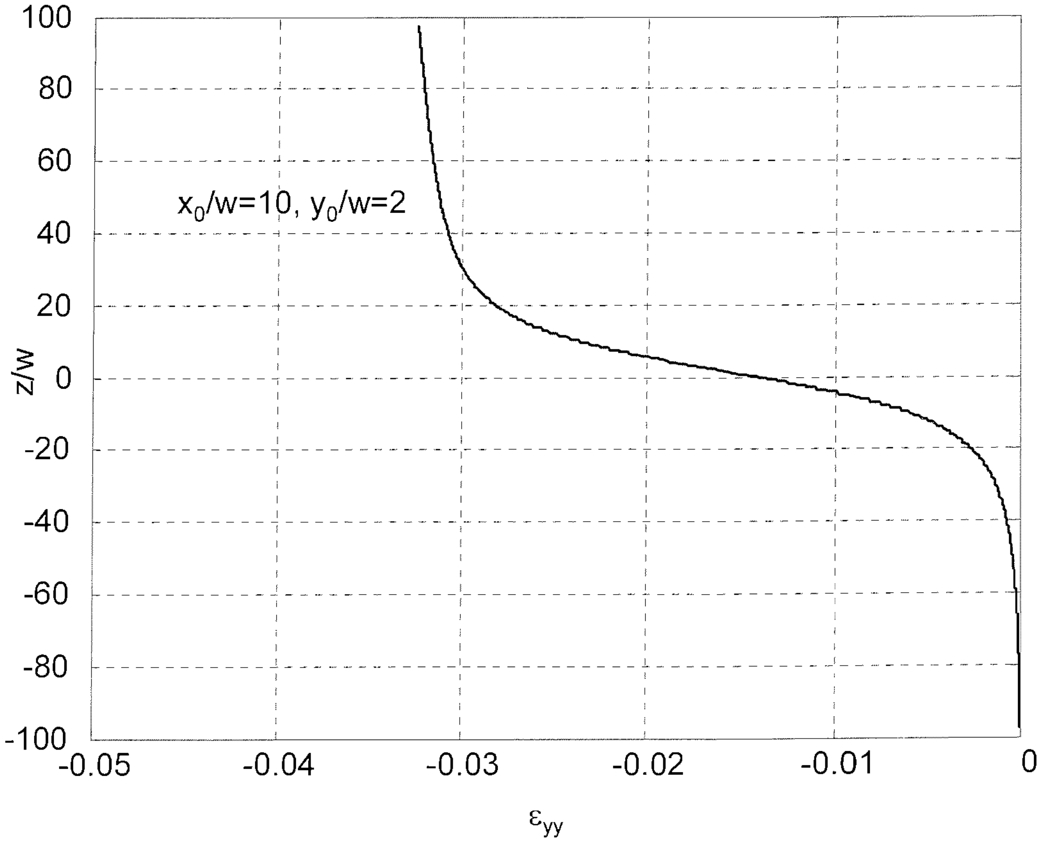

Figure 5-4 Strain path for longitudinal (ε_{yy}) strain in 3D fluid flow around the "chisel"

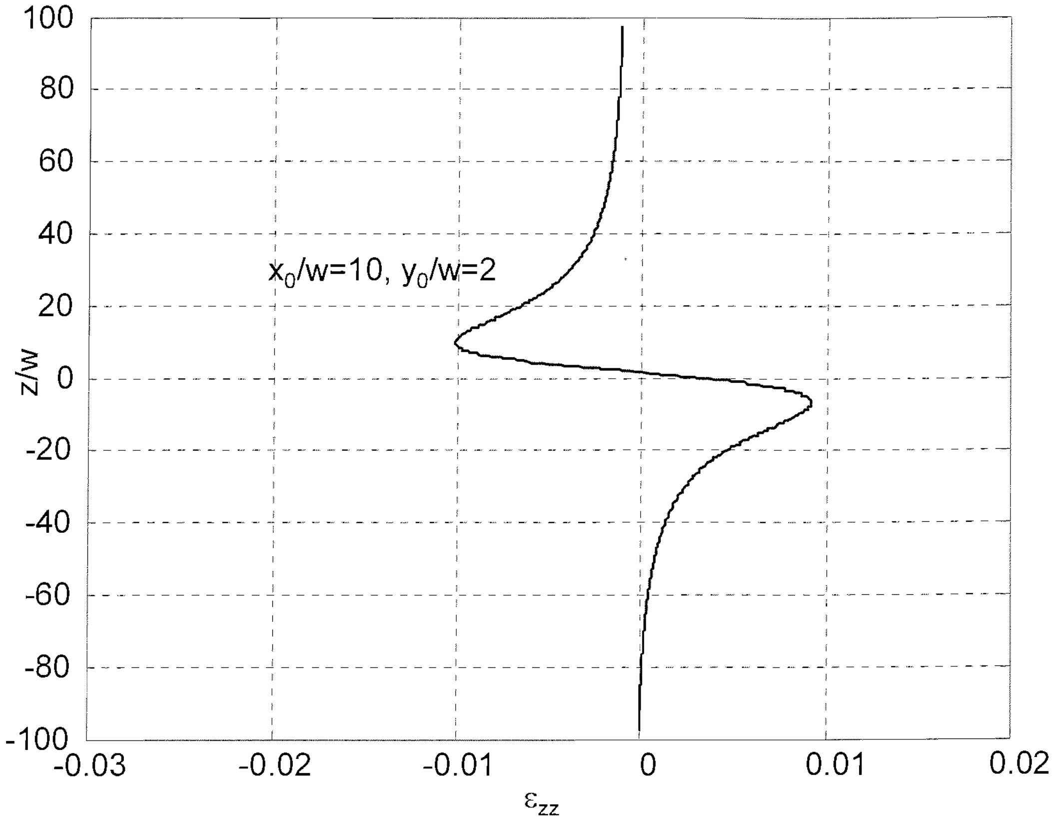

Figure 5-5 Strain path for vertical (ε_{zz}) strain in 3D fluid flow around the "chisel"

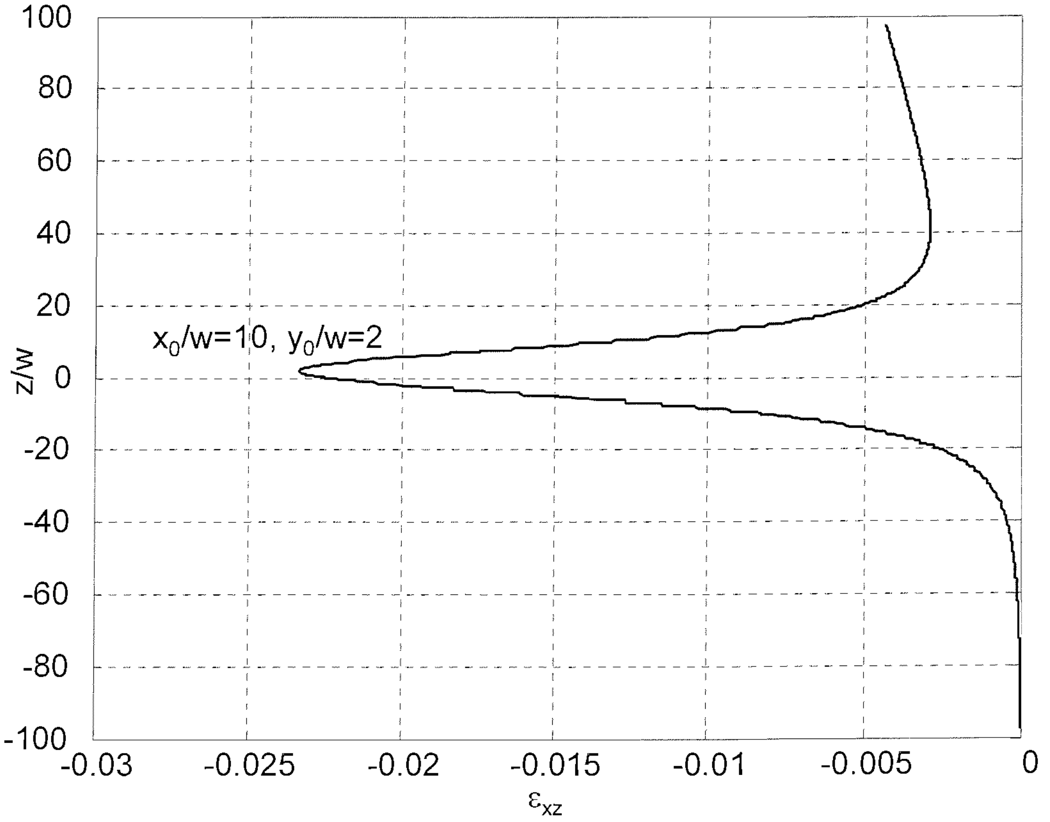

Figure 5-6 Strain path for shear (ε_{xz}) strain in 3D fluid flow around the "chisel"

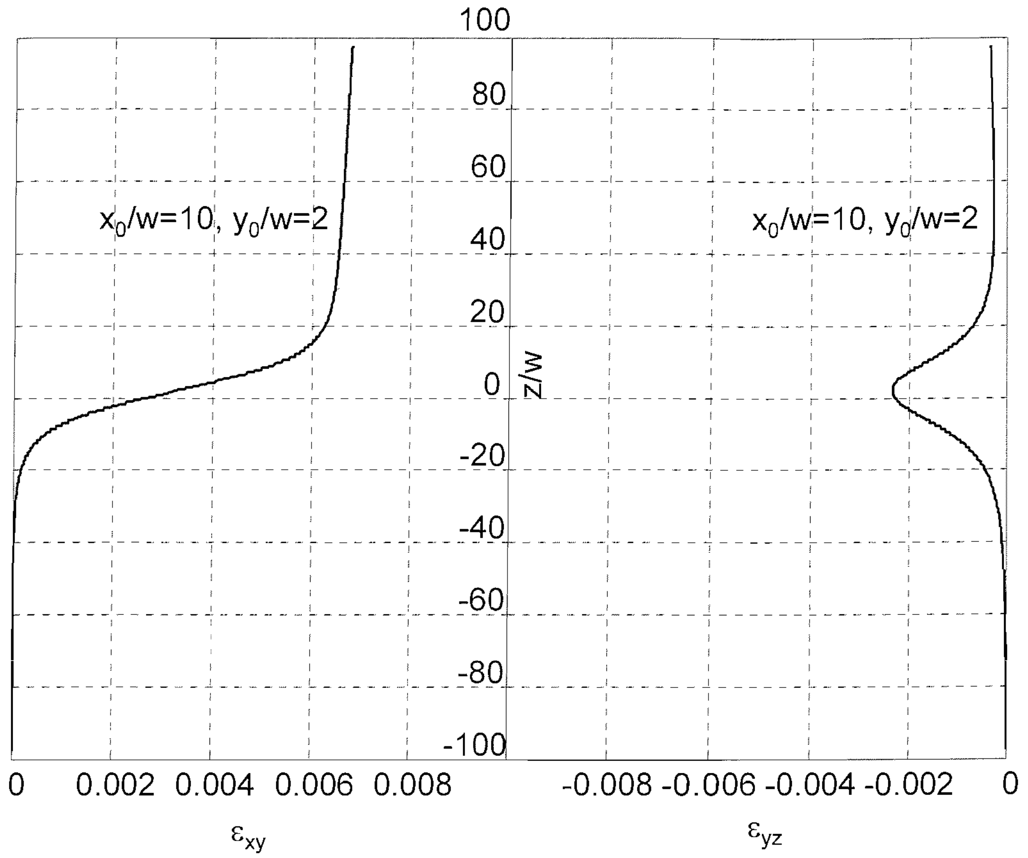

Figure 5-7 Strain path for (ε_{xy}) and (ε_{yz}) shear strains in 3D fluid flow around the "chisel"

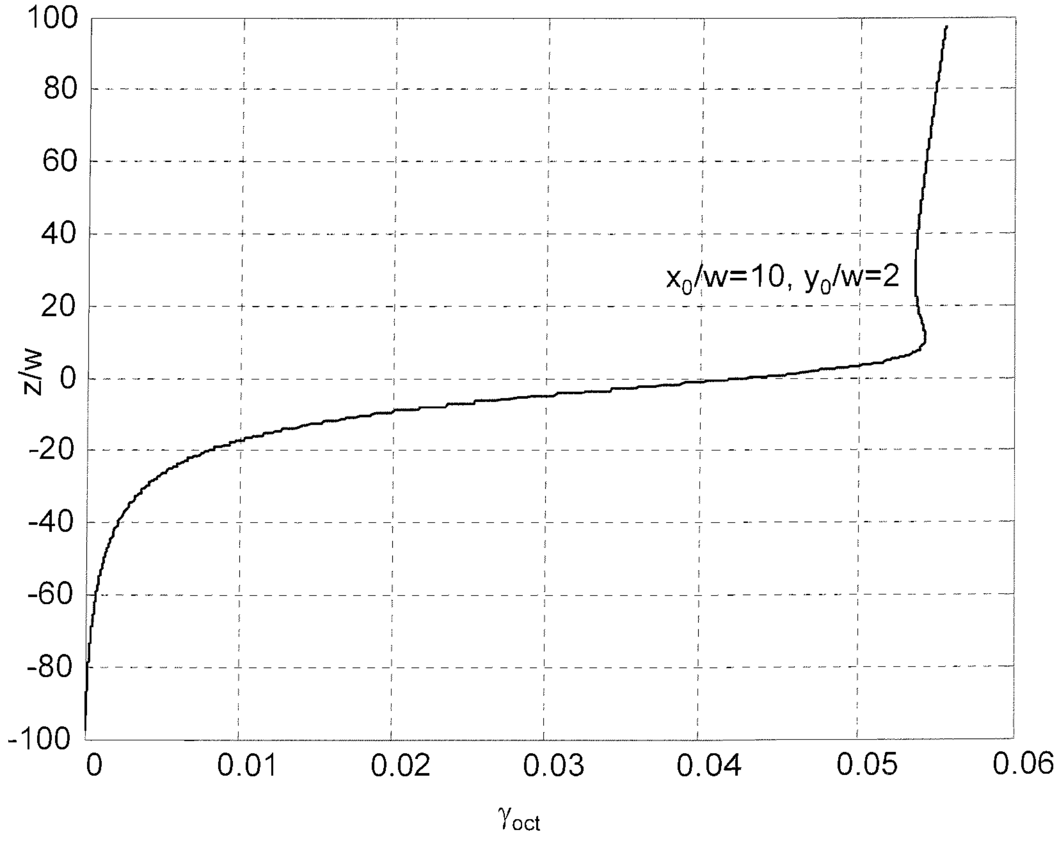

Figure 5-8 Strain path for octahedral (γ_{oct}) strain in 3D fluid flow around the "chisel"

6 THREE DIMENSIONAL SOIL PENETRATION ANALYSIS

6.1 Introduction

It may be argued that conditions close to the centreline of the spade cell during penetration approximate to plane strain. However, in common with many geotechnical problems, the penetration of a spade cell is a three-dimensional problem and if possible, it should be analysed as such. Three-dimensional models were therefore developed in the FLAC^{3D} program to analyse the penetration of an idealised spade cell geometry, termed the "chisel". The 3D soil penetration analyses were validated by comparing the strain paths determined from them with the 3D fluid flow results (Chapter 5). The influence of the undrained shear strength (S_u) and shear modulus (G) of soil, the adhesion of the interface (α), the aspect ratio of the "chisel" (B/w) and the boundary types (i.e. stress or displacement controlled) were investigated through a series of analyses. This chapter presents the methodology adopted for the 3D soil penetration analyses as well as the results obtained from them.

6.2 Model description

Effective stress formulations (refer to section 2.7.2) were employed in the three-dimensional analyses. Various aspects of 3D soil penetration models are discussed in the following sections.

6.2.1 Grid geometry and interfaces

Grid generation in FLAC^{3D} is a challenging process. Primitive grid shapes (e.g. bricks, wedges or tetrahedrons) from the in-built FLAC^{3D} mesh library are deformed and attached together to generate a complex geometry. Primitive blocks are automatically attached together when grid points along connecting faces coincide within the defined tolerance. Alternatively the **ATTACH** command can be used to connect faces with different zone sizes. The **ATTACH** command may introduce discontinuities in stress and displacement distributions and its influence on the calculations should be checked accordingly (Itasca, 2002a).

The symmetry of the penetration problem allowed the analysis to be performed for a quarter of the problem geometry. The geometry of the model consisted of three sub-grids, the CHISEL (1 primitive block), SOIL (24 primitive blocks) and MIRROR (1 primitive block) as shown in Figure 6.1. The CHISEL sub-grid represented the idealised three-dimensional spade cell geometry, the "chisel", the shape of which was illustrated in Figure 5.1. Although the flexibility of the spade cell influences the over-read values (Tory and Sparrow, 1967), the effects are relatively insignificant provided the ratio of cell to soil modulus is greater than 10 (Peattie and Sparrow, 1954). For the values of moduli used in these analyses and with the computational resources available, it was considered acceptable to model the spade cell as a solid body rather than a diaphragm. The SOIL sub-grid, which accommodated the CHISEL, consisted of a fine INNER_SOIL sub-grid attached to a coarse OUTER_SOIL sub-grid. The locations of **ATTACH**ed faces between the fine and coarse meshes are shown in Figure 6.1. The MIRROR was an auxiliary L-shaped sub-grid used to define boundary conditions on the two planes of symmetry. The sub-grids must be defined separated (rather than connected) prior to defining the interfaces between them. As a result, the CHISEL, SOIL and MIRROR sub-grids were initially defined with gaps in the z direction between them, as shown in Figure 6.1.

The mesh density in the SOIL sub-grid was increased gradually towards the location of the CHISEL tip. A fine mesh was also used at the surface of the SOIL sub-grid, as this area experienced high distortions during the penetration. The meshing strategy adopted in the 3D soil penetration models for various sub-grids is illustrated in Figure 6.2.

Interface elements were used to model the penetration of the CHISEL. As discussed in section 2.7.3, interfaces are one-sided elements in FLAC^{3D}. The smooth sliding of SOIL on the MIRROR sub-grid was simulated by defining interfaces 1 and 2 on the MIRROR, which had only a normal stiffness (k_n) assigned to them. Values of stiffnesses were calculated internally (by a FISH script) according to the FLAC^{3D} guidelines (refer to section 2.7.3). The SOIL-CHISEL interaction was simulated by defining interfaces 3, 4 and 5 on the CHISEL as shown in Figure 6.1. In the non-adhesive analyses, a normal stiffness (k_n) was only assigned to the SOIL-CHISEL interfaces. In the adhesive analyses, in addition to the normal stiffness, the shear stiffness (k_s) and the adhesion (C_{int}) were defined for the SOIL-CHISEL interfaces.

6.2.2 Boundary conditions and initial loading

Various boundary conditions were assigned to grid points on the external boundaries in three-dimensional soil penetration models, as shown in Figure 6.3. The velocities of the MIRROR and CHISEL grid points were constrained in all directions (**fix X Y Z**). The SOIL grid points on the z= -H boundary were constrained in the vertical direction (**fix Z**). The SOIL grid points on x=C and y=A boundaries were also constrained in the lateral directions, (**fix X**) and (**fix Y**) respectively. Boundary conditions for SOIL grid points on the axes of symmetries (x=y=0) were controlled by the MIRROR. The MIRROR sub-grid did not allow the SOIL grid points to move inside the axes of symmetry; however, as penetration took place (i.e. the CHISEL moved downward) the SOIL grid points were allowed to move in all other directions.

The initial loading and stress conditions defined for the 3D models were similar to those adopted for the 2D soil penetration analyses. An initial surface load of 150kPa was assigned to the upper boundary of the SOIL sub-grid as shown in Figure 6.3. Isotropic in-situ stress condition, with stress values equal to the surface load, was defined for the models to reduce the equilibrium time prior to the penetration phase of the analyses.

6.2.3 Constitutive model and material properties

In-built elastic and Tresca constitutive models were used for the CHISEL and SOIL sub-grids respectively. As analyses were under the no-gravity condition, it was not necessary to define mass densities for any of the sub-grids. Other material properties specified for sub-grids are reviewed below.

The values of shear (G) and bulk (K) moduli for the CHISEL sub-grid, were calculated internally (by a FISH script) from the specified Young's modulus and Poisson's ratio. The apparent modulus of the spade cell determined from LVDT (Linear Variable Differential Transformer) measurements was E_c=4.55GPa (Heymann, 2004). The Poisson's ratio of the CHISEL was assumed to be equal to that of steel (μ_c=0.33). For simplicity, the properties of the MIRROR sub-grid were set to those used for the CHISEL since the MIRROR only provided a boundary condition and its properties did not therefore influence the behaviour of soil.

In the coupled analyses, dry/drained soil properties as well as water properties must be defined (refer to section 2.7.2). The incompressible behaviour of the saturated cohesive soil was simulated by using a Poisson's ratio of μ_s=0.499 for the SOIL sub-grid. The SOIL sub-grid had a shear modulus of G=1MPa, a drained bulk modulus of K=2MPa, and an undrained shear strength of S_u=100kPa (consequently the rigidity index was $I_r=G/S_u$=10). The bulk modulus of water was K_w=2GPa (Itasca, 2002a). In contrast to the shear modulus, which is independent from the water properties (Berryman, 2004), other SOIL properties were internally calculated by the FLAC code depending on the drainage conditions defined on the external boundaries.

6.2.4 Penetration simulation and analysis methodology

Penetration was simulated by assigning a constant vertical velocity (U=0.0012mm/sec) to the CHISEL sub-grid. The model was then stepped through the analysis until the intended length of penetration was reached (length=velocity×time). The outputs of the FLAC^{3D} model were saved at various stages of penetration, for subsequent processing. At the end of the penetration process, the models were allowed to equilibrate. The equilibrium was assumed to be the state at which the "maximum unbalanced force ratio" (refer to section 2.7.1) in the model became less than 1×10^{-4}.

The methodology for the 3D soil penetration analyses was similar to that used in the 2D models (refer to section 4.2.4). Shape functions (Zienkiewicz, 1986) were used to calculate strain increments (within MATLAB) from changes in the element positions between successive stages of the penetration. The strain paths obtained from the soil penetration analyses (FLAC^{3D}) were compared with those derived from the 3D fluid flow analyses (FLUENT), presented in the previous chapter. The influences of various parameters on the stress-strain behaviour of soil were then evaluated in the 3D soil penetration models and are presented in the next section.

6.3 Results

Three-dimensional analyses are extremely time-consuming and computationally demanding. Consequently, the selection of the modelling/geometrical parameters was based on the outcomes of the two-dimensional analyses. The penetration rate (U) and interface stiffness (k_n) were set to values derived from the in section 4.4.1. As the boundary locations would be expected to have a less significant effect on the results of the 3D analyses, the selected boundary locations in the 2D analyses (refer to section 4.4.2) were adopted for the 3D models. The penetration length (L) was also similar to that used for the 2D analyses. The modelling/geometrical parameters used in 3D soil penetration analyses are as follows:

Penetration rate (U)	0.0012mm/sec
Interface stiffness (k_n)	10 times zone stiffness (refer to section 2.7.3)

• Upper/Lower boundaries (H)	630mm(150w)
• Lateral boundaries (A=C)	420mm(100w)
• Penetration length (L)	806.4mm(192w)

The "chisel" had a half-width of w=4.2mm and its tip was located at z=+L/2=96w above the origin at the start of penetration (i.e. tip was at H-L/2=54w below the soil surface), as shown in Figure 6.3. The influence of the following parameters on the behaviour of soil during penetration were investigated in three-dimensional penetration models:

- Soil undrained shear strength (S_u) and shear modulus (G);
- Interface adhesion factor (α);
- Aspect ratio of the "chisel" horizontal cross section (B/w); and
- Boundary types (stress or displacement controlled)

The values of S_u, G, α and B/w in various 3D soil penetration models are listed in Table 6.1. The soil behaviour during penetration was assessed by evaluating four types of outputs: strain paths, stress profiles, stress histories and the over-read plots. Figure 6.4 shows the convention used in the 3D analyses for positive stress-strain. The information derived from these outputs and their significance are explained here.

Strain paths

The strain path is a graphical means for highlighting changes in the soil strain levels during the penetration process. A strain path shows the cumulative strain increments ($\varepsilon=\sum\varepsilon_{inc}$) plotted for a particular soil element against its relative vertical position (relative to the position of the penetrating "chisel" tip) and normalised by the half-width of the "chisel" (z/w). Strain paths were presented for an element located at $P_0(x_0=10w, y_0=2w, z_0=0)$ at the start of penetration, as shown in Figure 6.3. Although P_0 should have been chosen on the "chisel" plane of symmetry (y=0), in order to evade the artefacts of the interface, P_0 was offset 2w from the centreline ($y_0=2w$). Figures illustrated in this chapter show the strain paths determined from the soil penetration analyses (outlined in section 6.2.4) as well as the strain paths determined from the fluid flow analyses (refer to section 5.4). The strain paths determined from the soil penetration models had a general pattern that could be described with reference to the results of the MAIN model (refer to Table 6.1). The strain path for the lateral (ε_{xx}) strain shows an initial extensive behaviour with minimum strain levels reached at z/w= -10, as shown in Figure 6.5. The change in lateral strains became compressive from this point onwards with the maximum compressive strain occurring at z/w=10. This peak compressive strain was greater than the peak extensive strain. The lateral strain decreased (still in compression) for a short length of the path (i.e. up to z/w=20) and remained relatively constant from this point onwards.

The strain path for the longitudinal (ε_{yy}) strain was extensive with minimum strain values occurring at z/w=10, as shown in Figure 6.6. The longitudinal strain declined slightly from this point until the z/w=40 level, and it became relatively constant afterwards.

The strain path for the vertical (ε_{zz}) strain consisted of three sections, an initial compression section with its peak at z/w= -10, an extension section with its peak at z/w=10 and finally a recompression section, as shown in Figure 6.7. It should be noted that at the end of penetration, the vertical (ε_{zz}) strain returned to zero, while the soil element attained compressive lateral (ε_{xx}) and extensive longitudinal (ε_{yy}) strains that balanced each other out.

The strain paths for the shear (ε_{xz}) and octahedral (γ_{oct}) strains are shown in Figures 6.8 and 6.9 respectively. Shear and octahedral strains increased as penetration continued, reaching their peak values at levels just above the tip (z/w=0). The shear strains decreased from the tip level up to the z/w=20 level, and remained relatively constant afterwards.

The shape of strain paths determined from soil penetration analyses (Figures 6.5-6.9 inclusive) were similar to those determined from the fluid flow analyses (Figures 5.3-5.8 inclusive). However, the peak strain values determined from the penetration analyses were usually higher than those determined from the fluid flow.

Stress profiles

FLAC^{3D} stores the value of various node and zone properties (e.g. velocities, strains and stresses) at prescribed stages of iteration. Although FLAC^{3D} is capable of illustrating the distribution of most of these properties as contour plots, quantitative comparison of contours, especially for a three-dimensional problem, is difficult. Consequently, the stress profiles, which show the spatial distribution of stresses in the x, y and z directions, were used to evaluate the induced stresses in various three-dimensional soil penetration models. FLAC^{3D} calculates and stores the stress values at the zone centroids. The inverse-distance law was used to interpolate the stress values at equally spaced points along any line (profile) from the stored data. The stress distributions were determined along three profiles (Figure 6.4) for the equilibrated model (unbalanced force ratio$<1\times10^{-4}$) at the end of the penetration phase (i.e. "chisel" tip at z= -96w):

- x-profile (normal to the "chisel" face) x=[0, C], y=5w , z= -70w
- y-profile (along the "chisel" face) x=5w , y=[0, 100w], z= -70w
- z-profile (in the direction of penetration) x=5w , y=5w , z=[-150w, 150w]

Similar to the strain paths, the general shapes of these profiles are described with reference to the results of the MAIN model. The horizontal stress (σ_{xx}) profiles in x, y and z directions are shown in Figures 6.10, 6.11 and 6.12 respectively. It can be seen that the horizontal stresses, which were higher than the initial in-situ stress (σ_{xx0}), decreased along the x-profile with distance from the "chisel" face. The y-profile shows that while the horizontal stresses were higher than σ_{xx0} along the "chisel" face (y/w<B/w), they were reduced to values less than σ_{xx0} at the "chisel" edge (y/w=B/w). Horizontal stresses returned to σ_{xx0} at some distance (aw) away from the "chisel" edge (y/w=a+B/w). In contrast to pile penetrations, where the "locked-in" horizontal stresses were only apparent at the tip level (Lehane *et al.*, 1993; Leung *et al.*, 1996; Klotz and Coop, 2001), horizontal stresses were higher than the σ_{xx0} on the entire penetration path of the "chisel" (-96<z/w<96) in the z-profile. However, the horizontal stresses were lower than the σ_{xx0} for a short length of the z-profile above and below the levels corresponding to the initial and final tip positions.

The shear stress (σ_{xz}) profiles in the y and z directions are illustrated in Figures 6.13 and 6.14 respectively. The y-profile shows that shear stresses returned to zero at some distance away from the "chisel" centreline. Common features of the z-profile for (σ_{xz}) were negative shears at the level corresponding to the initial position of the tip (z/w=96) and a change in the shear direction at the final position of the tip (z/w= -96).

Stress histories and over-read plots

The stress histories illustrate the changes that occur in the horizontal (σ_{xx}), vertical (σ_{zz}) and shear (σ_{xz}) stresses at various stages of the penetration. The inverse-distance law was used to determine and record the magnitude of stresses (σ_{xx}, σ_{zz}, σ_{xz}) for a point located on the centreline of the "chisel" face and 100mm above its tip in the z-direction during successive stages of the penetration.

Over-read plots show the trend between the change in the value of an individual parameter (e.g. undrained shear strength, shear modulus and interface adhesion) and the normalised horizontal stress change (β) recorded for a soil element located on the centreline of the "chisel" face and 100mm above its tip. The normalised horizontal stress change (β) was defined as the change in the horizontal stress ($\Delta\sigma_{xx}$), normalised by the initial horizontal stress (σ_{xx0}) value, $\beta=\Delta\sigma_{xx0}/\sigma_{xx0}$.

The fluctuations observed in stress profiles and histories were thought to be caused by numerical modelling effects (Susila and Hryciw, 2003). A smoother plot would be generated by increasing the mesh density adopted for the 3D soil penetration analyses. However, the computational resources required would be significantly higher and the time taken would become considerably longer. It should be noted that it took approximately a month to complete each of the analyses detailed in Table 6.1 (each model had approximately 30,000 zones) on a Dual AMD 64bit Athlon 2.41GHz workstation with 1GB of RAM. The existing profiles and history plots were generated from the data stored for 100 successive saved stages, where the size of each of the saved files was around 250MB.

6.3.1 Influence of soil parameters

The influence of an increase in the rigidity index (I_r=G/S_u) on the stresses and strains induced in the soil was investigated by reducing the undrained shear strength (S_u) and increasing the shear modulus (G) of soil independently.

The strain paths for the lateral (ε_{xx}), longitudinal (ε_{yy})and vertical (ε_{zz})strains are shown in Figures 6.5, 6.6 and 6.7 respectively for models with various undrained shear strengths (S_u=25, 50, 75 and 100kPa) and a constant shear modulus (G=1MPa). It can be seen that while strain paths for normal strains (ε_{xx}, ε_{yy} and ε_{zz}) were relatively insensitive to the S_u beneath the "chisel" tip, normal strains were slightly higher for a higher rigidity index (i.e. lower S_u) as the soil element passed the tip level (0<z/w<20).

The strain paths for the shear (ε_{xz}) and octahedral (γ_{oct}) strains determined for models with various undrained shear strength (S_u) values are shown in Figures 6.8 and 6.9 respectively. In common with the normal strains, these strain paths were also insensitive to the value of S_u beneath the tip (z/w<0). However, shear and octahedral strain levels were higher for a higher rigidity index (i.e. lower S_u) on the second half of the strain path (z/w>0).

The horizontal stress (σ_{xx}) profiles in the x, y and z directions are shown in Figures 6.10, 6.11 and 6.12 respectively. Soil elements had a higher horizontal stress in models where a higher undrained shear strength (S_u) was assigned to the soil. In the x-direction, horizontal stresses became insensitive to variations in S_u at x/w>60 and yielded to a final value of 155kPa (the initial in-situ stress (σ_{xx0}) was 150kPa), as shown in Figure 6.10. Although horizontal stresses did not return to σ_{xx0} on the x=C boundary, the penetration induced stresses were unaffected by the boundary location near the "chisel" face (x=w). The horizontal stress profile in the y-direction confirms that higher stress levels existed for a model with higher S_u (Figure 6.11). The horizontal stresses however, returned to the σ_{xx0} level at y/w>60. The z-profile also indicates that on the penetration path (-96<z/w<96), the recorded horizontal stresses increased with increasing the undrained shear strength (S_u) of the soil, as illustrated in Figure 6.12.

The shear stress (σ_{xz}) profiles in the y and z directions are shown in Figures 6.13 and 6.14 respectively. There was no evident trend between the shear stress and the undrained shear strength (S_u) of soil in these profiles. Shear stresses were relatively low (σ_{xz}<10kPa) in the y-profile and returned to zero at y/w>40, as shown in Figure 6.13. Figure 6.14 shows that although higher shear stresses were recorded for models with a higher S_u at the levels corresponding to the initial and final position of the tip, the shear stresses were close to zero on the penetration path (-96<z/w<96).

Figure 6.15 shows the history of horizontal (σ_{xx}), vertical (σ_{zz}) and shear (σ_{xz}) stresses at various penetration stages for models with undrained shear strengths of S_u=25 and 100kPa. It can be seen that the horizontal and vertical stresses were higher for models with a higher S_u. The shear stress, however, was insensitive to the value of soil undrained shear strength (S_u). The over-read plot also illustrates that the normalised horizontal stress change (β) increased with increasing S_u, as shown in Figure 6.16.

The influence of increasing the soil rigidity index (I_r) was also evaluated by keeping the undrained shear strength constant (S_u=100kPa) and increasing the shear modulus of the soil in various models (G=1, 2, 4 and 8MPa). The strain paths for normal strains (ε_{xx}, ε_{yy} and ε_{zz}) are shown in Figures 6.17, 6.18 and 6.19 respectively. Strain paths for normal strains were relatively insensitive to the G values beneath the tip level. However, it can be seen that lateral (ε_{xx}) and longitudinal (ε_{yy}) strains were higher in models with a higher rigidity index (i.e. higher G), as the soil element passed the tip level (z/w>0).

Figures 6.20 and 6.21 illustrate the strain paths for the shear (ε_{xz}) and octahedral (γ_{oct}) strains respectively in models with various shear moduli (G). Similar to the normal strains, the strain paths for these strains were insensitive to the value of the shear modulus (G) beneath the tip (z/w<0). However, higher strain levels are observed for models with a higher rigidity index (i.e. higher G) as the tip of the penetrating "chisel" passed the soil element level.

The horizontal stress (σ_{xx}) profiles in x, y and z directions were also investigated for models with various shear modulus values (G). A higher horizontal stress was encountered in the x-profile for models with a higher G, as shown in Figure 6.22. Although the trend between the horizontal stress and the G was not clear along the "chisel" face (y/w<12), it is evident that horizontal stresses were higher for models with a higher G on the 12<y/w<20 section of the y-profile (Figure 6.23). Horizontal stresses returned to the initial in-situ stress value (σ_{xx0}) at y/w>80. In the z-profile also, horizontal stresses on the penetration path increased with an increase of the soil shear modulus (G), as shown in Figure 6.24.

Figures 6.25 and 6.26 show the shear stress (σ_{xz}) profiles in the y and z directions respectively. There was no evident trend between the shear stresses and the soil shear moduli (G) in these profiles. As shown in Figure 6.25, shear stresses returned to zero at y/w>80. The shear stresses in the z-profile were also close to zero on the penetration path (-96<z/w<96), as illustrated in Figure 6.26.

The history of σ_{xx}, σ_{zz} and σ_{xz} stresses on the face of "chisel" for models with shear modulus values of G=1 and 8MPa is shown in Figure 6.27. It can be seen that the horizontal (σ_{xx}) and vertical (σ_{zz}) stresses were higher for models with a higher shear modulus (G) during the whole penetration process. However, shear (σ_{xz}) stresses were higher for a model with a higher shear modulus only on the z/w<35 section of the history plot. The normalised horizontal stress change (β) plotted against the shear modulus (G) values also indicates that the penetration-induced horizontal stresses for the soil element adjacent to the "chisel" face were higher for soils with a higher shear modulus (G), as illustrated in Figure 6.28.

6.3.2 Influence of interface adhesion

Two-dimensional penetration analyses have confirmed that the interface adhesion factor (α) played a significant role in the stress-strain response of a soil as a solid object was penetrated into it (Chapter 4). The stress-strain behaviour of soil during penetration was examined in the three-dimensional penetration models where a range of adhesion values were assigned to the CHISEL-SOIL interface (α=0, 0.25, 0.5 and 0.75).

The strain path for lateral (ε_{xx}) strain was insensitive to the value of interface adhesion factor (α), as shown in Figure 6.29. Although the strain paths for longitudinal (ε_{yy}) and vertical (ε_{zz}) strains were not influenced by the value of α below the tip level (z/w<0), it can be seen that higher strain levels existed for models with a higher α above the tip (Figures 6.30 and 6.31). Differences between longitudinal (ε_{yy}) strain values determined in models with various α reduced from its peak at z/w=20 towards the end of the strain path (z/w=96). A similar pattern of strain reduction is observed in strain paths for the vertical (ε_{zz}) strain and between z/w=20 and z/w=96 levels.

The strain paths for the shear (ε_{xz}) and octahedral (γ_{oct}) strains are shown for models with various adhesion factors (α) in Figures 6.32 and 6.33 respectively. Strain levels increased for a higher α as the tip of the penetrating "chisel" passed the soil element (z/w>0). In contrast to the model response to changes in S_u and G, the divergence between the shear strain paths as a result of a higher interface adhesion (α) increased from z/w=20 until the end of the strain path (z/w=96), as shown in Figure 6.32.

The horizontal stress (σ_{xx}) profiles in x, y and z directions were also evaluated for models with various interface adhesion factors (α). Horizontal stresses increased with increasing the adhesion factors (α) in all directions. Figure 6.34 illustrates that the difference between horizontal stresses due to various α values remained relatively uniform for the whole length of the x-profile. The horizontal stress profile in the y-direction also shows that higher stress levels existed in models with a higher adhesion (Figure 6.35). The differences between horizontal stress profiles determined from models with various α values became relatively constant at y/w>30. Figure 6.36 shows the horizontal stress distribution along the z-profile. Higher stress levels were observed for models with a higher α above the initial position of the tip (z/w>96) and on the z/w< -50 section of the z-profile.

The shear stress (σ_{xz}) profiles in the y and z directions are shown in Figures 6.37 and 6.38 respectively. These profiles show an increase in the value of shear stress by increasing the interface adhesion factor (α). In the y-direction, shear stresses returned to zero at y/w>30, as illustrated in Figure 6.37. Figure 6.38 also shows that shear stresses were higher for models with a higher α on the z- profile between the free surface and the final position of the tip (z/w> -96).

The influence of interface adhesion was also investigated by comparing the stress (σ_{xx}, σ_{zz} and σ_{xz}) histories for models with smooth (α=0) and rough (α=0.75) interfaces. As shown in Figure 6.39, the increases in lateral (σ_{xx}) and vertical (σ_{zz}) stresses as a result of increasing α were relatively insignificant. In contrast to the normal stresses, the shear (σ_{xz}) stresses in the adhesive model (α=0.75) were higher than those determined from the non-adhesive model (α=0). The normalised horizontal stress change (β) plotted for various α values also indicates an increase in the horizontal stress as a result of increasing α, as presented in Figure 6.40.

The principal stress indicators at the end of penetration are shown on two cross-section planes, x=5w (Figure 6.41) and y=5w (Figure 6.42). It is can be seen that in both the x and y cross-sections, principal stress indicators adjacent to the "chisel" were severely affected by introducing adhesion to the interface.

6.3.3 Influence of aspect ratio

The geometry of a range of in-situ measurement devices commonly used in geotechnical engineering including spade cells, can be represented as a flat blade with various aspect ratios (Table 6.2). The influence of the horizontal cross-section aspect ratio (B/w) on the stress-strain response of the soil adjacent to the penetrating object was examined by analysing the penetration of three "chisel" geometries with aspect ratios of B/w=6 (dilatometer), 12 and 24 (earth pressure cell).

Figures 6.43, 6.44 and 6.45 show the strain paths for normal strains (ε_{xx}, ε_{yy} and ε_{zz}) around these three "chisel" geometries. The lateral (ε_{xx}), longitudinal (ε_{yy}) and vertical (ε_{zz}) strains for the soil element were lower in models where the "chisel" had a higher aspect ratio (B/w). In contrast to the vertical (ε_{zz}) strain (Figure 6.45), the strain changes due to a variation in (B/w) were significant for lateral and longitudinal strains, shown in Figures 6.43 and 6.44 respectively.

The strain paths for the shear (ε_{xz}) and octahedral (γ_{oct}) strains for models with various aspect ratios (B/w) are shown in Figures 6.46 and 6.47 respectively. Strain paths for shear (ε_{xz}) strain show that the peak strains were lower in the models where the "chisel" had a higher aspect ratio (Figure 6.46). The differences between shear strains were, however, relatively insignificant at the end of the penetration path. Figure 6.47 also shows that above the tip (z/w>0), octahedral strains were higher in models with a lower aspect ratio.

Figure 6.48 shows the x-profile of horizontal stresses (σ_{xx}) for the three examined "chisel" geometries. It is evident that horizontal stresses were higher for the "chisel" with a higher aspect ratio at x/w>20. The differences between horizontal stresses; however, reduced with the distance from the "chisel" face.

The y-profile for horizontal (σ_{xx}) stresses is illustrated in Figure 6.49. Three sections of stress change were evident in the y-profile: compression (y/w<B/w-6), extension (B/w-6<y/w<B/w+3) and recompression (y/w>B/w+3). Horizontal stresses ($\sigma_{xx}>\sigma_{xx0}$) increased from the "chisel" centreline (y/w=0) until they reached their maximum values at 6w before the "chisel" edge. Horizontal stresses reduced from this point onwards and finally reached their minimum value at 3w after the "chisel" edge. Horizontal stresses increased and returned to σ_{xx0} irrespective of the "chisel" aspect ratio at y/w>60. It should be noted that along the y-profile and between y/w=20 and y/w=60, the extensive horizontal stresses ($\sigma_{xx}<\sigma_{xx0}$) were lower for "chisel"s with higher aspect ratios.

Figure 6.50 shows the z-profile for horizontal (σ_{xx}) stresses. The horizontal stresses were lower for a "chisel" with a higher aspect ratio (B/w) above and below levels corresponding to the initial and final tip position respectively (z/w>96 and z/w< -96). On the penetration path however, the horizontal stresses for the B/w=12 model was higher than the horizontal stresses for the B/w=6 and 24 models.

As can be seen from the y and z profiles for the shear (σ_{xz}) stress (Figures 6.51 and 6.52), the shear stresses were relatively insensitive to the value of "chisel" aspect ratio (B/w).

6.3.4 Influence of boundary type

Figure 2.4 shows a cross-section of the chamber geometry used for spade cell calibration. The thickness of the soil layer on the face of spade cell was approximately 200mm. Air bags were used to apply the stress changes in a series of chamber tests (Grobbelaar, 2002). One of the hypotheses for no observed over-read in these chamber tests was the use of flexible membrane to maintain the pressure, while in the majority of previous tests, rigid steel plates have been used to apply loads (Voyiadjis *et al.*, 1993; Kurup *et al.*, 1994; Salgado *et al.*, 1998; Hsu and Huang, 1999). In order to simulate the calibration chamber geometry, the width of the model in the x direction was changed to C=210mm(50w), refer to Figure 6.3. The effect of the boundary type was investigated by altering the boundary condition on the x=C boundary from displacement-controlled (constrained in the x direction) to stress-controlled. The boundary stress was equal to the initial in-situ stress (σ_{xx0}) of the soil.

The lateral (ε_{xx}) and longitudinal (ε_{yy}) strains were markedly higher for the displacement-boundary model, above the tip level, as shown in Figures 6.53 and 6.54 respectively. The strain path for vertical (ε_{zz}) strains were however, relatively insensitive to the boundary type (Figure 6.55). The influence of boundary type on the shear (ε_{xz}) strain paths was also relatively insignificant, as shown in Figure 6.56. The strain path for octahedral (γ_{oct}) strain shows that as the soil element passed the "chisel" tip, the overall induced strains were higher for the soil element in the model with a displacement-controlled boundary, as illustrated in Figure 6.57.

The horizontal stress (σ_{xx}) profiles in x, y and z directions are plotted in Figures 6.58, 6.59 and 6.60 respectively. The x-profile, Figure 6.58, shows that the horizontal stresses (σ_{xx}) returned to the initial in-situ stress value (σ_{xx0}) at x/w>40 for the stress-boundary model. However, in the displacement-boundary model, the horizontal stresses (σ_{xx}) were higher than (σ_{xx0}) on the whole length of the x-profile. In the y-profile, the horizontal stresses returned to σ_{xx0} at y/w>60 for the stress-boundary model, while for the displacement-boundary model, the stress levels were higher than σ_{xx0} on the entire length of the profile (Figure 6.59). Horizontal stresses were also higher for the displacement-boundary model in the z-profile, as shown in Figure 6.60.

The influence of the boundary types was also evident in the shear stresses (σ_{xz}) along the y and z profiles, as illustrated in Figures 6.61 and 6.62 respectively. The shear stresses were higher in models with a displacement-boundary; however, the difference between profiles determined for various boundaries became insignificant at y/w>20 and z/w< -70 along the y and z profiles respectively.

6.4 Summary

The three-dimensional undrained penetration of an idealised spade cell geometry, termed the "chisel", into a Tresca soil was simulated using FLAC^{3D}. Because of the significant computational resources required for 3D modelling, optimum modelling (e.g. interface stiffness and penetration rate) and geometrical (e.g. mesh density, boundary locations and penetration length) parameters determined in the 2D analyses were adapted for the 3D models.

The strain paths determined from the fluid flow analyses (Chapter 5) were used to validate the behaviour of soil predicted by a penetration analysis using the FLAC^{3D} program. The patterns of strain paths determined from these two methods were identical; however, the peak strain values determined from the soil penetration analyses were higher than those determined from the fluid flow.

Three-dimensional analyses showed that a number of factors affect the stress-strain behaviour of soil adjacent to the penetrating "chisel". The outcomes of the analyses are summarised below:

- Normal strains (ε_{xx}, ε_{yy} and ε_{zz}) were relatively insensitive to the value of soil undrained shear strength (S_u); however, shear strains (ε_{xz}) were higher for soils with higher rigidity indices (i.e. lower S_u);
- An increase in the shear modulus (G) of the soil (i.e. increase in rigidity index) caused an increase in lateral (ε_{xx}), longitudinal (ε_{yy}) and shear (ε_{xz}) strains, but not in the vertical (ε_{zz}) strain;
- The horizontal stresses measured on the face of the "chisel" increased by an increase in both the shear modulus (G) and the undrained shear strength (S_u) of soil. However, the relative influence of a change in shear modulus was greater than the same magnitude of change in the undrained shear strength;
- The normal strains (ε_{xx}, ε_{yy} and ε_{zz}) at the end of the strain path in models with various interface adhesion factors (α) were in the same range; however, the shear strains (ε_{xz}) were higher in models with a higher (α);
- The horizontal stresses recorded on the face of "chisel" increased almost linearly with increasing the interface adhesion (α);
- Lateral (ε_{xx}) and longitudinal (ε_{yy}) strains at the end of penetration were higher in a model with a lower aspect ratio (B/w); however, the shear (ε_{xz}) and vertical (ε_{zz}) strains appeared to be insensitive to the aspect ratio;
- Horizontal stresses along the face of the "chisel" (y-profile) were higher for models with a lower aspect ratio (B/w);
- At the end of penetration, the horizontal stresses were relatively uniform on the inner-half of the "chisel" face ($y<B/2$);
- The Lateral (ε_{xx}) and longitudinal (ε_{yy}) strains at the end of the penetration were higher in the displacement-boundary model; however, the shear (ε_{xz}) and vertical (ε_{zz}) strains were relatively insensitive to the boundary type; and
- The horizontal stresses recorded on the "chisel" face were lower in the model with a stress-boundary compared to the model with a displacement-boundary.

Table 6-1 Soil and interface parameters used in FLAC^{3D} penetration analyses

Model	Description	Shear modulus G (MPa)	Shear strength S_u (kPa)	Interface adhesion α (C_{int}/S_u)	Aspect ratio (B/w)
MAIN	Main model	1	100	0.00	12
STRE_1	Undrained shear strength	"	25	"	"
STRE_2	Undrained shear strength	"	50	"	"
STRE_3	Undrained shear strength	"	75	"	"
MODU_1	Shear modulus	2	100	"	"
MODU_2	Shear modulus	4	"	"	"
MODU_3	Shear modulus	8	"	"	"
ADHE_1	Interface adhesion	1	100	0.25	"
ADHE_2	Interface adhesion	"	"	0.50	"
ADHE_3	Interface adhesion	"	"	0.75	"
ASP_1	Aspect ratio	"	"	0.00	6
ASP_2	Aspect ratio	"	"	"	24

Table 6-2 Aspect ratio of blades in various devices

Device	B (mm)	w (mm)	Aspect ratio (B/w)
Dilatometer	47.5	7	6.8
Field vane	32.5	1	32.5
Earth pressure cell	150	6	25
Spade cell	50	3.38	14.8
Stepped blade	25.5	1.5, 2.25, 3, 3.75	17, 11.3, 8.5, 6.8

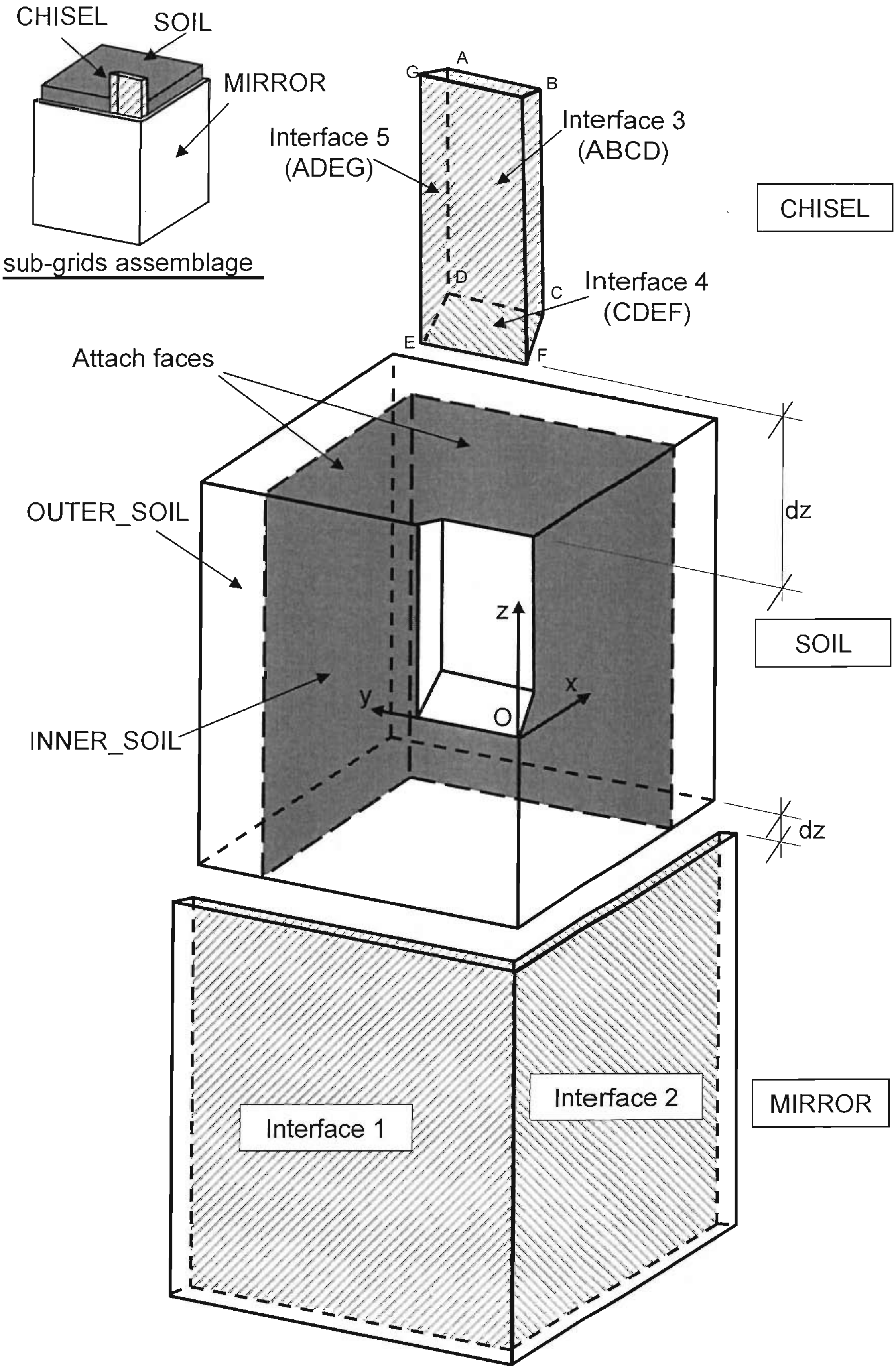

Figure 6-1 Schematic view of sub-grids, attach faces and interface surfaces in FLAC^{3D} models

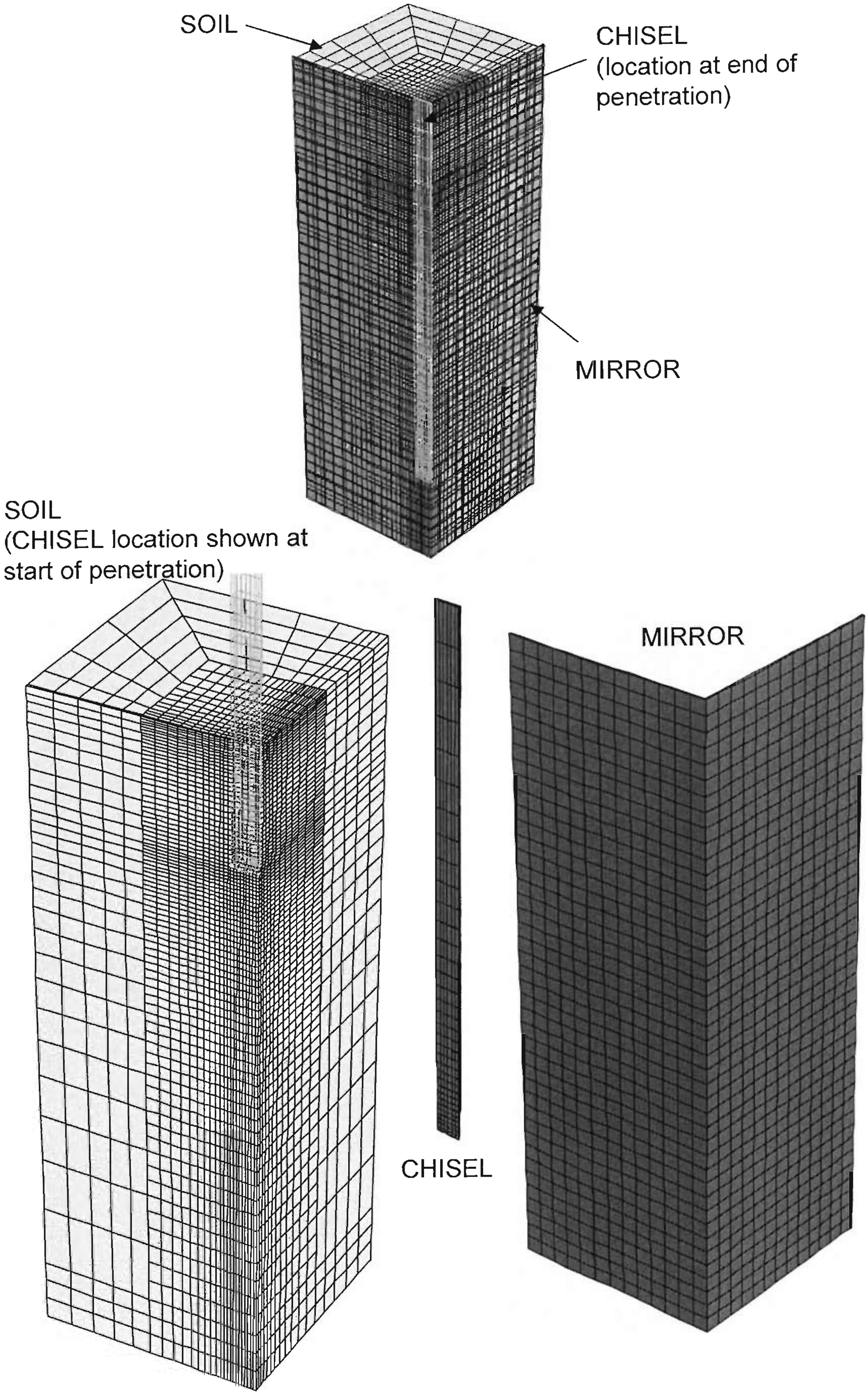

Figure 6-2 Grid density of MIRROR, CHISEL and SOIL sub-grids in FLAC^{3D} models

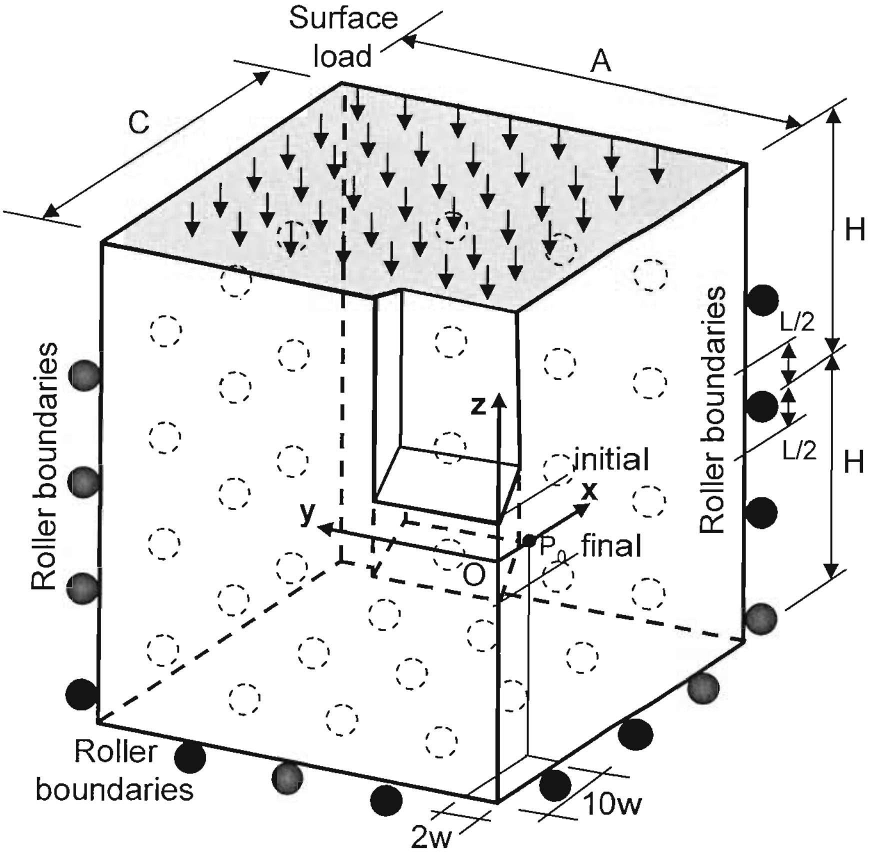

Figure 6-3 Schematic view of boundary conditions and initial loading for SOIL sub-grid in FLAC^{3D} models

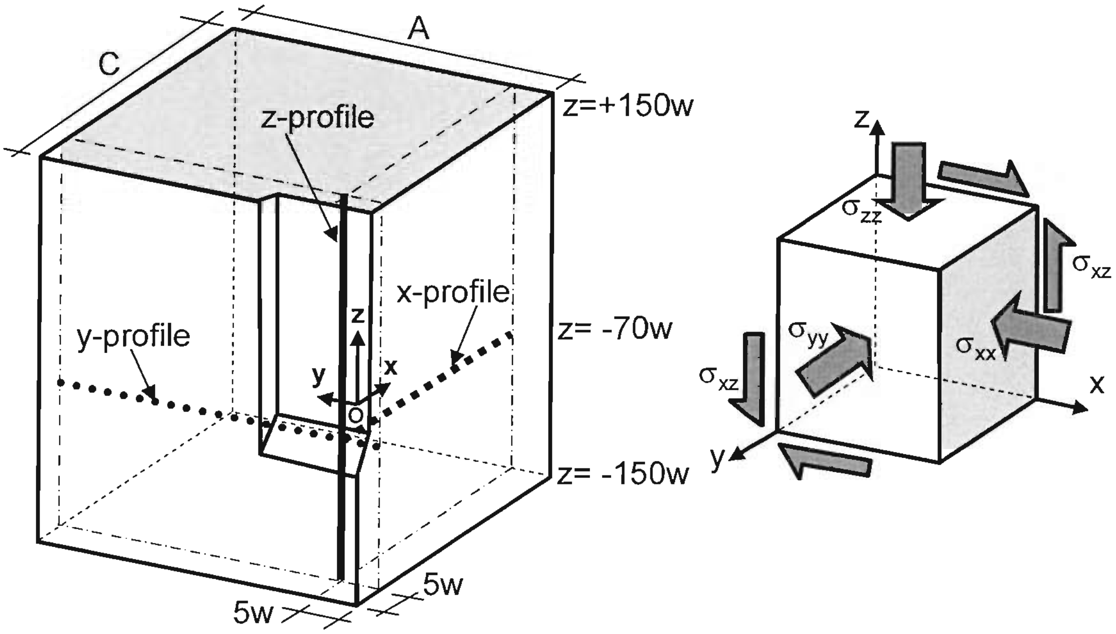

Figure 6-4 Location of stress profiles within SOIL sub-grid (w=4.2mm) at the end of penetration and the 3D convention for positive stress-strain

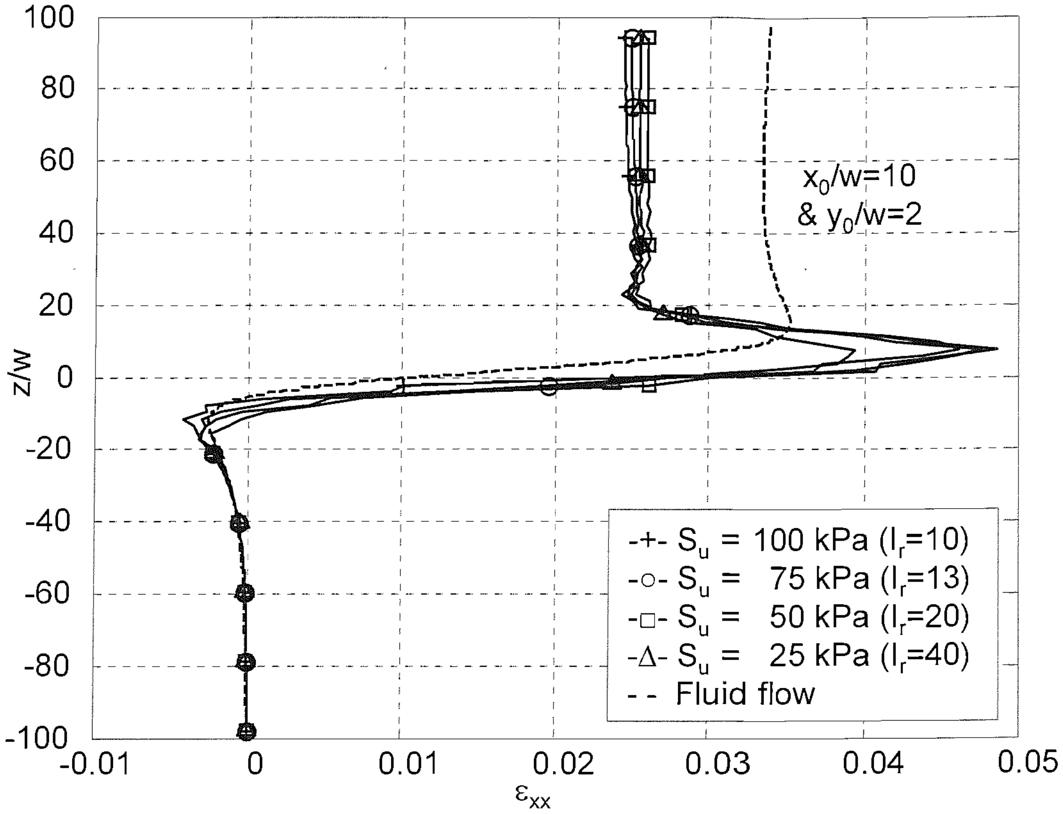

Figure 6-5 Influence of strength (S_u) on strain paths for (ε_{xx}) in 3D penetration models (G=1MPa)

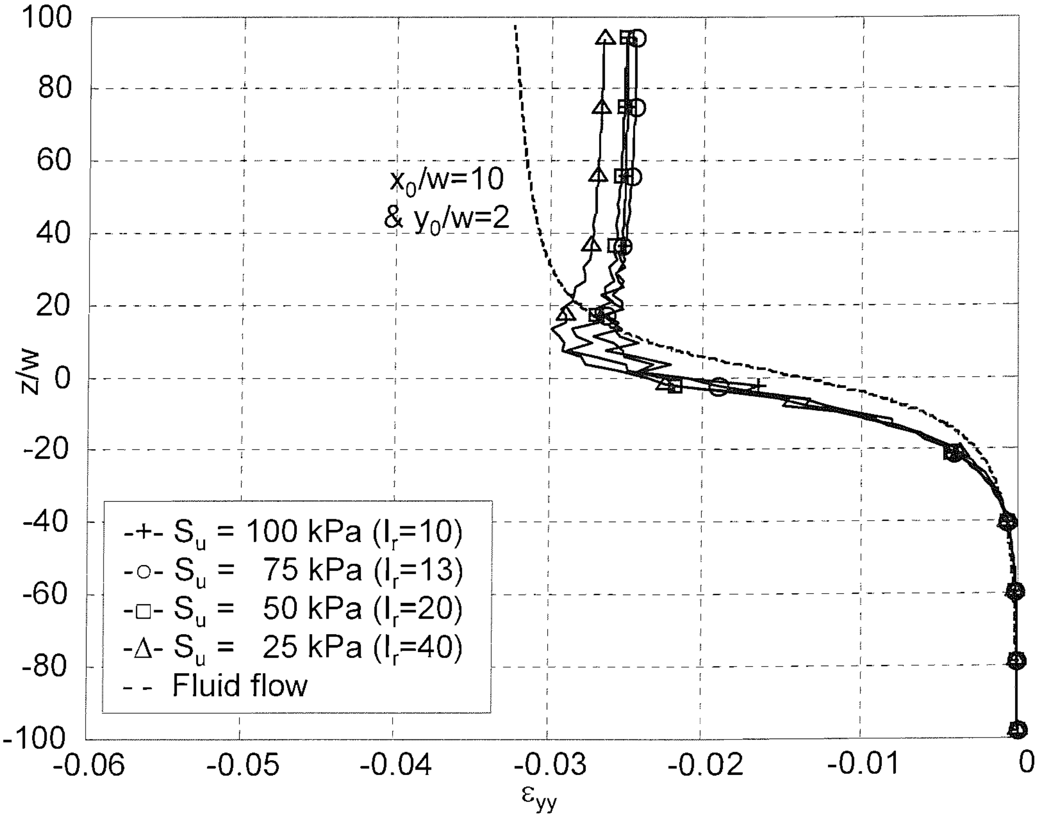

Figure 6-6 Influence of strength (S_u) on strain paths for (ε_{yy}) in 3D penetration models (G=1MPa)

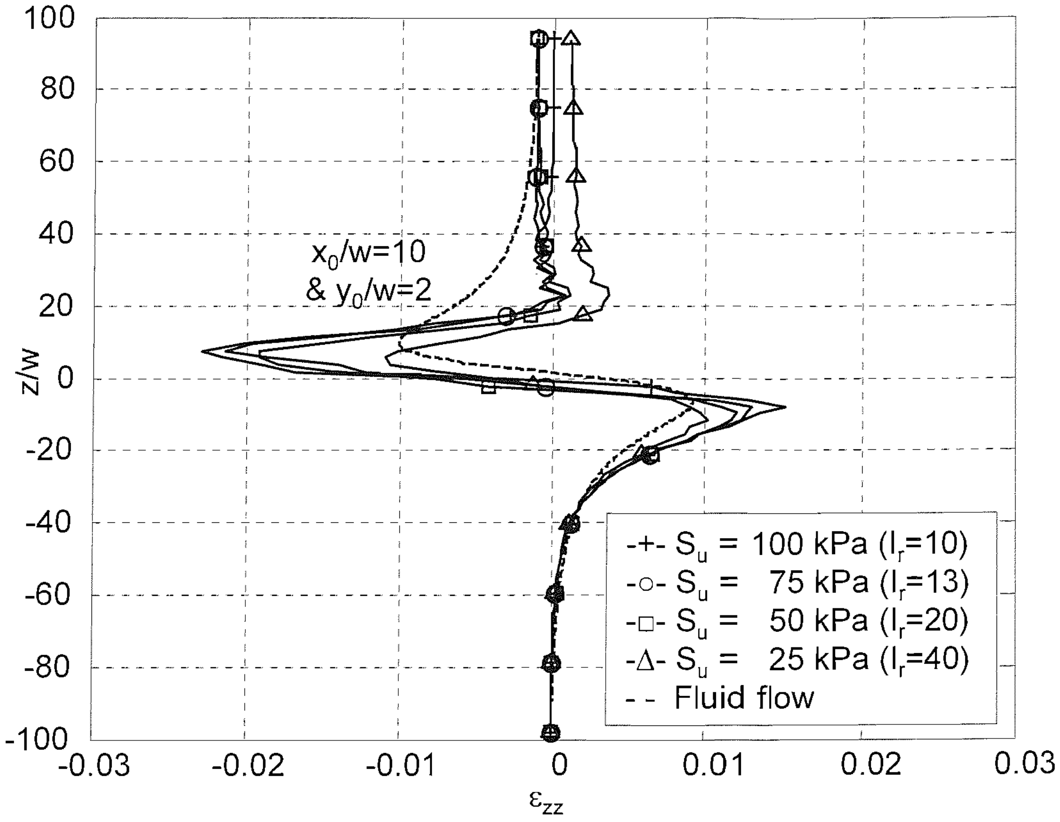

Figure 6-7 Influence of strength (S_u) on strain paths for (ε_{zz}) in 3D penetration models (G=1MPa)

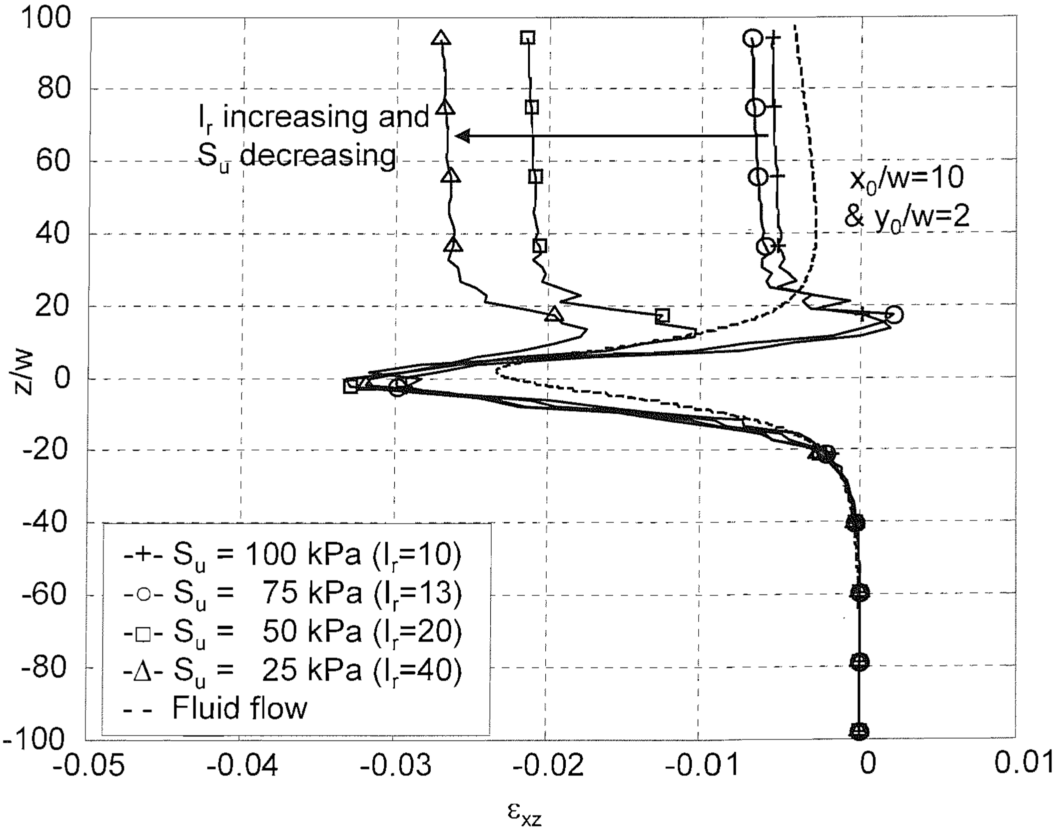

Figure 6-8 Influence of strength (S_u) on strain paths for (ε_{xz}) in 3D penetration models (G=1MPa)

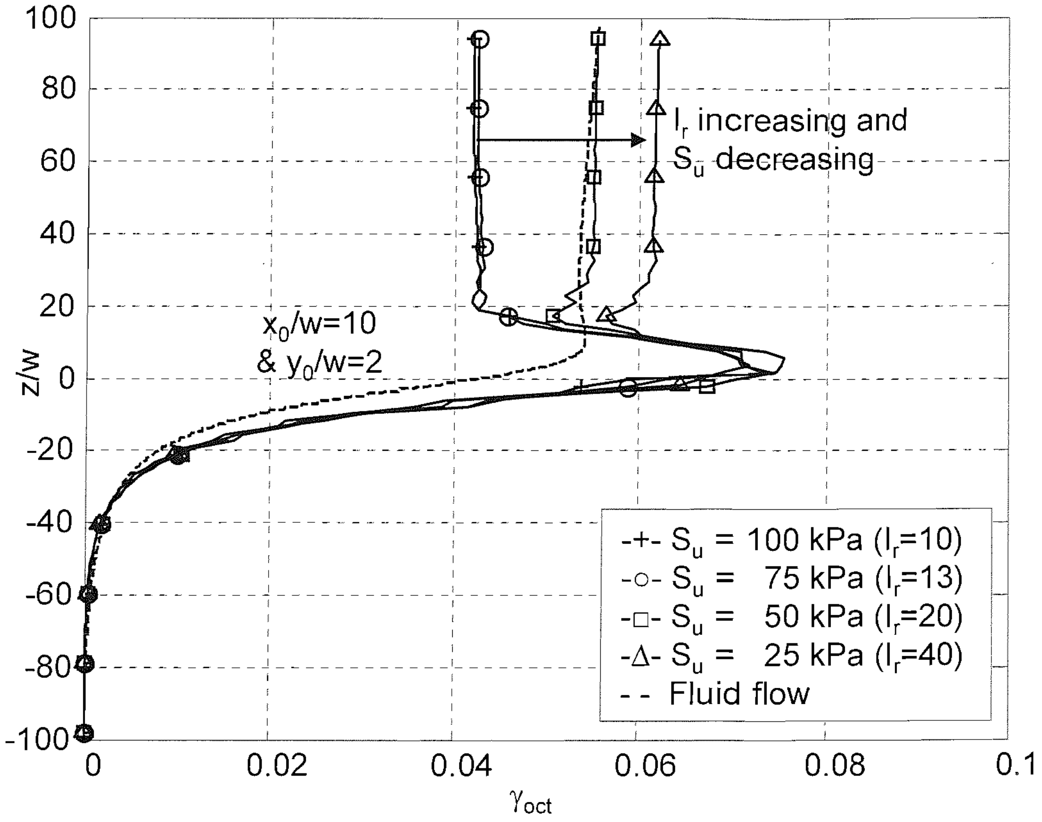

Figure 6-9 Influence of strength (S_u) on strain paths for (γ_{oct}) in 3D penetration models (G=1MPa)

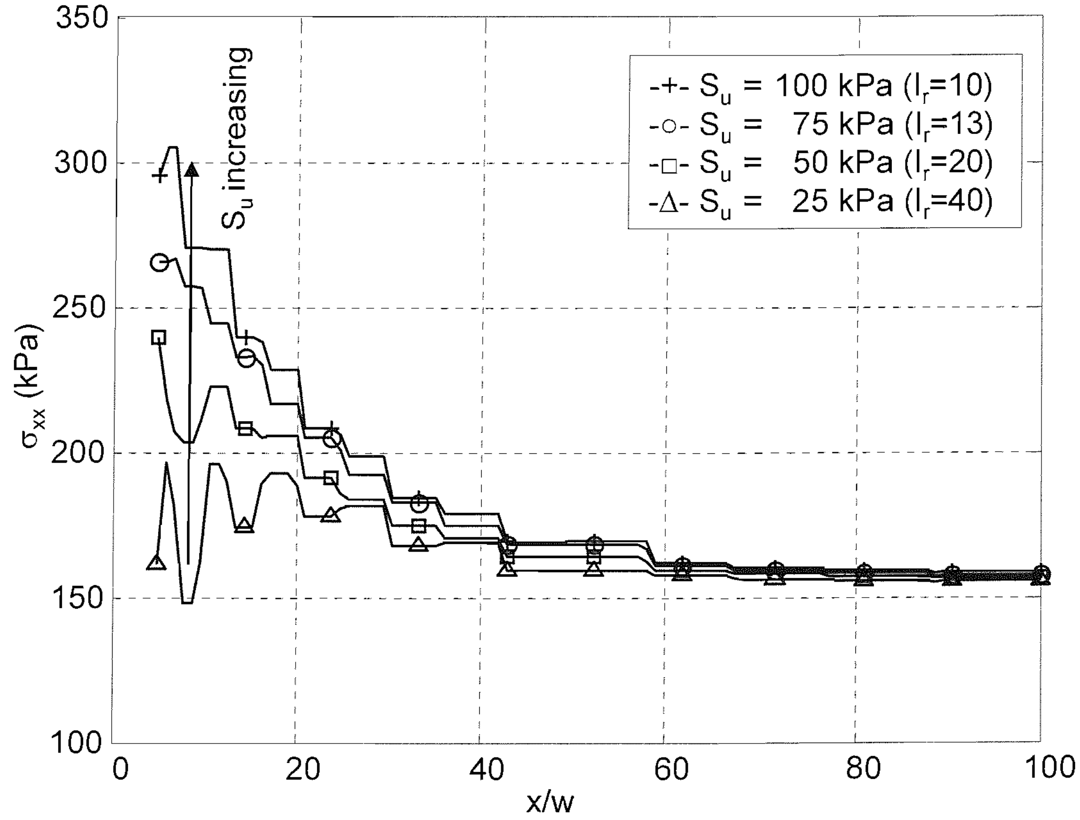

Figure 6-10 Influence of strength (S_u) on (σ_{xx}) along x-profile (y=5w, z=-70w) in 3D penetration models (G=1MPa)

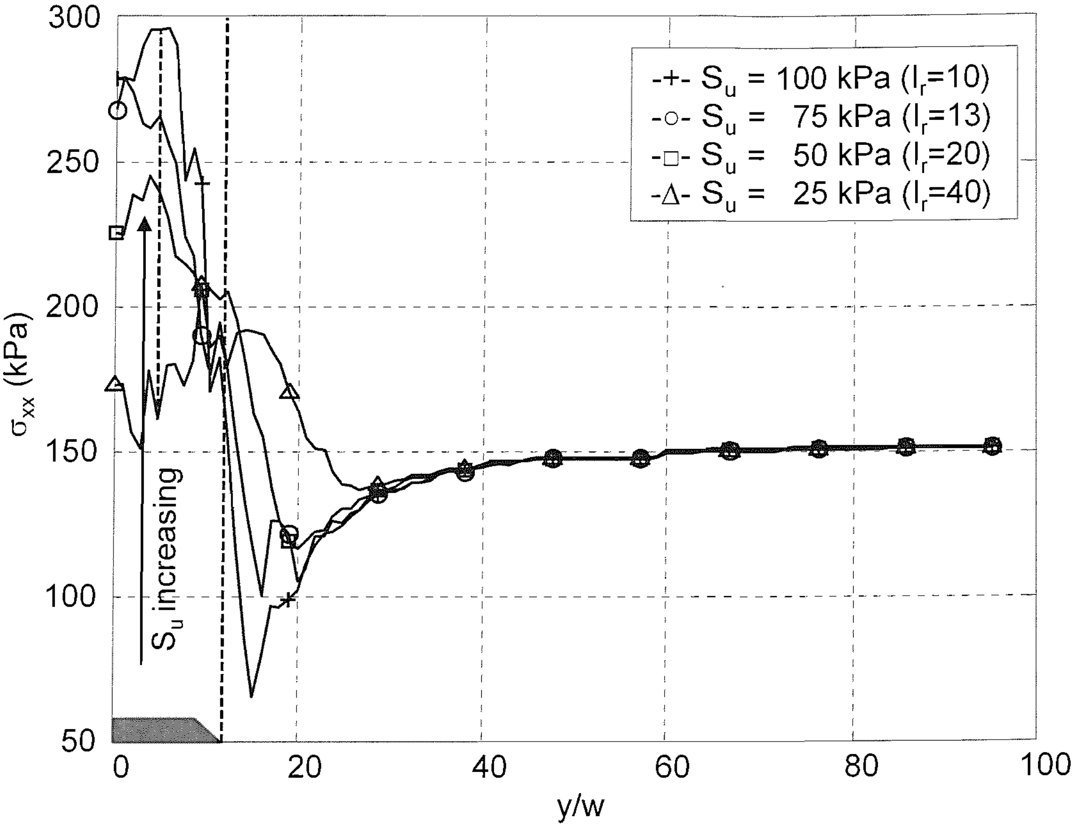

Figure 6-11 Influence of strength (S_u) on (σ_{xx}) along y-profile (x=5w, z=-70w) in 3D penetration models (G=1MPa)

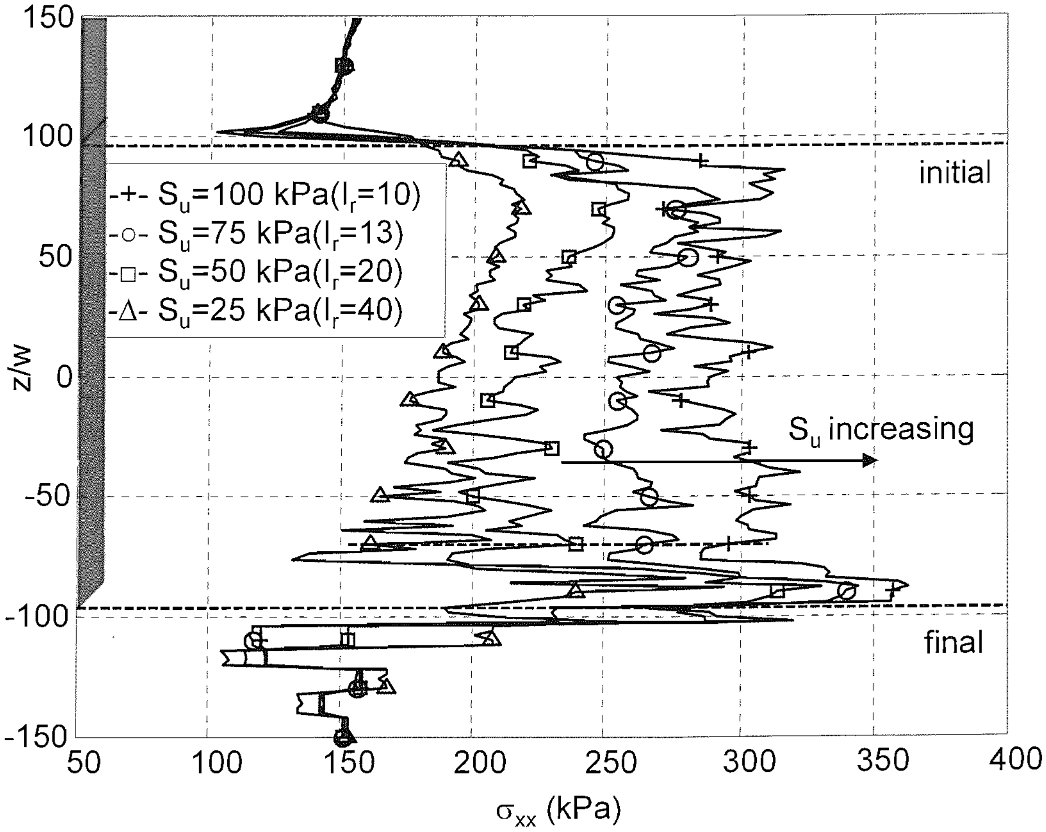

Figure 6-12 Influence of strength (S_u) on (σ_{xx}) along z-profile (x=y=5w) in 3D penetration models (G=1MPa)

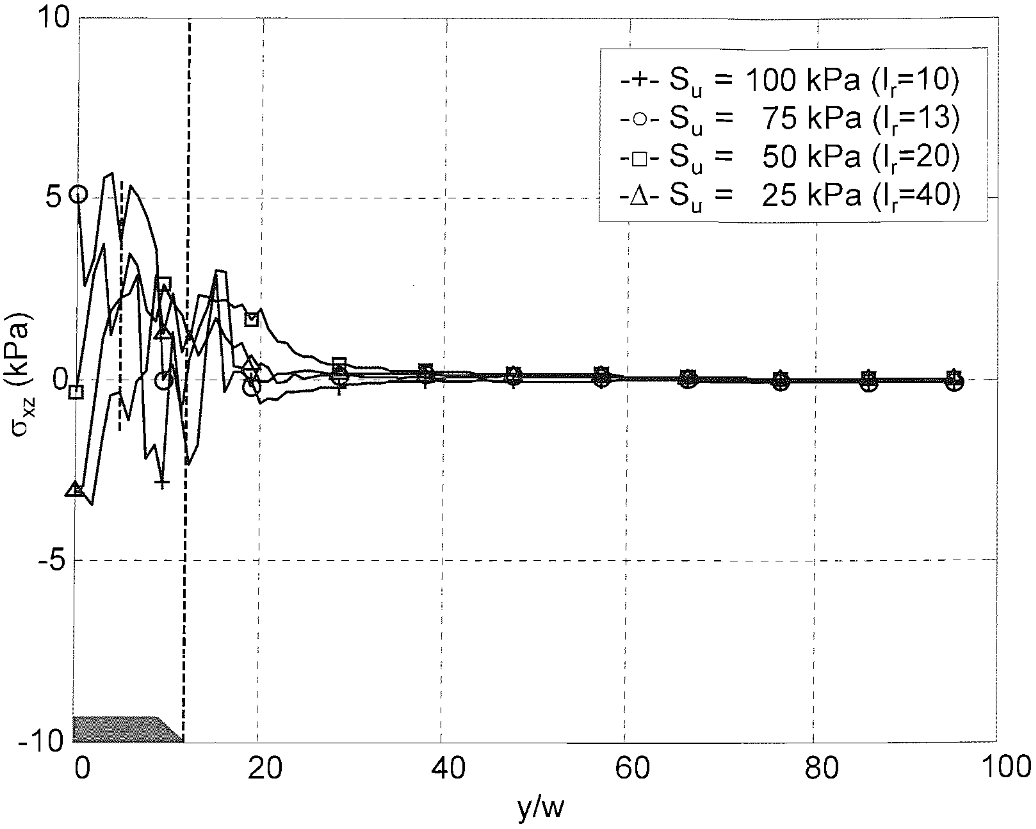

Figure 6-13 Influence of strength (S_u) on (σ_{xz}) along y-profile (x=5w, z=-70w) in 3D penetration models (G=1MPa)

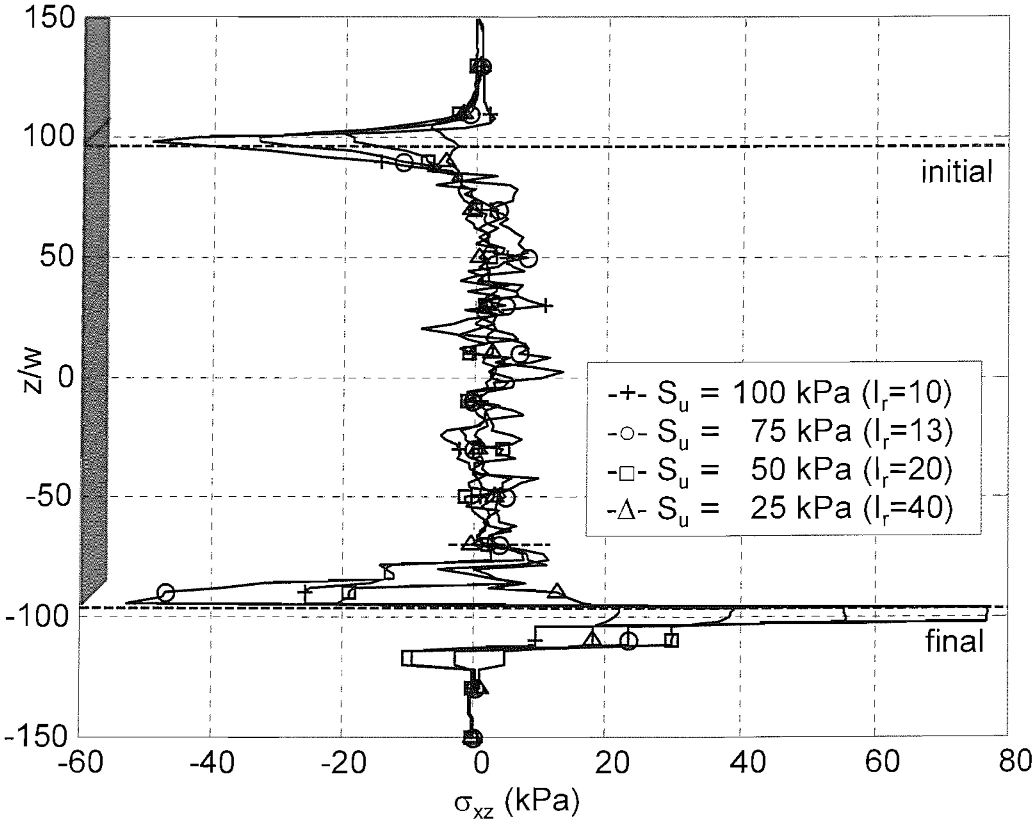

Figure 6-14 Influence of strength (S_u) on (σ_{xz}) along z-profile (x=y=5w) in 3D penetration models (G=1MPa)

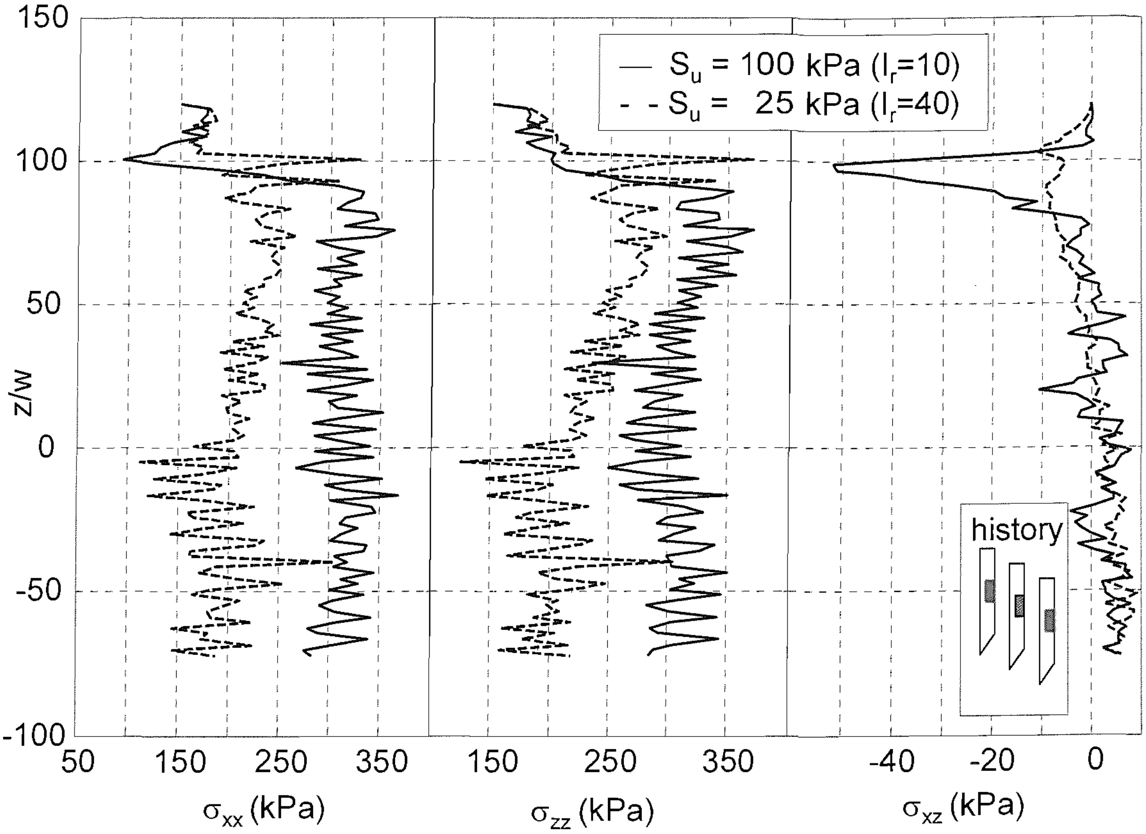

Figure 6-15 Influence of strength (S_u) on stresses at 100mm above tip in 3D penetration models (G=1MPa)

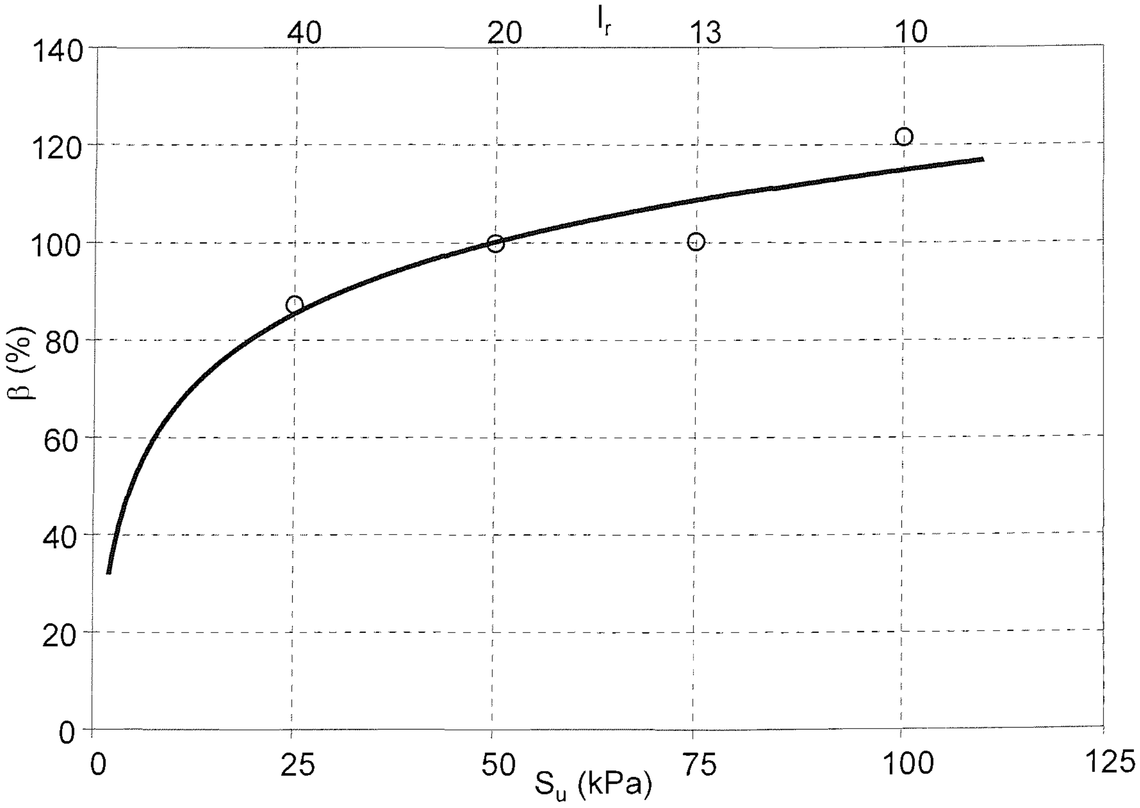

Figure 6-16 Influence of strength (S_u) on normalised horizontal stress change (β) at 100mm above tip in 3D penetration models (G=1MPa)

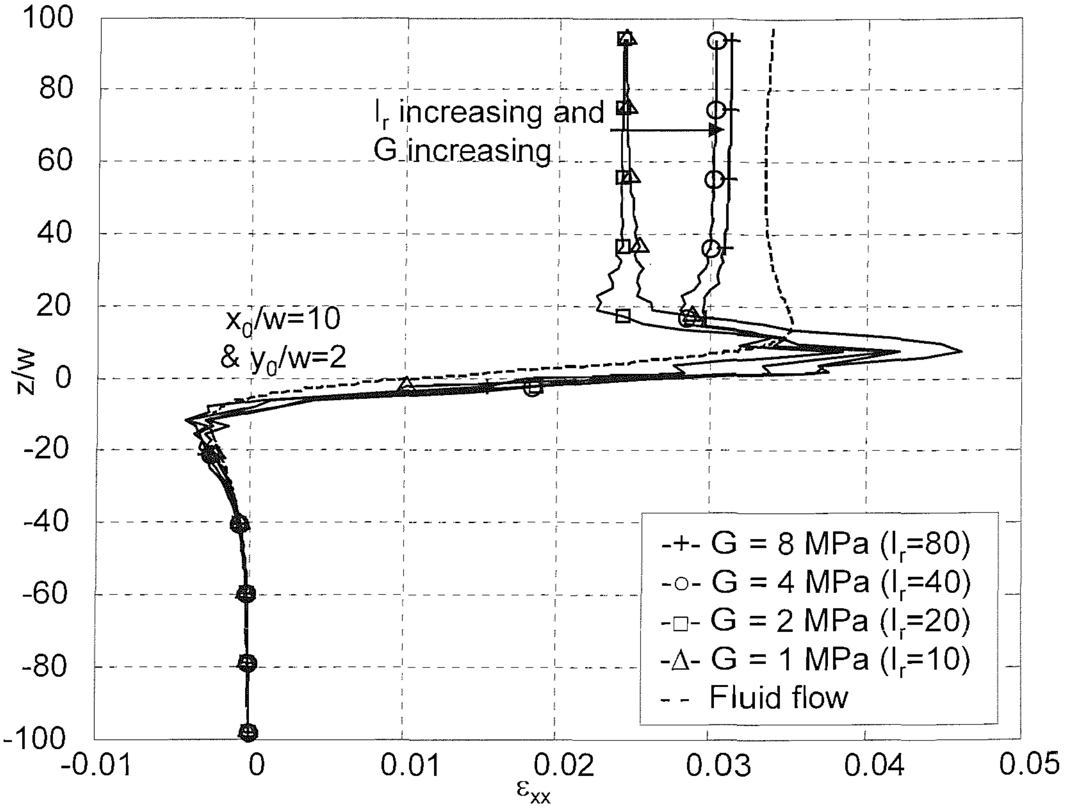

Figure 6-17 Influence of modulus (G) on strain paths for (ε_{xx}) in 3D penetration models (S_u=100kPa)

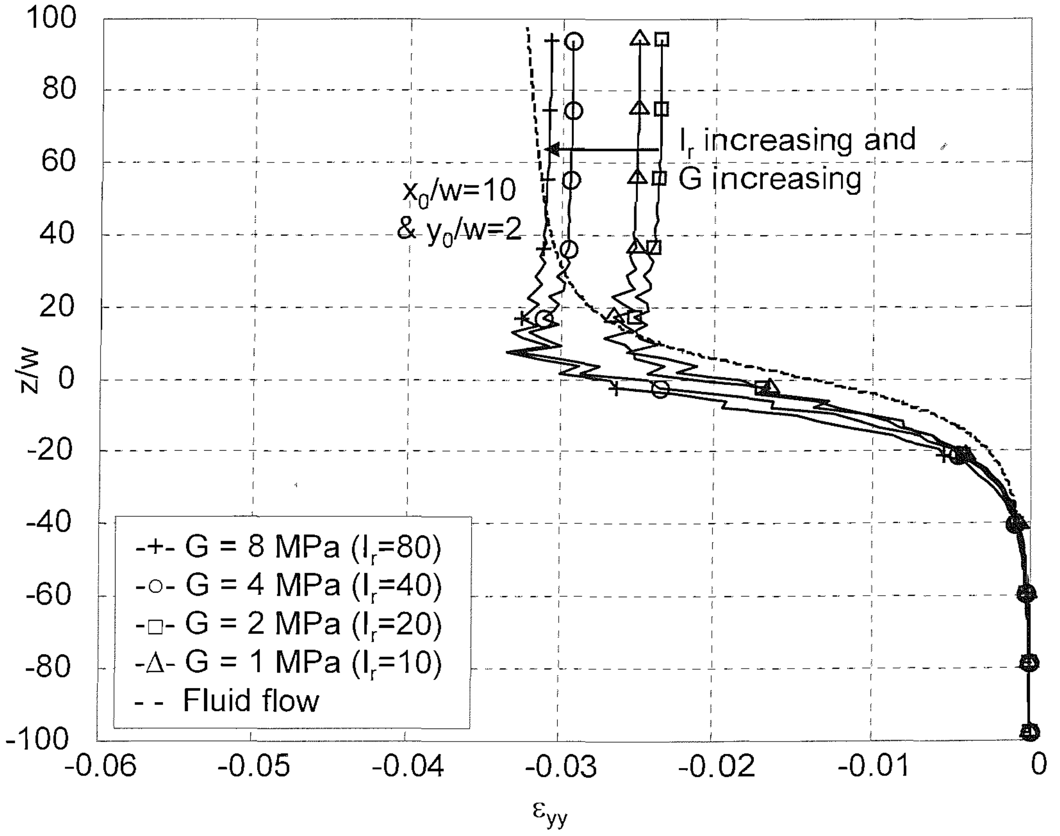

Figure 6-18 Influence of modulus (G) on strain paths for (ε_{yy}) in 3D penetration models (S_u=100kPa)

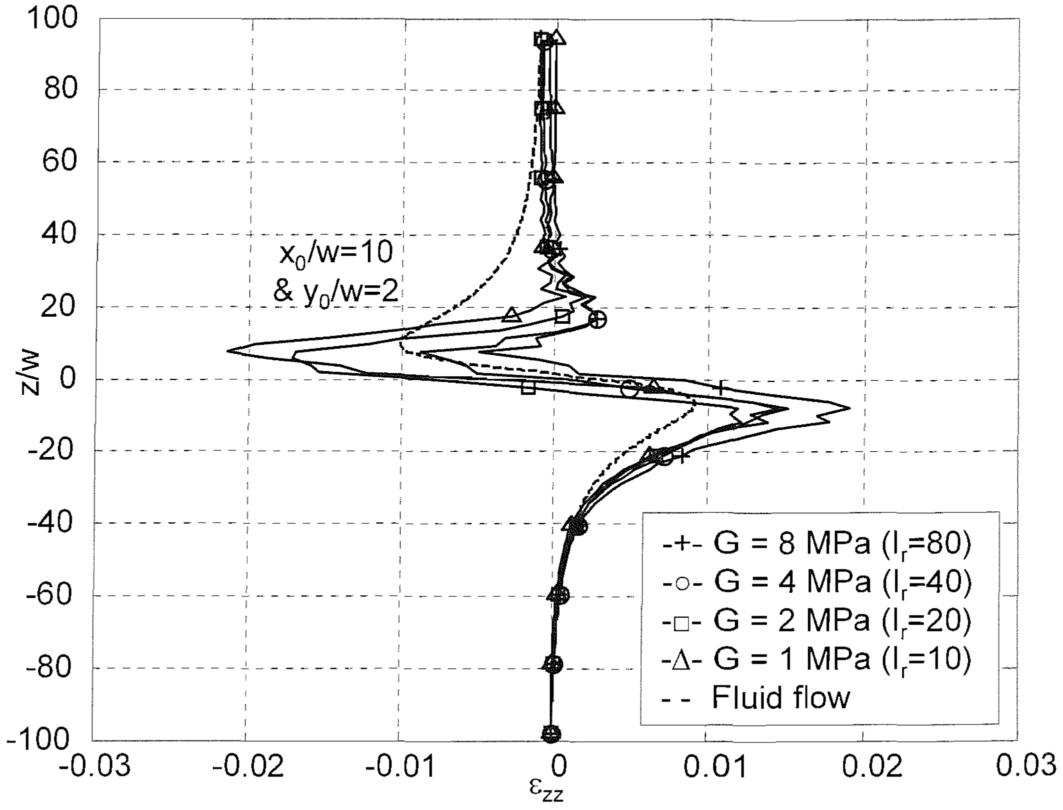

Figure 6-19 Influence of modulus (G) on strain paths for (ε_{zz}) in 3D penetration models (S_u=100kPa)

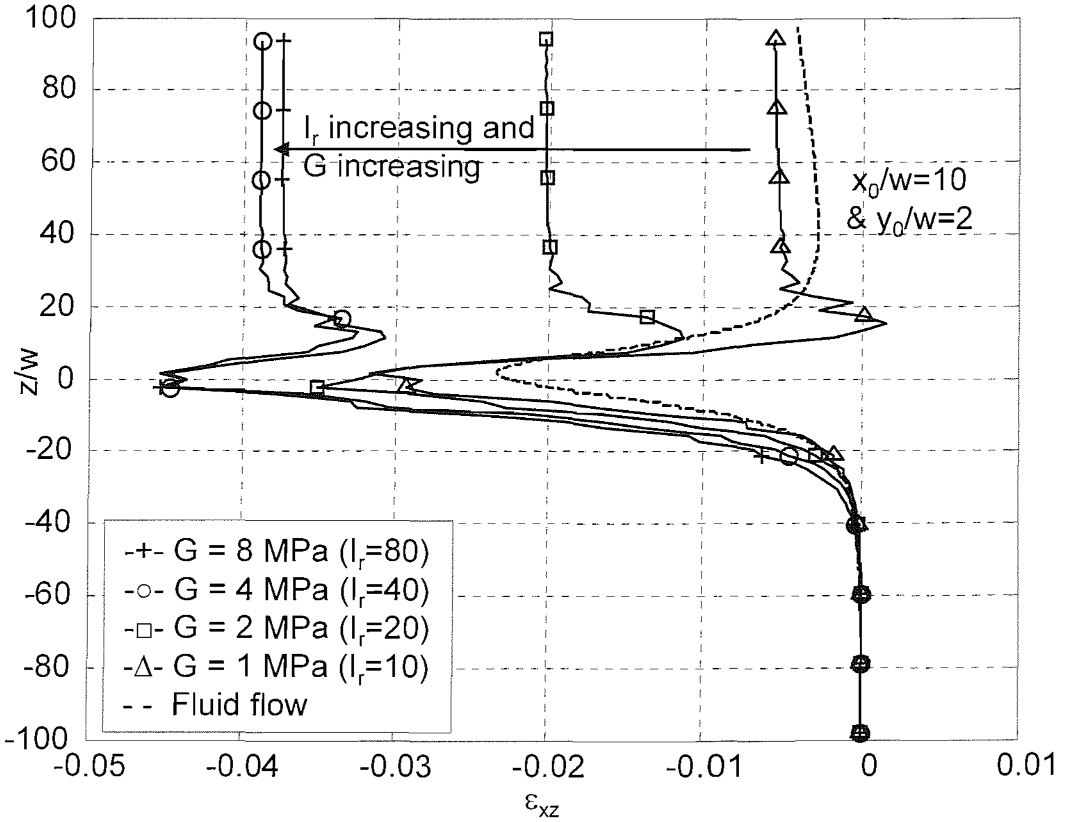

Figure 6-20 Influence of modulus (G) on strain paths for (ε_{xz}) in 3D penetration models (S_u=100kPa)

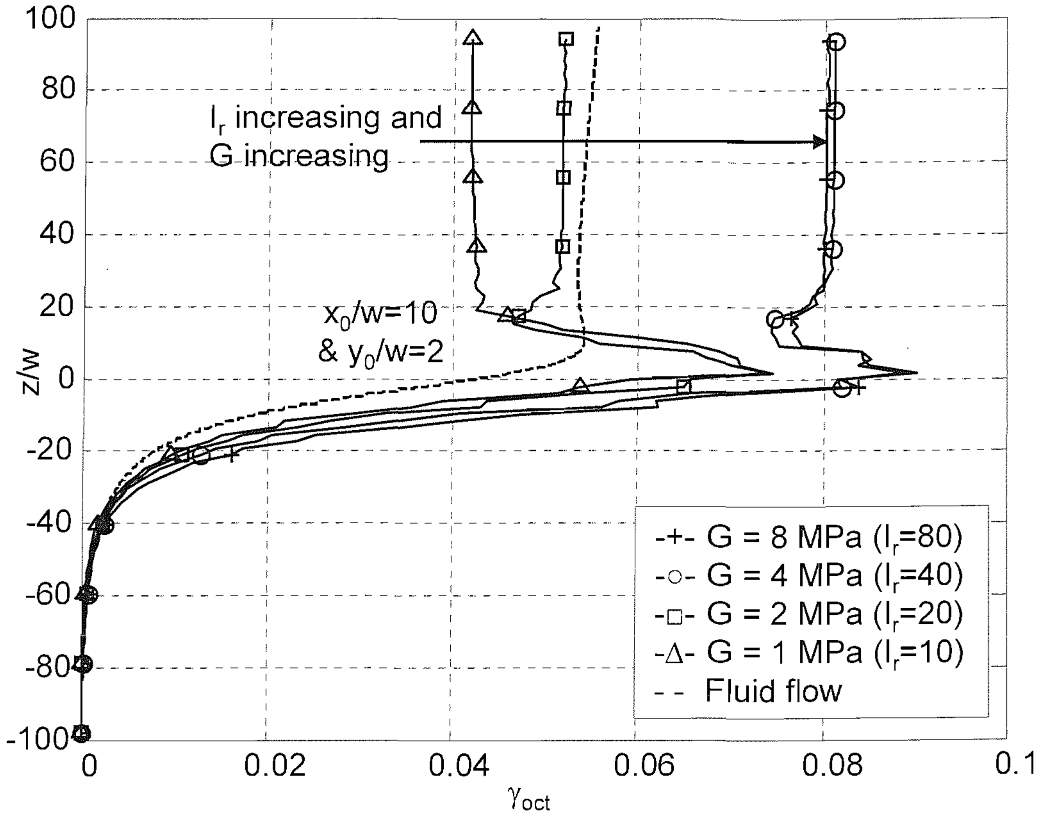

Figure 6-21 Influence of modulus (G) on strain paths for (γ_{oct}) in 3D penetration models (S_u=100kPa)

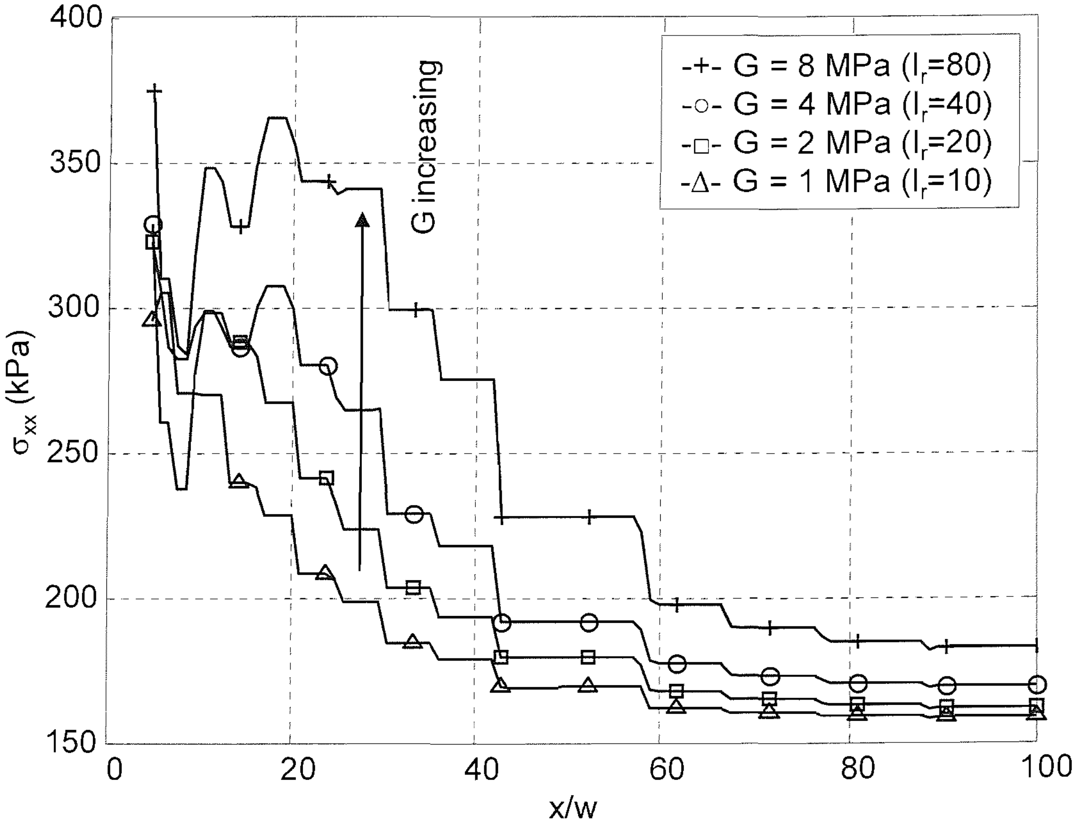

Figure 6-22 Influence of modulus (G) on (σ_{xx}) along x-profile (y=5w, z=-70w) in 3D penetration models (S_u=100kPa)

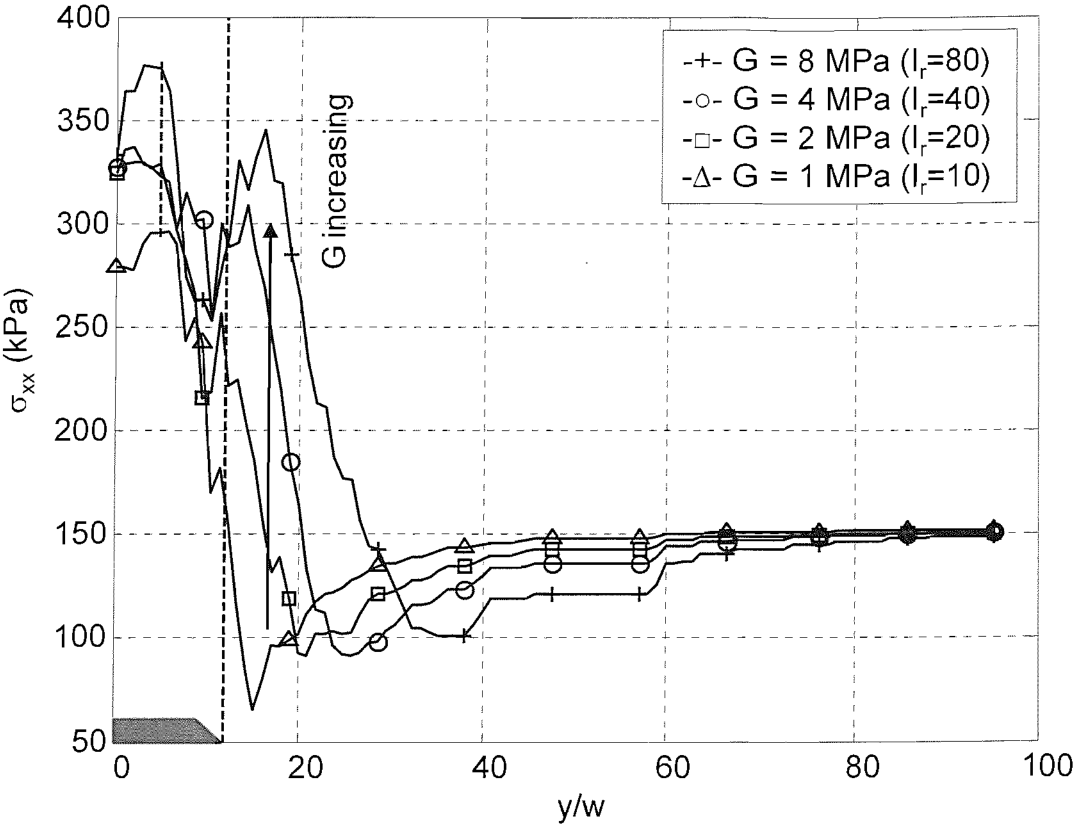

Figure 6-23 Influence of modulus (G) on (σ_{xx}) along y-profile (x=5w, z=-70w) in 3D penetration models (S_u=100kPa)

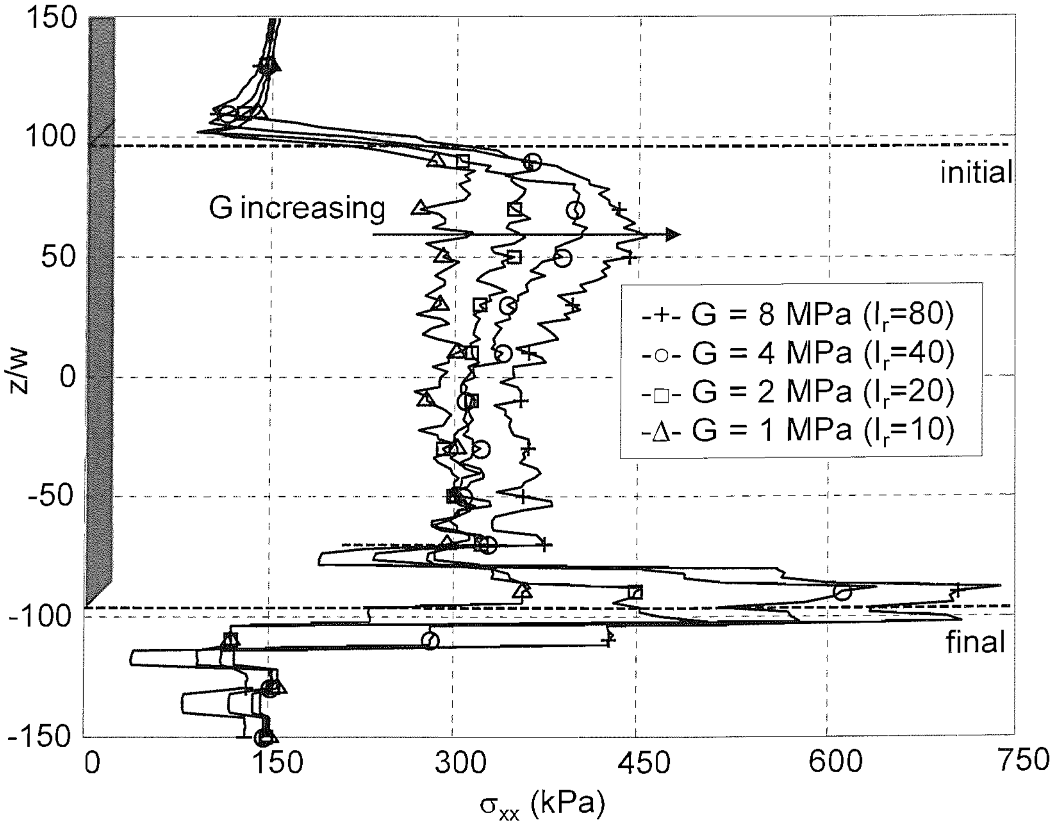

Figure 6-24 Influence of modulus (G) on (σ_{xx}) along z-profile (x=y=5w) in 3D penetration models (S_u=100kPa)

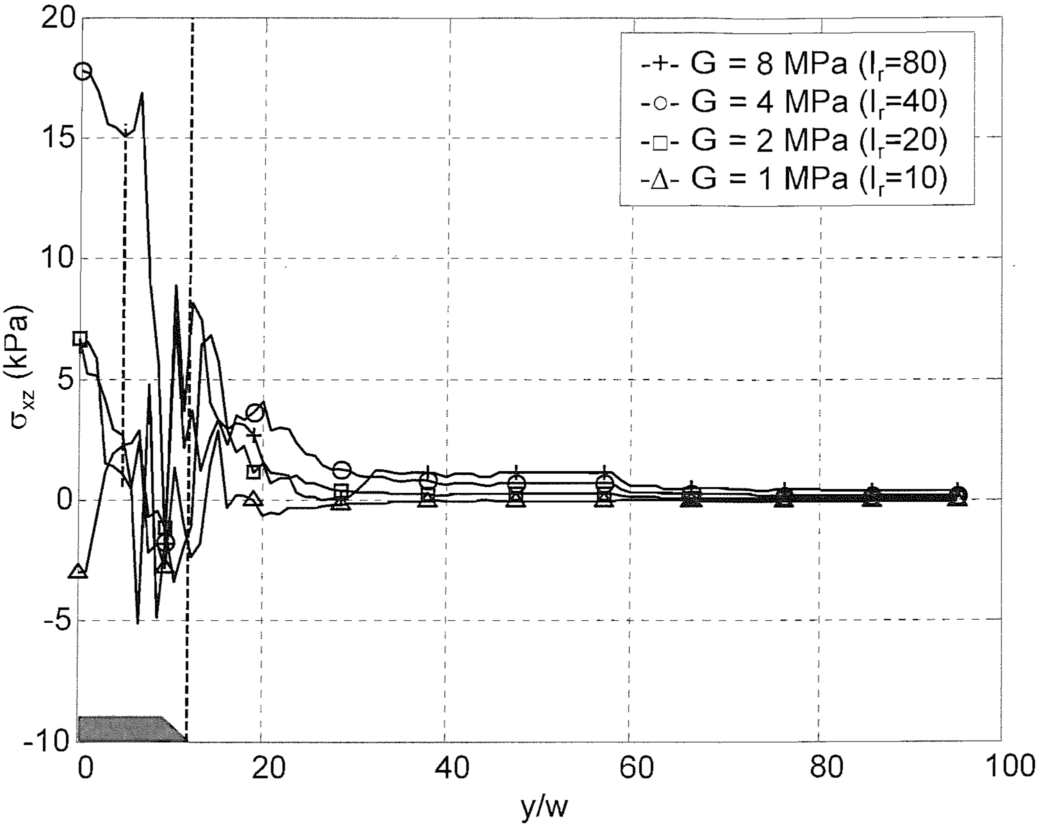

Figure 6-25 Influence of modulus (G) on (σ_{xz}) along y-profile (x=5w, z=-70w) in 3D penetration models (S_u=100kPa)

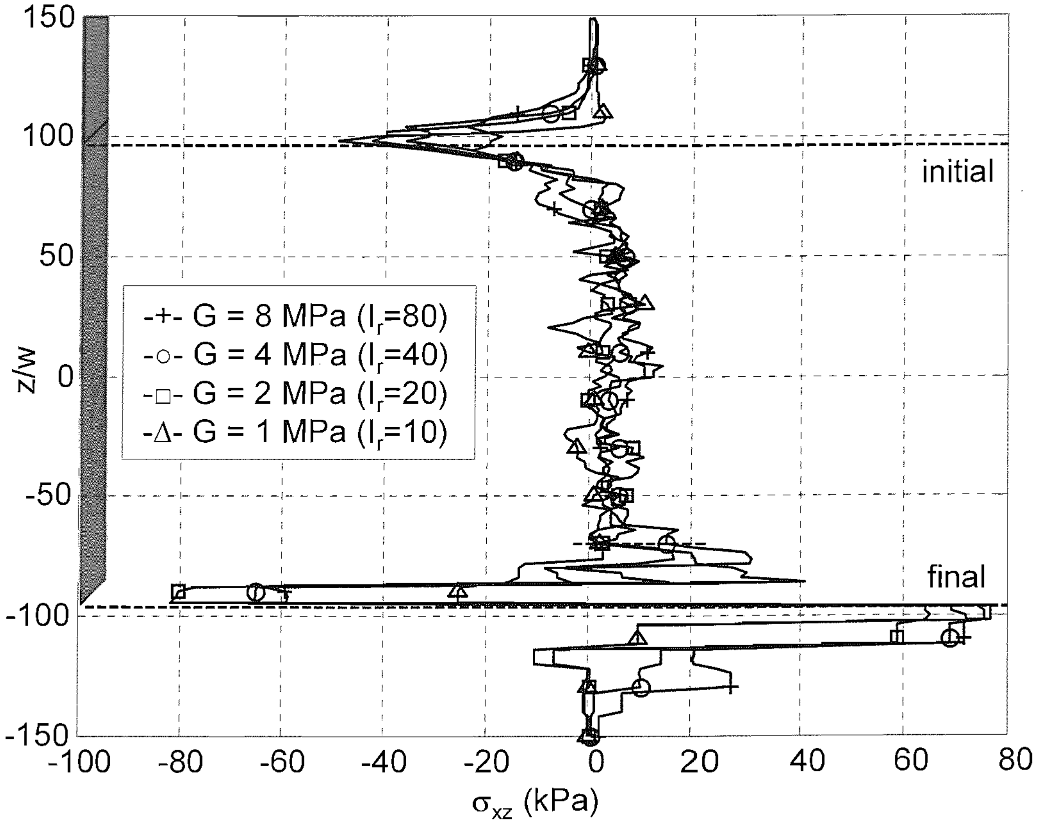

Figure 6-26 Influence of modulus (G) on (σ_{xz}) along z-profile (x=y=5w) in 3D penetration models (S_u=100kPa)

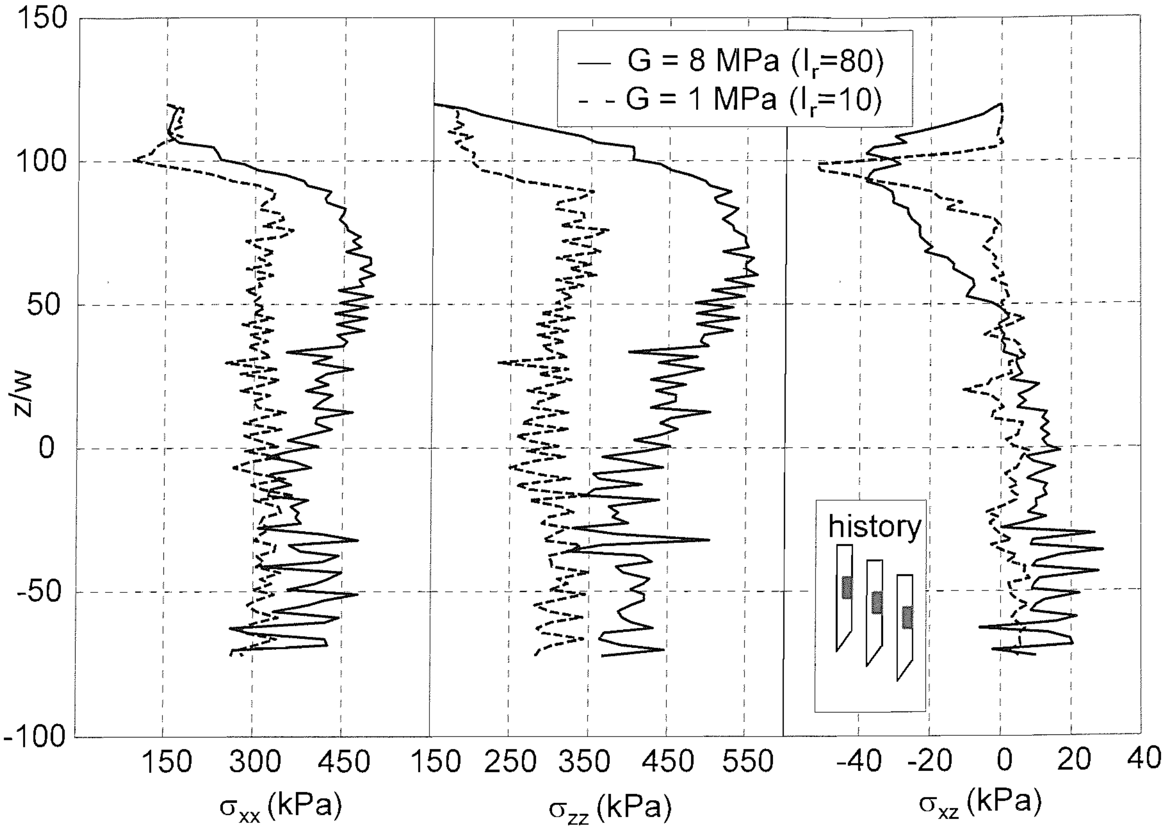

Figure 6-27 Influence of modulus (G) on stresses at 100mm above tip in 3D penetration models (S_u=100kPa)

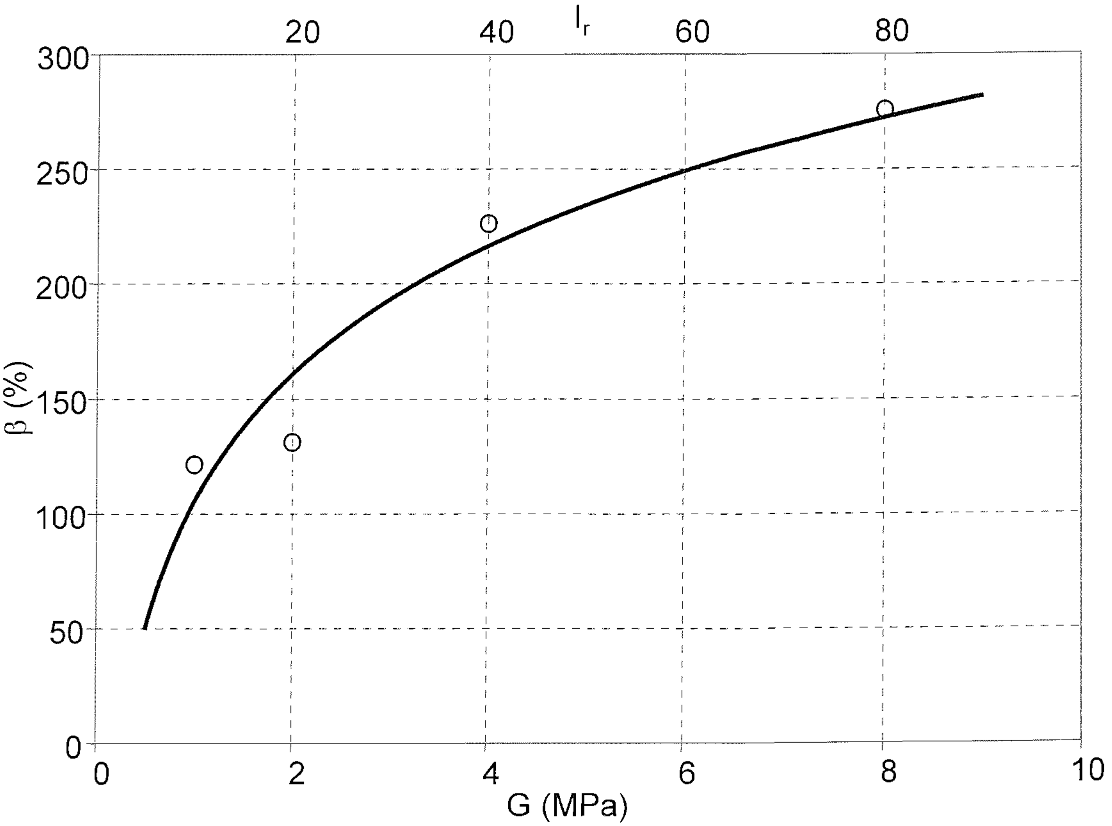

Figure 6-28 Influence of modulus (G) on normalised horizontal stress change (β) at 100mm above tip in 3D penetration models (S_u=100kPa)

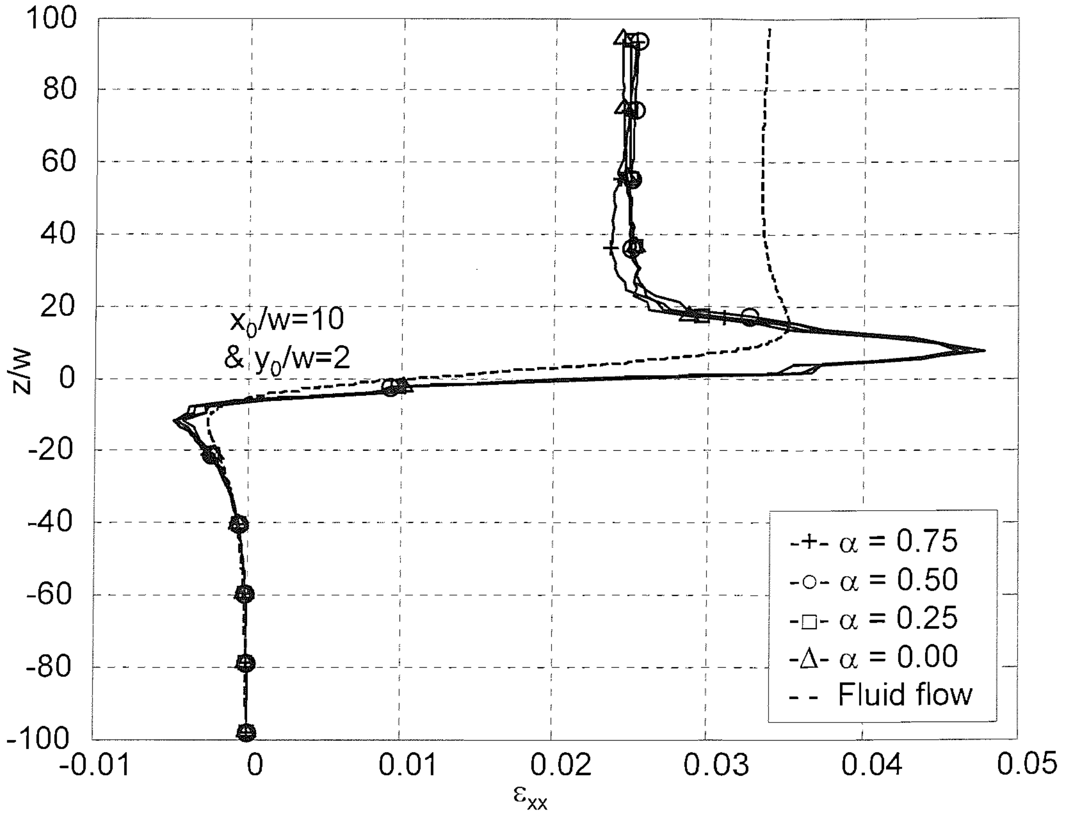

Figure 6-29 Influence of adhesion (α) on strain paths for (ε_{xx}) in 3D penetration models

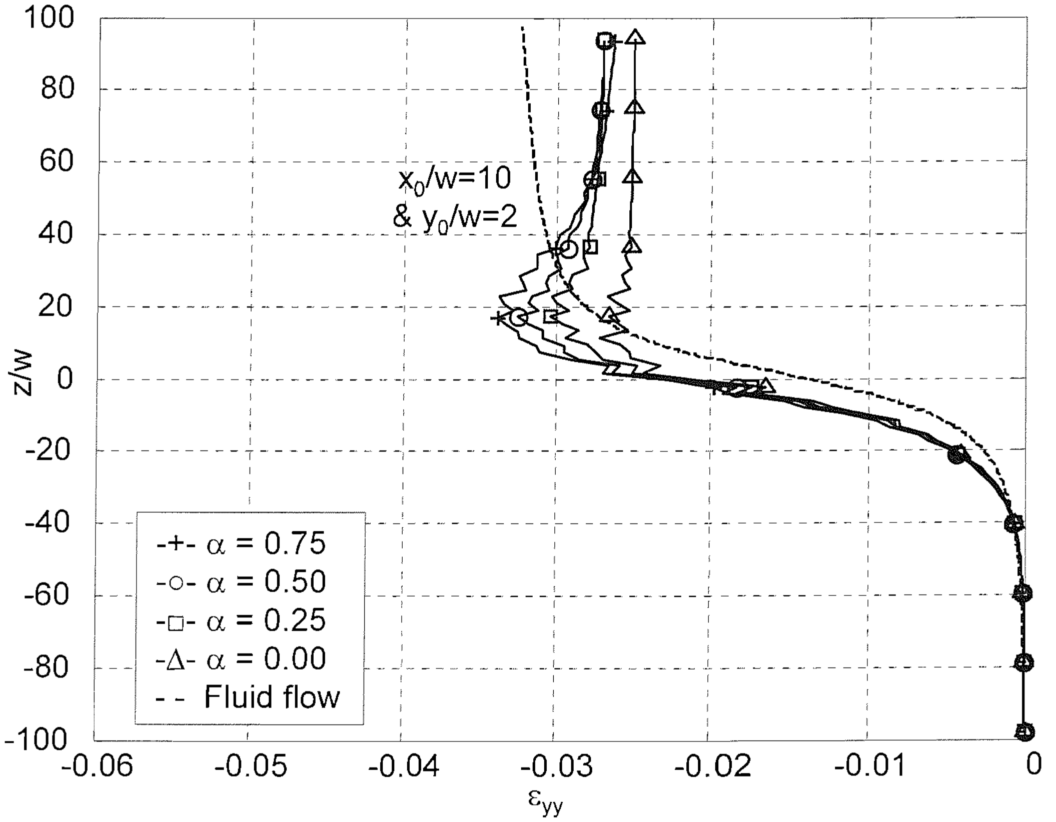

Figure 6-30 Influence of adhesion (α) on strain paths for (ε_{yy}) in 3D penetration models

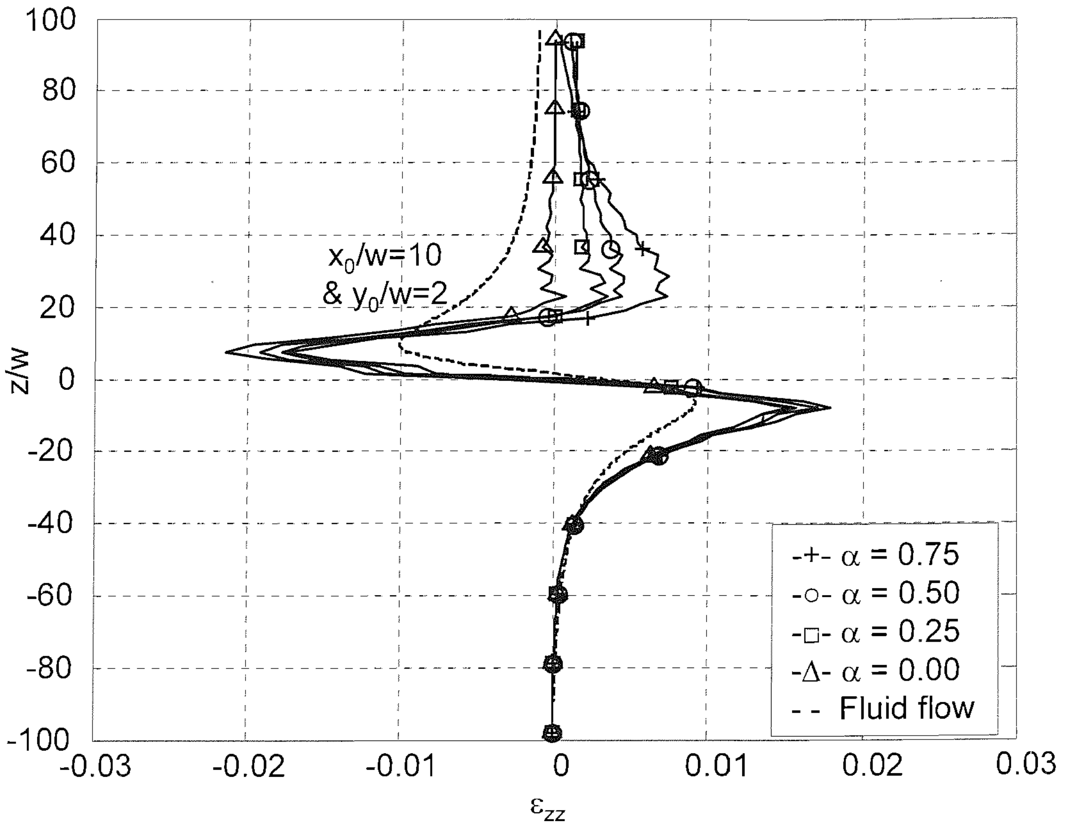

Figure 6-31 Influence of adhesion (α) on strain paths for (ε_{zz}) in 3D penetration models

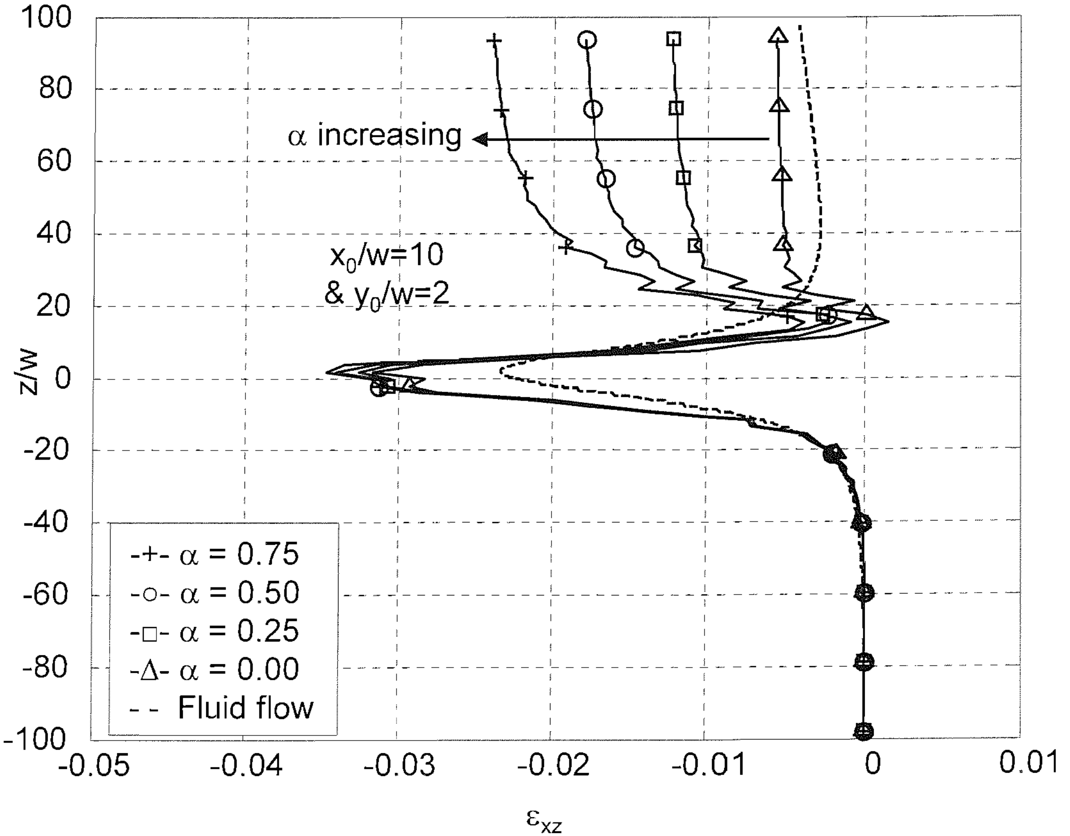

Figure 6-32 Influence of adhesion (α) on strain paths for (ε_{xz}) in 3D penetration models

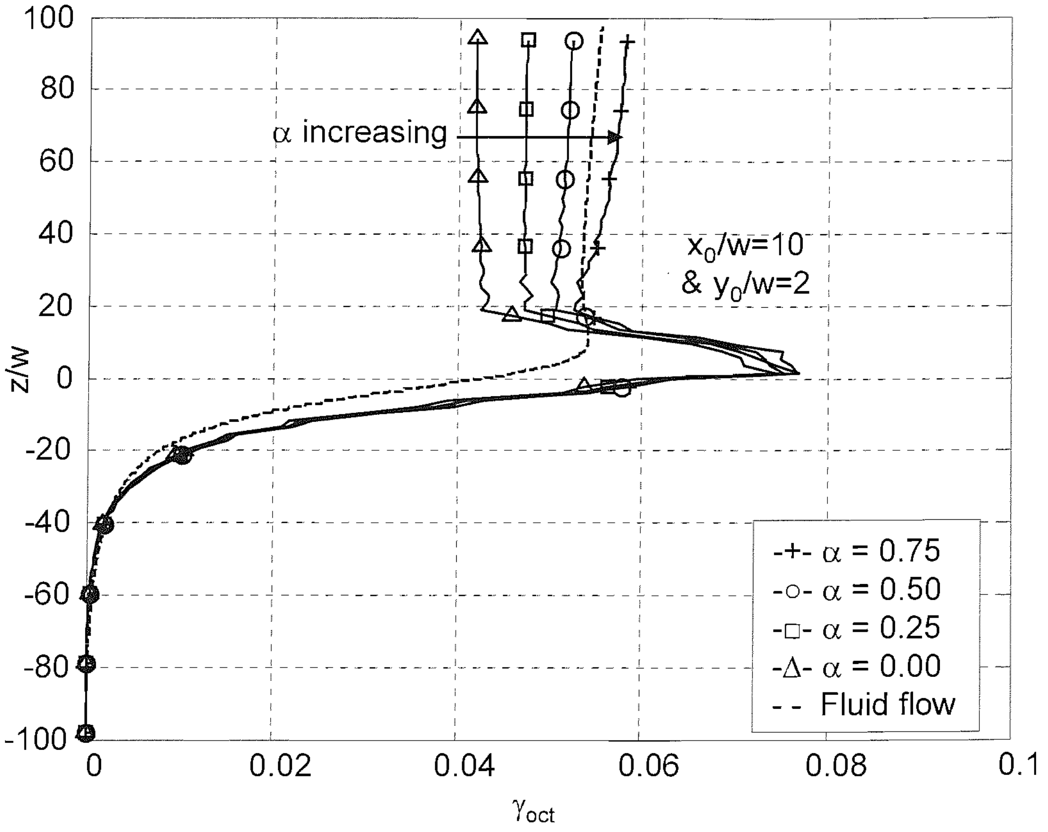

Figure 6-33 Influence of adhesion (α) on strain paths for (γ_{oct}) in 3D penetration models

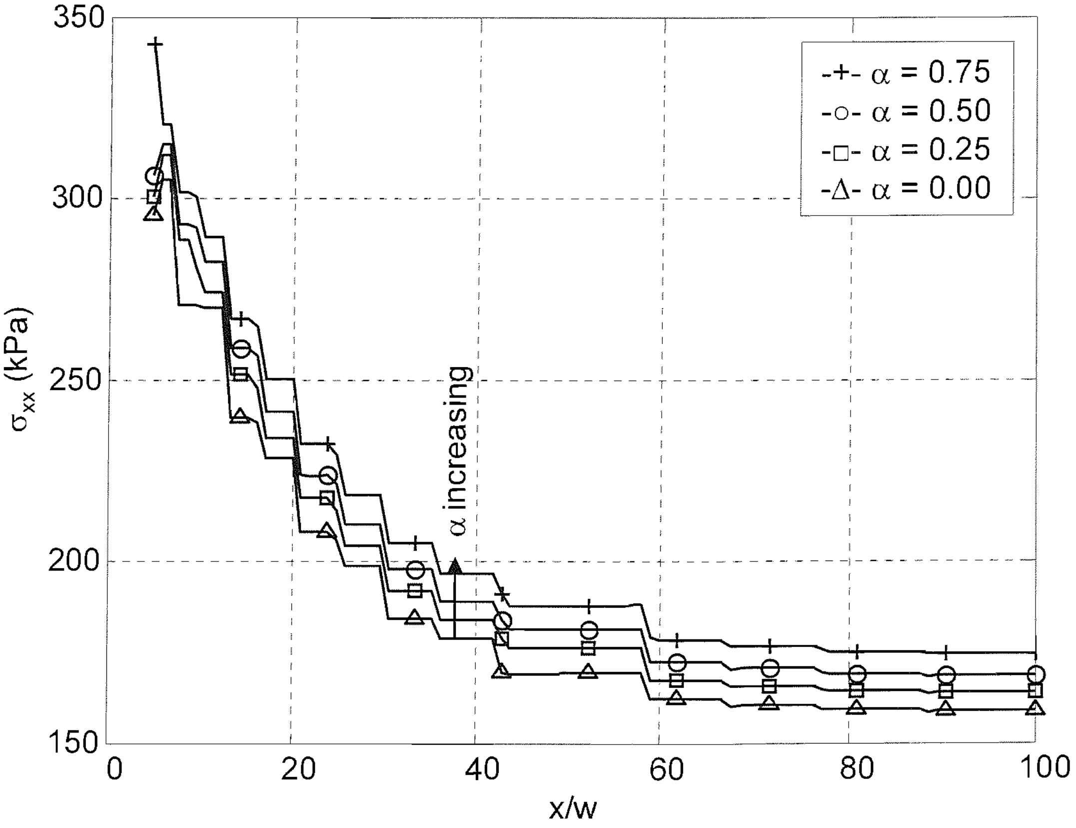

Figure 6-34 Influence of adhesion (α) on (σ_{xx}) along x-profile (y=5w, z=-70w) in 3D penetration models

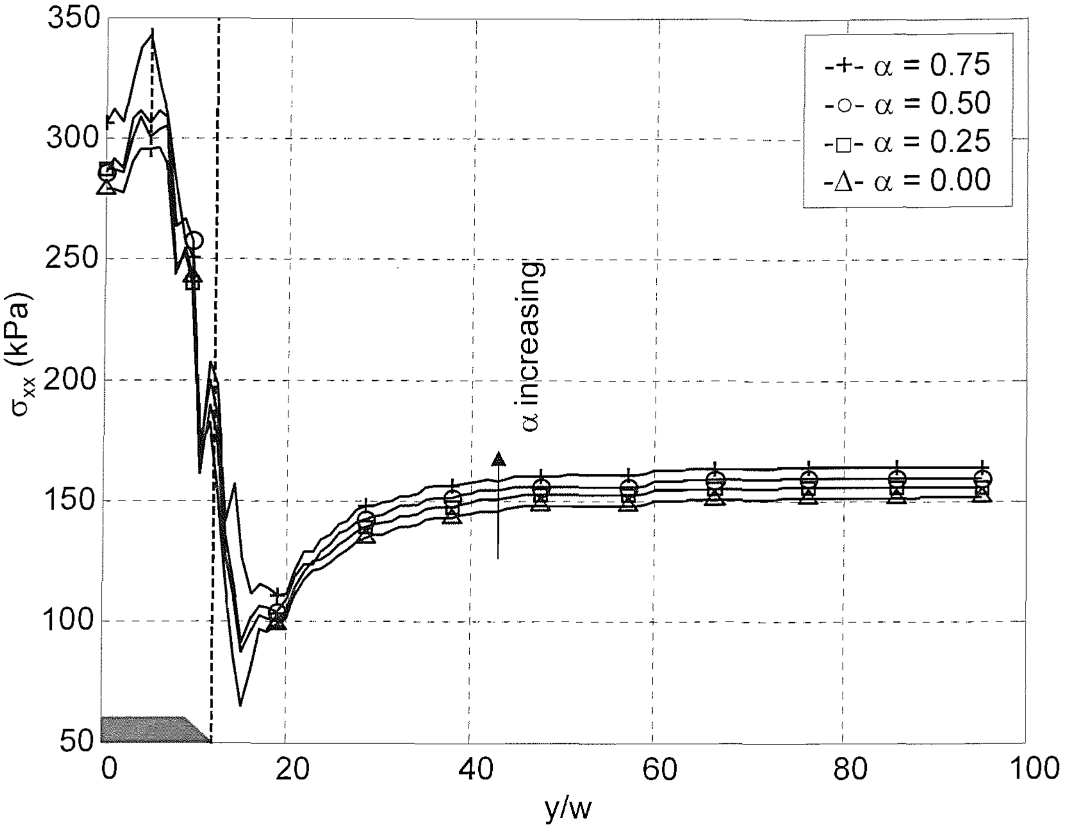

Figure 6-35 Influence of adhesion (α) on (σ_{xx}) along y-profile (x=5w, z=-70w) in 3D penetration models

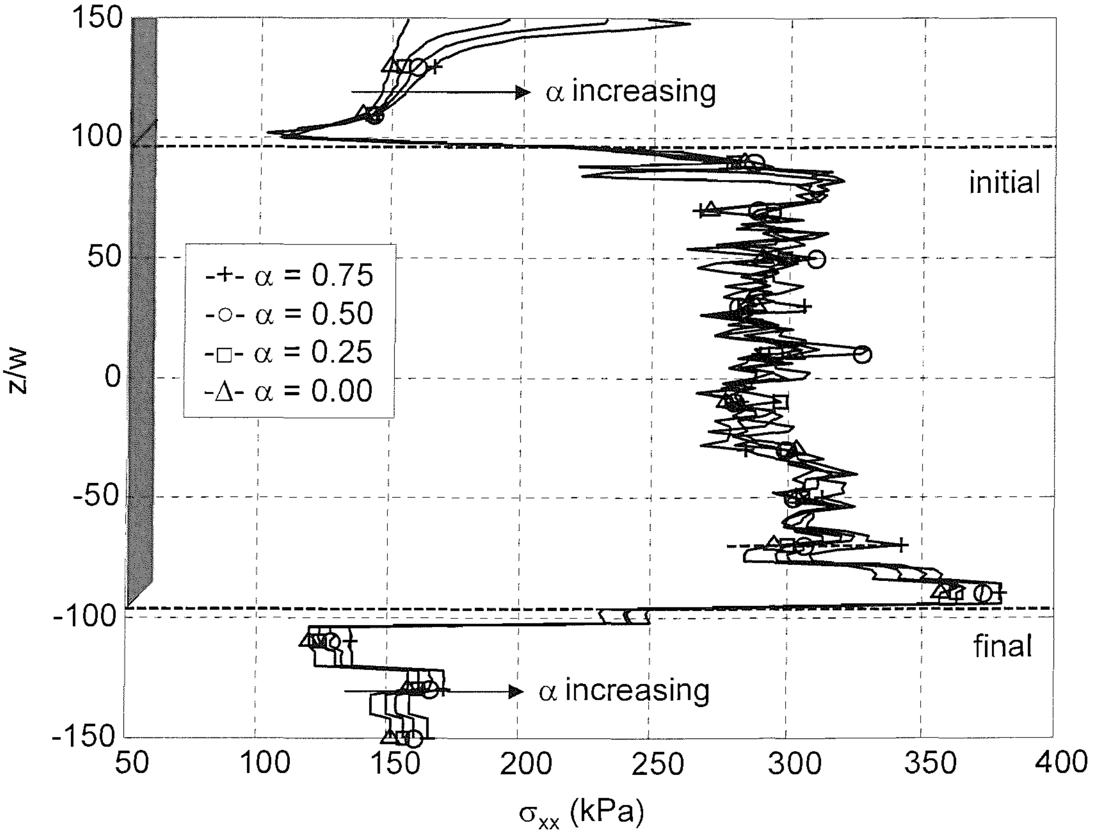

Figure 6-36 Influence of adhesion (α) on (σ_{xx}) along z-profile (x=y=5w) in 3D penetration models

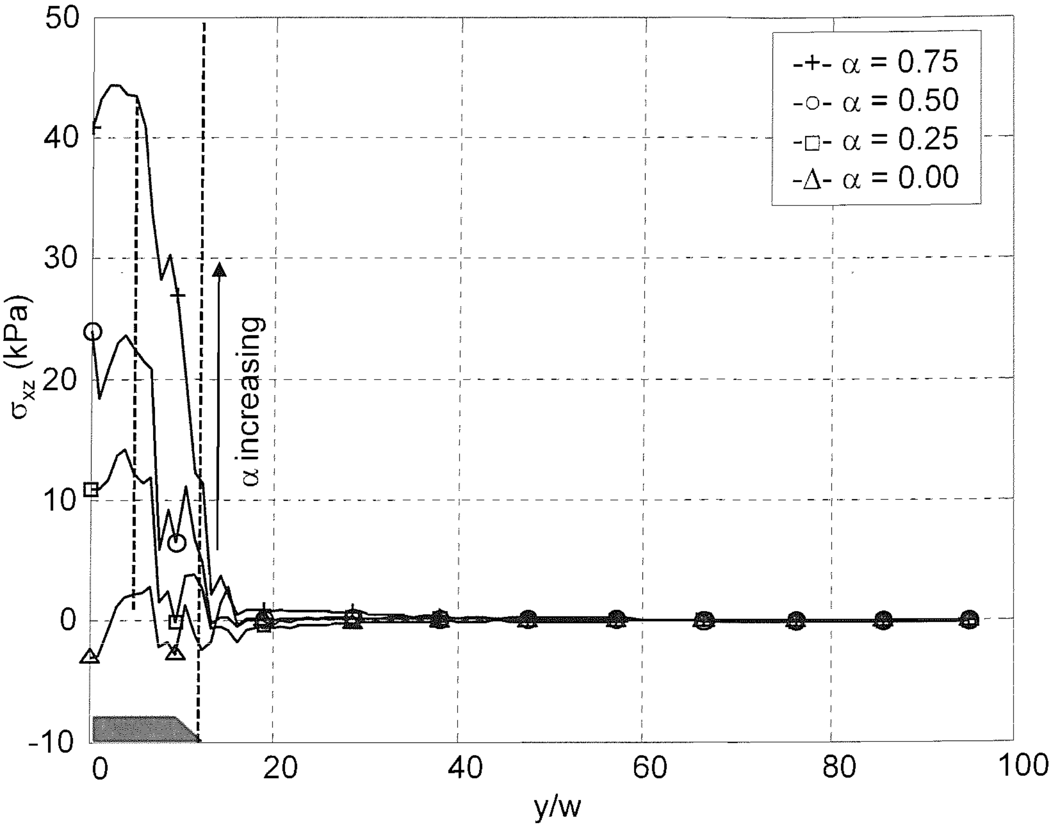

Figure 6-37 Influence of adhesion (α) on (σ_{xz}) along y-profile (x=5w, z=-70w) in 3D penetration models

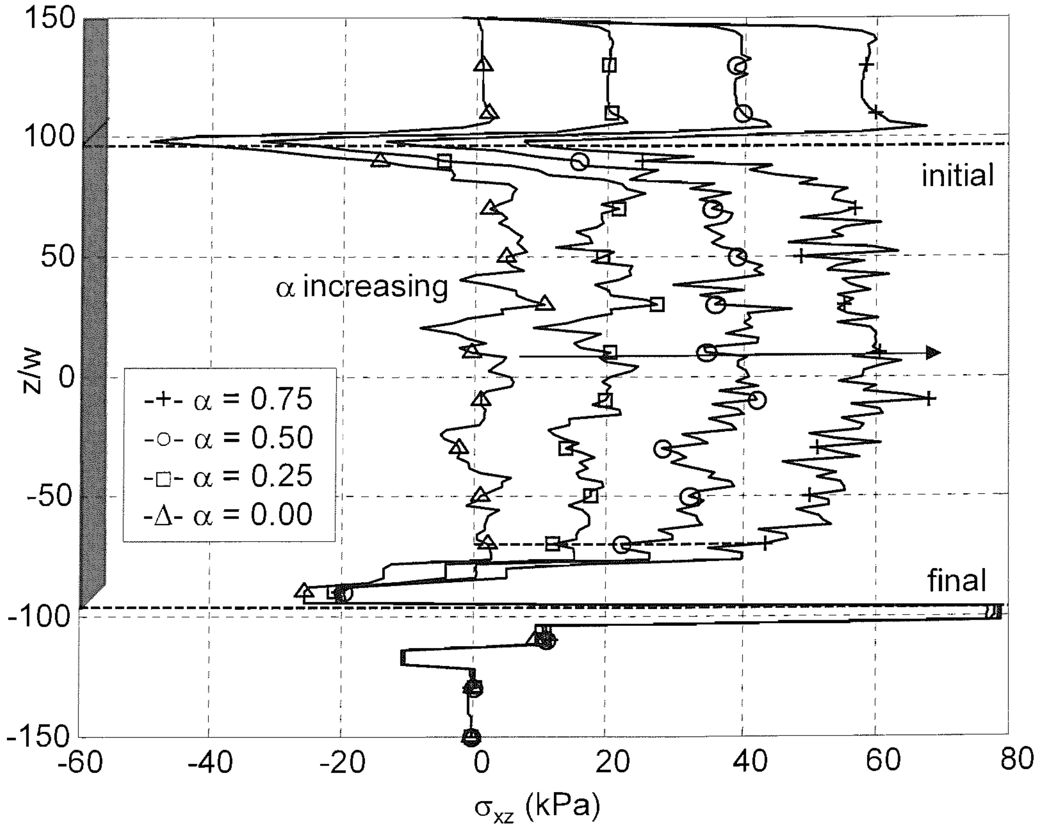

Figure 6-38 Influence of adhesion (α) on (σ_{xz}) along z-profile (x=y=5w) in 3D penetration models

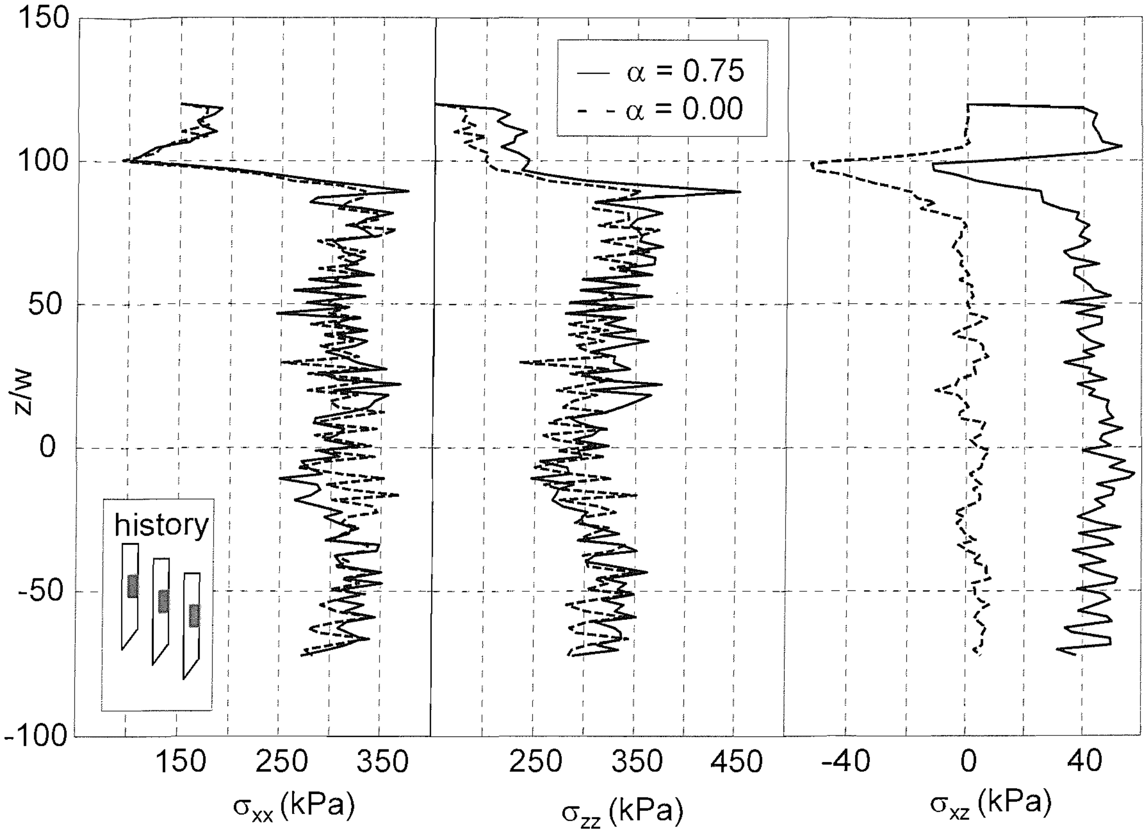

Figure 6-39 Influence of adhesion (α) on stresses at 100mm above tip in 3D penetration models

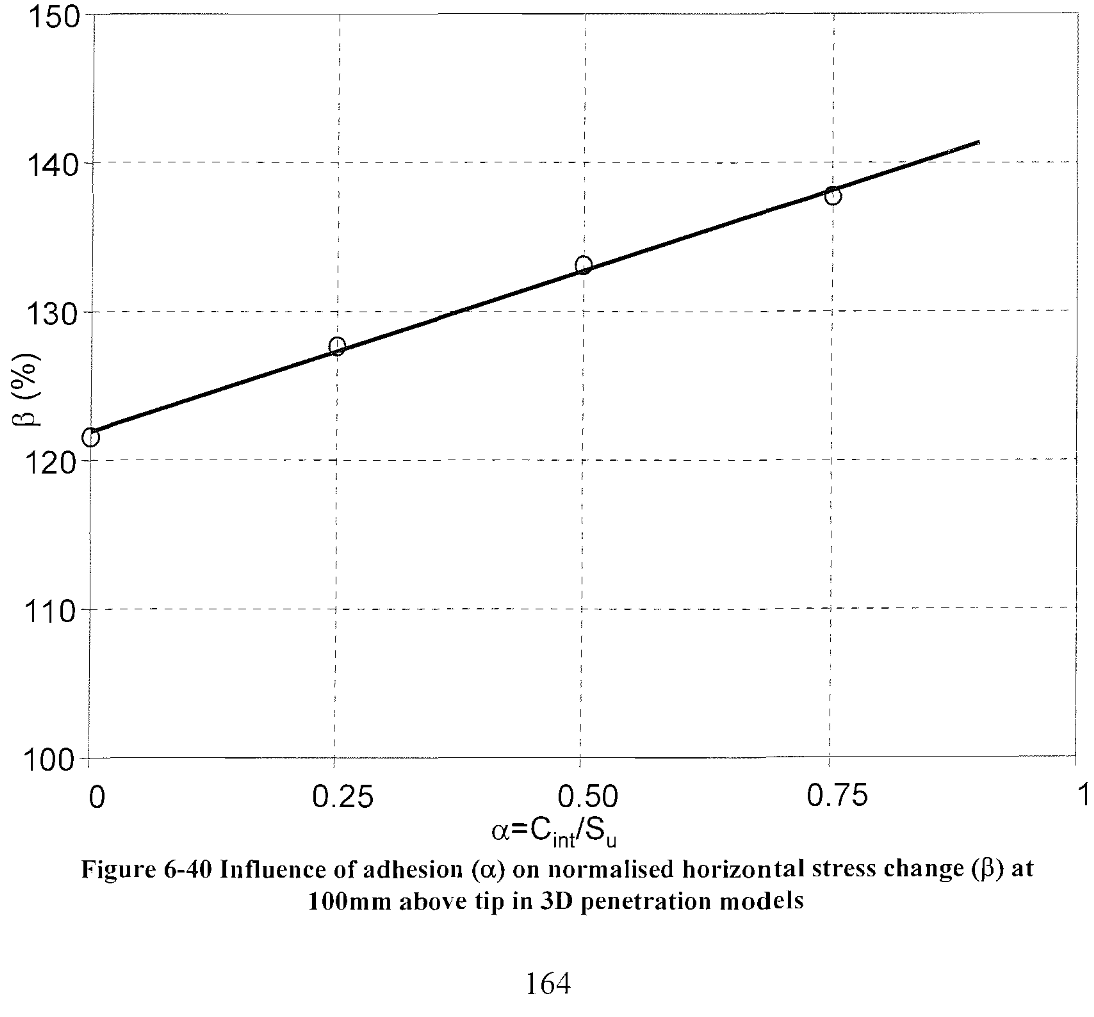

Figure 6-40 Influence of adhesion (α) on normalised horizontal stress change (β) at 100mm above tip in 3D penetration models

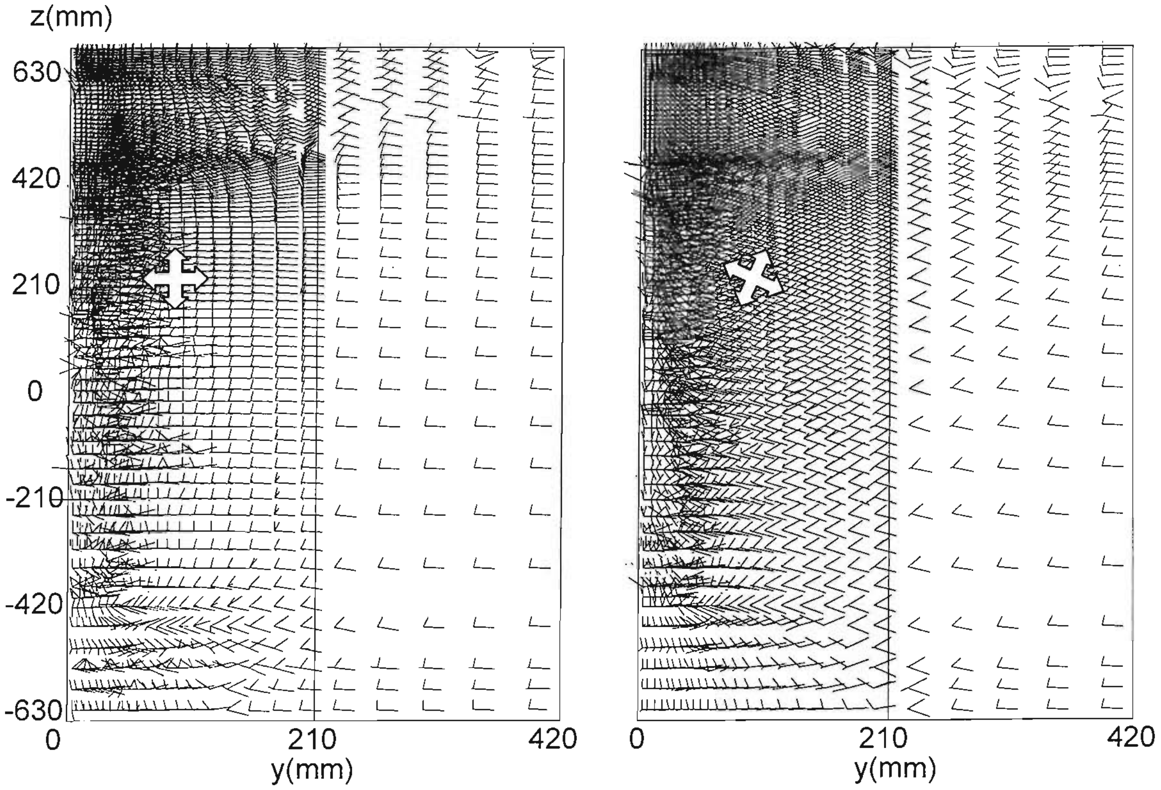

(a) α=0

(b) α=0.75

Figure 6-41 Influence of interface adhesion (α) on principal stress indicators at the end of penetration (3D models on x=5w plane)

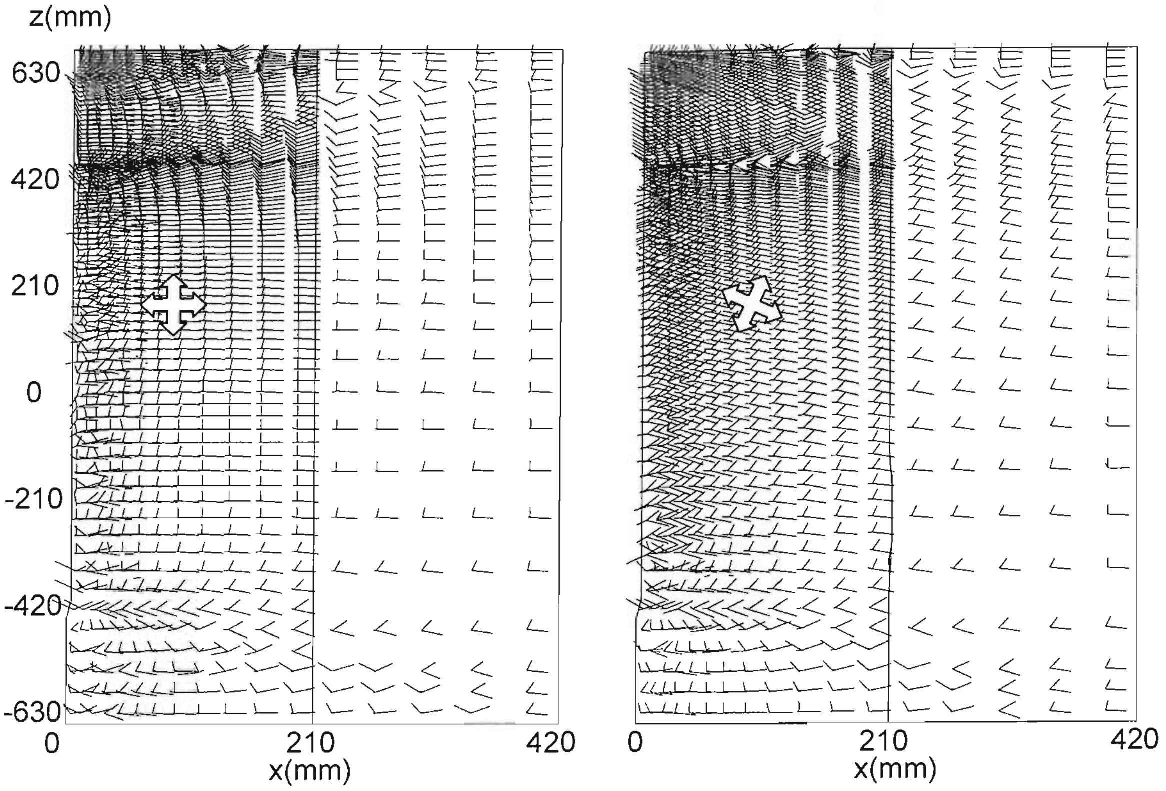

(a) α=0

(b) α=0.75

Figure 6-42 Influence of interface adhesion (α) on principal stress indicators at the end of penetration (3D models on y=5w plane)

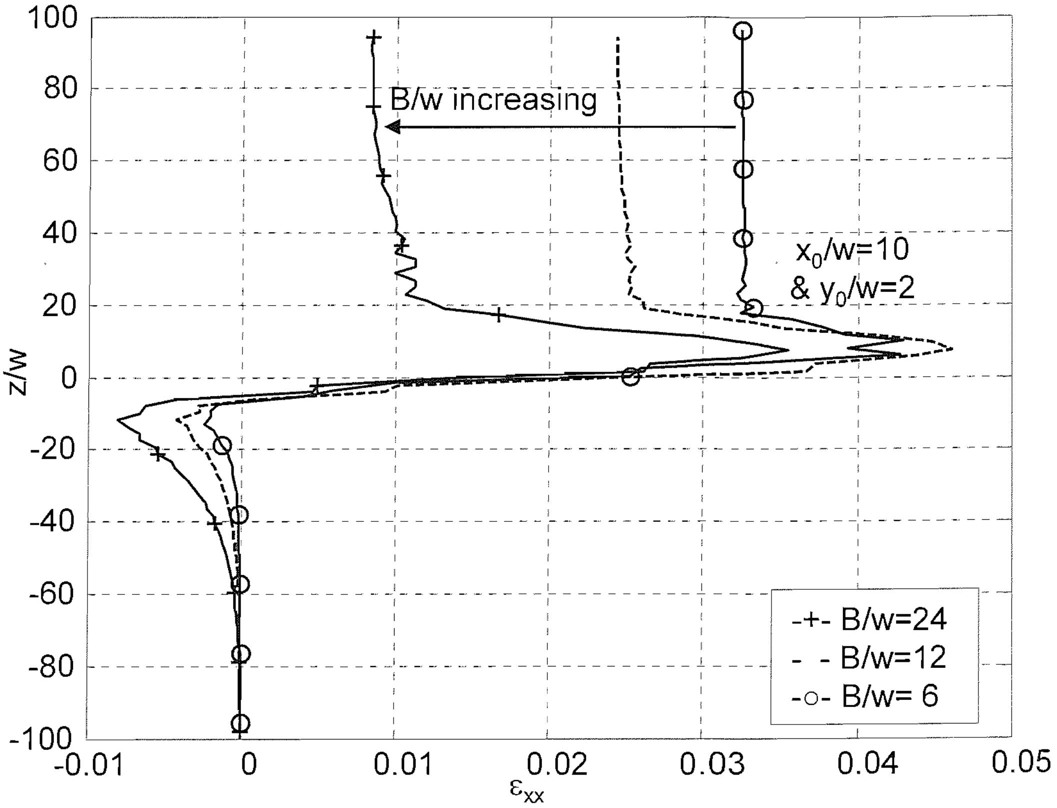

Figure 6-43 Influence of aspect ratio (B/w) on strain paths for (ε_{xx}) in 3D penetration models

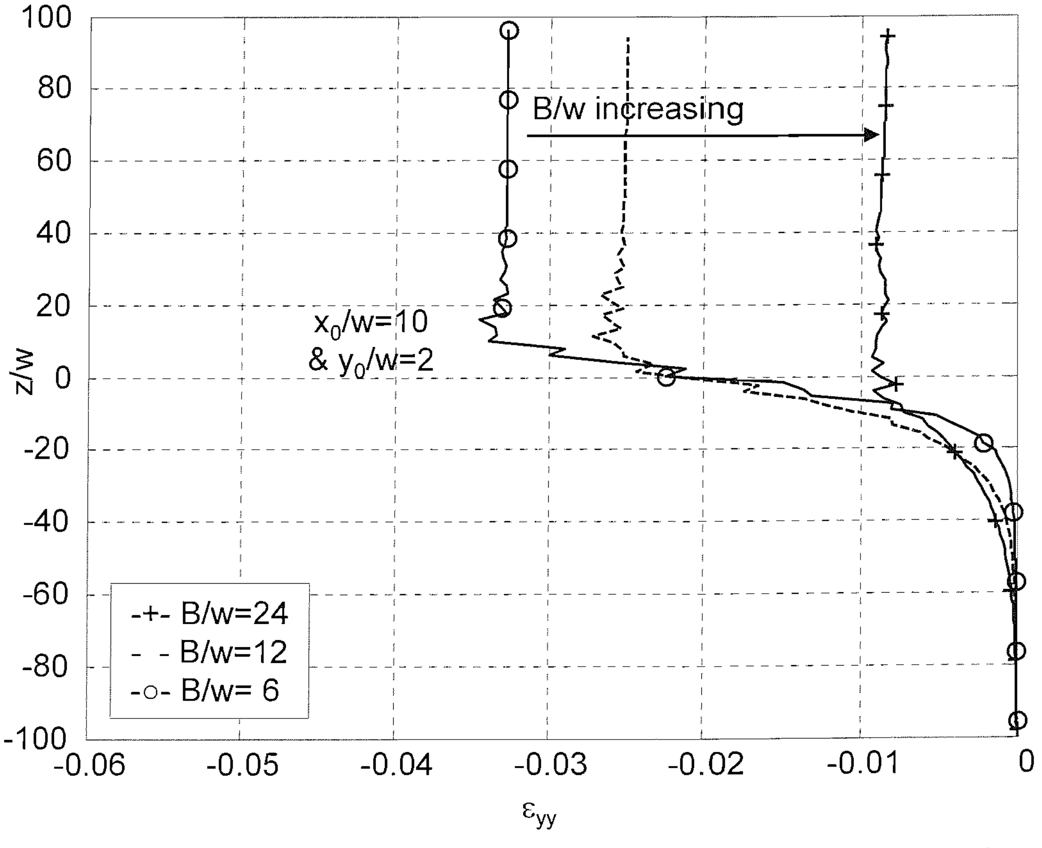

Figure 6-44 Influence of aspect ratio (B/w) on strain paths for (ε_{yy}) in 3D penetration models

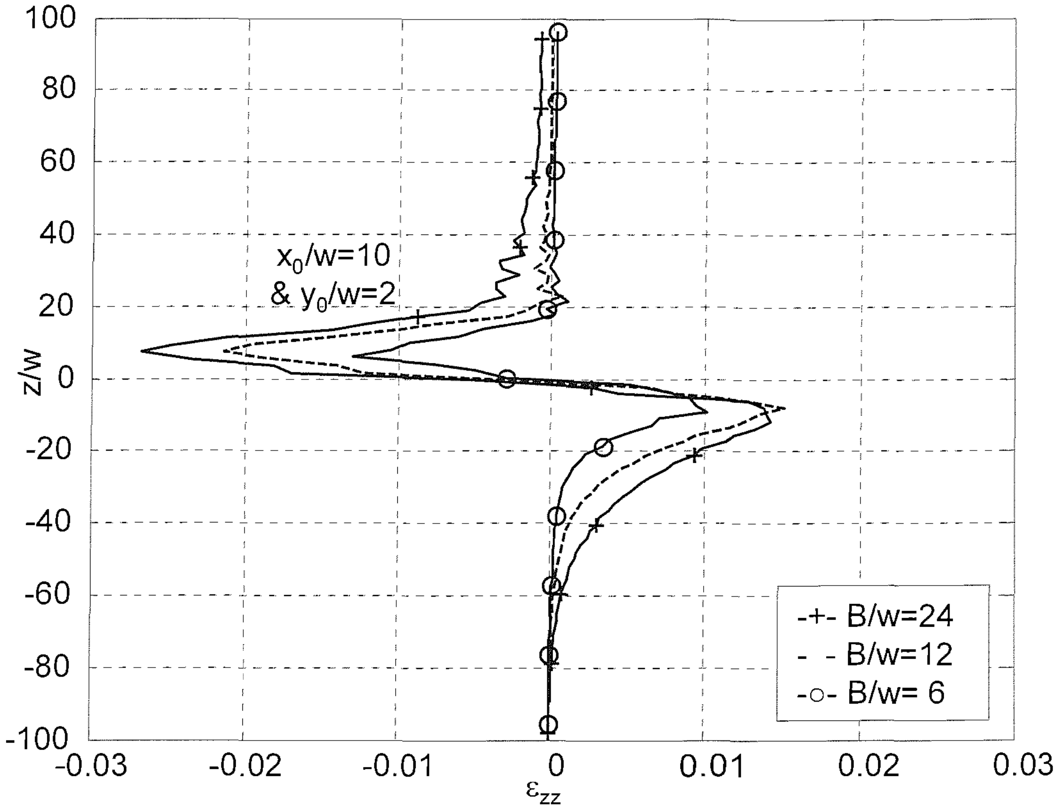

Figure 6-45 Influence of aspect ratio (B/w) on strain paths for (ε_{zz}) in 3D penetration models

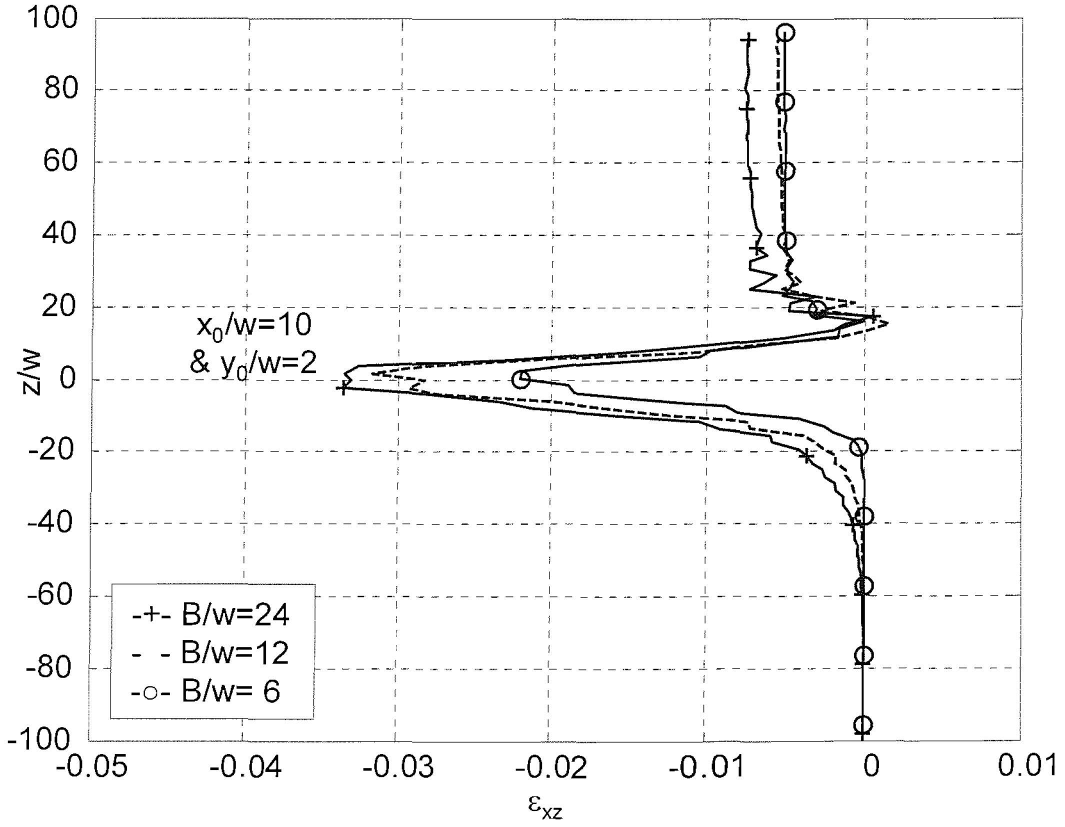

Figure 6-46 Influence of aspect ratio (B/w) on strain paths for (ε_{xz}) in 3D penetration models

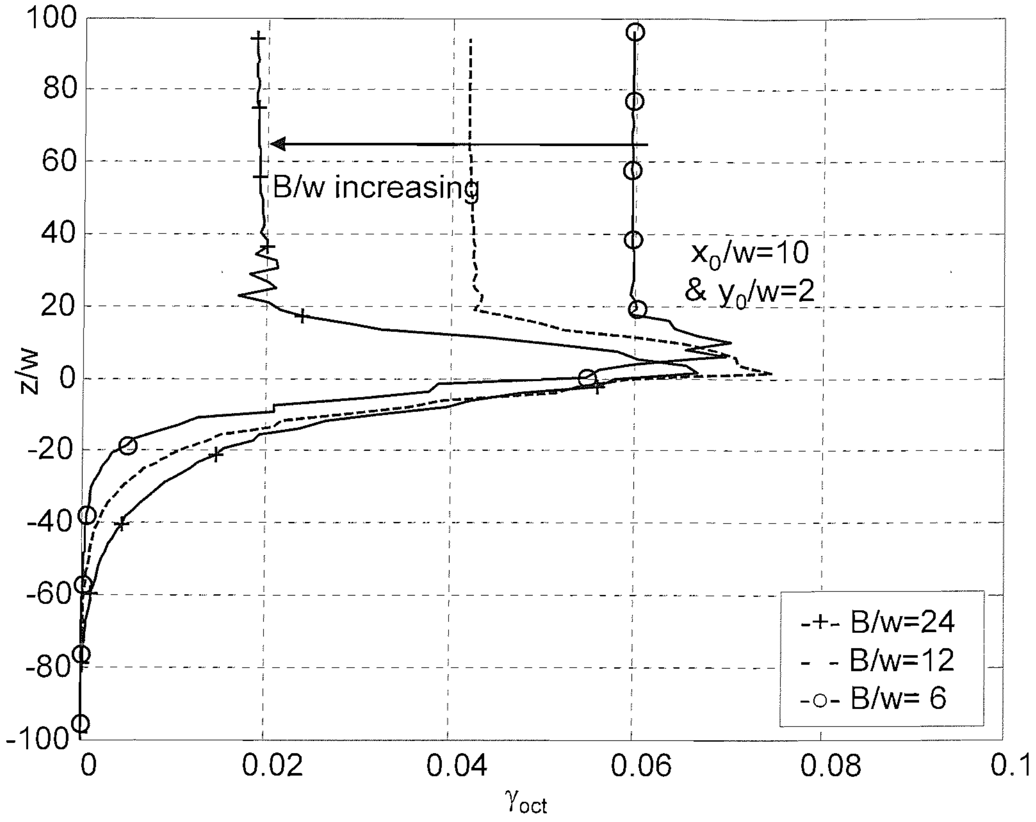

Figure 6-47 Influence of aspect ratio (B/w) on strain paths for (γ_{oct}) in 3D penetration models

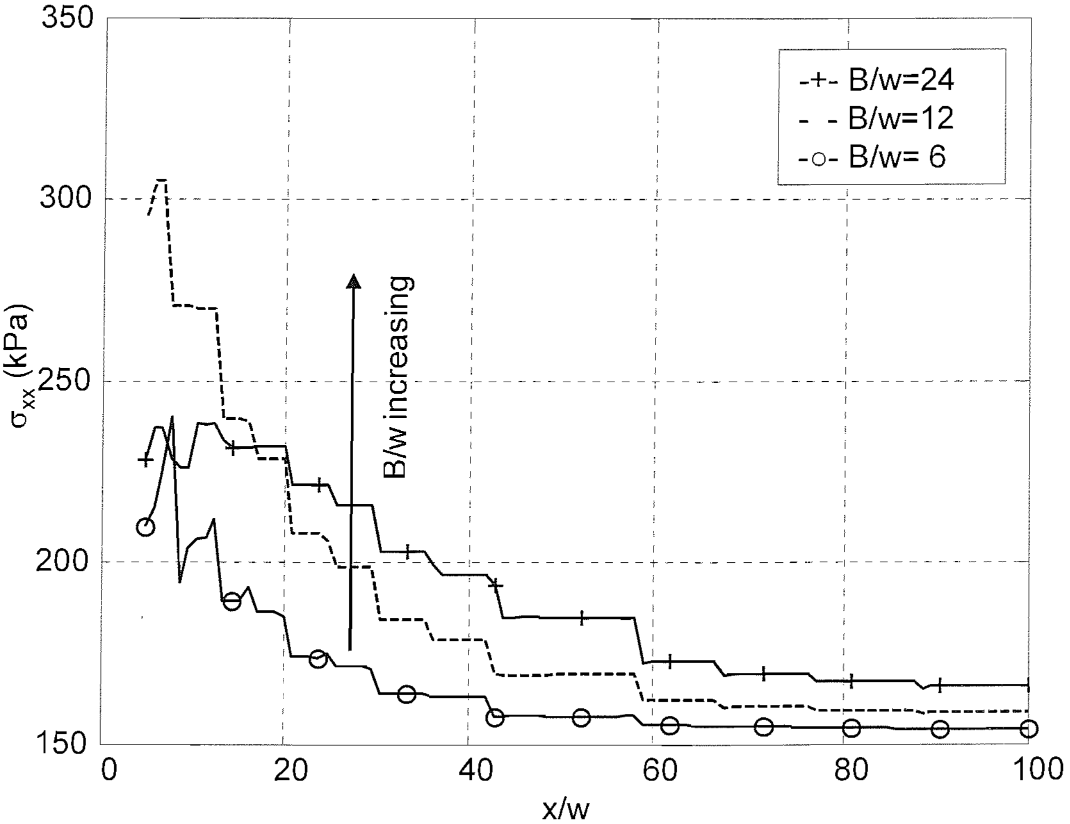

Figure 6-48 Influence of aspect ratio (B/w) on (σ_{xx}) along x-profile (y=5w, z=-70w) in 3D penetration models

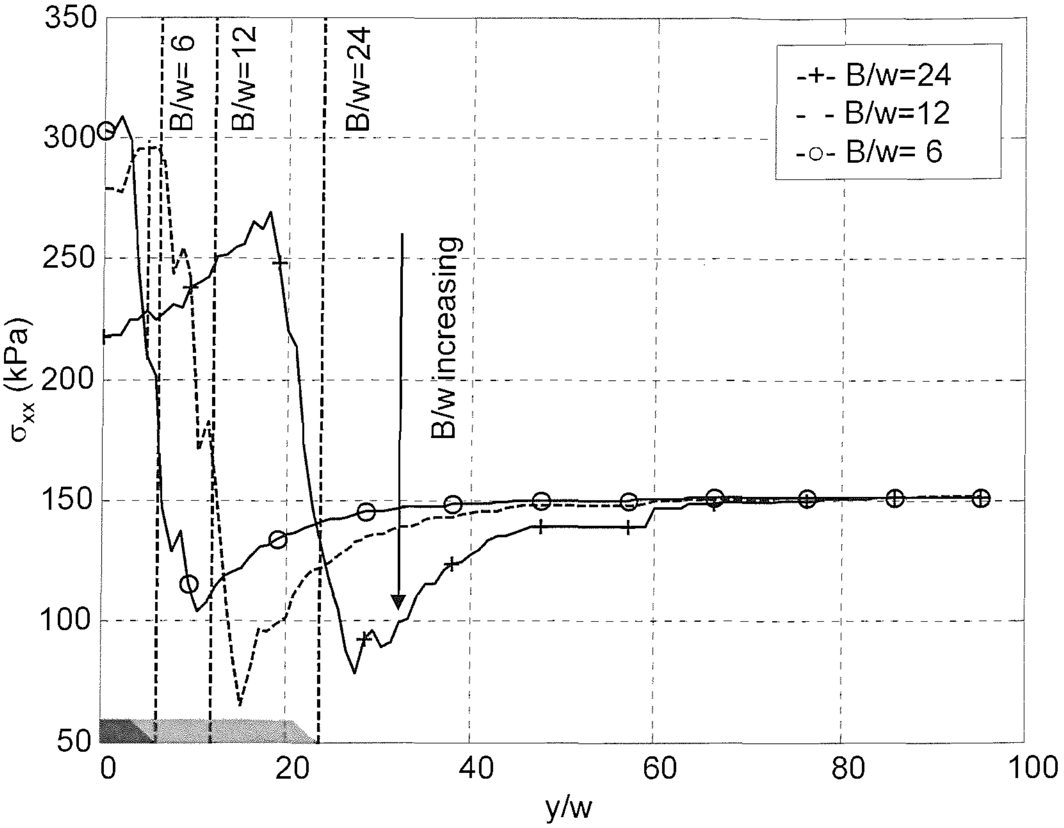

Figure 6-49 Influence of aspect ratio (B/w) on (σ_{xx}) along y-profile (x=5w, z=-70w) in 3D penetration models

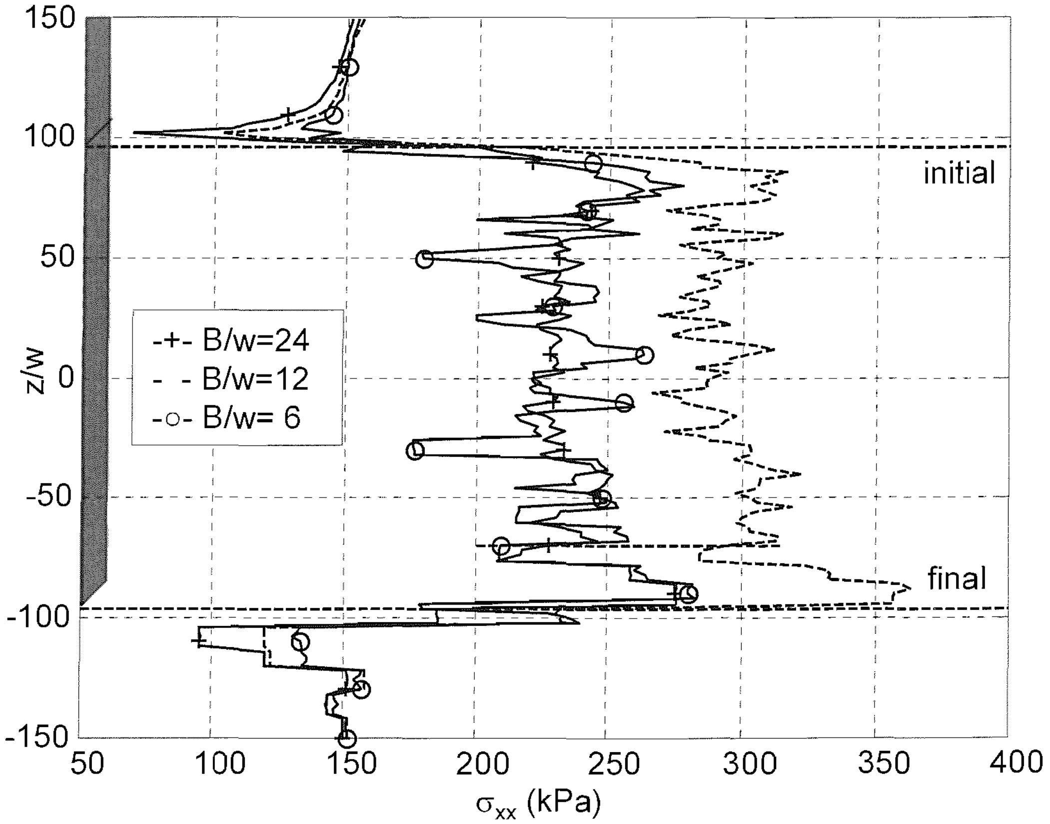

Figure 6-50 Influence of aspect ratio (B/w) on (σ_{xx}) along z-profile (x=y=5w) in 3D penetration models

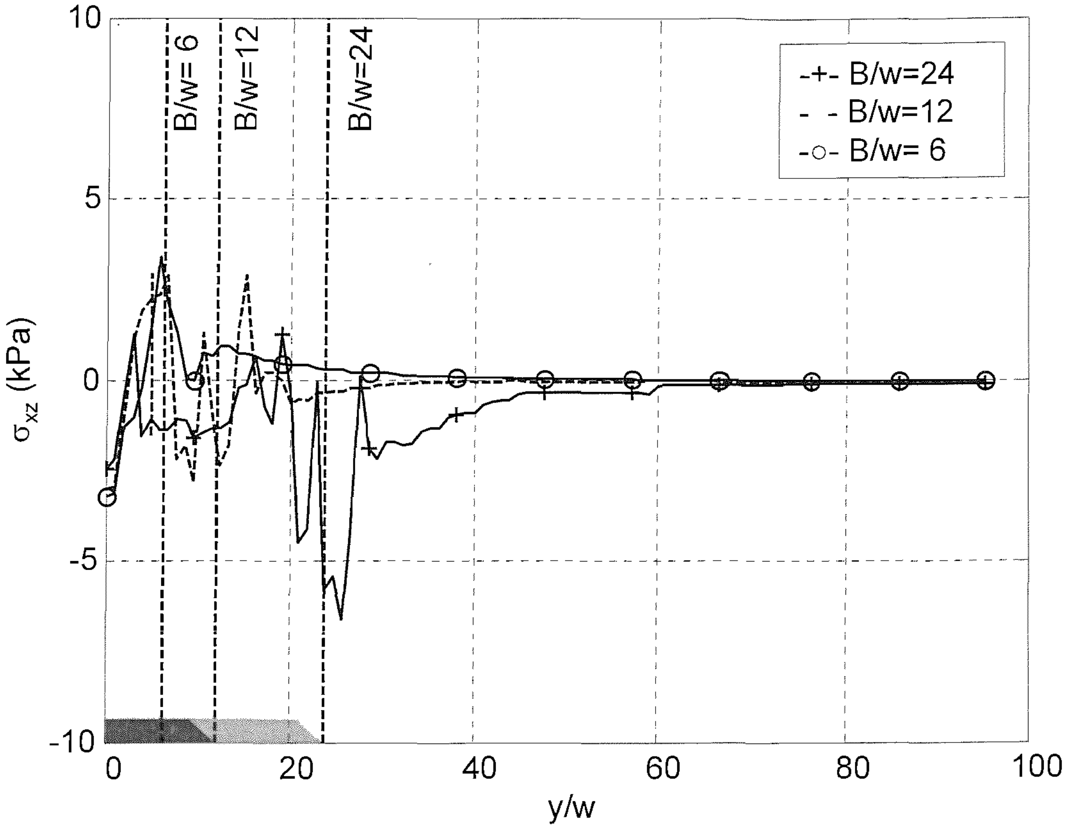

Figure 6-51 Influence of aspect ratio (B/w) on (σ_{xz}) along y-profile (x=5w, z=-70w) in 3D penetration models

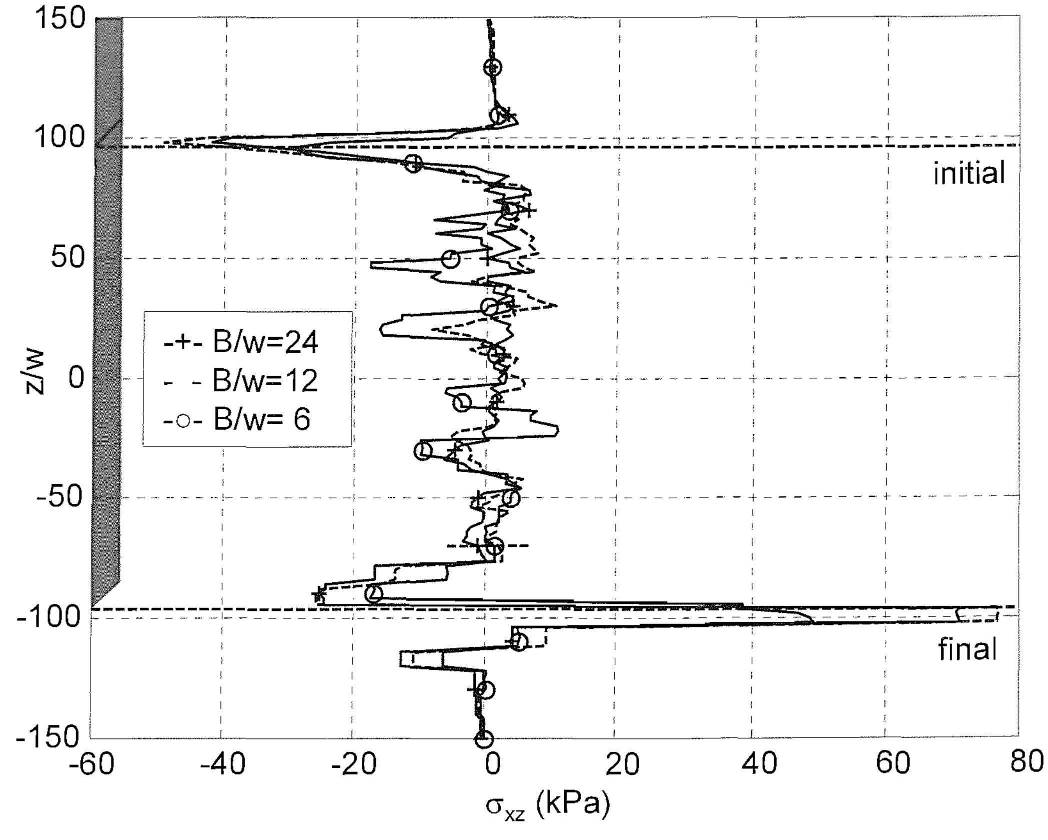

Figure 6-52 Influence of aspect ratio (B/w) on (σ_{xz}) along z-profile (x=y=5w) in 3D penetration models

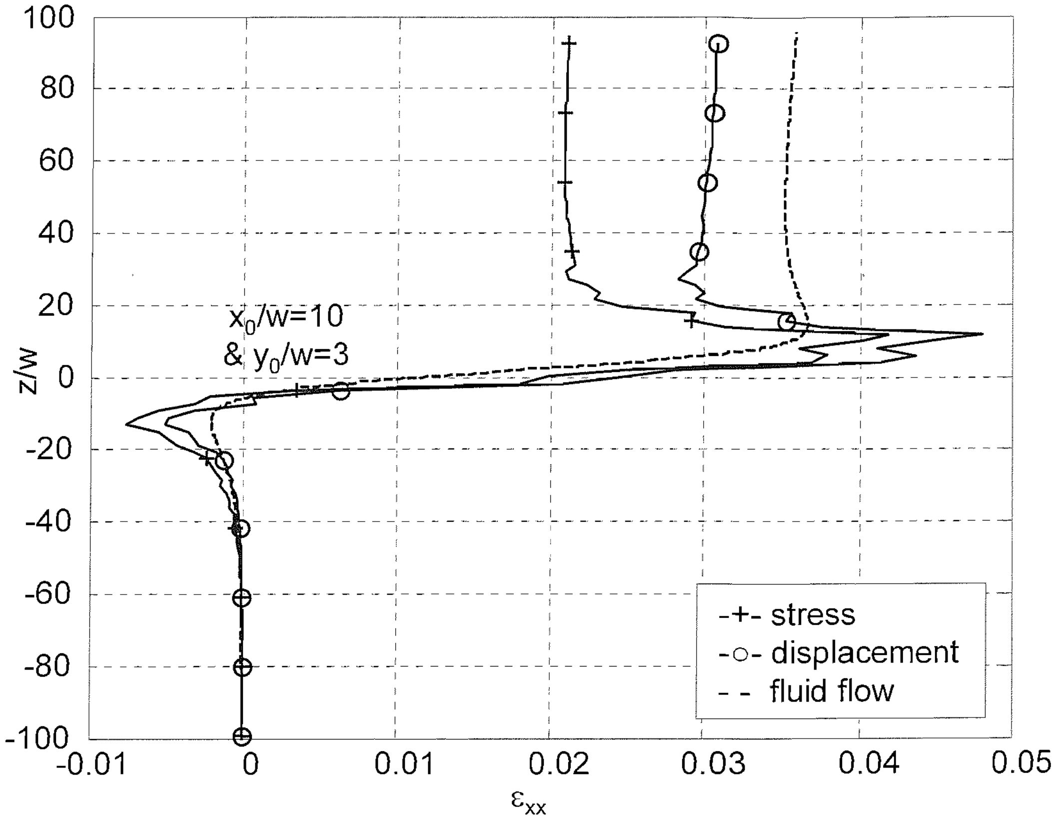

Figure 6-53 Influence of boundary type (stress/displacement controlled) on strain paths for (ε_{xx}) in 3D penetration models

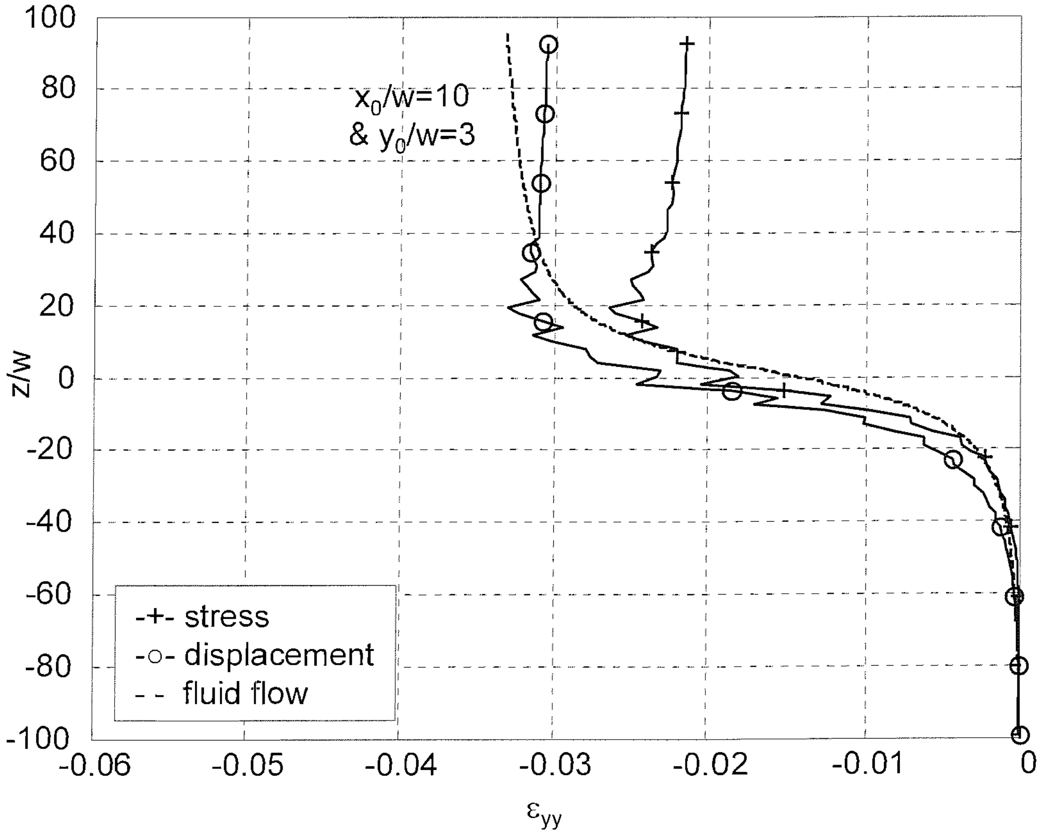

Figure 6-54 Influence of boundary type (stress/displacement controlled) on strain paths for (ε_{yy}) in 3D penetration models

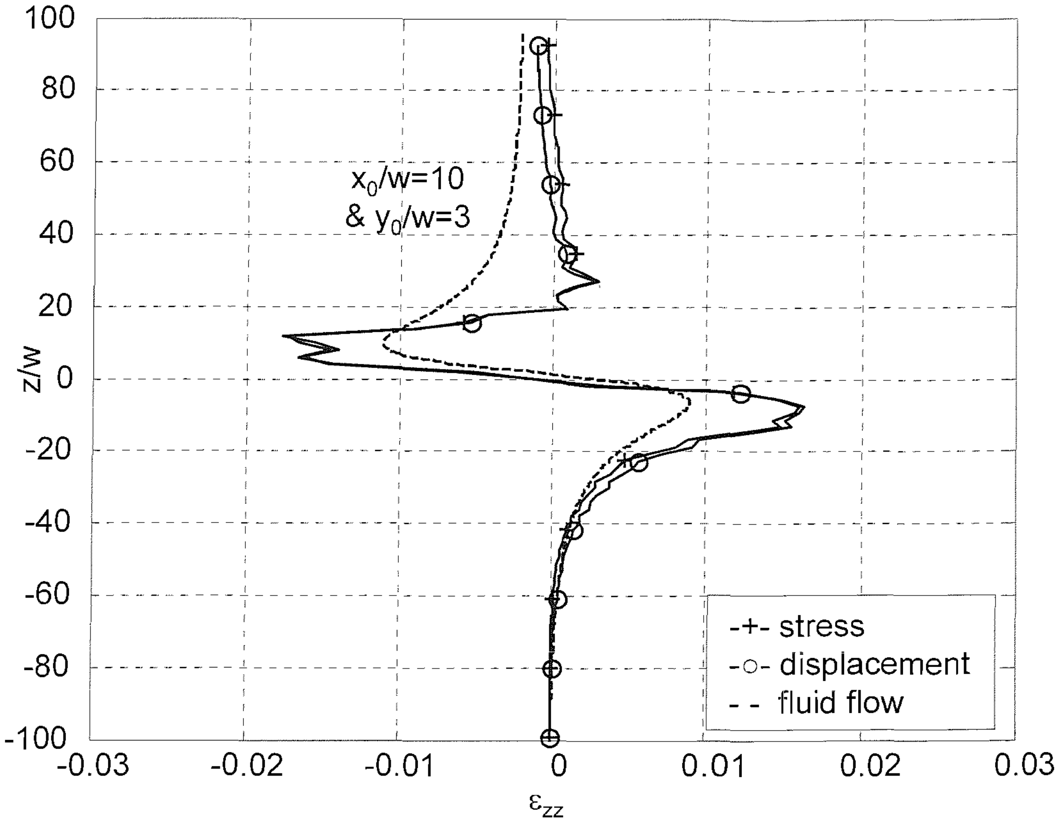

Figure 6-55 Influence of boundary type (stress/displacement controlled) on strain paths for (ε_{zz}) in 3D penetration models

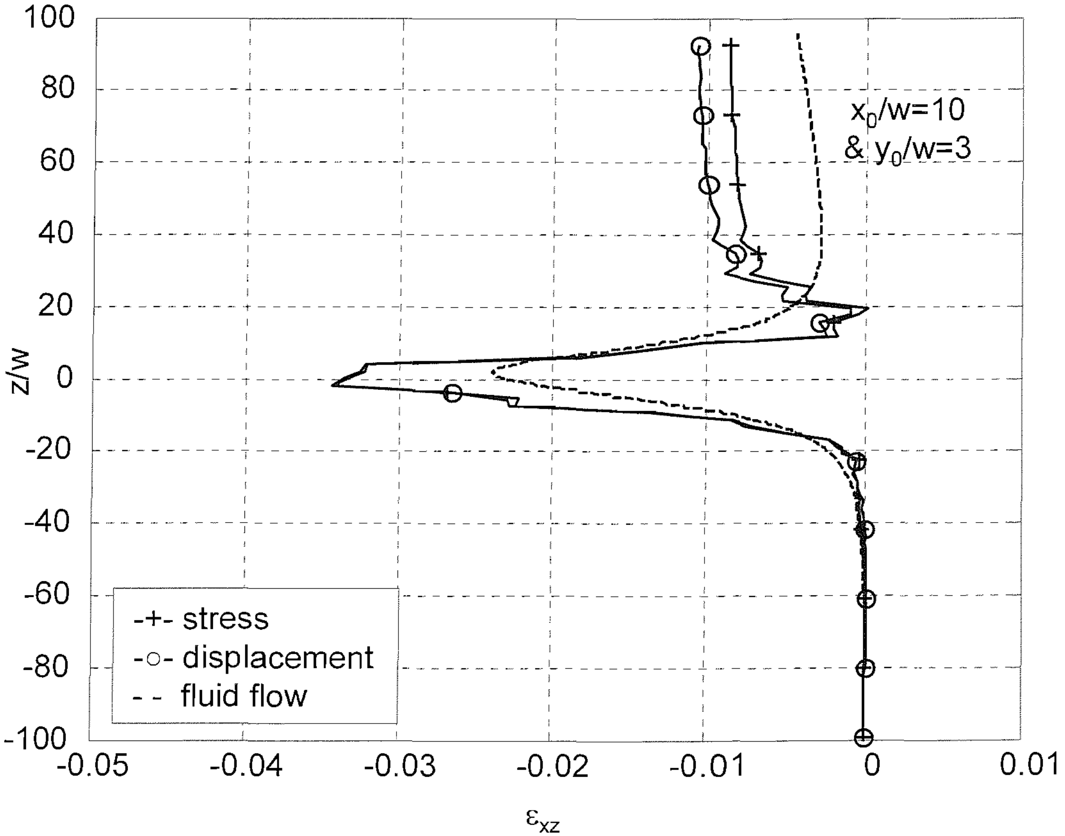

Figure 6-56 Influence of boundary type (stress/displacement controlled) on strain paths for (ε_{xz}) in 3D penetration models

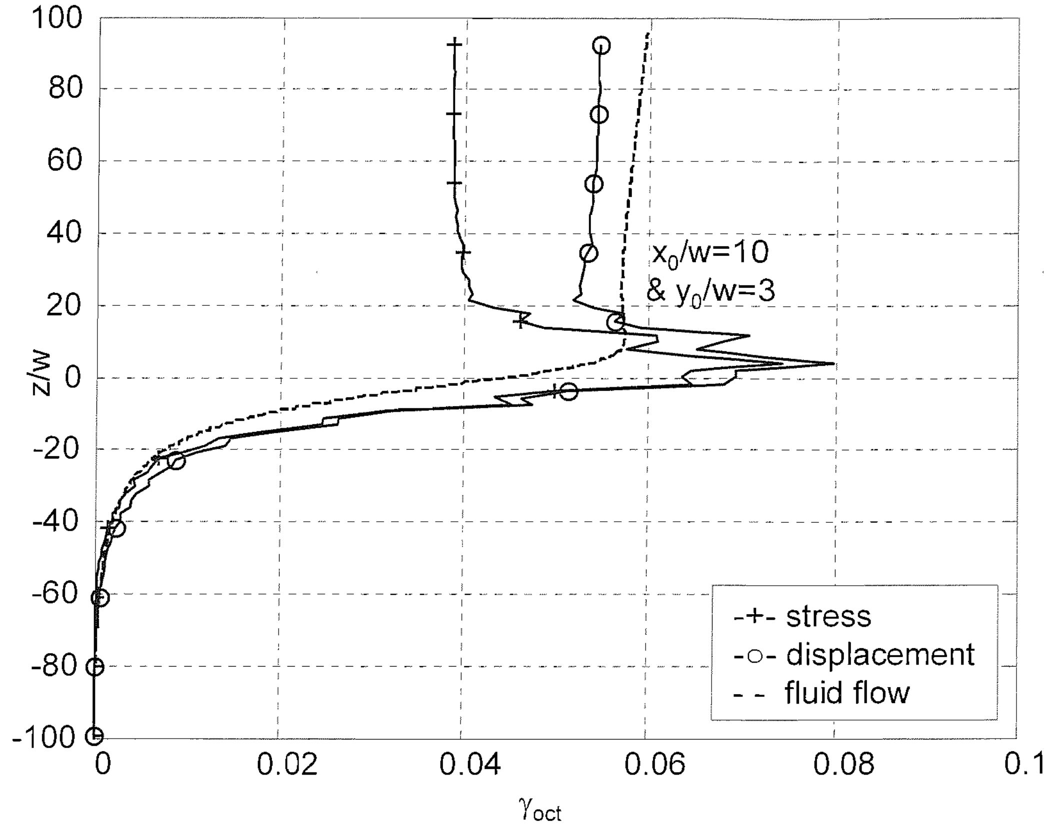

Figure 6-57 Influence of boundary type (stress/displacement controlled) on strain paths for (γ_{oct}) in 3D penetration models

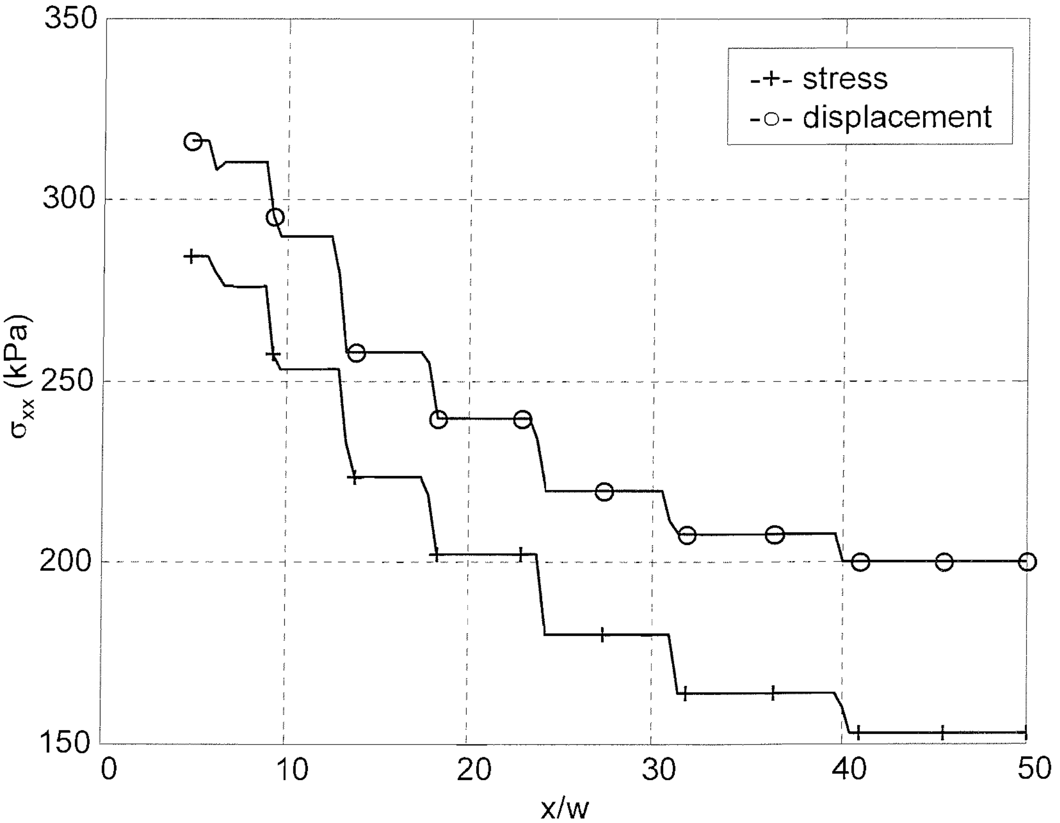

Figure 6-58 Influence of boundary type (stress/displacement controlled) on (σ_{xx}) along x-profile (y=5w, z=-70w) in 3D penetration models

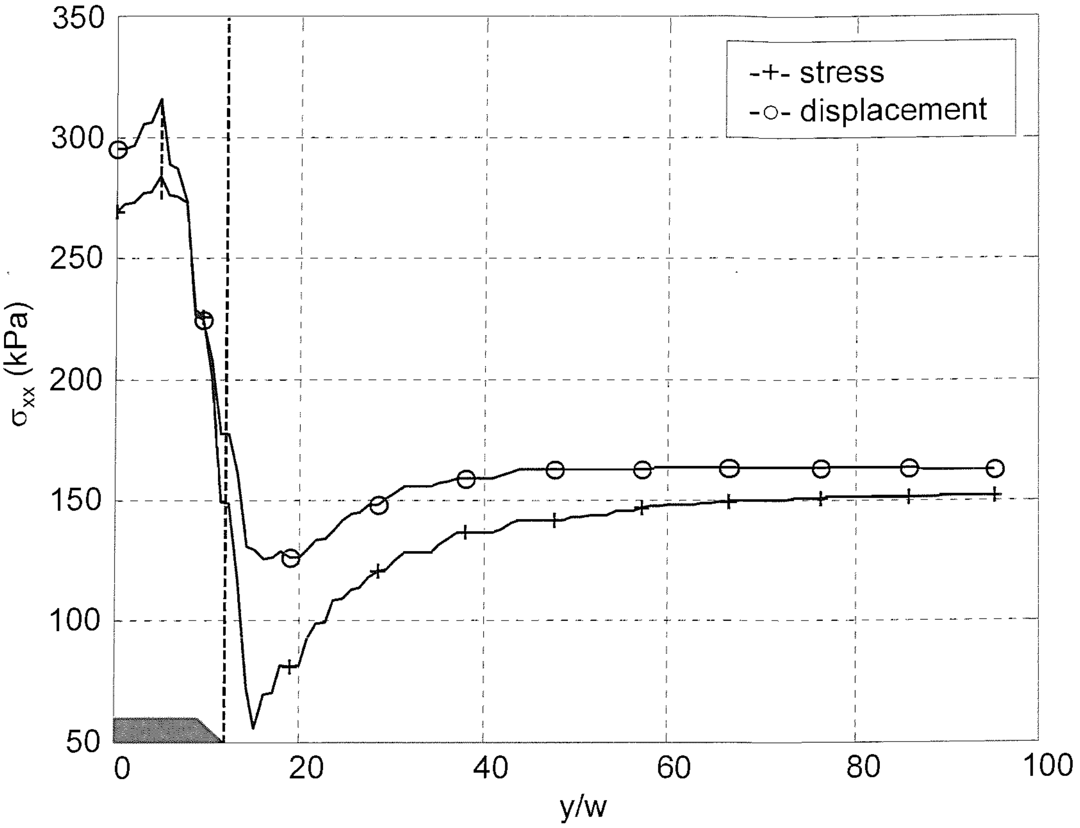

Figure 6-59 Influence of boundary type (stress/displacement controlled) on (σ_{xx}) along y-profile (x=5w, z=-70w) in 3D penetration models

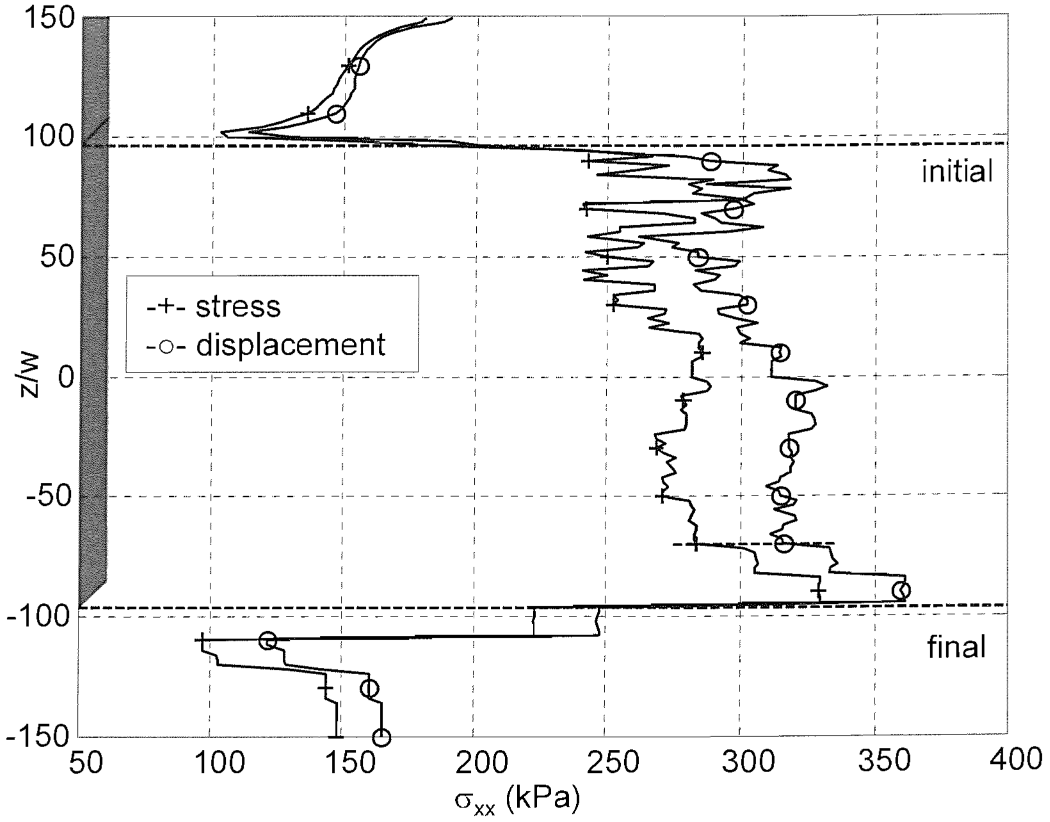

Figure 6-60 Influence of boundary type (stress/displacement controlled) on (σ_{xx}) along z-profile (x=y=5w) in 3D penetration models

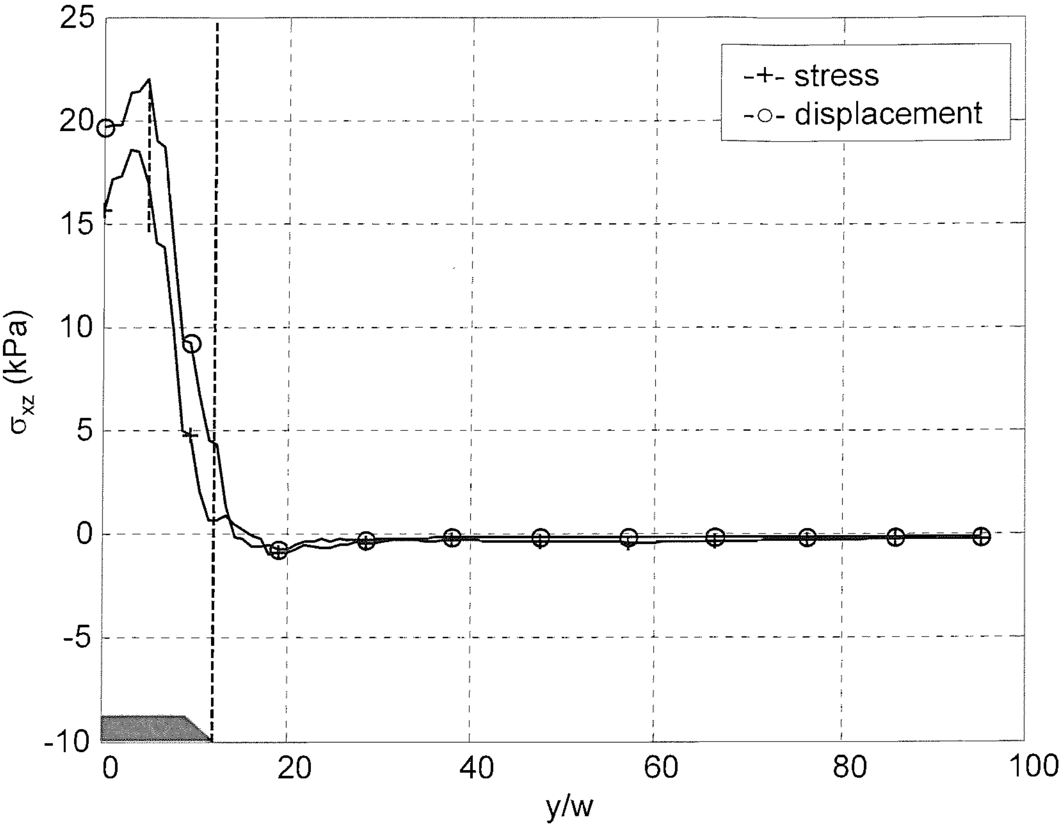

Figure 6-61 Influence of boundary type (stress/displacement controlled) on (σ_{xz}) along y-profile (x=5w, z=-70w) in 3D penetration models

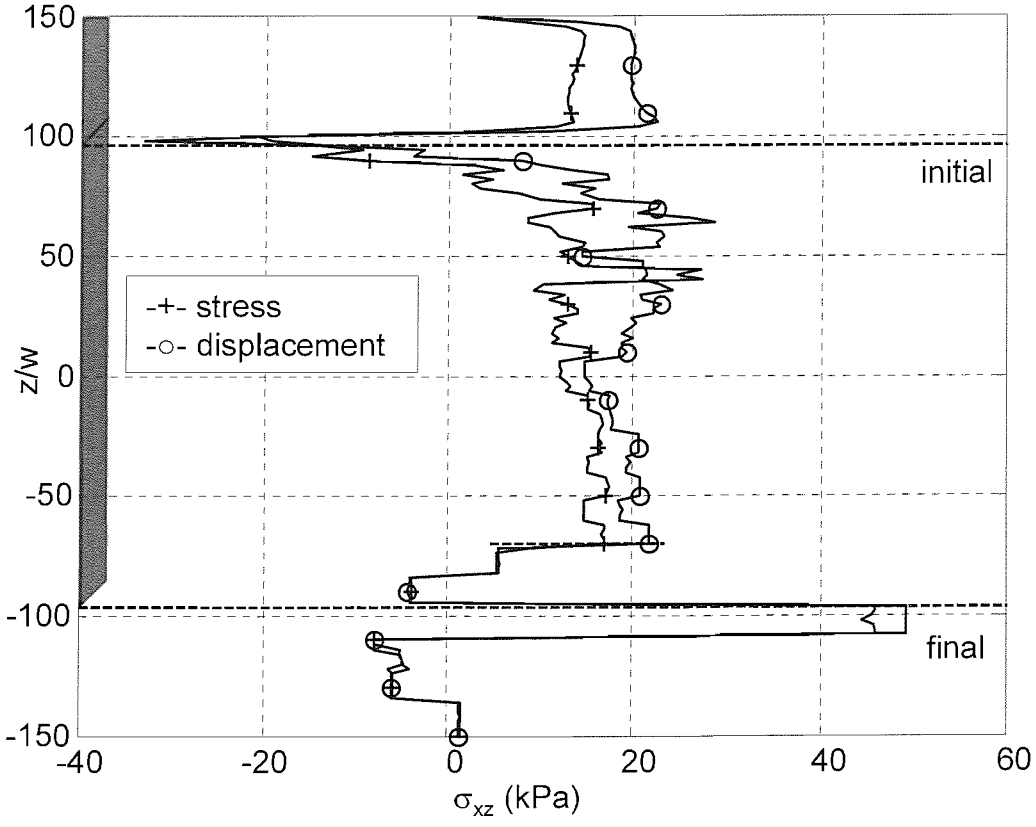

Figure 6-62 Influence of boundary type (stress/displacement controlled) on (σ_{xz}) along z-profile (x=y=5w) in 3D penetration models

7 DISCUSSION

7.1 Introduction

It was established in the literature review (Chapter 2) that the existing empirical correlations used for interpreting spade cell measurements were inadequate and that there was a need for a novel interpretation approach. Numerical modelling techniques were used to examine the influences of various parameters (e.g. soil strength and interface adhesion) on the stress-strain behaviour of soil during the penetration of a spade cell. The outcomes of these models may later be used to devise a robust interpretation technique for spade cells as well as modifying current chamber test practice.

Numerical modelling was performed for the idealised spade cell geometries, the "simple wedge" and "chisel" in the 2D and 3D analyses respectively. 2D fluid flow analyses were also performed for three other geometries, the "simple wall", "sharp wedge" and "blunt wedge". FLAC was used for both the 2D fluid flow (Chapter 3) and soil penetration (Chapter 4) analyses. FLUENT and GAMBIT were used for the 3D fluid flow analyses (Chapter 5), whilst the 3D soil penetration analyses were carried out using FLAC^{3D} (Chapter 6).

In this chapter, the results from various 2D and 3D analyses are summarised, discussed and compared with previous investigations. The seven key topics discussed are:

- Influence of tip geometry;
- Influence of out-of-plane strain (2D/3D);
- Influence of soil shear modulus (G);
- Influence of soil undrained shear strength (S_u);

- Influence of interface adhesion (α);
- Influence of aspect ratio (B/w); and
- Influence of boundary types (in chamber simulations).

7.2 Influence of tip geometry

Two-dimensional fluid flow analyses were carried out for four geometries, the "simple wall", "simple wedge", "sharp wedge" and "blunt wedge", all of which have a half-width (w) of 4.2mm and are shown in Figures 3.2, 3.14, 3.25 and 3.26 respectively. The strain paths around these geometries were compared to assess the influence of the tip geometry on the penetration-induced disturbances.

The "simple wall" had a rounded tip, while the tip of the "simple wedge" was sharp. Strain paths were determined for the infinite flow field around these two geometries using analytical (superposition) as well as numerical (FLAC) methods. The values of peak normal strains ($\varepsilon_{xx\ min}$, $\varepsilon_{xx\ max}$, $\varepsilon_{zz\ min}$ and $\varepsilon_{zz\ max}$) determined for the "simple wall" (Figures 3.3 and 3.4) were approximately equal to those determined for the "simple wedge" (Figures 3.15 and 3.16). However, in comparison to the "simple wall" results, the normal peak strains around the "simple wedge" were reached later (i.e. further along streamlines) due to the sharp tip. Comparison of shear (ε_{xz}) strain paths showed that the peak strains for the "simple wedge" (Figure 3.17) were less than those determined for the "simple wall" (Figure 3.5). The shift in the location of peak strains was also observed for the peak shear (ε_{xz}) strain.

The influence of the tip angle was further investigated by comparing the strain paths determined for the "sharp wedge" and the "blunt wedge" with apex angles of 18° and 60° respectively. FLAC was used to determine strain paths numerically for the flow around these two geometries. The peak normal and shear strains (ε_{xx}, ε_{yy} and ε_{xz}) were higher and reached earlier for the "blunt wedge" in comparison with the results of the "sharp wedge", as illustrated in Figures 3.27, 3.28 and 3.29.

In common with previous experimental and numerical investigations (La Rochelle *et al.*, 1987; Siddique, 1990; Clayton *et al.*, 1998) it is evident from these outputs that the shape of the tip of a penetrating object significantly influences the disturbance generated as a result of penetration.

7.3 Influence of out-of-plane strain

The adequacy of two-dimensional plane strain analyses for estimating the three-dimensional changes that occur around the spade cell during penetration was examined by comparing the strain paths determined from the 2D analyses with the results of the 3D analyses. The outcomes of the comparison of strain paths determined from both the fluid flow and soil penetration analyses are summarised in the following section.

7.3.1 Fluid flow analysis

Figure 7.1 shows the “sharp wedge” and “chisel” geometries. It may be argued that strain paths determined for a streamline close to the centreline of the “chisel” geometry should be similar to those determined for the “sharp wedge” geometry. This was evaluated by comparing strain paths determined for a streamline located at $x_0/w=10$ and $y_0/w=2$ from the “chisel” centreline (3D) with those determined for the $x_0/w=10$ streamline around the “sharp wedge” (2D). Due to the difference in the tip angle between the “chisel” and “sharp wedge”, a quantitative comparison between strain values is not possible. However, the general pattern of strain changes for streamlines around these two geometries may be compared to investigate the role of the out-of-plane strain component.

The strain paths for ε_{xx} strains, which are shown in Figure 7.2 for the 2D and 3D models, were substantially similar consisting of three sections: extension, followed by compression and the re-extension. In both the 2D and 3D fluid flow models, the extensive strain changes were relatively small and the dominant strain gradient was a compressive strain change between $z/w= -10$ and $z/w=10$.

The strain path determined from the three-dimensional fluid flow analysis for the out-of-plane strain (ε_{yy}) showed an extensive behaviour for the examined streamline with the maximum gradient of change being between z/w= -10 and z/w=10, Figure 5.4.

Although in both 2D and 3D analyses, strain paths for the vertical strain (ε_{zz}) consisted of three sections (compression, extension and recompression), there was a difference between the magnitude of strains determined from the 2D and 3D analyses, as shown in Figure 7.3. In the 2D analysis the absolute value of vertical extensive strain (ε_{zz}) at any level above the tip was higher than the strain value at the corresponding level below the tip, ε_{zz} (z/w=a)>ε_{zz} (z/w= -a). In the 3D analysis however, the absolute value of vertical strain (ε_{zz}) at any level above the tip was approximately equal to the strain value at the corresponding level below the tip.

It is observed that, even in the case of a streamline close to the centreline, there was a difference between the deformation of a streamline predicted by the 3D and the 2D analyses. This difference may be readily explained within the concept of the conservation of volume. In the 2D analysis, as the out-of-plane strain was zero ($\varepsilon_{yy}=0$), the conservation of volume ($\varepsilon_{xx}+\varepsilon_{yy}+\varepsilon_{zz}=0$) required that the shape of strain paths for the horizontal and vertical strains mirror each other ($\varepsilon_{zz}=-\varepsilon_{xx}$). Due to the existence of the out-of-plane strain (ε_{yy}); however, the pattern of the vertical (ε_{zz}) strain path in the 3D analysis was different from the strain path for the horizontal (ε_{xx}) strain, $\varepsilon_{zz}=-(\varepsilon_{xx}+\varepsilon_{yy})$.

The strain paths for shear (ε_{xz}) strains determined from the 2D and 3D analyses are shown in Figure 7.4. In both the 2D and 3D analyses, the shear strains increased and reached their peak values immediately above the tip level. The shear strains reduced from the tip level and attained values close to zero at the end of the strain path.

The differences observed between the results of 2D and 3D fluid flow analyses were similar to those determined from the fluid flow analyses for the dilatometer (refer to section 2.5.3). The reversal of vertical strains around the three-dimensional "chisel" geometry has also been observed by other researchers for various geometries, including the "simple pile" (Baligh, 1985), dilatometer (Huang, 1989), "simple plate" (Aubeny, 1992) and cone (Gill and Lehane, 2000).

7.3.2 Soil penetration analysis

The strain paths determined from the 2D and 3D soil penetration models were also compared. Strain paths were evaluated from the incremental deformations of a soil element as the "simple wedge" or "chisel" (Figure 7.1) was penetrated into a soil. Due to the geometrical differences, a quantitative comparison of the strain paths determined from the 2D and 3D analyses was not justifiable; however, their general pattern may be evaluated.

The strain path for the ε_{xx} strains had a similar pattern in both the 2D and 3D penetration models, as shown in Figure 7.5. The ε_{xx} strain path consisted of three sections: extension, compression and re-extension with the peak compression and extension strain values reached at 10w above and below the tip level.

In common with the behaviour predicted in the 3D fluid flow analyses, the strain path for the longitudinal (ε_{yy}) strain in the 3D soil penetration model showed an extensive strain change, Figure 6.6. In contrast to the fluid flow analyses (Figure 5.4) however, the peak lateral strain was reached at the z/w=10 level above the tip.

The strain path for vertical (ε_{zz}) strains determined in the 2D analyses were different from those obtained from the 3D models, as shown in Figure 7.6. In the 2D analyses, the absolute value of vertical strain at any level above the tip was higher than the strain value at the corresponding level below the tip. In the 3D analyses however, vertical strains above the tip were approximately equal to strain values at the corresponding level below the tip.

Figure 7.7 shows that the strain paths for shear (ε_{xz}) strains determined from both the 2D and 3D soil penetration analyses. The peak shear strains were attained as the soil elements passed the tip level. The shear strains reduced slightly from the tip level until z/w=20, before increasing again.

Figure 7.8 shows the displacement pattern determined for a soil element in the 3D model, as the "chisel" penetrated the soil. It is evident (in the non-adhesive condition) that the soil element is monotonically pushed away from the "chisel" in the x-y plane during penetration. The soil element however, returned to its initial vertical position (z) as penetration took place. This feature has also been observed in the displacement measurements obtained from the penetration tests in artificial soil (Gill and Lehane, 2001).

The following points are paraphrased here:

1. The agreement observed between the strain paths determined from the fluid flow and soil penetration analyses in both the 2D (Chapter 4) and 3D (Chapter 6) models confirmed that the penetration-induced deformations around an object may be readily estimated using the strain path method (fluid flow analysis); and
2. As soils are non-linear (Atkinson, 2000), the history of changes they undergo affects their current stress-strain behaviour. The estimation of soil behaviour in a three-dimensional penetration problem, with a two-dimensional model could hence lead to significant errors in the behaviour predicted for soils around a penetrating object.

7.4 Influence of soil rigidity

The rigidity index (I_r) of a soil defined as the ratio of its shear modulus to undrained shear strength (G/S_u) and has been used for comparing different types of soil (Atkinson, 2000). Vesic (1972) showed that for a Tresca soil, cavity expansion pressure is a function of I_r. The cone factor (N_c) determined from the cavity expansion analysis can hence be given as a function of the rigidity index. Conventionally, numerical methods employed to determine the cone factor have also correlated the N_c to the rigidity index of soil (Teh and Houlsby, 1991; Yu *et al.*, 2000; Abu-Farsakh *et al.*, 2003b; Lu *et al.*, 2004).

The rigidity index is not however, an intrinsic soil parameter, as the measured values of shear modulus (G) and undrained shear strength (S_u) of the soil are influenced by various parameters. Experimental studies have shown that the shear parameters of soil were affected by the over consolidation ratio (Wroth *et al.*, 1979), the method of measurements (Wroth, 1984), stress history (Jardine *et al.*, 1984; Atkinson *et al.*, 1990), strain rate (Jardine, 1992b) and the sampling disturbance (Hight *et al.*, 1992). In this thesis, the influence of a higher rigidity index on the penetration-induces stresses and strains within the soil was evaluated by decreasing the undrained shear strength and increasing the shear modulus independently.

7.4.1 Decreasing undrained shear strength

The undrained shear strength (S_u) of the soil was reduced from 100 to 25kPa, while the shear modulus (G) was kept constant and equal to 1MPa in both the 2D and 3D soil penetration models. The influence of a change in the soil's undrained shear strength (S_u) was evident on the strain paths. The ε_{xx} strain paths were relatively insensitive to the value of S_u, as illustrated in Figures 4.19 and 6.5 for the 2D and 3D models respectively. The influence of S_u on the ε_{yy} strain path was insignificant in the 3D model, as shown in Figure 6.6. The strain path for vertical (ε_{zz}) strains was also insensitive to the S_u in both the 2D and 3D soil penetration analyses (Figures 4.20 and 6.7). In contrast to the normal strains, soils with a lower S_u (i.e. higher rigidity index) attained higher shear strains (ε_{xz}) above the tip level, as shown in Figures 4.21 and 6.8 in both the 2D and 3D analyses respectively. Figure 7.9(a, b & c) shows the values of strains at the end of the strain path. This figure shows that in both the 2D and 3D analyses, the ε_{xx} and ε_{zz} strains were relatively insensitive to the undrained shear strength, while the ε_{xz} was higher in models with a lower S_u. The strain path for octahedral strains (γ_{oct}), determined in the 3D soil penetration analyses also confirmed that the penetration-induced strains above the tip were higher for soils with a higher S_u, as shown in Figure 6.9.

The normalised horizontal stress changes ($\beta=\Delta\sigma_{xx}/\sigma_{xx0}$) on the spade cell face are plotted against the value of undrained shear strength (S_u) in both the 2D and 3D models, Figure 7.9(d). The horizontal stresses (σ_{xx}), and consequently the over-reads (β) were higher for soils with a higher undrained shear strength (S_u). The increase in over-read with an increase in the undrained shear strength (S_u) has also been observed in experimental spade cell interpretations (refer to section 2.2.2). In contrast to the experimental interpretations that suggest linear or bi-linear correlations (Tedd and Charles, 1983; Carder and Symons, 1989; Tedd *et al.*, 1989;

Ryley and Carder, 1995), the results of the numerical analyses showed an exponential relationship between the spade cell over-read and the undrained shear strength (S_u).

The influence of S_u on the horizontal stresses (σ_{xx}) in the 3D soil penetration models is also evident in the stress profiles, which show the spatial distribution of stresses in various directions at the end of the penetration process. Horizontal stresses were higher for soils with a higher S_u over the whole length of the x-profile (Figure 6.10), along the face of "chisel" ($y/w<B/w$) in the y-profile (Figure 6.11) and on the penetration path ($-96<z/w<96$) in the z-profile (Figure 6.12).

The stress history plot (Figure 6.15) shows stresses recorded on the spade cell centreline and 100mm above its tip during various stages of penetration in the 3D models. The horizontal (σ_{xx}) and vertical (σ_{zz}) stresses were higher for soils with a higher S_u. In contrast to normal stresses (σ_{xx} and σ_{zz}), the shear stress (σ_{xz}) was relatively insensitive to S_u, which is also evident in the y and z profiles of shear stress (Figures 6.13 and 6.14).

7.4.2 Increasing shear modulus

The shear modulus (G) of soil was increased from 1 to 8MPa, while the undrained shear strength (S_u) was kept constant at 100kPa in both the 2D and 3D soil penetration models. Increasing the soil shear modulus did not affect the final ε_{xx} strains in the 2D models, as shown in Figure 4.22. However, in the 3D models, the ε_{xx} and ε_{yy} strains shown in Figures 6.17 and 6.18 respectively were slightly higher for soils with a higher shear modulus (G). The strain paths for vertical (ε_{zz}) strains were insensitive to the value of the shear modulus (G) in both the 2D and 3D analyses (Figures 4.23 and 6.19). Shear strains (ε_{xz}) above the tip were, however, higher for soils with a higher G (i.e. higher rigidity index), as illustrated for the 2D and 3D models in Figures 4.24 and 6.20 respectively. Figure 7.10(a, b & c) shows the values of ε_{xx}, ε_{zz} and ε_{xz} strains at the end of the strain path in both the 2D and 3D analyses. The strain path for the octahedral strains (γ_{oct}) obtained from the 3D models, also shows that the penetration-induced strains above the tip were higher for soils with a higher shear modulus, as shown in Figure 6.21.

Figure 7.10(d) shows the normalised horizontal stress change (β) against the shear moduli (G) in both the 2D and 3D models. This figure indicates that the horizontal stresses (σ_{xx}) and consequently the over-reads (β) were higher for soils with a higher shear modulus (G).

The horizontal stress (σ_{xx}) profiles in the x, y and z directions in the 3D penetration models for soils with a range of shear moduli (G) were examined. The trend between σ_{xx} and G was not clear in the y-profile (along the face), as shown in Figure 6.23. However, it is evident that the horizontal stresses (σ_{xx}) were higher for soils with a higher shear modulus along the whole length of x-profile and on the penetration path in the z-profile, shown in Figures 6.22 and 6.24 respectively.

The stress history plot illustrates the horizontal (σ_{xx}), vertical (σ_{zz}) and shear (σ_{xz}) stresses recorded on the spade cell face at various stages of penetration (Figure 6.27). These histories show that while horizontal (σ_{xx}) and vertical (σ_{zz}) stresses were higher for soils with a higher shear modulus (G), the shear stress (σ_{xz}) was relatively insensitive to the value of G. The y and z profiles for the shear stress (σ_{xz}) also illustrate that the shear stresses, at the end of penetration, were relatively insensitive to the value of soil shear modulus (Figures 6.25 and 6.26).

Comparison of the influence of the undrained shear strength (S_u) and shear modulus (G) on the behaviour of soil reveals that in contrast to cone penetration studies (Teh and Houlsby, 1991; Van den Berg, 1994; Yu *et al.*, 2000; Abu-Farsakh *et al.*, 2003b; Lu *et al.*, 2004), the penetration-induced stresses and strains could not be normalised by the rigidity index of the soil. This is because a change in the value of G had a greater effect on the soil behaviour compared to the same magnitude of change in S_u. For example, by increasing G from 1 to 4MPa (I_r increased from 10 to 40), the final shear (ε_{xz}) strain in the 3D model increased by a factor of 6.5, while reducing S_u from 100 to 25kPa (I_r increased from 10 to 40), caused the final shear strain to increase by a factor of 4.5 (Figures 7.9 and 7.10).

Additional 2D penetration analyses were performed to further evaluate the relative effect of changes in the undrained shear strength (S_u) and shear modulus (G), on the behaviour of soil. Figure 7.11 shows the normalised horizontal stress change (β) in these analyses. The G and S_u values of the soil were increased by the same factor in six models so that the rigidity index of the soil remained constant ($I_r=G/S_u=10$). It is evident that (β) cannot be normalised by the value of soil rigidity index, as horizontal stresses were higher for soils with higher values of G and S_u but the same value of I_r.

Figure 7.12 shows the effect of changes in soil shear moduli (G) and undrained shear strengths (S_u) on the horizontal stress (σ_{xx}) profile in the 3D analyses. The stress profiles were smoothed using **LOESS** the "weighted locally regression smoothing" technique (MathWorks, 2005). It is evident that the horizontal stresses (σ_{xx}) increased with increasing the shear modulus (G) as well as the undrained shear strength (S_u) of the soil.

In order to avoid the complications associated with advanced constitutive models and to understand the basic nature of the changes around a penetrating object, a simple Tresca model was assigned to the soil in the analyses within this thesis. The deficiencies of the Tresca model in addressing the non-linearity, rate-dependency and dilatancy of real soils should be considered in generalising the behaviour predicted by these analyses (Duncan and Chang, 1970; Simpson *et al.*, 1979; Duncan *et al.*, 1980; Jardine *et al.*, 1986; Byrne *et al.*, 1987; Lade, 1988; Al-Sahyea *et al.*, 2003; Houlsby, 2003).

7.5 Influence of interface adhesion

The adhesion mechanism between soils and solid objects was recognised as early as the 1920's (Terzaghi, 1925b). Ongoing experimental and theoretical work has been carried out over many years to determine the governing parameters that control the shear resistance developed between soils and solid objects (refer to section 2.6). Table 7.1 lists the interface adhesion factors ($\alpha=C_{int}/S_u$) measured in a range of tests between saturated clays and various materials, where C_{int} and S_u are the interface adhesion and the soil undrained shear strength respectively. Development of interface elements in numerical modelling has made FE/FD analyses capable of incorporating adhesion effects in the simulations, as discussed in section 2.7.3. Due to modelling constraints, many of previous numerical penetration analyses have modelled the interface as either rough or smooth (i.e. no slip or full slip) and few of them have assessed the influence of various adhesion levels on the behaviour of soil during the penetration process (Table 7.2). In this thesis, the influence of interface adhesion levels has been assessed on the stress-strain behaviour of soil during the undrained penetration of the 2D "simple wedge" and the 3D "chisel" geometries. The results of these analyses are discussed below.

Adhesion (α) influences the strain paths of horizontal (i.e. lateral and longitudinal) strains in the soil penetration models. The ε_{xx} strains above the tip were lower for models with higher interface adhesion values in the 2D analyses, as shown in Figure 4.27. The ε_{xx} strains were, however, relatively insensitive to the interface adhesion in the 3D models (Figure 6.29). Figure 7.13(a) shows the values of ε_{xx} strains at the end of the strain path in both the 2D and 3D analyses. Nevertheless, the interface adhesion (α) affected the ε_{yy} strains in the 3D models and strains were lower for models with higher α values (Figure 6.30).

In both the 2D and 3D analyses, vertical strains (ε_{zz}) above the tip were higher in models with a higher interface adhesion (Figures 4.28 and 6.31). The length of the vertical (ε_{zz}) strain path affected by the adhesion was however, different in the 2D from the 3D analyses. In the 2D analyses, the divergence between vertical strains as a result of the interface adhesion was initiated at the tip level and increased until the end of the penetration path. In the 3D analyses, the effect of the interface adhesion, which commenced at the tip level, reached its maximum at z/w=20 above the tip and reduced towards the end of the penetration path. Figure 7.13(b) shows the values of ε_{zz} strains at the end of the strain path in both the 2D and 3D analyses. The localised adhesion effect in 3D models was due to the fact that the adhesion on surfaces parallel to the penetration direction (i.e. the "chisel" vertical surfaces) had a relatively small effect on the soil behaviour. This feature has also been observed in cone penetration analyses (Teh and Houlsby, 1991; Lu *et al.*, 2004).

Introducing interface adhesion had a similar effect on the strain paths for shear strains (ε_{xz}) in both the 2D and 3D soil penetration analyses, as shown in Figures 4.29 and 6.32 respectively. Shear strain paths (ε_{xz}) diverged from the non-adhesive path by increasing the interface adhesion (α) as the soil element passed the tip level. Figure 7.13(c) shows the values of ε_{xz} strains at the end of the strain path in the 2D and 3D models. Figure 6.33 shows that the overall penetration-induced strains γ_{oct} (octahedral strain) above the tip were higher in models where a higher adhesion (α) was assigned to the interface.

Figure 7.13(d) illustrates the correlation between the normalised horizontal stress change (β) and interface adhesion (α) in both the 2D and 3D models. In common with the results of previous cone penetration analyses (Teh and Houlsby, 1991; Yu *et al.*, 2000; Lu *et al.*, 2004), a linear trend was observed between the horizontal stress change (β) and interface adhesion (α) in both the 2D and 3D penetration analyses. However, the gradient of horizontal stress change following an increase in the adhesion factor (α) in the 2D analyses was higher than that observed in the 3D. The correlation between the normalised horizontal stress change (β) and interface adhesion (α) was also valid for soils with a higher shear modulus (G=100MPa), as shown in Figure 7.14 for the 2D penetration models.

The profiles of horizontal (σ_{xx}) and shear (σ_{xz}) stresses also illustrate the effects of interface adhesion on soil behaviour in 3D penetration models. Along the entire length of x and y profiles, shown in Figures 6.34 and 6.35 respectively, horizontal stresses (σ_{xx}) were slightly higher for models with a higher interface adhesion. The smoothed z-profile of horizontal stress (σ_{xx}) for models with various adhesion (α) values is shown in Figure 7.15. Horizontal stresses (σ_{xx}) were higher in models with a higher adhesion above the initial position of the tip (z/w>96) and at z/w<-50 (z/w= -96 is the final position of the tip). The increase in horizontal stresses (σ_{xx}) due to an increase in the interface adhesion coincides with the results of cone penetration analyses (Abu-Farsakh *et al.*, 1998). It is also observed that shear stresses (σ_{xz}) were higher in models with a higher adhesion (α), along the "chisel" face in the y-profile (y/w<B/w) and above the final position of the tip in the z-profile (z/w>-96), as shown in Figures 6.37 and 6.38 respectively.

The influence of the interface adhesion is also evident in the history plots. Figure 6.39 shows the history of σ_{xx}, σ_{zz} and σ_{xz} stresses acting on the face of the spade cell at various stages of penetration for models with smooth (α=0) and rough (α=0.75) interfaces. This figure shows that the horizontal (σ_{xx}), vertical (σ_{zz}) and shear (σ_{xz}) stresses were higher in the rough model (α=0.75). The increase of the shear stress (σ_{xz}) due to the interface adhesion was however larger than the increases observed for the normal stresses(σ_{xx} and σ_{zz}).

The influence of interface adhesion was graphically illustrated using displacement vectors in the 2D models (Figure 4.32). By introducing adhesion (α) on the interface between the spade cell and soil, the direction of displacement vectors for soil elements adjacent to the spade cell changed from horizontal to pointing diagonally down and away from the spade cell. In other words, shear (i.e. drag) forces were generated along the interface in the adhesive model, which has also been observed in adhesive cone penetration analyses (De Borst and Vermeer, 1984; Teh, 1987).

The displacement pattern for a soil element in adhesive (α=0.75) and non-adhesive (α=0) 3D penetration models can be compared in Figure 7.8. This figure shows that although the horizontal displacements (x and y) were relatively similar in adhesive and non-adhesive penetration models, the vertical displacements (z) were markedly different. The influence of the adhesion on displacement patterns predicted in these soil penetration analyses was similar to the influence of viscosity in the fluid flow analyses, obtained by Gill and Lehane (2000).

The influence of interface adhesion was also evident on the principal stress rotations as shown in Figure 4.33 for the 2D analyses, and in Figures 6.41 and 6.42 for the 3D models. Figure 7.16 shows the direction and magnitude of principal stresses for a soil element at various stages of penetration for adhesive (α=0.75) and non-adhesive (α=0) 2D models. It is evident that higher principal stresses existed in models where an adhesive interface was defined.

These results show that, in common with samplers (Budhu and Wu, 1992) and cones (Abu-Farsakh *et al.*, 1998), the soil disturbances (e.g. strains, displacements, stress rotations) around the spade cell were increased by increasing the interface adhesion. Furthermore, horizontal stresses acting on the spade cell face were higher in conditions where the soil-spade cell interface had a higher adhesion (α).

7.6 Influence of aspect ratio

The effects of the "chisel" horizontal cross-section aspect ratio (B/w) on the stress-strain changes induced by penetration was assessed in three-dimensional models, which their results are summarised here.

The influence of increasing the aspect ratio of the "chisel" is evident in strain paths. The lateral (ε_{xx}) and longitudinal (ε_{yy}) strains were lower for a soil element above the tip, in models where the "chisel" had a higher aspect ratio (B/w), as shown in Figures 6.43 and 6.44 respectively. The strain paths for the vertical (ε_{zz}) and shear (ε_{xz}) strains were however, relatively insensitive to the value of aspect ratio (Figures 6.45 and 6.46). It is observed that at the end of the penetration, the octahedral strain (γ_{oct}) for the fat "chisel" (B/w=6) was 4% higher than the γ_{oct} for the slender "chisel" (B/w=24), as illustrated in Figure 6.47. The influence of aspect ratio (B/w) on strain paths determined from these 3D soil penetration analyses were similar to the effects predicted from the 3D fluid flow simulations presented by other researchers (Rafalovich, 1989; Aubeny, 1992; Finno, 1993).

The profiles of horizontal (σ_{xx}) and shear (σ_{xz}) stresses can be used to investigate the spatial distribution of stress changes caused by the penetration of the spade cell. The horizontal stress over-reads reduced with distance in the direction normal to the "chisel" face (x-profile), as illustrated in Figure 6.48. Figure 7.17 shows the smoothed horizontal stresses (σ_{xx}) profile along the "chisel" face (y-profile). The horizontal stresses (σ_{xx}) increased from the centreline of the "chisel" and reached their maximum at 6w before the "chisel" edge (y/w=B/w-6). The horizontal stresses reduced from this point until reaching minimum stress values at 3w after the "chisel" edge (y/w=B/w+3). From this point, horizontal stresses increased until the initial in-situ stress (σ_{xx0}) was reached at some distance (aw) away from the "chisel" edge (y/w=B/w+a). The shear stresses (σ_{xz}) determined along the y and z-profiles were relatively insensitive to the values of "chisel" aspect ratio, as shown in Figures 6.51 and 6.52 respectively. These profiles however show the occurrence of the shear direction change at the "chisel" edge (y/w=B/w) in the y-profile and at levels corresponding to the initial (z/w=96) and final (z/w= -96) positions of the tip in the z-profile.

The y-profile (Figure 7.17) shows that the horizontal stresses (σ_{xx}) were relatively uniform along the inner-half of the "chisel" face and horizontal stresses were higher in models where the "chisel" had a lower aspect ratio (B/w). Consequently, for a lower disturbance and a more representative measurement, the aspect ratio of the spade cell should be set higher and the stress sensor should be placed in the inner-half of the spade cell width. These conclusions coincide with the criteria outlined for optimum push-in pressure cell design set by Tavenas *et al.* (1975).

7.7 Influence of boundary types

The three-dimensional penetration analyses have also been performed for the chamber test geometry, where the boundary parallel to the "chisel" face (x=C) was located at C=210mm(50w). The influence of the boundary type (stress or displacement prescribed) for the x=C boundary has been evaluated on model outputs. The outcomes of these analyses are summarised in the following paragraphs.

It was observed that the lateral (ε_{xx}), longitudinal (ε_{yy}) and octahedral (γ_{oct}) strains were higher in the displacement-controlled model as the soil element passed the tip level, shown in Figures 6.53, 6.54 and 6.57 respectively. The influence of the boundary type was however, relatively insignificant on strain paths for the vertical (ε_{zz}) and shear (ε_{xz}) strains (Figures 6.55 and 6.56).

The profiles of horizontal (σ_{xx}) and shear (σ_{xz}) stresses were also examined to evaluate the spatial distribution of penetration-induced stresses for the two boundary types. Horizontal stresses (σ_{xx}) were higher for displacement-controlled boundaries along the whole length of x, y and z profiles, shown in Figures 6.58, 6.59 and 6.60 respectively. Shear stresses (σ_{xz}) were also slightly higher for the displacement-controlled boundary, as shown along the y and z profiles in Figures 6.61 and 6.62 respectively.

Figure 6.10 shows the horizontal (σ_{xx}) stress distribution along the x-profile for the MAIN model C=420(=100w). This figure can be compared to Figure 6.58 where C=210mm(=50w) to assess the effect of the boundary location on horizontal (σ_{xx}) stress distributions. The horizontal (σ_{xx}) stresses returned to the initial in-situ level (σ_{xx}) at x/w>60. It can be concluded hence that the thickness of soil above the penetrating spade cell in chamber tests was insufficient.

The choice of the correct boundary type is an important aspect of modelling. If the soil penetration analysis simulates a confined test (e.g. chamber test), boundary types should be defined according to the loading conditions within the test. However, if the analysis aims to simulate the penetration into a semi-infinite soil mass, it should be noted that the true solution for the stress-strain behaviour of soil is bracketed between the results determined from stress and displacement controlled boundary models (Fahey *et al.*, 1989).

Table 7-1 Measured interface adhesion factor (α) for saturated clays

Test	Structural material	Adhesion factor ($\alpha = C_{int}/S_u$)	Reference
Pile loading	Steel	44-103	Tomlinson, 1957
	Timber	57-88	
	Concrete	84-100	
Shear box test	Steel	25-50	Potyondy, 1961
	Timber	40-50	
	Concrete	40-60	
Ring shear	Steel	34-56	Lemos & Vaughan, 2000
	Glass	24-52	

Table 7-2 Interface conditions used in previous soil penetration analyses

Author	Year	Geometry	Interface Condition
De Borst and Vermeer	1984	Cone	Rough
Teh	1987	Cone	Smooth or rough
Kiousis	1988	Cone	Smooth
Budhu and Wu	1992	Sampler	C_{int}=0, 25 kPa, ϕ_{int}=0, 30
Van Den Berg	1994	Cone	C_{int}=0, 10, 20 kPa
Abu-Farsakh	1998	Cone	ϕ_{int}=0, 14
Yu	2000	Cone	ϕ_{int}=0, 7.5, …, 30
Liyanapathirana *et al.*	2000	Open-ended pile	Rough
Susila and Hryciw	2003	Cone	ϕ_{int}=16, 18, …, 22
Masbout and Sadek	2003	Pre-bored pile	Rough
Lu *et al.*	2004	Cone	Smooth or rough

Note: C_{int} and ϕ_{int} are the cohesion and friction angle of the interface respectively

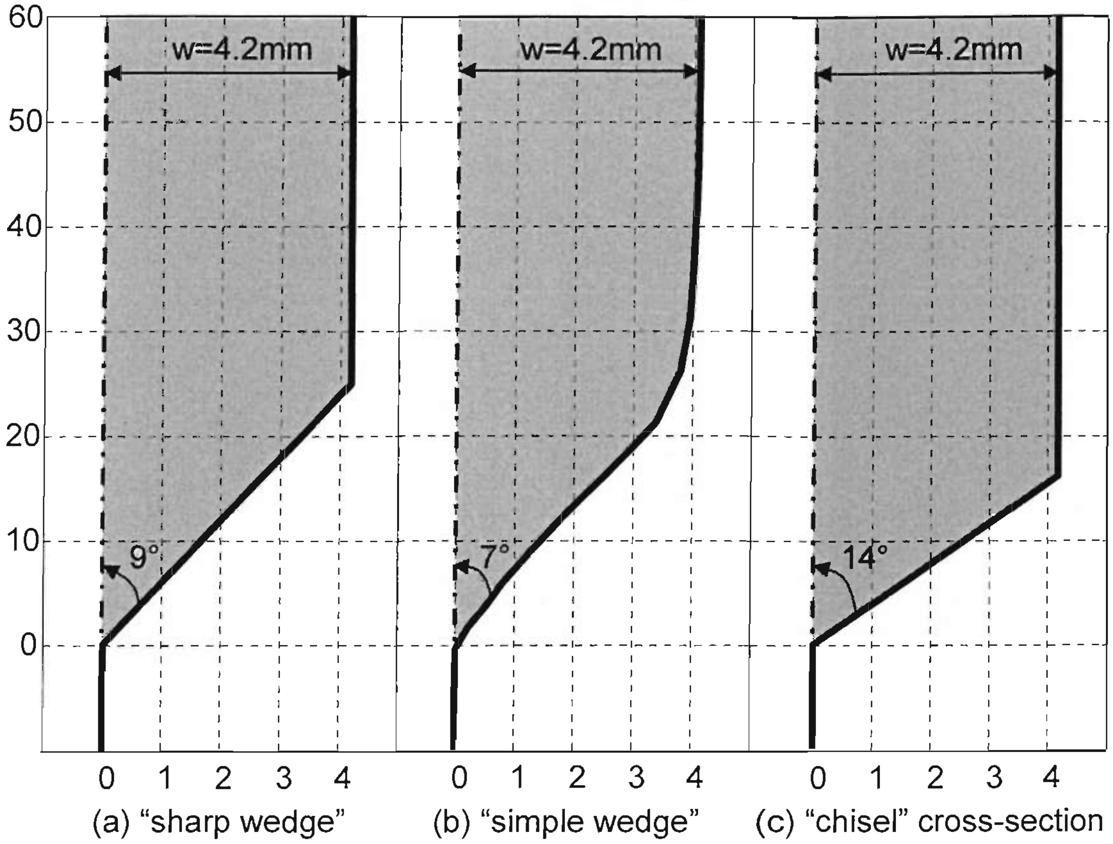

(a) "sharp wedge" (b) "simple wedge" (c) "chisel" cross-section

Figure 7-1 Comparison of the (a) "sharp wedge", (b) "simple wedge" and (c) "chisel" geometries (mm)

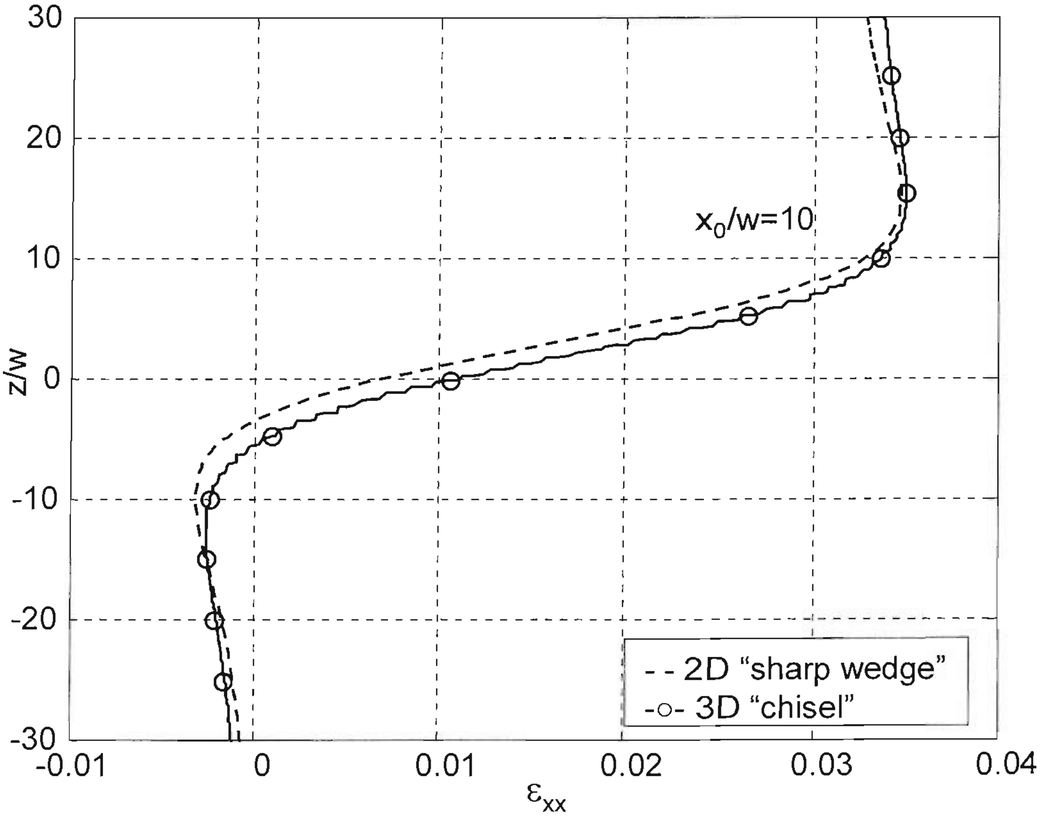

Figure 7-2 Comparison of strain path for (ε_{xx}) strain around "sharp wedge" and "chisel" (fluid flow)

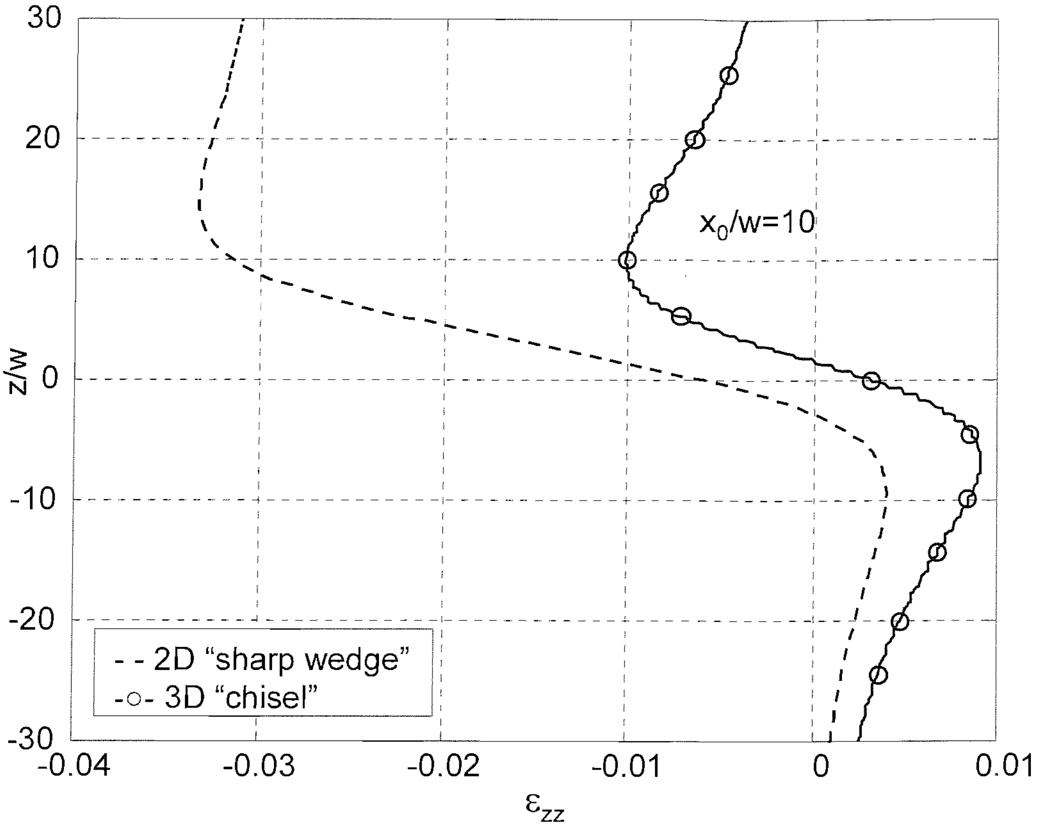

Figure 7-3 Comparison of strain path for (ε_{zz}) strain around "sharp wedge" and "chisel" (fluid flow)

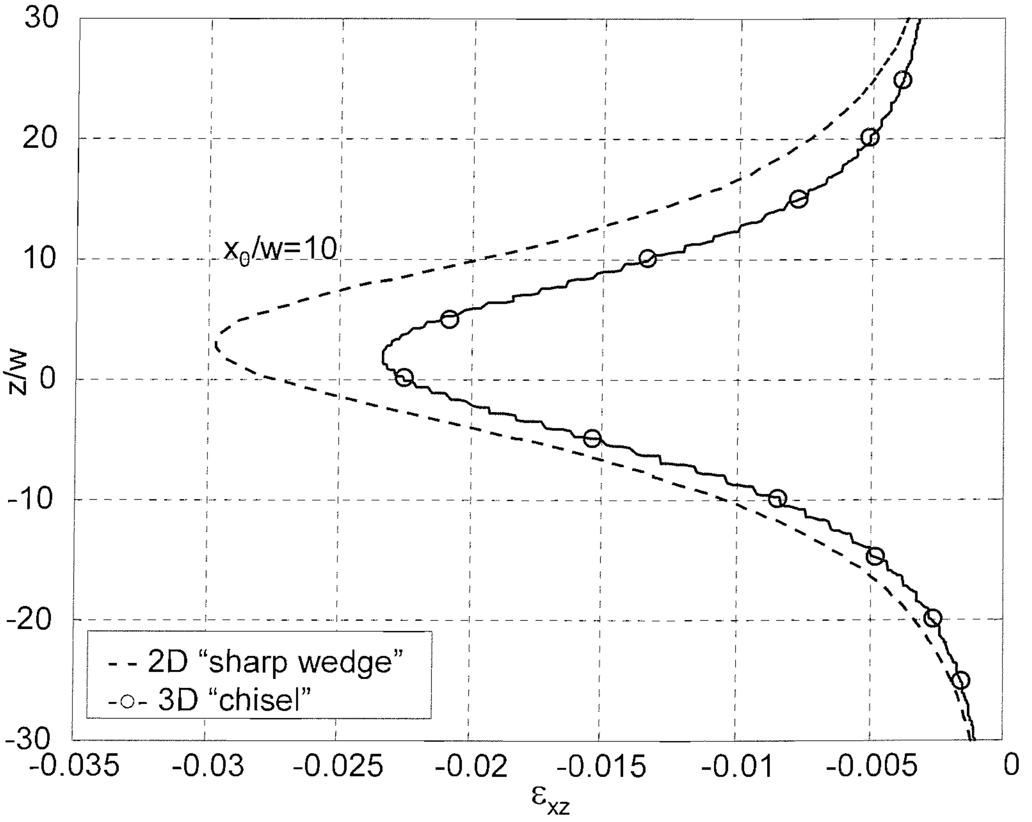

Figure 7-4 Comparison of strain path for (ε_{xz}) strain around "sharp wedge" and "chisel" (fluid flow)

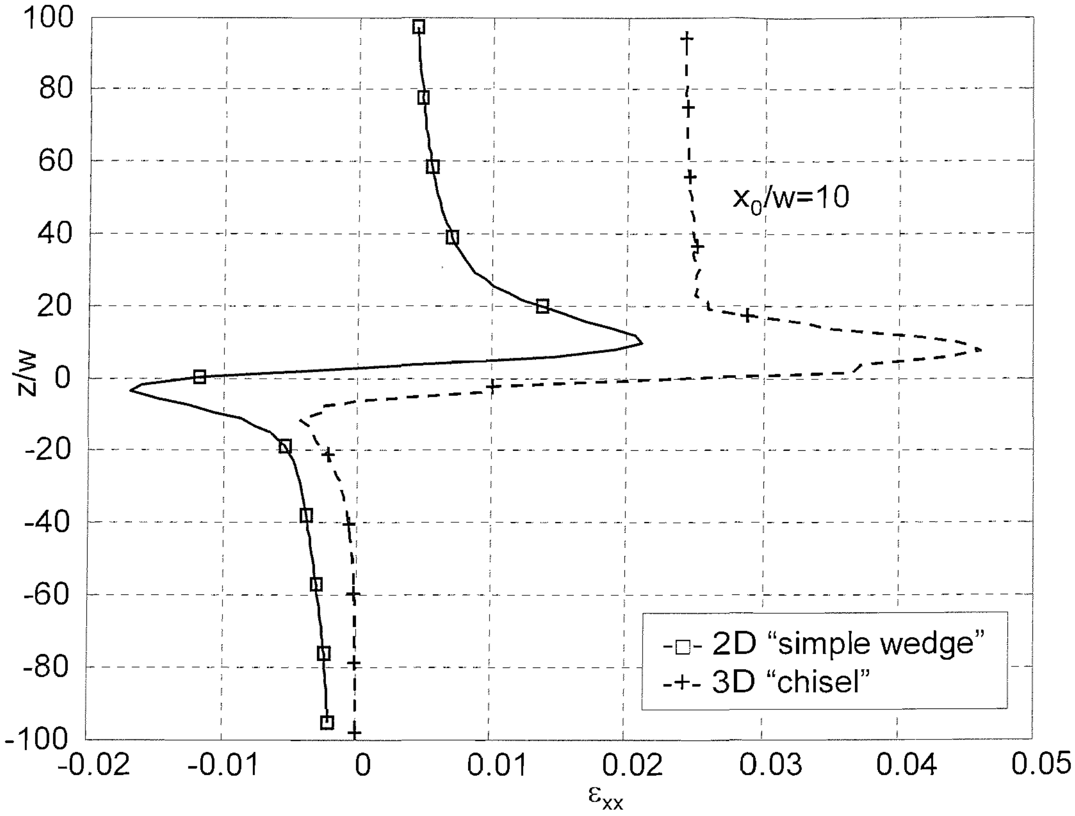

Figure 7-5 Comparison of strain path for (ε_{xx}) strain around "simple wedge" and "chisel" (soil penetration)

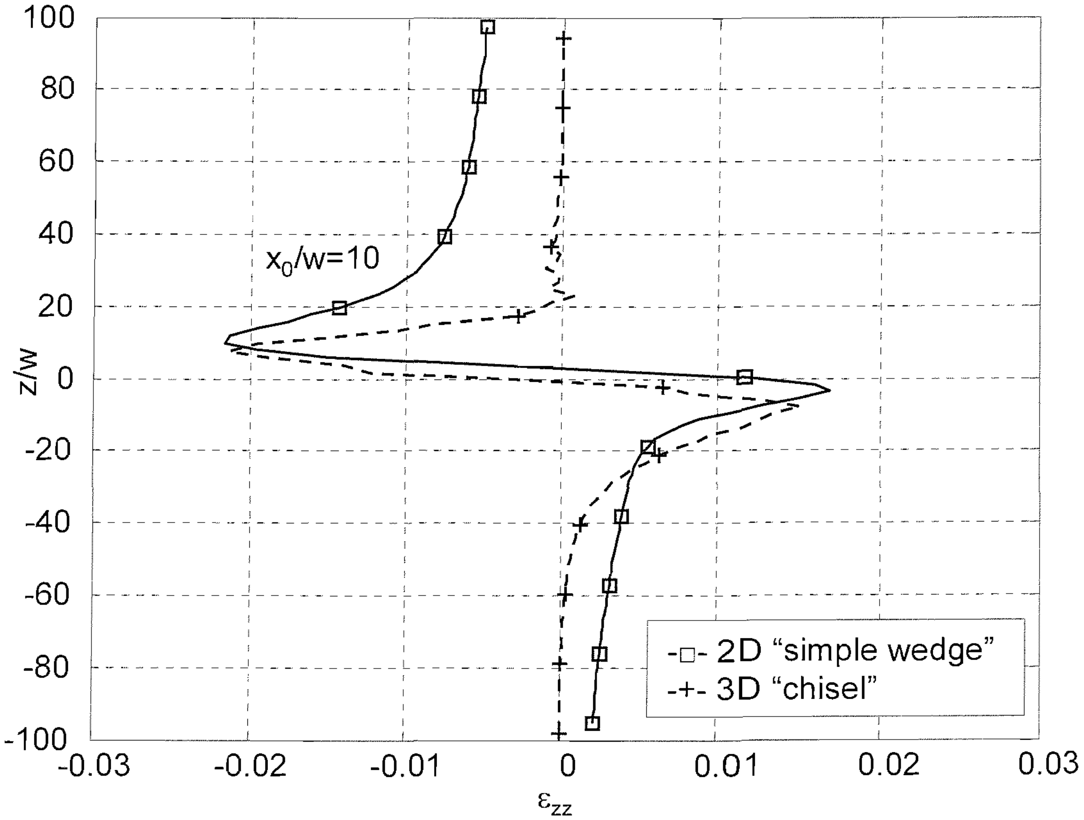

Figure 7-6 Comparison of strain path for (ε_{zz}) strain around "simple wedge" and "chisel" (soil penetration)

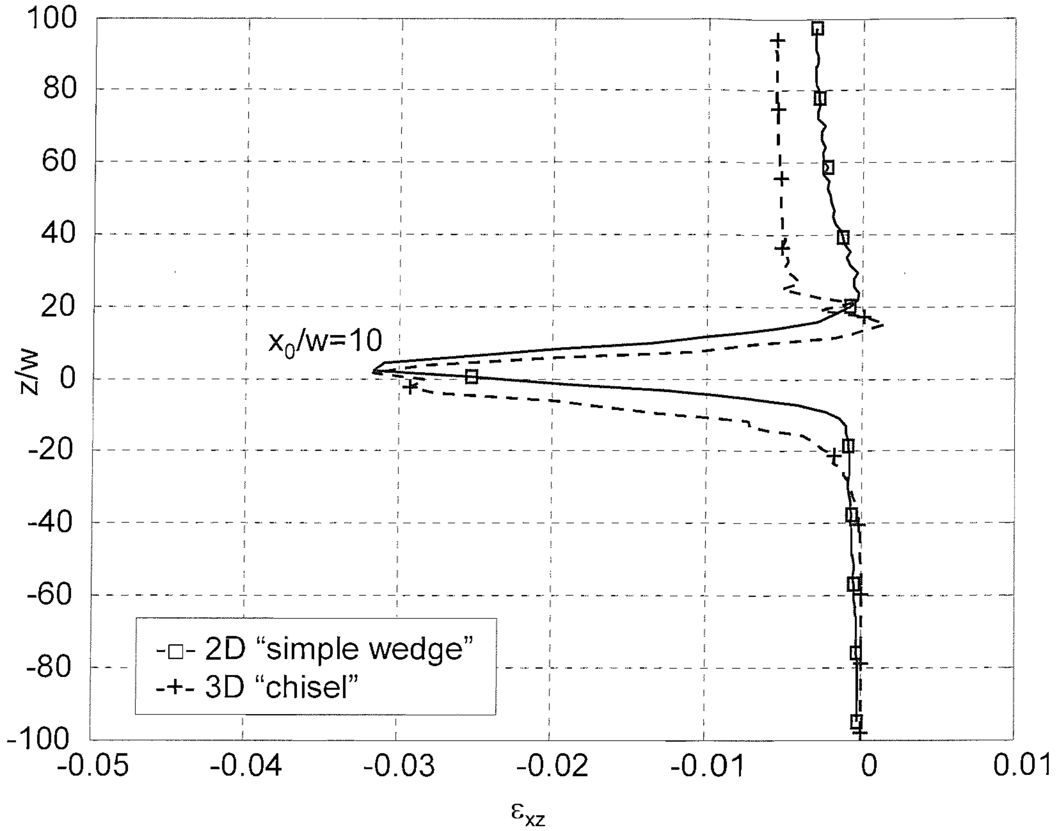

Figure 7-7 Comparison of strain path for (ε_{xz}) strain around "simple wedge" and "chisel" (soil penetration)

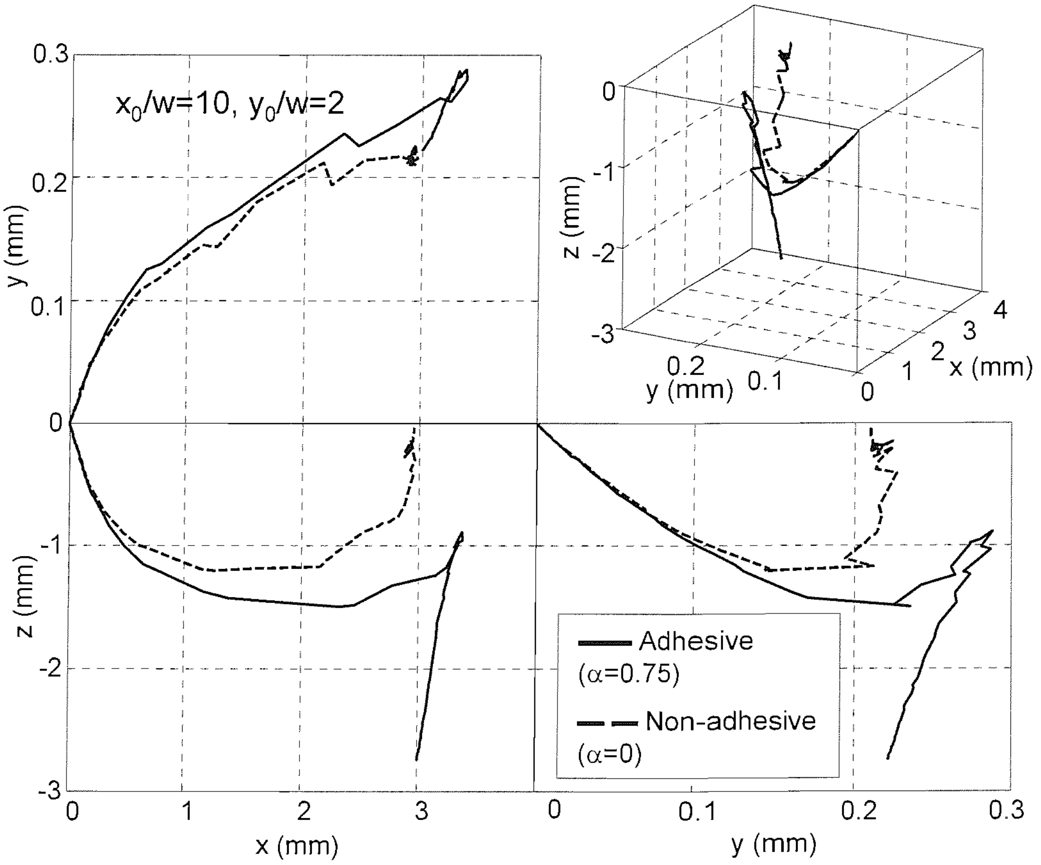

Figure 7-8 Computed displacements around "chisel" from 3D soil penetration analysis

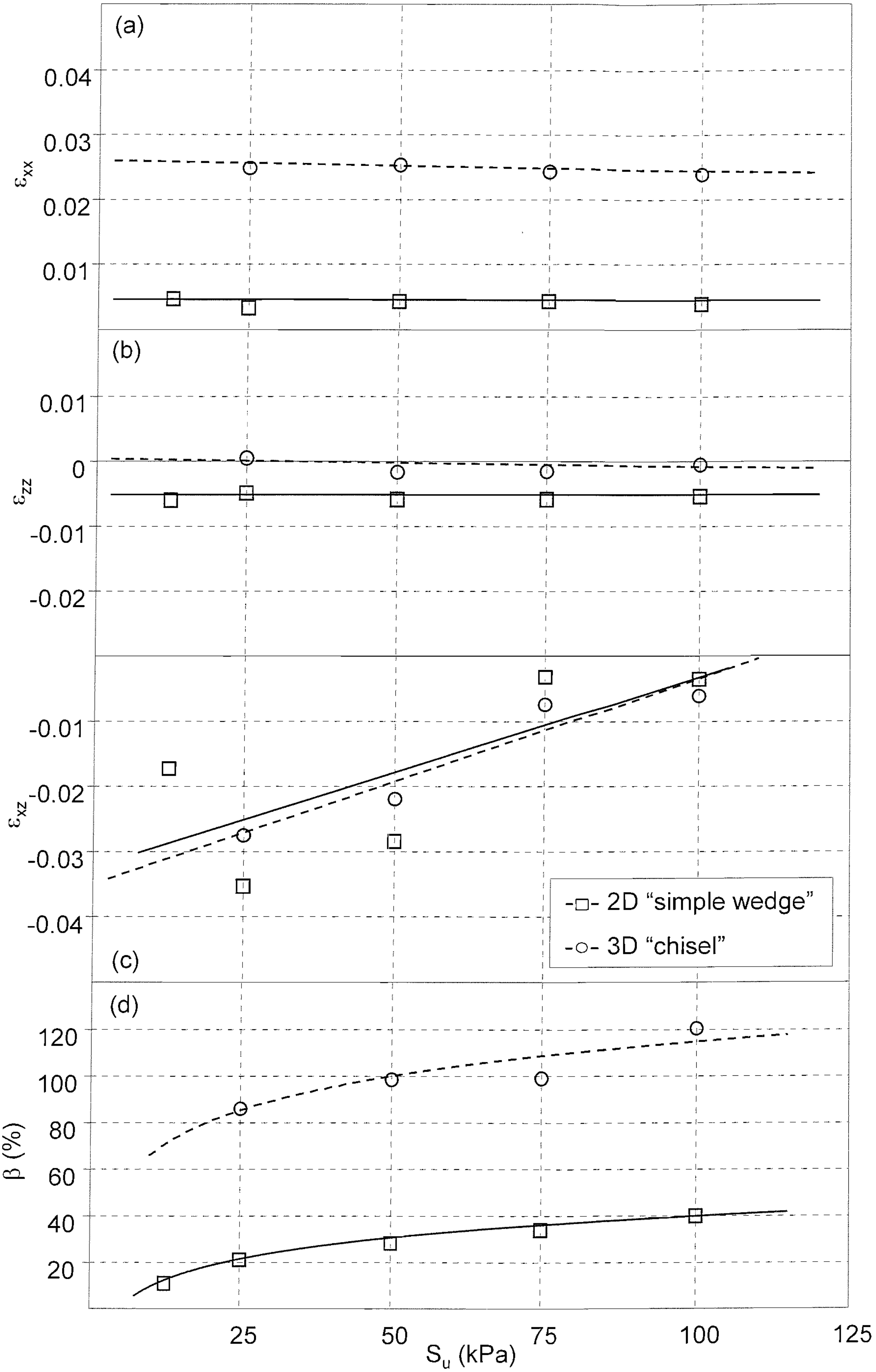

Figure 7-9 Influence of undrained shear strength (S_u) on the behaviour of soil in the 2D and 3D soil penetration models (G=1MPa, α=0)

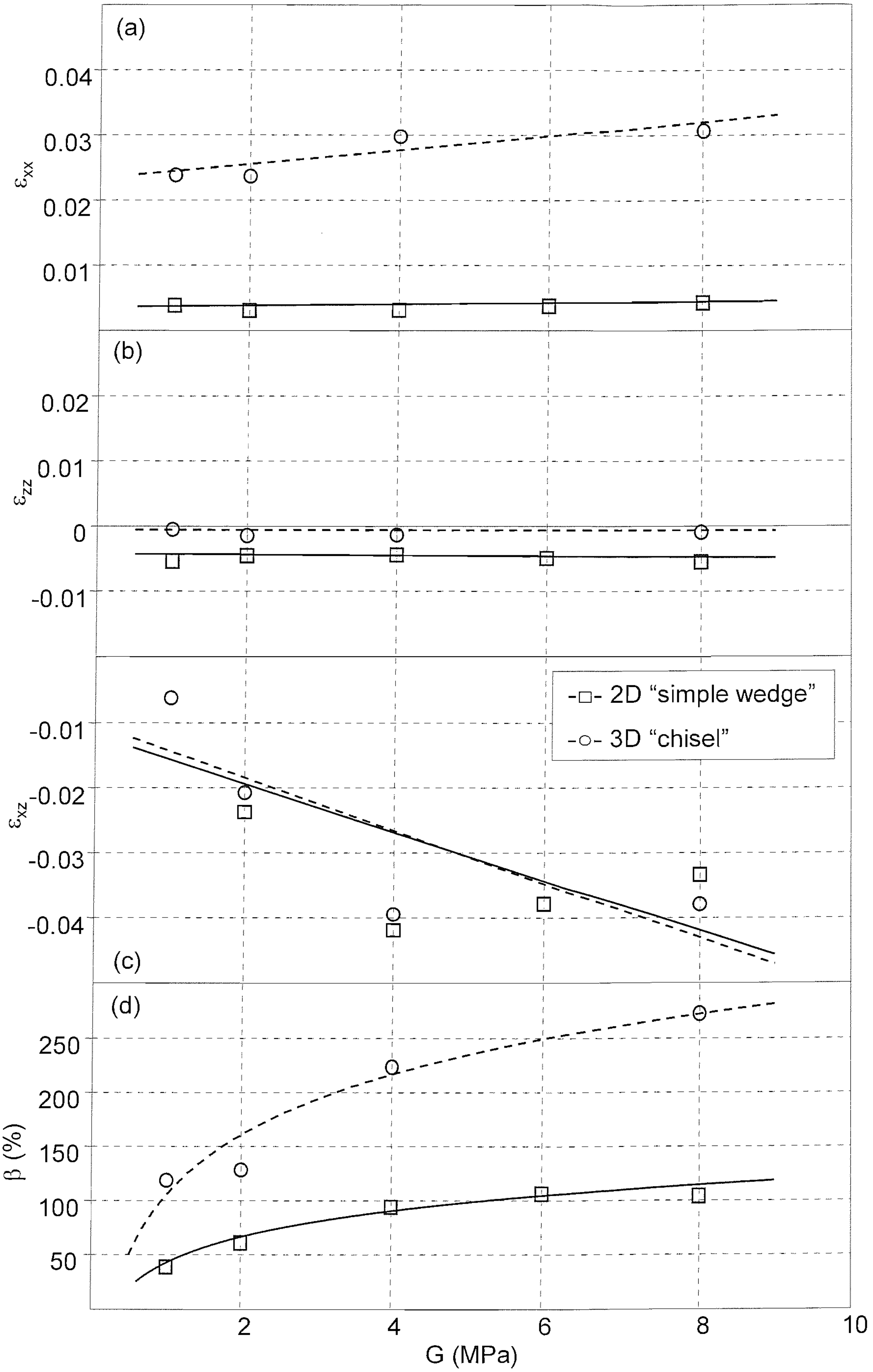

Figure 7-10 Influence of shear modulus (G) on the behaviour of soil in the 2D and 3D soil penetration models (S_u=100kPa, α=0)

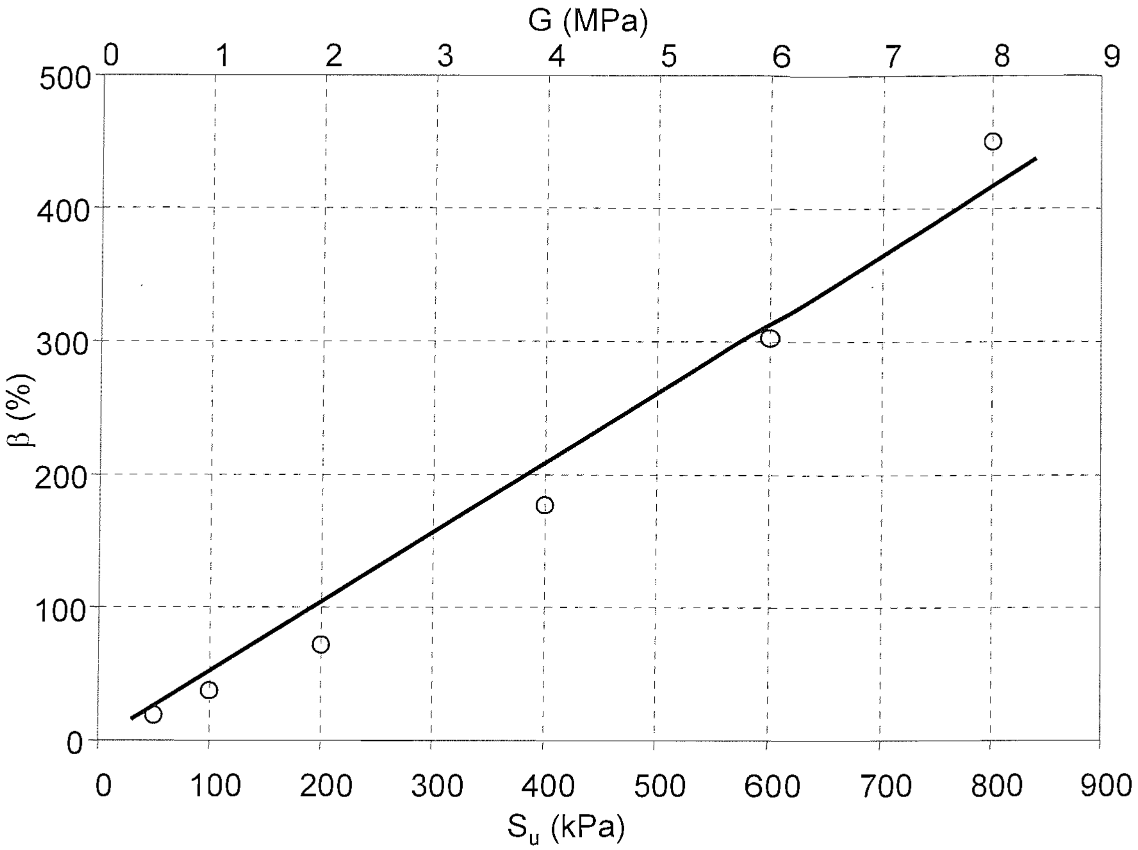

Figure 7-11 Influence of increasing (S_u) and (G) on normalised horizontal stress change (β) at 100mm above tip in 2D soil penetration models

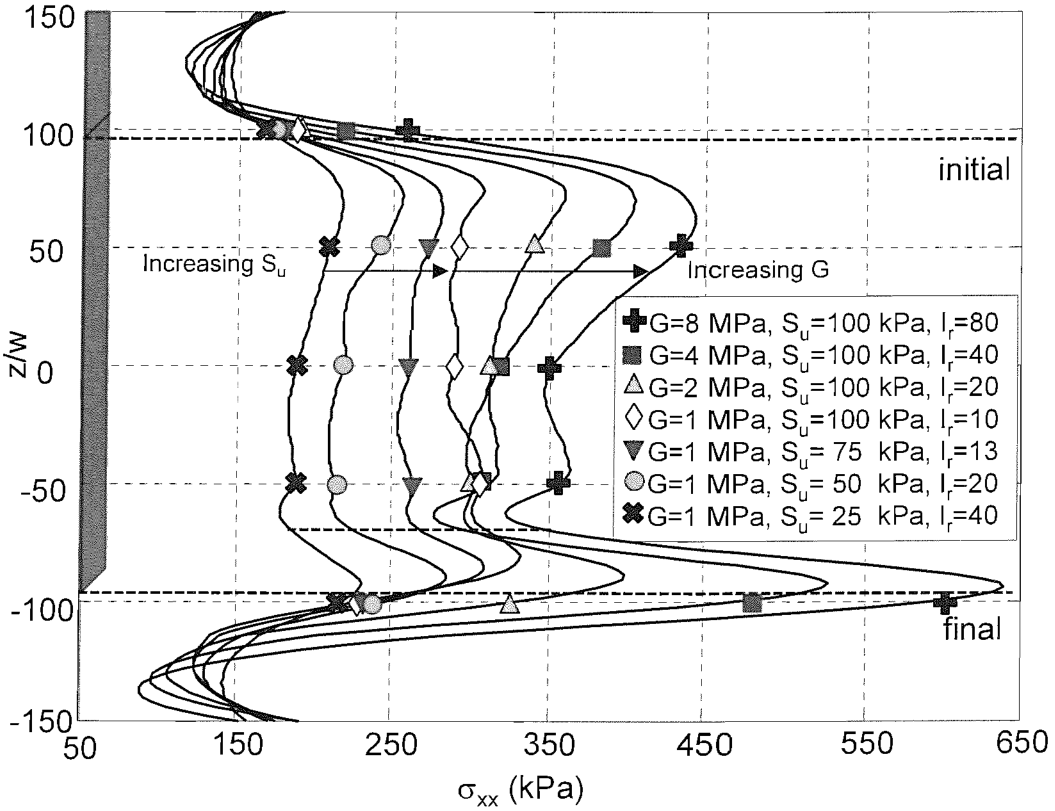

Figure 7-12 Influence of increasing strength (S_u) and increasing modulus (G) on horizontal stress (σ_{xx}) profile (x=y=5w) in 3D soil penetration models

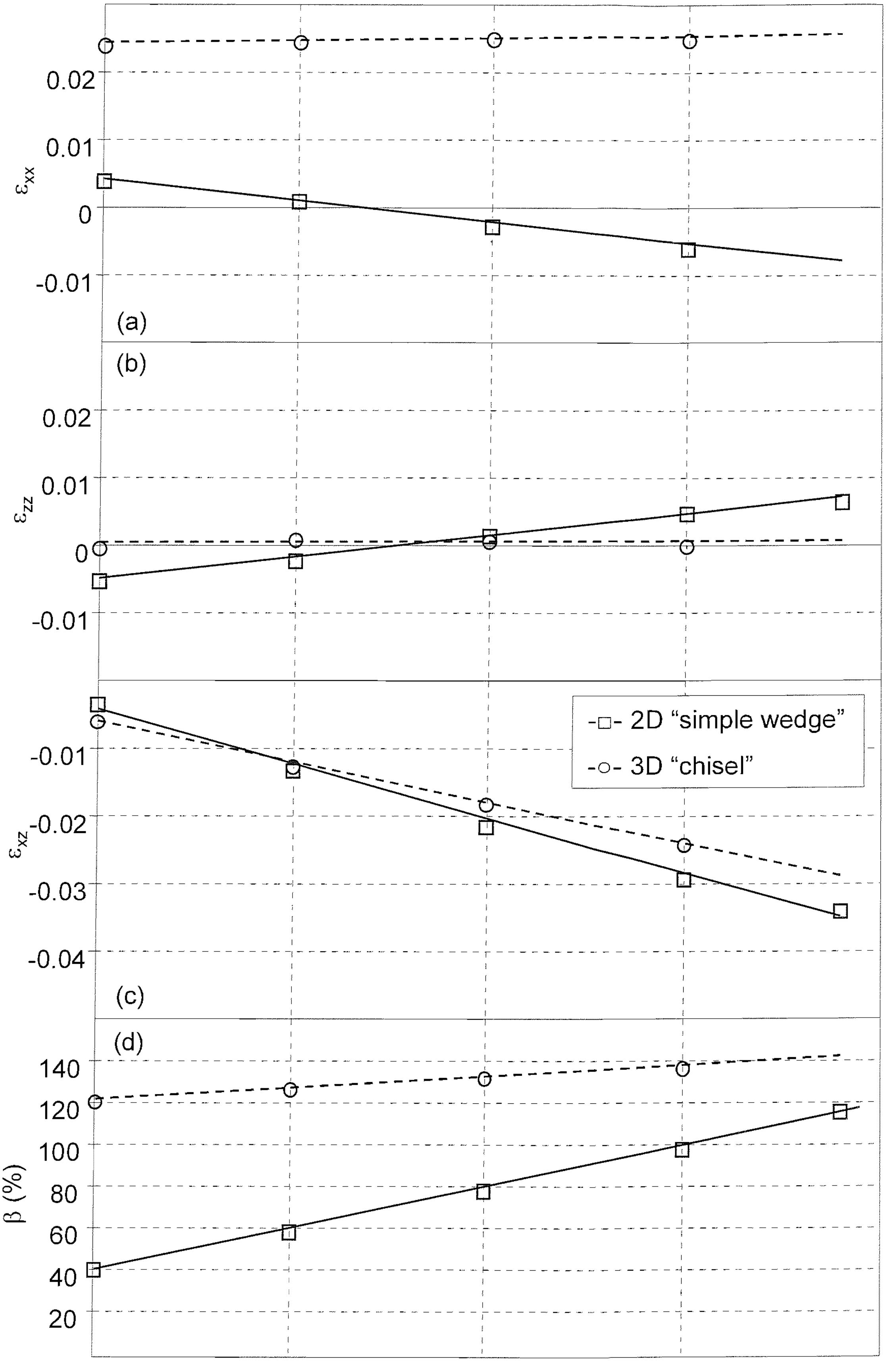

Figure 7-13 Influence of interface adhesion (α) on the behaviour of soil in the 2D and 3D soil penetration models (S_u=100kPa, G=1MPa)

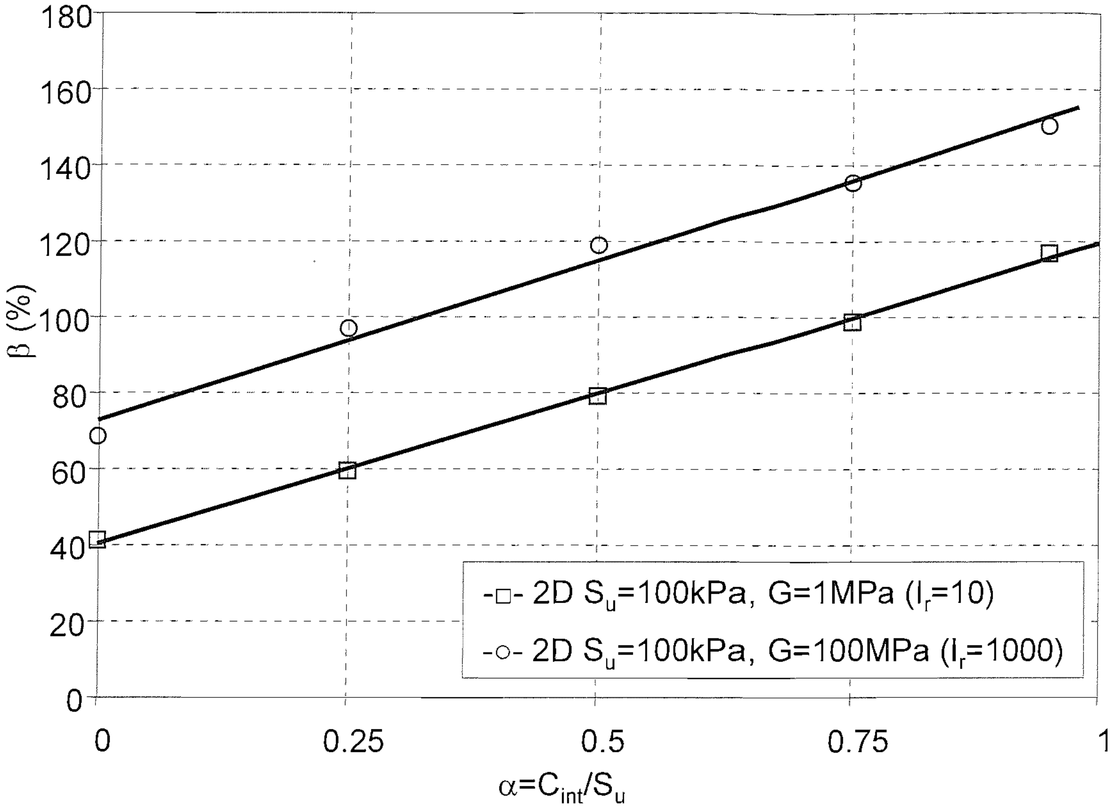

Figure 7-14 Influence of adhesion (α) on normalised horizontal stress change (β) at 100mm above tip in 2D soil penetration models (I_r=10 and 1000)

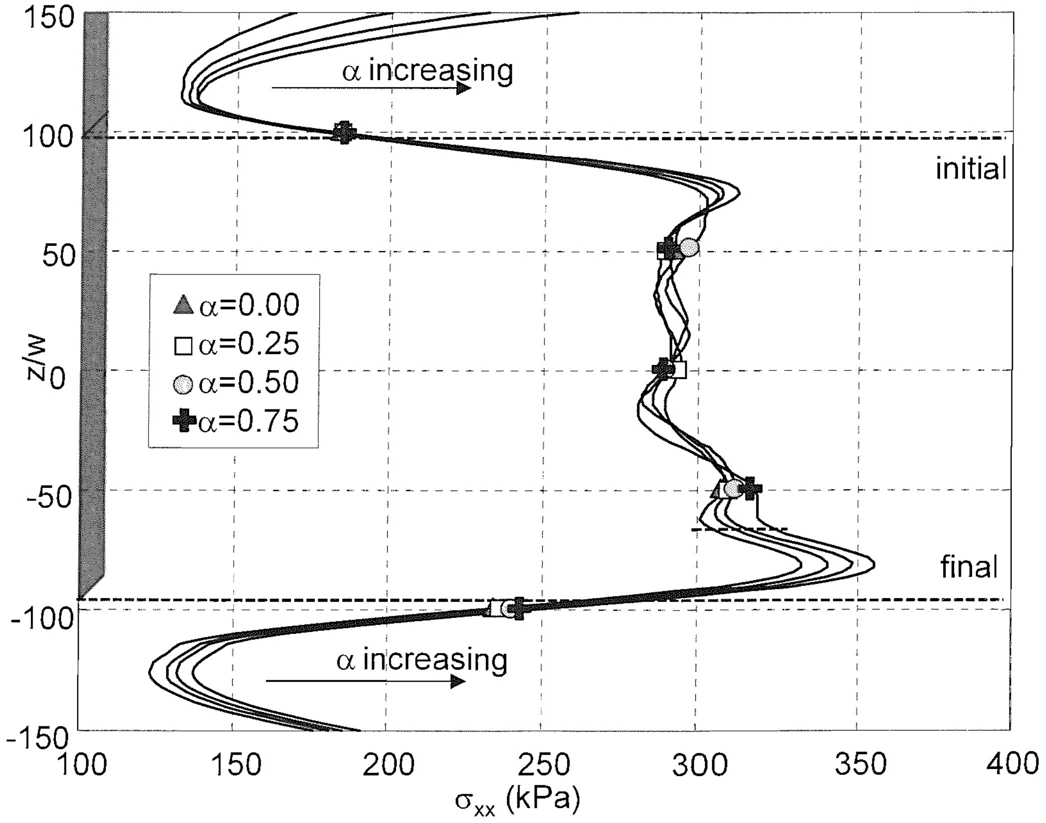

Figure 7-15 Influence of adhesion (α) on (σ_{xx}) along z-profile (x=y=5w) in 3D soil penetration models (smoothed)

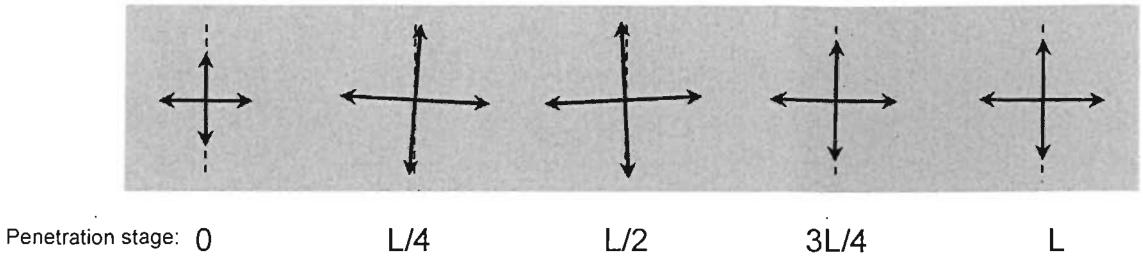

(a) Smooth interface (α=0.00)

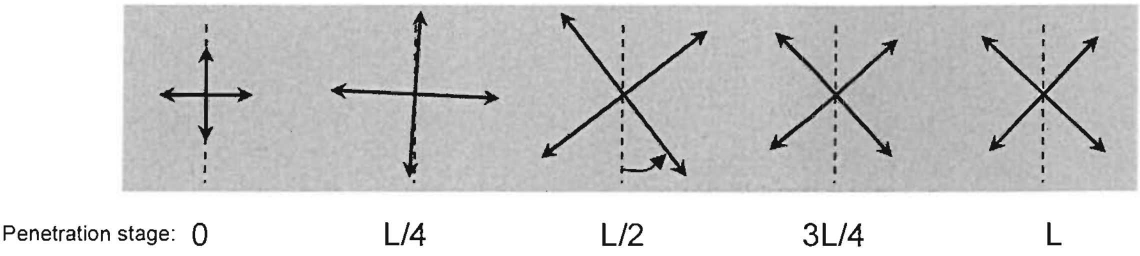

(b) Rough interface (α=0.75)

Figure 7-16 Rotation of principal stress indicators in 2D soil penetration models for smooth (α=0) and rough (α=0.75) interfaces

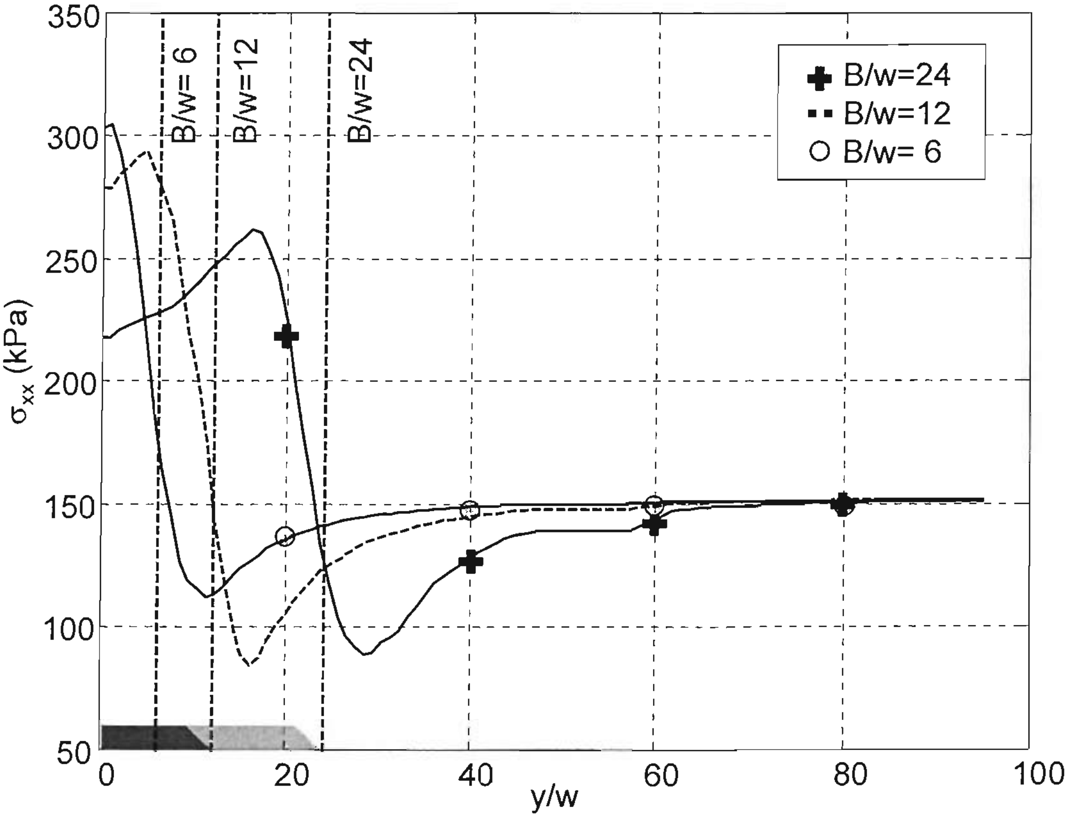

Figure 7-17 Influence of aspect ratio (B/w) on (σ_{xx}) along y-profile (x=5w, z=0) in 3D soil penetration models (smoothed)

8 CONCLUSIONS AND RECOMMENDATIONS

The objective of this research was to establish a better understanding of the stress-strain changes that occur in a soil as a spade cell is pushed into it. The relative influence of various penetration parameters on the behaviour of soil adjacent to a penetrating spade cell were determined. Two and three dimensional numerical modelling was undertaken to analyse the undrained penetration of idealised spade cell geometries into a Tresca soil. The conclusions derived from the literature review and results obtained from the numerical analyses are presented together with recommendations for further work.

8.1 Conclusions

Determination of a realistic value for the soil in-situ stress is essential for the optimum design or the precise analysis of a wide range of geotechnical problems. As laboratory measurement methods introduce additional disturbances that affect the behaviour of a soil, various direct measurement techniques have been developed to determine the in-situ stresses. The push-in pressure cell (i.e. spade cell) has been used increasingly to assess the soil in-situ stresses as well as stress changes during various stages of a construction project.

As a spade cell is pushed into the ground, it alters the stress/strain state of the soil adjacent to it and consequently the measurements made by it need to be interpreted to determine the initial in-situ stresses within the soil. The existing interpretation techniques, which are largely based on comparison of spade cell readings with measurements made by alternative devices, recommend a deduction of $0.5S_u$ (S_u is the undrained shear strength of soil) from spade cell measurements.

The validity of this approach is questionable as it is based on limited, inconsistent and scattered data. Furthermore, it has been illustrated by various researches that the behaviour of a soil around a penetrating object is influenced by various soil and interface properties and consequently the correlation of over-read to a single parameter (undrained shear strength) would not be robust. Understanding the relative influence of the penetration parameters on the soil behaviour may be used to devise novel interpretation techniques for the spade cell readings.

Various methods have previously been employed to investigate the soil penetration process. However, none of them is individually capable of incorporating all aspects of the penetration into the analysis. In this thesis, parallel fluid flow-soil penetration analyses were carried out to determine the stress-strain changes around a spade cell. The analyses were conducted for idealised spade cell geometries, termed the "simple wedge" and the "chisel" in two and three dimensional models respectively. In the fluid flow analyses, the strain paths around these geometries were evaluated from the deformation of streamlines when placed in a uniform flow. In the soil penetration analyses, the changes in the behaviour of a Tresca soil were investigated during the undrained penetration of these geometries. Notable features of the parallel fluid flow-soil penetration analyses were the capability to investigate the three-dimensional penetration processes, incorporation of soil-object interface adhesion and the capability for simulating deep penetrations.

The analysis scheme consisted of two steps: evaluation of the effects of modelling/geometrical parameters, and determination of the influences of soil/interface properties. In the first step, the strain paths determined from soil penetration analysis, with low soil shear modulus and without adhesion, were compared with those determined from the fluid flow analysis to ensure that the effects of the modelling and geometrical parameters on the predicted soil behaviour were insignificant. In the second step, the influence of various soil and interface parameters on the behaviour of soil during the penetration were evaluated by examining the outputs of various models.

These analyses have three important practical implications for pushed-in pressure cells. Firstly, the rigidity index of a soil is not sufficient to estimate the over-read of a spade cell being penetrated into it. Secondly, the penetration-induced stresses and strains within the soil are lower for a cell with a higher aspect ratio (i.e. slender). Finally, the interface adhesion has a less significant effect in a three-dimensional penetration problem, compared to plane-strain conditions. The detailed results of numerical evaluations are listed in the following paragraphs:

1. The shape of the penetrating object's tip influenced the magnitude and extent of disturbances (e.g. strains) generated around the penetrating object. The comparison of 2D fluid flow analyses results indicated that the peak normal and shear strains were higher and were reached earlier along streamlines for a blunt object, in comparison with an object with a sharp tip.

2. The strain path method was capable of predicting soil deformations in deep penetrating problems. The pattern of strain changes determined from the fluid flow analyses (strain path method) were similar to those evaluated from the soil penetration analyses for both the 2D and 3D models. Although the pattern of changes and the location of peak strains determined from these two methods were similar, the magnitudes of peak strains determined from the soil penetration analyses were generally higher. This difference can be attributed to the development of shear stresses, on the interface adhesion and within the soil, that the inviscid fluid flow could not sustain.

3. The discrepancies between the strain paths determined from the 2D and 3D analyses indicated that the deformations generated around the spade cell during penetration could only be successfully evaluated by performing a three-dimensional analysis. In contrast to the lateral (ε_{xx}) and shear (ε_{xz}) strains that had a similar pattern in the 2D and 3D analyses, there was a difference between the vertical (ε_{zz}) strains determined from the 2D and 3D models. It was shown that, the strain reversal and return of soil elements to their initial vertical position could not be predicted by the 2D plane-strain analyses. As the stress-strain relationships for soils are generally inelastic-nonlinear, differences in the strain-history of the soil could lead to unrealistic estimations of stresses.

4. Both the 2D and 3D penetration analyses showed that the undrained shear strength (S_u) of the soil influenced the stress-strain changes induced by penetration. In contrast to normal strains (ε_{xx}, ε_{yy} and ε_{zz}), the shear strain (ε_{xz}) above the tip was higher for soils with a higher rigidity index (i.e. lower S_u). The horizontal stresses (σ_{xx}) acting on the spade cell face at the end of penetration were higher for soils with a higher undrained shear strength.

5. The shear modulus (G) influenced the changes in the stress-strain behaviour of soil in 2D and 3D penetration models. In contrast to normal strains (ε_{xx}, ε_{yy} and ε_{zz}), the shear strains above (ε_{xz}) the tip, were higher for soils with a higher rigidity index (i.e. higher G). The horizontal stresses (σ_{xx}) acting on the spade cell face at the end of penetration were higher for soils with a higher shear modulus. The influence of a change in the shear modulus (G) on the horizontal stress over-read was greater than the influence of a relatively similar change in the undrained shear strength (S_u).

6. The value of interface adhesion (α) also influenced the penetration-induced changes determined from the 2D and 3D soil penetration analyses. The vertical (ε_{zz}) and shear (ε_{xz}) strains above the tip were higher in models with higher interface adhesion (α). Increasing the interface adhesion reduced the ε_{xx} strain in the 2D models, while the ε_{yy} strain was reduced by an adhesion increase in the 3D models. The horizontal stresses (σ_{xx}) on the spade cell face at the end of penetration were higher in models where a higher adhesion value (α) was assigned to the soil-spade cell interface. It was observed that the magnitudes and directions of principal stresses and displacements for soil elements adjacent to the spade cell were severely affected by the value of interface adhesion.

7. The effect of interface adhesion on the soil penetration analysis results was similar to the influence of viscosity on the fluid flow analysis outputs. The divergence in the displacement pattern of a soil element due to introducing adhesion (penetration analyses) was similar to the difference observed in the particle position as a result of using a viscid rather than inviscid fluid (flow analyses).

8. The horizontal cross-section aspect ratio (B/w) of the spade cell influenced the penetration induced stresses and strains. The 3D soil penetration analyses indicated that the lateral (ε_{xx}) and longitudinal (ε_{yy}) strains above the tip level, as well as horizontal stresses (σ_{xx}) on the spade cell face (at the end of the penetration) were higher for a spade cell with a lower aspect ratio (B/w).

9. The evaluation of various 2D and 3D analyses indicated that the soil behaviour adjacent to a penetrating spade cell is influenced by a number of parameters. The numerical soil penetration analyses showed that the stress-strain changes in the soil adjacent to a penetrating spade cell were dependent on the soil undrained shear strength (S_u), the soil shear modulus (G), the interface adhesion (α) and the aspect ratio of the spade cell (B/w). The relative influence of these parameters (G, S_u, α and B/w) on the spade cell measurements should therefore be incorporated in comparing the in-situ stresses determined in various field and laboratory experiments.

10. The variation of horizontal stresses (σ_{xx}) along the face of the penetrating object in 3D models indicated that the stress distributions were relatively uniform along the inner-half of the penetrometer width. Consequently, for a representative measurement, the stress sensor should be located within the mid-width of the stress measurement device (e.g. dilatometer) and away from the edges.

11. In the 3D chamber test simulations, the penetration induced stresses and strains were influenced by the type of the horizontal boundary parallel to the spade cell face. The results of numerical models for the chamber test analyses indicated that the lateral (ε_{xx}) and longitudinal (ε_{yy}) strains above the tip as well as the horizontal (σ_{xx}) stresses on the spade cell face at the end of penetration were higher in the models where the boundary was displacement-controlled (rather than stress-controlled).

8.2 Recommendations for further work

During the course of this research, areas of further work have been identified, which are divided into two broad categories: numerical and experimental extensions.

8.2.1 Numerical modelling

In order to avoid the complications associated with advanced constitutive models and to understand the basic nature of the soil changes around a penetrating object, a simple Tresca model was assigned to soil for the undrained penetration analyses within this thesis. More advanced constitutive models (Potts and Zdravkovic, 1999) could now be employed to predict a realistic soil behaviour. Rapid advances in computer technology could also make the use of particle flow codes (e.g. PFC), which incorporate the effects of particles shape, size and arrangement in predicting soil behaviour (Cundall and Strack, 1979; Powrie *et al.*, 2005), relevant for analysing the soil flow around a penetrating object in the future.

In this thesis, in order to reduce the computational requirements and as the focus of the research was on the behaviour of soil rather than the cell, the spade cell was modelled as a continuum (solid object). The accuracy of simulations could however be increased by analysing the spade cell as a flexible diaphragm (Timoshenko and Woinowsky-Krieger, 1959; Clayton and Bica, 1993). In addition, the plate deflections could be used to calculate the volume change in the spade cell oil-chamber and consequently to evaluate the calibration coefficients employed for spade cells.

Spade cells are typically installed at the bottom of a borehole. The borehole geometry influences the stress-strain behaviour of a soil adjacent to the spade cell and its effect should be incorporated into future analyses. The existing 2D and 3D soil penetration models have been set up in a manner that their expansion and incorporation of the borehole geometry is relatively easy and straightforward.

The penetration of more complex geometries could be simulated by improving the meshing strategy in the soil penetration models. FLAC and FLAC^{3D} programs are capable of computing the soil behaviour during the penetration process, provided that the area (volume) ratio of the deformed triangular (tetrahedral) sub zones to the zones in 2D (3D) analyses remains positive (i.e. illegal geometry criteria). The robustness of FLAC models to analyse penetrating objects with concave corners would increase by adding an automated remeshing scheme to FLAC that updates the mesh before reaching the illegal geometry criterion.

8.2.2 Experimental tests

The outcomes of numerical models developed in this thesis provided a better picture of stress-strain changes occurring in a soil during the penetration. The relative effect of various parameters on the penetration-induced changes in a soil has been determined in a series of three-dimensional models. The results of penetration analyses should be further validated by performing experimental tests. The results of 3D numerical penetration analyses could by compared with outcomes of chamber tests where a "chisel" prototype is penetrated into a soil under a range of conditions. The existing chamber test practice could also be improved by increasing the thickness of the soil layer above the spade cell face and using rigid rather than flexible boundaries.

9 REFERENCES

ABAQUS. (2003). *Getting Started with ABAQUS/Explicit: Keywords Version*. 6.2 Contact definition in ABAQUS/Explicit, 1-13.

Abu-Farsakh, M. Y., Tumay, M. T. and Voyiadjis, G. Z. (2003a). Finite element modeling and studying of factors affecting the Piezocone penetration test results. *In*: *82th Transportation Research Board Annual Meeting*, Washington, D.C.

Abu-Farsakh, M. Y., Tumay, M. T. and Voyiadjis, G. Z. (2003b). Numerical Parametric Study of Piezocone Penetration Test in Clays. *ASCE International Journal of Geomechanics*, 3 (2), 170-181.

Abu-Farsakh, M. Y., Voyiadjis, G. Z. and Tumay, M. T. (1998). Numerical analysis of the miniature piezocone penetration tests (PCPT) in cohesive soils. *International Journal for Numerical and Analytical methods in Geomechanics*, 22 (10), 791-818.

Acar, Y. B. and Tumay, M. T. (1986). Strain field around cones in steady penetration. *ASCE Journal of Geotechnical Engineering*, 112 (2), 207-213.

Acar, Y. B., Tumay, M. T. and Chan, A. (1982). Interpretation of the dissipation of penetration pore pressures. *In*: *International Symposium on Numerical Models in Geomechanics*, Zurich, Switzerland, Balkema, Rotterdam, 353-358.

Ahmadi, M. M., Byrne, P. M. and Campanella, R. G. (1999). Simulation of Cone Penetration with FLAC. *In*: *XI Pan American Conference on Geotechnical Engineering*, Igusau Falls, Brazil, 1365-1369.

Akbar, A. and Clarke, B. G. (2001). A Flat Dilatometer to Operate in Glacial Tills. *Geotechnical Testing Journal*, 24 (1), 51–60.

Al-Sahyea, N., Abduljauwad, S., Bashir, R., Al-Ghamedy, H. and Asi, I. (2003). Determination of parameters for a hyperbolic model of soils. *Proceedings of the Institution of Civil Engineers-Geotechnical Engineering*, 156 (2), 105-117.

Anderheggen, E. and Renau-Munoz, J. F. (2000). A parallel explicit solver for simulating impact and penetration of a three-dimensional body into a solid substrate. *Advances in Engineering Software*, 31 (12), 901-911.

Appel, D. W., Hubbard, P. G., Landweber, L., Laursen, E. M., McNown, J. S., Rouse, H., Siao, T. T., Toch, A. and Yih, C. S. (1965). Principle of irrotational flow. *In*: *Advanced Mechanics of Fluids*, New York, John Wiley & Sons, 68-82.

Atkinson, J. H. (2000). Non-linear soil stiffness in routine design. *Geotechnique*, 50 (5), 487-508.

Atkinson, J. H., Richardson, D. and Stallebrass, S. E. (1990). Effect of recent stress history on the stiffness of overconsolidated soil. *Geotechnique*, 40 (4), 531-540.

Aubeny, C. P. (1992). *Rational interpretation of in-situ tests in cohesive soils*. PhD thesis, Dept. of Civil Engineering, Massachusetts Institute of Technology, Cambridge, Massachusetts.

Aubeny, C. P. (2004). *Simple Plate*. (Personal communication), 15th July.

Aubeny, C. P., Whittle, A. J. and Ladd, C. C. (2000). Effects of disturbance on undrained strengths interpreted from pressuremeter tests. *ASCE Journal of Geotechnical and Geoenvironmental Engineering*, 126 (12), 1133-1144.

Baguelin, F., Jezequel, J. F., Lemee, E. and Mehaute, A. L. (1972). Expansion of cylindrical probes in cohesive soils. *ASCE Journal of the Soil Mechanics and Foundations*, 98 (11), 1129-1142.

Baker, T. H., Fox, L., Mayers, D. F. and Eright, K. (1964). Numerical solution of Fredholm integral equations of first kind. *Computer Journal*, 7, 141-148.

Baldi, G., Bellotti, R., Ghionna, V. and Jamiolkowski, M. (1986). Flat dilatometer tests in calibration chamber. *In*: *Use of in situ tests in geotechnical engineering*, Virginia, American Society of Civil Engineers Press, 431-446.

Baligh, M. M. (1975). *Theory of Deep Site Static Penetration Resistance*. Dept. of Civil Engineering, Massachusetts Institute of Technology, Cambridge, Massachusetts, Research Report R75-56.

Baligh, M. M. (1984). *The strain path method*. Dept. of Civil Engineering, Massachusetts Institute of Technology, Cambridge, Massachusetts, Research Report R84-01.

Baligh, M. M. (1985). Strain Path Method. *ASCE Journal of Geotechnical Engineering*, 111 (9), 1108-1136.

Baligh, M. M. (1986a). Undrained deep penetration, I: shear stresses. *Geotechnique*, 36 (4), 471-485.

Baligh, M. M. (1986b). Un-drained deep penetration, II: pore pressures. *Geotechnique*, 36 (4), 487-501.

Baligh, M. M., Azzouz, A. S. and Chin, C.-T. (1987). Disturbance due to "Ideal" tube sampling. *ASCE Journal of Geotechnical Engineering*, 113 (7), 739-757.

Baligh, M. M. and Chin, C.-T. (1987). Discussion: Flow field around cones in steady penetration. *ASCE Journal of Geotechnical Engineering*, 113 (1), 74-77.

Baligh, M. M. and Levadoux, J.-N. (1986). Consolidation after Undrained Piezocone penetration. II: Interpretation. *ASCE Journal of Geotechnical Engineering*, 112 (7), 727-745.

Baligh, M. M. and Scott, R. F. (1975). Quasi-static deep penetration in clays. *ASCE Journal of Geotechnical Engineering*, 101 (11), 1119-1133.

Baligh, M. M. and Scott, R. F. (1976). Analysis of wedge penetration in clay. *Geotechnique*, 26 (1), 185-208.

Barensten, P. (1936). Short description of a field testing method with a cone shaped sounding apparatus. *In*: *1st International Conference of Soil Mechanics and Foundation Engineering*, Harvard University, Boston, Massachusetts.

Batchelor, G. K. (1967). Kinematics of flow field. *In*: *An introduction to fluid dynamics*, 1st ed., Cambridge, Cambridge University Press, 74-79.

Berryman, J. G. (2004). Poroelastic shear modulus dependence on pore fluid properties arising in a model of thin isotropic layers. *International Geophysical Journal*, 157, 415-425.

Biran, A. and Breiner, M. M. G. (2002). *MATLAB 6 for Engineers*. 3rd ed., Harlow, England, Prentice Hall.

Bishop, A. W. and Eldin, G. (1950). Undrained triaxial test on saturated sands and their significance in the general theory of shear strength. *Geotechnique*, 2, 13-32.

Bishop, A. W. and Hight, D. W. (1977). The value of Poisson's ratio in saturated soils and rocks stressed under undrained conditions. *Geotechnique*, 27 (3), 369-384.

Bishop, A. W., Webb, D. L. and Lewin, P. I. (1965). Undisturbed samples of London Clay from the Ashford Common shaft : strength-effective stress relationship. *Geotechnique*, 15 (1), 1-31.

Bishop, R. F., Hill, R. and Mott, N. F. (1945). Theory of Indentation and Hardness Tests. *In*: *Physical Society of London*, 147-159.

Bolton, M. D. and Whittle, R. W. (1999). A non-linear elastic perfectly plastic analysis for plane strain undrained expansion tests. *Geotechnique*, 49 (1), 133-141.

Bond, A. J. and MacLeod, I. A. (2001). A strategy for computer modelling in geotechnical design. *Proceedings of the Institution of Civil Engineers-Geotechnical Engineering*, 149 (2), 95-102.

Bowden, F. P., Moore, A. J. W. and Tabor, D. (1943). The Ploughing and Adhesion of Sliding Metals. *Journal of Applied Physics*, 14 (2), 80-91.

Bowden, F. P. and Tabor, D. (1950). Adhesion between Solid Surfaces. *In*: *The friction and lubrication of solids*, Oxford, Clarendon Press, 299-314.

BSI. (1986). *Code of practice for foundations. BS 8004:1986.* British Standards Institution, London.

BSI. (1990). *Methods of test for Soils for civil engineering purposes-Part 5: Compressibility, permeability and durability tests. BS 1377-5:1990.* British Standards Institution, London.

BSI. (1999). *Code of practice for site investigations. BS 5930:1999.* British Standards Institution, London.

Budhu, M. and Wu, C., S. (1992). Numerical analysis of sampling disturbances in clay soils. *International Journal for Numerical and Analytical Methods in Geomechanics*, 16 (7), 467-492.

Burd, H. J. and Frydman, S. (1997). Bearing capacity of plane-strain footings on layered soils. *Canadian Geotechnical Journal*, 34, 241–253.

Burland, J. B. and Maswoswe, J. (1982). Discussion: In situ measurements of horizontal stress in over consolidated clay using push in spade shaped pressure cells. *Geotechnique*, 32 (3), 285-286.

Butterfield, R., Harkness, R. M. and Andrawes, K. Z. (1970). A stereo-photogrammetric method for measuring displacement fields. *Geotechnique*, 20 (3), 308-314.

Byrne, P. M., Cheung, H. and Yan, L. (1987). Soil parameters for deformation analysis of sand masses. *Canadian Geotechnical Journal*, 24 (3), 366-376.

Carder, D. R. and Bush, D. (2001). Development and testing of load cell pressuremeter. *Proceedings of the Institution of Civil Engineers-Geotechnical Engineering*, 149 (3), 141-142.

Carder, D. R. and Symons, I. F. (1989). Long-term performance of an embedded cantilever retaining wall. *Geotechnique*, 39 (1), 55-75.

Carder, D. R., Watson, G. V. R., Chandler, R. J. and Powrie, W. (1999). Long-term performance of an embedded retaining wall with a stabilizing base slab. *Proceedings of the Institution of Civil Engineers-Geotechnical Engineering*, 137 (2), 63-74.

Carter, J. P., Desai, C. S., Potts, D. M., Schweiger, H. F. and Sloan, S. W. (2000). Computing and Computer Modelling in Geotechnical Engineering. *In*: *GeoEng2000*, Melbourne, Australia, Technomic Publishing Co., 1157-1252.

Chandler, R. J. and Gutierrez, C. I. (1986). Filter-paper method of suction measurement. *Geotechnique*, 36 (2), 265-8.

Chin, C. T. (1986). *Open-ended pile penetration in saturated clays*. PhD thesis, Dept. of Civil Engineering, Massachusetts Institute of Technology, Cambridge, Massachusetts.

Chow, C. Y. (1983). Incompressible Potential Flows. *In*: *An introduction to computational fluid mechanics*, 2nd ed., Colorado, Johnson Publishing Company, 70-95.

Clark, J. (2005). *Performance of propped retaining wall at the CTRL, Ashford*. PhD thesis, School of Civil Engineering and the Environment, University of Southampton, Southampton, UK.

Clark, J., Richards, D. J. and Powrie, W. (2004). Wall installation effects-preliminary findings from a field study at the CTRL, Ashford. *In*: *Advances in Geotechnical Engineering: The Skempton Conference*, London, Thomas Telford, 691-699.

Clarke, B. G. (1995). *Pressuremeters in Geotechnical Design*. 1st ed., London, Chapman & Hall.

Clayton, C. R. I. and Bica, A. V. D. (1993). The design of diaphragm-type boundary total stress cells. *Geotechnique*, 43 (4), 523-535.

Clayton, C. R. I., Matthews, M. C. and Simons, N. E. (1995). *Site Investigation*. 2nd ed., Blackwell Science.

Clayton, C. R. I., Siddique, A. and Hopper, R. (1998). Effects of sampler design on tube sampling disturbance-numerical and analytical investigations. *Geotechnique*, 48 (6), 847-867.

Coetzee, M. J., Hart, R. D., Varona, P. M. and Cundall, P. A. (1993). *FLAC Basics*. 1st ed., Minnesota, Itasca Consulting Group Inc.

Cudmani, R. and Osinov, V. A. (2001). The cavity expansion problem for the interpretation of cone penetration and pressuremeter tests. *Canadian Geotechnical Journal*, 38, 622–638.

Cundall, P. A. (1976). *Explicit finite-difference methods in geomechanics*. Blacksburg, Virginia, American Society of Civil Engineers Press.

Cundall, P. A. and Hart, R. D. (1992). Numerical modelling of discontinua. *Engineering Computations*, 9 (2), 101-113.

Cundall, P. A. and Strack, O. D. L. (1979). A discrete numerical model for granular assemblies. *Geotechnique*, 29 (1), 47-65.

Dai, C. and Pells, P. J. N. (1999). Two-dimensional large strain consolidation prediction and incrementally deposited tailings. *In*: *FLAC and numerical modeling in geomechanics*, Minneapolis, Minnesota, Balkema, Rotterdam, 123-131.

Day, R. A. and Potts, D. M. (1994). Zero thickness interface elements-Numerical stability and application. *International Journal for Numerical and Analytical Methods in Geomechanics*, 18 (10), 689-708.

Day, R. A. and Potts, D. M. (1998). The effect of interface properties on retaining wall behaviour. *International Journal for Numerical and Analytical Methods in Geomechanics*, 22 (12), 1021-1033.

De Borst, R. and Vermeer, P. A. (1984). Possibilities and limitations of finite elements for limit analysis. *Geotechnique*, 34 (2), 199-210.

Desai, C. S., Lightner, J. G., Siriwardane, H. J. and Zaman, M. M. (1984). Thin layer element for interfaces and joints. *International Journal for Numerical and Analytical Methods in Geomechanics*, 8 (1), 19-43.

DiMaggio, F. L. and Sandler, I. S. (1971). Material model for granular soils. *ASCE Journal of Engineering Mechanics*, 97 (3), 935-950.

Donath, A. D. (1891). Unteruschungen uber Erdduck Stutzwande (referred by Tavenas et al. 1975). *Zeitschrift fur Bauwessen, Berlin.*

Doran, I. G., Sivakumar, V., Graham, J. and Johnson, A. (2000). Estimation of in situ stresses using anisotropic elasticity and suction measurements. *Geotechnique*, 50 (2), 189-196.

Duncan, J. M., Byrne, P., Wong, K. and Mabry, P. (1980). *Strength, stress-strain and Bulk modulus parameters for finite element analysis of stresses and movements in soil masses*. Dept. of Civil Engineering, University of California, Berkeley, UCB/GT/80-01.

Duncan, J. M. and Chang, C. Y. (1970). Nonlinear analysis of stress and strain in soils. *ASCE Journal of Soil Mechanics and Foundations*, 96 (5), 1629-1653.

Durgunoglu, H. T. and Mitchell, J. K. (1975a). Static penetration resistance of soils: I. Analysis. *In*: *The Conference on In Situ Measurement of Soil properties*, North Carolina, American Society of Civil Engineers Press, 151-171.

Durgunoglu, H. T. and Mitchell, J. K. (1975b). Static penetration resistance of soils: II. Evaluation of theory and implications for practice. *In*: *The Conference on In Situ Measurement of Soil properties*, North Carolina, American Society of Civil Engineers Press, 172-189.

Elsworth, D. (1998). Indention of a sharp penetrometer in a poroelastic medium. *International Journal of Solids and Structures*, 35 (34-35), 4895-4904.

Fahey, M., Been, K., Horsfield, D. and Jefferies, M. G. (1989). Discussion: Calibration chamber tests of a cone penetrometer in sand. *Geotechnique*, 39 (4), 729-731.

Fakharian, K. and Evgin, E. (2000). Elasto-plastic modeling of stress-path dependent behaviour of interfaces. *International Journal for Numerical and Analytical Methods in Geomechanics*, 24, 183-199.

Farhangi, S., Clayton, C. R. I. and Richards, D. J. (2006). Comparison of analytically and numerically determined strain paths around two geometries (to be presented). *In*: *4th International FLAC Symposium*, Madrid, Spain.

Farhangi, S., Richards, D. J. and Clayton, C. R. I. (2005). A review of the interpretation techniques for push-in pressure cell measurements. *In*: *50 years of pressuremeters international symposium*, Paris, ENPC, 279-280.

Finn, L. W. D. (1963). Boundary value problems of soil mechanics. *ASCE Journal of Soil Mechanics and Foundations*, 89 (5), 39-72.

Finno, R. J. (1993). Analytical Interpretation of Dilatometer Penetration Through Saturated Cohesive Soils. *Geotechnique*, 43 (2), 241-254.

Fioravante, V., Jamiolkowski, M., Lo Presti, D. C. F., Manfredini, G. and Pedroni, S. (1998). Assessment of the coefficient of the earth pressure at rest from shear wave velocity measurements. *Geotechnique*, 48 (5), 657-666.

Fluent. (2005). *CFD Flow Modelling Software and Services from Fluent Inc.* Available from: http://www.fluent.com/ [Accessed July 2005].

Frank, R., Guenot, A. and Humbert, P. (1982). Numerical analysis of contacts in geomechanics. *In*: *Numerical Methods in Geomechanics.*, Edmonton, Alberta, Canada, Balkema, Rotterdam, 37-45.

Frydman, S. and Burd, H. J. (1997). Numerical Studies of Bearing-Capacity Factor Nγ. *ASCE Journal of Geotechnical and Geoenvironmental Engineering*, 123 (1), 20-29.

Gadala, M. S., Oravas, G. A. E. and Dokainish, M. A. (1983). A Consistent Eulerian Formulation of Large Deformation problems in Statics and Dynamics. *International Journal of Non-Linear Mechanics*, 18 (1), 21-35.

Gander, W. and Gautschi, W. (2000). Adaptive Quadrature - Revisited. *BIT*, 40 (1), 84-101.

Gerber, E. (1929). *Untersuchungen uber die Druck-verteilung im Oertlick Belasteten Sand.* Dissertation Technische Hochschule, Zurich.

Ghionna, V. N. and Mortara, G. (2002). An elastoplastic model for sand-structure interface behaviour. *Geotechnique*, 52 (1), 41-50.

Giannakopoulos, A. E. and Suresh, S. (1997). Indentation of solids with gradients in elastic properties: 2. Axisymmetric indentors. *International Journal of Solids and Structures*, 34 (19), 2393-2428.

Gill, D. R. and Lehane, B. M. (2000). Extending the Strain Path Method analogy for modelling penetrometer installation. *International Journal for Numerical and Analytical Methods in Geomechanics*, 24 (5), 477-489.

Gill, D. R. and Lehane, B. M. (2001). An Optical Technique for Investigating Soil Displacement Patterns. *Geotechnical Testing Journal*, 24 (3), 324-329.

Goodman, R. E. (1999). *Karl Terzaghi: The Engineer as Artist*. Virginia, American Society of Civil Engineers Press.

Goodman, R. E., Taylor, R. L. and Brekke, T. L. (1968). A model for the mechanics of jointed rock. *ASCE Journal of Soil Mechanics and Foundations*, 94 (3), 637-659.

Green, R. A. and Ebeling, R. M. (2003). Modeling the Dynamic Response of Cantilever Earth-Retaining Walls Using FLAC. *In*: *3rd International Symposium on FLAC and FLAC3D Numerical Modeling in Geomechanics*, Sudbury, ON, Canada, Balkema, Rotterdam, 333-342.

Griffiths, D. V. (1982). Elasto-Plastic Analyses of Deep Foundations in Cohesive Soil. *International Journal for Numerical and Analytical Methods in Geomechanics*, 6, 211-218.

Grobbelaar, C. (2002). *The Performance of a Push-in Total Stress Cell under One-dimensional Loading Conditions*. BEng, Faculty of Engineering, University of Pretoria, Pretoria.

Gupta, R. C. (1991). Finite strain analysis for deep cone penetration. *ASCE Journal of Geotechnical Engineering*, 117 (10), 1610-1630.

Haber, R. B. (1984). A mixed Eulerian-Lagrangian displacement model for large-deformation analysis in solid mechanics. *Computer Methods in Applied Mechanics and Engineering*, 43 (3), 277-292.

Handy, R. L., Remmes, B., Moldt, S., Lutenegger, A. J. and Trott, G. (1982). In situ stress determination by Iowa stepped blade. *ASCE Journal of Geotechnical Engineering*, 108 (11), 1405-1422.

Head, K. H. (1998). Rowe cell consolidation and permeability tests. *In*: *Effective Stress Tests, Volume 3, Manual of Soil Laboratory Testing*, 2nd ed., John Wiley & Sons, 1129-1167.

Hermann, L. R. (1978). Finite element analysis of contact problems. *ASCE Journal of Engineering Mechanics*, 104 (5), 1043-1057.

Hess, J. L. (1975). Review of integral-equation techniques for solving potential-flow problems with emphasis on the surface-source method. *Computer Methods in Applied Mechanics and Engineering*, 5 (2), 145-196.

Heymann, G. (2004). *Spade cell stiffness.* (Personal communication), 16th September.

Hight, D. W. (1993). A review of sampling effects in clays and sands. *In*: *Conference on Advances in Underwater Technology, Ocean Science and Offshore Engineering*, London, UK, Kluwer Academic Publishers, 115-146.

Hight, D. W. (2001). Sampling effects in soft clay: An update on Ladd and Lambe (1963). *In*: *Soil Behavior and Soft Ground Construction*, Cambridge, Massachusetts, American Society of Civil Engineers, 86-121.

Hight, D. W., Boese, R., Butcher, A. P., Clayton, C. R. I. and Smith, P. R. (1992). Disturbance of the Bothkennar clay prior to laboratory testing. *Geotechnique*, 42 (2), 199-217.

Hight, D. W. and Leroueil, S. (2003). Characterisation of soils for engineering purposes. *In*: *Characterisation and Engineering Properties of Natural Soils*, Tokyo, 255-360.

Hoek, E., Grabinsky, M. W. and Diederichs, M. S. (1991). Numerical modeling of underground excavation design. *Transactions of Institute of Mining and Metallurgy, Section A*, 100, A22-A30.

Ho-Le, K. (1988). Finite Element Mesh Generation Methods: A Review and Classification. *Computer Aided Design*, 20 (1), 27-38.

Hopper, R. J. (1992). *The effects and implications of sampling clay soils.* PhD thesis, Department of Civil Engineering, University of Surrey, Guildford.

Horn, H. M. and Deere, D. U. (1962). Frictional Characteristics of Minerals. *Geotechnique*, 12 (4), 319-335.

Houlsby, G. T. (2003). Discussion: Determination of parameters for a hyperbolic model of soils. *Proceedings of the Institution of Civil Engineers-Geotechnical Engineering*, 156 (4), 225.

Houlsby, G. T. and Hitchman, R. (1988). Calibration chamber tests of a cone penetrometer in sand. *Geotechnique*, 38 (1), 39-44.

Houlsby, G. T., Wheeler, A. A. and Norbury, J. (1985). Analysis of undrained cone penetration as a steady state flow problem. *In*: *5th International Conference on Numerical Methods in Geomechanics*, Nagoya, Balkema, Rotterdam, 1767-1773.

Hsu, H.-H. and Huang, A.-B. (1999). Calibration of Cone Penetration Test in Sand. *Proceedings of National Science Council ROC(A)*, 23 (5), 579-590.

Hu, L. and Pu, J. (2004). Testing and modeling of soil-structure interface. *ASCE Journal of Geotechnical and Geoenvironmental Engineering*, 130 (8), 851-859.

Hu, Y. and Randolph, M. F. (1998a). H-adaptive FE Analysis of Elasto-Plastic Non-homogeneous Soil with Large Deformation. *Computers and Geomechanics*, 23 (1/2), 61-84.

Hu, Y. and Randolph, M. F. (1998b). A practical numerical approach for large deformation problems in soil. *International Journal for Numerical and Analytical Methods in Geomechanics*, 22 (5), 327-350.

Huang, A.-B. (1989). Strain-Path Analyses for arbitrary three-dimensional penetrometers. *International Journal for Numerical and Analytical Methods in Geomechanics*, 13 (5), 551-564.

Itasca. (2002a). *FLAC 3D ver. 2.1, Fast Lagrangian Analysis of Continua in 3 Dimensions User's guide*. 1st ed., Minnesota, Itasca Consulting Group Inc.

Itasca. (2002b). *FLAC ver. 4.0, Fast Lagrangian Analysis of Continua User's guide*. 2nd ed., Minnesota, Itasca Consulting Group Inc.

Itasca. (2004). *Itasca: Software*. Available from: http://www.itascacg.com/index.html [Accessed May 2005].

Jaky, J. (1944). The Coefficient of Earth Pressure at Rest. *Journal for Society of Hungarian Architects and Engineers*, 355-358.

Janbu, N. (1975). In situ measurement of initial stresses and deformation characteristics. *In*: *In situ measurement of soil properties*, North Carolina, American Society of Civil Engineers Press, 253-254.

Jardine, R. J. (1992a). Non-linear stiffness parameters from undrained pressuremeter tests. *Canadian Geotechnical Journal*, 29, 436-447.

Jardine, R. J. (1992b). Some observations on the kinematic nature of soil stiffness. *Soils and Foundations*, 32 (2), 111-124.

Jardine, R. J., Potts, D. M., Fourie, A. B. and Burland, J. B. (1986). Studies of the influence of non-linear stress–strain characteristics in soil–structure interaction. *Geotechnique*, 36 (3), 377-396.

Jardine, R. J., Symes, M. J. and Burland, J. B. (1984). The measurement of soil stiffness in the triaxial apparatus. *Geotechnique*, 34 (3), 323-340.

Johnson, K. L. (1970). The correlation of indentation experiments. *Journal of the Mechanics and Physics of Solids*, 18, 115-126.

Katona, M. G. (1983). A simple contact-friction interface element with applications to buried culverts. *International Journal of Numerical and Analytical Methods in Geomechanics*, 7 (3), 371-384.

Kenwright, D. and Mallinson, G. (1992). A 3-D Streamline Tracking Algorithm Using Dual Stream Functions. *In*: *IEEE Visualization 92*, Boston, Massachusetts, 62-68.

Kiousis, P. D., Voyiadjis, G. Z. and Tumay, M. T. (1988). A large strain theory and its application in the analysis of the cone penetration mechanism. *Journal for Numerical and Analytical Methods in Geomechanics*, 12 (1), 45-60.

Klar, A. and Einav, I. (2003). Pile installation using FLAC. *In*: *3rd International FLAC Symposium*, Sudbury, Canada, Balkema, Rotterdam.

Klotz, E. U. and Coop, M. R. (2001). An investigation of the effect of soil state on the capacity of driven piles in sands. *Geotechnique*, 51 (9), 733-751.

Konietzky, H., Kamp, L. t. and Kamlot, P. (1999). A simple procedure to model flow through fractures and double porosity and its practical application. *In*: *FLAC and numerical modeling in geomechanics*, Minneapolis, Minnesota, Balkema, Rotterdam, 141-145.

Kuchemann, D. and Weber, J. (1953). *Aerodynamics of porpoulsion*. New York, McGraw Hill.

Kulhawy, F. H. (1975). Stress deformation properties of rock and rock discontinuities. *Engineering Geology*, 9 (4), 327-350.

Kurup, P. U., Voyiadjis, G. Z. and Tumay, M. T. (1994). Calibration chamber studies of piezocone test in cohesive soils. *ASCE Journal of Geotechnical Engineering*, 120 (1), 81-107.

La Rochelle, P., Leroueil, S. and Tavenas, F. (1987). Discussion: Strain Path Method. *ASCE Journal of Geotechnical Engineering*, 113 (9), 1088-1090.

Ladd, C. C., Foott, R., Ishihara, K., Schlosser, F. and Poulos, H. G. (1977). Stress-deformation and strength characteristics. State of the art report. *In*: *Ninth International Conference on Soil Mechanics and Foundation Engineering*, Tokyo, 421-494.

Lade, P. V. (1988). Effects of voids and volume changes on the behaviour of frictional materials. *International Journal for Numerical and Analytical Methods in Geomechanics*, 12, 351–370.

Lambe, T. W. (1967). The Stress Path Method. *ASCE Journal of Soil Mechanics and Foundations*, 93 (6), 309-331.

Lambe, T. W. and Marr, W. A. (1979). Stress Path Method: Second Edition. *ASCE Journal of Geotechnical Engineering*, 105 (6), 727-738.

Lambe, T. W. and Whitman, R. V. (1969). Fundamentals of frictional behavior. *In*: *Soil mechanics*, New York, Wiley, 61-69.

Lee, J., Salgado, R. and Paik, K. (2003). Estimation of the load capacity of pipe piles in sand based on CPT results. *ASCE Journal of Geotechnical and Geoenvironmental Engineering*, 129 (5), 391-403.

Lehane, B. M. and Gavin, K. G. (2001). Base resistance of jacked pipe piles in sands. *ASCE Journal of Geotechnical and Geoenvironmental Engineering*, 127 (6), 473-480.

Lehane, B. M. and Jardine, R. J. (1994). Shaft capacity of driven piles in sand: a new design approach. *In*: *Conference on the Behaviour of Offshore Structures*, Boston, Massachusetts, 23–36.

Lehane, B. M., Jardine, R. J., Bond, A. J. and Frank, R. (1993). Mechanisms of shaft friction in sand from instrumented pile tests. *ASCE Journal of Geotechnical Engineering*, 119 (1), 19-35.

Lemos, L. J. L. and Vaughan, P. R. (2000). Clay interface shear resistance. *Geotechnique*, 50 (1), 55-64.

Leroueil, S. and Vaughan, P. R. (1990). The general and congruent effects of structure in natural soils and weak rocks. *Geotechnique*, 40 (3), 467-488.

Leung, C. F., Lee, F. H. and Yet, N. S. (1996). The role of particle breakage in pile creep in sand. *Canadian Geotechnical Journal*, 33 (6), 888-898.

Levadoux, J. N. and Baligh, M. M. (1980). *Pore pressures during cone penetration in clays*. Dept. of Civil Engineering, Massachusetts Institute of Technology, Cambridge, Massachusetts, Research report R80-15.

Levadoux, J.-N. and Baligh, M. M. (1986). Consolidation after Undrained Piezocone penetration. I: Prediction. *ASCE Journal of Geotechnical Engineering*, 112 (7), 707-726.

Liyanapathirana, D. S., Deeks, A. J. and Randolph, M. F. (2000). Numerical modelling of large deformations associated with driving of open-ended piles. *International Journal for Numerical and Analytical Methods in Geomechanics*, 24 (14), 1079-1101.

Lu, Q., Hu, Y. and Randolph, M. F. (2001). Deep penetration in soft clay with strength increasing with depth. *In*: *11th International Offshore and Polar Engineering Conference*, Stavanger, International Society of Offshore and Polar Engineers, 453-458.

Lu, Q., Randolph, M. F., Hu, Y. and Bugarski, I. C. (2004). A numerical study of cone penetration in clay. *Geotechnique*, 54 (4), 257-267.

Lutenegger, A. and Timian, D. (1986). In situ tests with K0 stepped blade. *In*: *Use of in situ tests in geotechnical engineering*, Virginia, American Society of Civil Engineers Press, 731-751.

Mabsout, M. and Sadek, S. (2003). A study of the effect of driving on pre-bored piles. *International Journal for Numerical and Analytical Methods in Geomechanics*, 27 (2), 133-146.

Mair, R. J. and Wood, D. M. (1987). *Pressuremeter Testing. Methods and Interpretation*. Construction Industry Research and Information Association (CIRIA), London.

Mantaras, F. M. and Schnaid, F. (2002). Cylindrical cavity expansion in dilatant cohesive-frictional materials. *Geotechnique*, 52 (5), 337-348.

Marchetti, S. (1980). In situ tests by flat dilatometer. *ASCE Journal of Geotechnical Engineering*, 106 (3), 299-321.

Marsland, A. and Randolph, M. F. (1977). Comparison of the results from pressuremeter tests and large in-situ plate tests in London clay. *Geotechnique*, 27 (2), 217–243.

Massarsch, K. R. (1979). Lateral earth pressure in normally consolidated clay. *In*: *7th European Conference Soil Mechanics*, Brighton, 245-250.

Massarsch, K. R., Broms, B. B. and Holtz, D. (1975a). Measurement of in-situ stresses and stress changes. *In*: *In situ measurement of soil properties*, North Carolina, American Society of Civil Engineers Press, 260-262.

Massarsch, K. R., Holtz, R. D., Holm, B. G. and Frediksson, A. (1975b). Measurement of horizontal in-situ stresses. *In*: *In situ measurement of soil properties*, North Carolina, American Society of Civil Engineers Press, 266-286.

MathWorks. (2004). *The MathWorks - MATLAB and Simulink*. Available from: http://www.mathworks.com/ [Accessed July 2004].

MathWorks. (2005). Curve fitting toolbox for use with MATLAB. *In*: *MATLAB User's guide, version 1*.

Mayne, P. W. and Kulhawy, F. H. (1982). K0-OCR relationship in soil. *ASCE Journal of Geotechnical Engineering*, 108 (6), 851-872.

Meigh, A. C. (1987). *Cone Penetration Testing. Methods and Interpretation*. Construction Industry Research and Information Association (CIRIA), London.

Meyerhof, G. G. (1951). The Ultimate Bearing Capacity of Foundations. *Geotechnique*, 2 (4), 301-331.

Meyerhof, G. G. (1961). The ultimate bearing capacity of wedge-shaped foundations. *In*: *5th International Conference on Soil Mechanics and Foundation Engineering*, 105-109.

Milne-Thomson, L. M. (1968). Theorem of Schwarz and Christoffel. *In*: *Theoretical Hydrodynamics*, 5th ed., London, The Macmillan Press Ltd, 274-292.

Mitchell, J. K. (1993). Strength and Deformation Behavior. *In*: *Fundamentals of soil behavior*, 2nd ed., New York, Wiley, 360-375.

New, B. M. and Bowers, K. H. (1994). Ground movement model validation at the Heathrow Express trial tunnel. *In*: *Tunnelling 94*, London, Chapman and Hall, 301-329.

Norrany, I., Frydman, S. and Detournay, C. (1999). Prediction of soil slope deformation due to wetting. *In*: *FLAC and numerical modeling in geomechanics*, Minneapolis, Minnesota, Balkema, Rotterdam, 101-107.

Nunn, R. H. (1989). Stream function. *In*: *Intermediate fluid mechanics*, 1st ed., New York, Hemisphere Publishing Corporation, 32-83.

Pande, G. N. and Sharma, K. G. (1979). On joint/interface elements and associated problems of numerical ill conditioning. *International Journal for Numerical and Analytical Methods in Geomechanics*, 3, 293-300.

Peattie, K. R. and Sparrow, R. W. (1954). The Fundamental Action of Earth Pressure Cells. *Journal of Mechanics and Physics of Solids*, 2, 141-155.

Pedersen, R. C., Olson, R. E. and Rauch, A. F. (2003). Shear and Interface Strength of Clay at Very Low Effective Stress. *Geotechnical Testing Journal*, 26 (1), 1-8.

Penman, A. D. M. and Charles, J. A. (1981). Assessing the risk of hydraulic fracturing in dam cores. *In*: *10th International Conference of Soil Mechanics and Foundation Engineering*, Stockholm, 457-462.

Potts, D. M., Axelsson, K., Grande, L., Schweiger, H. and Long, M. (2002). *Guidelines for the Use of Advanced Numerical Analysis*. Thomas Telford, Ltd.

Potts, D. M. and Zdravkovic, L. (1999). *Finite element analysis in geotechnical engineering: theory*. London, Thomas Telford.

Potyondy, J. G. (1961). Skin friction between various soils and construction material. *Geotechnique*, 11, 339-353.

Powell, J. J. M., Marsland, A. and Alkafaji, A. N. (1983). Pressuremeter testing of glacial clay tills. *In*: *International Symposium of Soil and Investigations by in situ testing*, Paris, 373-378.

Powrie, W. (2004). *Soil mechanics: Concepts and Applications*. 2nd ed., London, Spon Press.

Powrie, W., Chandler, R. J., Carder, D. R. and Watson, G. V. R. (1999). Back-analysis of an embedded retaining wall with a stabilizing base slab. *Proceedings of the Institution of Civil Engineers-Geotechnical Engineering*, 137 (2), 75-86.

Powrie, W., Ni., Q., Harkness, R. M. and Zhang, X. (2005). Numerical modelling of plane strain tests on sands using a particulate approach. *Geotechnique*, 55 (4), 297-306.

Prevost, J. H. (1978). Anisotropic Undrained Stress-Strain Behaviour of Clays. *ASCE Journal of Geotechnical Engineering*, 104 (8), 1075-1090.

Rafalovich, A. (1989). *The mechanics of plate penetration in clays*. MSc thesis, Dept. of Civil Engineering, Massachusetts Institute of Technology, Cambridge, Massachusetts.

Randolph, M. F., Dolwin, J. and Beck, R. (1994). Design of driven piles in sand. *Geotechnique*, 44 (3), 427-448.

Randolph, M. F. and Wroth, C. P. (1978). Analysis of Deformation of Vertically Loaded Piles. *ASCE Journal of the Soil Mechanics and Foundations*, 104 (12), 1465-1488.

Reddy, E. S., Chapman, D. N. and Sastry, V. (2000). Direct Shear Interface Test for Shaft Capacity of Piles in Sand. *Geotechnical Testing Journal*, 23 (2), 199-205.

Richards, D. J., Clark, J., Powrie, W. and Heyman, G. (2005). An evaluation of total horizontal stress measurements using push-in pressure cells in an overconsolidated clay deposit. *Proceedings of the Institution of Civil Engineers-Geotechnical Engineering (accepted for publication)*.

Roy, M., Blanchet, R., Tavenas, F. and Larochelle, P. (1981). Behaviour of a sensitive clay during pile driving. *Canadian Geotechnical Journal*, 18 (1), 67-85.

Rust, E. (1996). *The interpolation of incomplete piezocone dissipation tests*. PhD thesis, Department of Civil Engineering, University of Surrey, Guildford.

Ryley, M. D. and Carder, D. R. (1995). The performance of push-in spade cells installed in stiff clay. *Geotechnique*, 45 (3), 533-539.

Sagaseta, C. (1987). Analysis of undrained soil deformation due to ground loss. *Geotechnique*, 37 (3), 301-320.

Sagaseta, C. and Whittle, A. J. (2001). Prediction of ground movements due to pile driving in clay. *ASCE Journal of Geotechnical and Geoenvironmental Engineering*, 127 (1), 55-66.

Sagaseta, C., Whittle, A. J. and Santagata, M. (1997). Deformation analysis of shallow penetration in clay. *International Journal for Numerical and Analytical Methods in Geomechanics*, 21 (10), 687-719.

Salgado, R., Mitchell, J. K. and Jamiolkowski, M. (1997). Cavity expansion and penetration resistance in sand. *ASCE Journal of Geotechnical and Geoenvironmental Engineering*, 123 (4), 344-354.

Salgado, R., Mitchell, J. K. and Jamiolkowski, M. (1998). Calibration chamber size effects on penetration resistance in sand. *ASCE Journal of Geotechnical and Geoenvironmental Engineering*, 124 (9), 878-888.

Santagata, M. C. and Germaine, J. T. (2002). Sampling Disturbance Effects in Normally Consolidated Clays. *ASCE Journal of Geotechnical and Geoenvironmental Engineering*, 128 (12), 997-1006.

Schmertmann, J. H. (1980). Discussion: In situ test by flat dilatometer. *ASCE Journal of Geotechnical Engineering*, 106 (3), 831-837.

Schnaid, F. and Houlsby, G. T. (1991). An Assessment of Chamber Size Effects in the Calibration of In Situ Tests in Sand. *Geotechnique*, 41 (3), 437-445.

Shohet, E. D. C. (1995). Prediction of in situ horizontal stresses in clay soils from the measurement of undrained shear strength, plasticity index and vertical effective stress. *Proceedings of the Institution of Civil Engineers-Geotechnical Engineering*, 113 (4), 206-214.

Siddique, A. (1990). *A numerical and experimental study of sampling disturbance*. PhD thesis, Department of Civil Engineering, University of Surrey, Guildford.

Siddique, A., Clayton, C. R. I. and Hopper, R. J. (1999). The Effects of Varying Centreline Tube Sampling Disturbance on the Behaviour of Reconstituted Clay. *Geotechnical Testing Journal*, 22 (3), 245-256.

Silvestri, V. and Tabib, C. (1993). Flow field around a cylindrical pile during steady penetration. *Canadian Geotechnical Journal*, 30 (2), 369-376.

Simpson, B., O'Riordan, N. J. and Croft, D. D. (1979). A computer model for the analysis of ground movements in London Clay. *Geotechnique*, 29 (2), 149-175.

Skempton, A. W. (1943). Notes on the compressibility of clays. *Quarterly Journal of the Geological Society of London*, 100, 119–135.

Skempton, A. W. (1951). The Bearing Capacity of Clays. *Building Research Congress, Division 1*, 180-189.

Skempton, A. W. and Sowa, V. A. (1963). The behaviour of saturated clays during sampling and testing. *Geotechnique*, 13 (4), 269-290.

Sokolovski, V. V. (1965). *Statics of granular media.* Tarrytown, New York, Pergamon Press.

Streeter, V. L. (1961). *Handbook of fluid dynamics.* New York, McGraw Hill.

Subba Rao, K. S., Allam, M. M. and Robinson, R. G. (2001). Discussion on 'Direct Shear Interface Test for Shaft Capacity of Piles in Sand'. *Geotechnical Testing Journal*, 24 (3), 334-335.

Sullivan, T. A. (1994). *Catalog of Apollo Experiment Operations.* NASA - Johnson Space Center, Houston, Texas, Reference Publication 1317.

Susila, E. and Hryciw, R. D. (2003). Large displacement FEM modelling of the cone penetration test (CPT) in normally consolidated sand. *International Journal for Numerical and Analytical Methods in Geomechanics*, 27 (7), 585-602.

Tarchetti, S. (1975). A new in situ test for the measurement of horizontal soil deformability. *In*: *In situ measurement of soil properties*, North Carolina, American Society of Civil Engineers Press, 255-259.

Tavenas, F. A. (1975). In situ measurement of initial stresses and deformation characteristics. *In*: *In situ measurement of soil properties*, North Carolina, American Society of Civil Engineers Press, 263-270.

Tavenas, F. A., Blanchette, G. and Leroueil, S. (1975). Difficulties in the in situ determination of Ko in soft sensitive clays. *In*: *in situ measurement of soil properties*, North Carolina, American Society of Civil Engineers Press, 450-476.

Tedd, P., Chard, B. M., Charles, J. A. and Symons, I. F. (1984). Behaviour of a propped embedded retaining wall in stiff clay at Bell Common Tunnel. *Geotechnique*, 34 (4), 513-532.

Tedd, P. and Charles, J. A. (1981). In situ measurement of horizontal stress in over-consolidated clay using push-in spade-shaped pressure cells. *Geotechnique*, 31 (4), 554-558.

Tedd, P. and Charles, J. A. (1983). Evaluation of push-in pressure cell results in stiff clay. *In*: *Symposium International - Reconnaissance des Sols et des Roches par Essais en Place (In situ Testing)*, Paris, Int. Assoc of Engineering Geology, 579-584.

Tedd, P., Charles, J. A. and Clarke, B. G. (1985). The measurement of horizontal stress changes in stiff clay using push-in spade-shaped pressure cells and a self-boring pressure-meter. *Ground Engineering*, 18 (1), 28, 30-31.

Tedd, P., Towell, J. J., Charles, J. A. and Uglow, I. M. (1989). In-situ measurement of earth pressures using push-in spade-shaped cells-10 years' experience. *In*: *Geotechnical Instrumentation in Civil Engineering Projects*, Nottingham, Thomas Telford, 701-715.

Teh, C. I. (1987). *An analytical study of cone penetration test*. PhD thesis, Hertford College, University of Oxford, Oxford.

Teh, C. I. and Houlsby, G. T. (1991). An analytical study of cone penetration test in clay. *Geotechnique*, 41 (1), 17-34.

Temporal, J. and Lawrence, G. J. L. (1985). Tunnelling machine performance in the Oxford clay. *In*: *Tunnelling 85*, London, Institution of Mining and Metallurgy, 317-327.

Terzaghi, C. (1925a). Principles of Soil Mechanics: II-Compressive Strength of Clay. *Engineering News-Record*, 95 (20), 796-800.

Terzaghi, C. (1925b). Principles of Soil Mechanics: VII-Friction in Sand and in Clay. *Engineering News-Record*, 95 (26), 1026-1029.

Terzaghi, K. (1941). Undisturbed clay samples and undisturbed clays. *Journal of the Boston society of Civil Engineers*, 28 (3), 211-231.

Terzaghi, K. (1960). Fundamental studies of shearing strength. *In*: *From theory to practice in soil mechanics*, New York, John Wiley & Sons, 164-181.

Terzaghi, K. and Peck, R. B. (1962). *Soil Mechanics in Engineering Practice*. 12th ed., New York, John Wiley & Sons.

Thomas, A. H. (2003). *Numerical modelling of sprayed concrete lined (SCL) tunnels*. PhD thesis, School of Civil Engineering and the Environment, University of Southampton, Southampton, UK.

Timoshenko, S. and Woinowsky-Krieger, S. (1959). *Theory of plates and shells*. 2nd ed., New York, McGraw-Hill.

Tomlinson, M. J. (1957). The adhesion of Clay Piles Driven in
Clay Soils. *In*: *4th International Conference on Soil Mechanics and Foundation Engineering*, London, Butterworths scientific publications, 66-71.

Tory, A. C. and Sparrow, R. W. (1967). The influence of diaphragm flexibility on the performance of an earth pressure cell. *Journal of Scientific Instruments*, 44.

Tsubakihara, Y., Kishida, H. and Nishiyama, T. (1993). Friction between cohesive soils and steel. *Soils and Foundations*, 33 (2), 145-156.

Tumay, M., Acar, Y., Cekirge, M. H. and Ramesh, N. (1985). Flow field around cones in steady penetration. *ASCE Journal of Geotechnical Engineering*, 111 (2), 193-204.

Uesugi, M. and Kishida, H. (1986). Influential factors of friction between steel and dry sands. *Soils and Foundations*, 26 (2), 29-42.

Uesugi, M., Kishida, H. and Tsubakihara, Y. (1988). Behaviour of sand particles in sand-steel friction. *Soils and Foundations*, 28 (1), 107-118.

Uglow, I. M. (1989). *The measurement of In-situ horizontal earth pressures in a range of cohesive soils*. MSc thesis, Department of Civil Engineering, University of Surrey, Guildford.

Van den Berg, P. (1994). *Analysis of soil penetration*. PhD thesis, Strategic Research Department of Geotechnics, Delft University of Technology, Delft.

Van den Berg, P., De Borst, R. and Huetink, H. (1996). An Eulerian finite element model for penetration in layered soil. *International Journal for Numerical and Analytical Methods in Geomechanics*, 20, 865-886.

Vaughan, P. R., Maccarini, M. and Mokhtar, S. M. (1988). Indexing the engineering properties of residual soil. *Quarterly Journal of Engineering Geology & Hydrogeology*, 21 (1), 69-84.

Vesic, A. S. (1972). Expansion of Cavities in Infinite Soil Mass. *ASCE Journal of Soil Mechanics and Foundations*, 98 (3), 265-290.

Voyiadjis, G. Z., Kurup, P. U. and Tumay, M. T. (1993). Preparation of large-size cohesive specimens for calibration chamber testing. *Geotechnical Testing Journal*, 16 (3), 339–349.

Watts, K. S. and Charles, J. A. (1988). In situ measurement of vertical and horizontal stress from a vertical borehole. *Geotechnique*, 38 (4), 619-626.

Weiler, W. A. and Kulhawy, F. H. (1982). Factors affecting stress cell measurements in soil. *ASCE Journal of Geotechnical Engineering*, 108 (12), 1529-1548.

Weinstein, A. (1946). On axially symmetric flows. *Quarterly of Applied Mathematics*, 5 (4), 419-423.

Welker, A. L., Bowders, J. J. and Gilbert, R. B. (1999). Applied Research Using a Transparent Material with Hydraulic Properties Similar to Soil. *Geotechnical Testing Journal*, 22 (3), 266-270.

White, D. J. (2002). *An investigation into the behaviour of pressed-in piles*. PhD thesis, Churchill College, University of Cambridge.

White, D. J. and Bolton, M. D. (2004). Displacement and strain paths during plane-strain model pile installation in sand. *Geotechnique*, 54 (6), 375-397.

White, D. J., Take, W. A. and Bolton, M. D. (2003). Soil deformation measurement using particle image velocimetry (PIV) and photogrammetry. *Geotechnique*, 53 (7), 619-631.

Whittle, A. J. (1992). Constitutive modelling for deep penetration problems in clay. *In*: *3rd International Conference on Computational Plasticity: Fundamentals and Applications*, 883-894.

Whittle, A. J. (1994). Discussion: Analytical interpretation of dilatometer penetration through saturated cohesive soils. *Geotechnique*, 44 (3), 545-550.

Whittle, A. J. and Aubeny, C. P. (1991). Pore pressure fields around piezocone penetrometers installed in clays. *In*: *International Conference on Computer Methods and Advances in Geomechanics*, Cairns, Austria, Balkema, Rotterdam, 285-290.

Whittle, A. J. and Aubeny, C. P. (1993). The effect of installation disturbance on interpretation of in-situ tests in clay. *In*: *Worth Memorial Symposium*, St Catherine's College, Oxford, Thomas Telford Services Ltd, 742-767.

Whittle, A. J. and Kavvadas, M. J. (1994). Formulation of MIT-E3 constitutive model for overconsolidated clays. *ASCE Journal of Geotechnical Engineering*, 120 (1), 173-198.

Whittle, A. J., Sutabutr, T., Germaine, J. T. and Varney, A. (2001). Prediction and interpretation of pore pressure dissipation for a tapered piezoprobe. *Geotechnique*, 51 (7), 601-617.

Witte, F. C. D. and Wolthers, A. (2002). *DIANA-Finite Element Analysis User's Manual release 8.1*. 1st ed., Delft, Amsterdam, TNO Building and Construction Research.

Wood, D. M. (1992). *Soil behaviour and critical state soil mechanics*. Cambridge, Cambridge University Press.

Wood, D. M. and Wroth, C. P. (1977). Some laboratory experiments related to the results of pressuremeter tests. *Geotechnique*, 27 (2), 181-201.

Woods, R. I. and Clayton, C. R. I. (1993). The Application of the CRISP Finite Element Program to Practical Retaining Wall Problems. *In*: *Retaining Structures*, London, Thomas Telford, 102-111.

Wroth, C. P. (1975). In situ measurement of initial stresses and deformation characteristics. *In*: *In situ measurement of soil properties*, North Carolina, American Society of Civil Engineers Press, 181-230.

Wroth, C. P. (1984). The interpretation of in situ soil tests. *Geotechnique*, 34 (4), 449-489.

Wroth, C. P., Randolph, M. F., Houslby, G. T. and Fahey, M. (1979). *A review of the engineering properties of soils with particular reference to the shear modulus*. University of Oxford, Oxford, Report No. 1523/84.

Xu, M. (2005). *The behaviour of soil behind full-height integral abutments*. PhD thesis, School of Civil Engineering and the Environment, University of Southampton, Southampton, UK.

Yih, C. S. (1957). Stream Functions in Three Dimensional Flows. *La Houlle Blanche*, 3, 445-450.

Yu, H. S. (2004). James K. Mitchell Lecture: In situ soil testing: from mechanics to interpretation. *In*: *ISC-2 on Geotechnical and Geophysical Site Characterization*, Millpress, Rotterdam, 1575-1582.

Yu, H. S., Herrmann, L. R. and Boulanger, R. W. (2000). Analysis of steady cone penetration in clay. *ASCE Journal of Geotechnical and Geoenvironmental Engineering*, 126 (7), 594-605.

Yu, H. S. and Mitchell, J. K. (1998). Analysis of cone resistance: Review of methods. *ASCE Journal of Geotechnical and Geoenvironmental Engineering*, 124 (2), 140-149.

Zienkiewicz, O. C. (1986). *The finite element method*. 3rd ed., London, UK, McGraw Hill.

Zienkiewicz, O. C. and Zhu, J. Z. (1991). Adaptivity and mesh generation. *International Journal for Numerical Methods in Engineering*, 32, 783-810.

10 APPENDICES

10.1 Flow equations around the “simple wall”

This appendix summarises the closed-form solutions for flow characteristics around the “simple wall” geometry.

10.1.1 Velocity of superimposed flow

The velocity equations for the flow around the “simple wall” were derived using superposition. Uniform flow was assumed to be in the vertical direction, having a velocity of U[LT^{-1}], Equation 10-1:

$$v_x = 0, v_z = U$$

Equation 10-1

A line source located at the origin with strength of V[LT^{-3}] emits flow in all directions. For a unit thickness of the line source, the vertical and horizontal components of the velocity are given by Equation 10-2:

$$v_x = \frac{V}{2\pi r} \cdot \frac{x}{r},\ v_z = \frac{V}{2\pi r} \cdot \frac{z}{r}\ ,\ r = \sqrt{x^2 + z^2}$$

Equation 10-2

The velocity equations for the superimposed flow around the “simple wall” were obtained by adding up the corresponding velocity components of the uniform flow to those of the line source, Equation 10-3:

$$v_x = \frac{V}{2\pi r} \cdot \frac{x}{r}, v_z = \frac{V}{2\pi r} \cdot \frac{z}{r} + U$$

Equation 10-3

10.1.2 The geometry of the "simple wall"

The geometry of the "simple wall" was derived from the stream function (Ψ) of the half-body. The definition of streamlines (Batchelor, 1967) was used to obtain the stream function by integrating the vertical velocity, Equation 10-4:

$$v_z = -\frac{\partial \Psi}{\partial x} \rightarrow \Psi = -\int v_z dx \Rightarrow \Psi = -Ux + \frac{V}{2\pi}\tan^{-1}\left(\frac{z}{x}\right) - \frac{V}{4}$$ **Equation 10-4**

In the next step, the value of the stream function for the half-body was evaluated (Ψ_0). The half-body streamline passes through the point (0,- ∞). Substituting this point in the stream function (Equation 10-4) gives the stream function value for the half-body, Equation 10-5:

$$\Psi_0 = -\frac{V}{2}$$ **Equation 10-5**

Finally, Equation 10-6 was solved for the known value of (Ψ_0) to determine the coordinates (x,z) of the "simple wall" geometry.

$$\Psi(x,z) - \Psi_0 = 0$$ **Equation 10-6**

The tip location S(0,a) can be derived from velocity expressions. The tip is a stagnation point (i.e. vertical component of the velocity for the superimposed flow becomes zero at this point). The location of the stagnation point was therefore determined by setting the vertical velocity of the superimposed flow equal to zero Equation 10-7:

$$v_z = 0 \rightarrow a = -\frac{V}{2\pi U}$$ **Equation 10-7**

The half-width of the "simple wall" (w) can be calculated from the stream function. The maximum half-width of the "simple wall" is reached at infinity above the tip. By solving Equation 10-6 for the point (w,+∞), the half-width of the "simple wall" can be determined, Equation 10-8:

$$\Psi\left(w,+\infty\right)-\Psi_0=0\rightarrow w=\frac{V}{2U}=-\pi a \qquad \textbf{Equation 10-8}$$

It can be seen from the last two equations that the half-width of the "simple wall" (w) is π times the distance between the tip and the origin (a).

10.1.3 Strain rates and strain paths

Strain rates were derived by obtaining partial derivatives from the velocity equations. Various components of the strain rate tensor are given in Equations 10-9, 10-10 and 10-11:

$$\dot{\varepsilon}_{xx}=-\partial v_x/\partial x=+V/(2\pi r^2)\cdot\cos(2\alpha),\ \ \sin\alpha=z/r \qquad \textbf{Equation 10-9}$$

$$\dot{\varepsilon}_{zz}=-\partial v_z/\partial z=-V/(2\pi r^2)\cdot\cos(2\alpha),\ \ \cos\alpha=x/r \qquad \textbf{Equation 10-10}$$

$$\dot{\varepsilon}_{xz}=-1/2\cdot(\partial v_x/\partial z+\partial v_z/\partial x)=+V/(2\pi r^2)\cdot\sin(2\alpha) \qquad \textbf{Equation 10-11}$$

It is evident that the total sum of the principal strain rates is equal to zero (i.e. the conservation of volume). Strains were calculated by integrating strain rates on the time domain (dt) along each streamline. The definition of the velocity (v) was used to convert the time integral (dt) to a length (ds) and subsequently to an angle integral (dα) using trigonometric relations in the ABC triangle where AB=ds was a segment of the streamline, as shown in Figure 10.1. Equation 10-12 shows the strain path integral on the (dα) domain:

$$\varepsilon=\int\dot{\varepsilon}dt=\int\frac{\dot{\varepsilon}}{v}ds=\int\frac{\dot{\varepsilon}.r}{v\cos\gamma}d\alpha \qquad \textbf{Equation 10-12}$$

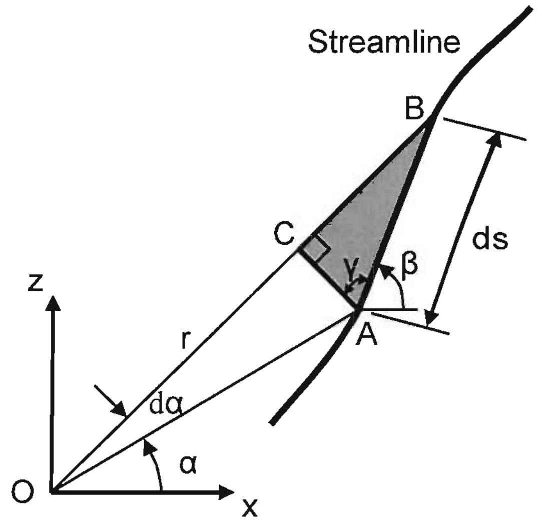

Figure 10.1 The length segment (ds) of the strain integral on a streamline

By substituting Equations 10-13, 10-14 and 10-15 in the strain path integral, the general strain path expression for the "simple wall" can be calculated, Equation 10-16.

$$\gamma + (\beta - \alpha) = \frac{\pi}{2} \rightarrow \cos\gamma = \sin(\beta - \alpha) = \sin\beta\cos\alpha - \cos\beta\sin\alpha$$

Equation 10-13

$$v_x = v\cos\beta, v_z = v\sin\beta \rightarrow \cos\gamma = v_z / v\cos\alpha - v_x / v\sin\alpha$$

Equation 10-14

$$v_x = \frac{V}{2\pi r}\cdot\cos\alpha,\ v_z = \frac{V}{2\pi r}\cdot\sin\alpha\ + U \rightarrow \cos\gamma = \frac{U\cos\alpha}{v}$$

Equation 10-15

$$\varepsilon = \int \frac{\dot{\varepsilon} r}{U\cos\alpha} d\alpha, \dot{\varepsilon} = \frac{V}{2\pi r^2} f(\alpha) \rightarrow \varepsilon = \frac{V}{2\pi U}\int_{\alpha_0}^{\alpha} \frac{f(\alpha)}{[x_0 - V/(2\pi U)\cdot(\alpha_0 - \alpha)]} d\alpha$$

Equation 10-16

10.1.4 The lower boundary condition

The lower boundary of the strain path integral, (α_0) in Equation 10-16 represents the undisturbed upstream flow corresponding to the $z_0 = -\infty$ level. To solve the strain integral numerically, this lower boundary needs to be estimated with a finite value ($z_0 \neq -\infty$). The lower boundary of the integral was set to a level on which the vertical component of the superimposed velocity was η times the uniform velocity at infinity

(U). The (z_0) level corresponding to the (α_0) was determined by solving Equation 10-17:

$$v_z = \eta U \rightarrow z_0 = -V/[2\pi U(1-\eta)] = -w/[\pi(1-\eta)]$$ **Equation 10-17**

For η=99% for example, the lower boundary should be set at z_0= -31.8w below the origin (i.e. 31.5w below the tip).

10.1.5 The fluid pressure

To solve a flow model in FLAC, pressure differences must be defined for external boundaries. For a known velocity (v_z), the pressure difference ($p-p_0$) can be determined by integrating Darcy's law (Equation 10-18), where (k) is the permeability:

$$v_z = -k\frac{\partial p}{\partial z} \rightarrow p = p_0 - \frac{1}{k}\int v_z dz$$ **Equation 10-18**

Alternately, the correlation between the potential function (Φ) and velocity (Appel *et al.*, 1965) can be used to calculate the velocity integral (Equation 10-19):

$$v_z = \frac{\partial \Phi}{\partial z} \rightarrow \int v_z dz = \Delta\Phi$$ **Equation 10-19**

Combining these equations gives Equation 10-20, which shows the correlation between the pressure difference and the potential function:

$$p = p_0 - \frac{1}{k}\Delta\Phi$$ **Equation 10-20**

Therefore, to derive pressure differences for the external boundaries in various FLAC flow models, it is necessary to determine the potential function for the flow around "simple wall". The potential function (Φ) for the flow field can be calculated by integrating the velocity, Equations 10-21, 10-22 and 10-23:

$$v_x = \frac{\partial \Phi}{\partial x} \rightarrow \Phi = \int v_x dx + f(z) = g(x,z) + f(z) \qquad \textbf{Equation 10-21}$$

$$v_z = \frac{\partial \Phi}{\partial z} \rightarrow v_z = \frac{\partial g(x,z)}{\partial z} + f'(z) \rightarrow f(z) = \int \left(v_z - \frac{\partial g(x,z)}{\partial z} \right) dz + C \qquad \textbf{Equation 10-22}$$

$$\Phi = g(x,z) + \int \left(v_z - \frac{\partial g(x,z)}{\partial z} \right) dz + C \qquad \textbf{Equation 10-23}$$

Consequently, for the flow field around the "simple wall", the potential function (Φ) is given as Equation 10-24, where C is the integral constant:

$$\Phi = \frac{V}{2\pi} \ln(r) + Uz + C \qquad \textbf{Equation 10-24}$$

By substituting Equation 10-24 into Equation 10-20, the pressure can be calculated at any point in the flow around the "simple wall".

10.2 Flow equations around the "simple wedge"

This appendix summarises the closed-form solutions for flow characteristics around the "simple wedge" geometry.

10.2.1 The velocity of the superimposed flow

Superposition was used to derive the velocity equations for the flow around the "simple wedge". For a line source/sink with strength of $V_i[LT^{-3}]$ located at $(0,- d_i)$, the velocity equations are given by Equation 10-25:

$$v_{xi} = \frac{V_i \cdot x}{2\pi(x^2 + (z - d_i)^2)}, \quad v_{zi} = \frac{V_i \cdot (z - d_i)}{2\pi(x^2 + (z - d_i)^2)}$$

Equation 10-25

The "simple wedge" was created by superimposing a series of singularities (source/sink) to a uniform flow with the velocity of $U[LT^{-1}]$. Consequently, the velocity equations for the flow around the "simple wedge" have the form of Equation 10-26:

$$v_x = \sum_i \frac{V_i \cdot x}{2\pi(x^2 + (z - d_i)^2)}, \quad v_z = \sum_i \frac{V_i \cdot (z - d_i)}{2\pi(x^2 + (z - d_i)^2)} + U$$

Equation 10-26

10.2.2 The geometry of the "simple wedge"

Superposition was applied to derive the stream function (Ψ) for the flow field around the "simple wedge" (Equation 10-27):

$$\Psi = -Ux + \frac{1}{2\pi}\sum_i V_i \tan^{-1}\left(\frac{z-d_i}{x}\right) - \frac{1}{4}\sum_i V_i$$ **Equation 10-27**

The value of the stream function (Ψ_0) for the half-body is given in Equation 10-28:

$$\Psi_0 = -\sum_i \frac{V_i}{2}$$ **Equation 10-28**

In common with the procedure adopted for the "simple wall", by substituting Equations 10-27 and 10-28 in Equation 10-6, the coordinates (x,z) of the "simple wedge" profile can be determined. The coordinates of the tip was determined by numerically solving Equation 10-7. Having the general stream function expression (Ψ) and the value of stream function for the half-body(Ψ_0), the half-width (w) of the "simple wedge" was determined from Equation 10-8, and is given in Equation 10-29:

$$w = \frac{1}{2U}\sum_i V_i$$ **Equation 10-29**

10.2.3 Strain rates and strain paths

Partial derivate of the velocity equations provided the strain rates, which are shown in Equations 10-30, 10-31 and 10-32:

$$\dot{\varepsilon}_{xx} = \sum_i \frac{V_i}{2\pi}\frac{x^2-(z-d_i)^2}{(x^2+(z-d_i)^2)^2}$$ **Equation 10-30**

$$\dot{\varepsilon}_{zz} = \sum_i \frac{V_i}{2\pi}\frac{(z-d_i)^2-x^2}{(x^2+(z-d_i)^2)^2}$$ **Equation 10-31**

$$\dot{\varepsilon}_{xz} = \sum_i \frac{V_i}{\pi}\frac{x(z-d_i)}{(x^2+(z-d_i)^2)^2}$$ **Equation 10-32**

The conservation of volume was upheld as the sum of principal strain rates were equal to zero. Due to the complexity of strain rate functions ($\varepsilon^{\cdot}_{ij}$), the strain path integral was solved numerically (sum of increments), Equation 10-33:

$$\varepsilon \approx \sum \dot{\varepsilon} \frac{ds}{v}$$ **Equation 10-33**

In this equation, (ds) is a small segment of the streamline and (v) is the flow velocity, which was assumed to be constant over (ds).

10.2.4 The lower boundary condition and the pressure

Equation 10-17 can be solved for an intended value of η to determine the location of the lower boundary for the strain sum, which estimates the undisturbed flow at upstream. The potential function (Φ) for the superimposed flow utilized to determine the pressure difference on the boundaries in FLAC models (Equation 10-20) was derived by solving Equations 10-21, 10-22 and 10-23 and is given in Equation 10-34:

$$\Phi = \sum_{i} \frac{V_i}{4\pi} \ln\left(x^2 + \left(z - d_i\right)^2\right) + Uz + C$$ **Equation 10-34**